High-resolution detectors for soft X-ray spectroscopy

Thesis

High-resolution detectors for soft X-ray spectroscopy

Thesis submitted for the degree of

Doctor of Philosophy

at The Open University

by

Matthew Richard Soman

e2v Centre for Electronic Imaging

Department of Physical Sciences

The Open University

18 March 2014

High-resolution detectors for soft X-ray spectroscopy

Matthew Richard Soman

Abstract

Resonant Inelastic X-ray Scattering (RIXS) is a modern soft X-ray spectroscopy technique used to investigate the structure of and excitations in materials. It requires high resolution spectrometers and a brilliant, tunable, X-ray source and therefore is carried out at spectrometers such as SAXES at the Swiss Light Source Light, a synchrotron at the Paul Scherrer Institut.

SAXES uses a grating to disperse X-rays scattered from a sample across a position sensitive detector, a Charge-Coupled Device (CCD). It has been recognised that the spatial resolution of the CCD currently limits the spectrometer resolution and therefore the investigations described in this thesis focus on developing and testing methods of improving the detector resolution. Whilst this thesis addresses improving the resolution of the detector at SAXES specifically, the methods and results are applicable to other applications requiring high spatial resolution soft X-ray detection.

After an introduction, Chapters 2 and 3 describe the importance of RIXS, operation of SAXES and background of soft X-ray detection in CCDs. A comparison of models that describe charge spreading in a CCD is in Chapter 4, and the best model is implemented in a simulation package that generates populations of soft X-ray events. Chapter 5 explores the resolution improvements possible through applying centroid algorithms to simulated X-ray events, and Chapter 6 begins by describing experimental work undertaken to verify simulation results. Due to the limitations of applying centroiding algorithms to the current SAXES camera, a small-area Electron Multiplying CCD (EM-CCD) is experimentally tested (Chapter 7). Results with the EM-CCD proved positive, therefore in Chapter 8 the spatial resolution achievable with a large area EM-CCD is verified for a future SAXES camera upgrade.

Due to the successful results presented in this thesis, negotiations to develop a new camera system for SAXES are underway, and interest from other RIXS beamlines in the community may lead to the work also being applied elsewhere. The detection of soft X-rays with high spatial resolution is applicable to other future CCD and EM-CCD instruments, such as astronomical X-ray observatories.

Declaration

I hereby declare that no part of this thesis has been previously submitted to this or any other university as part of the requirement for a higher degree. The work described herein was conducted solely by the undersigned except for those colleagues and other workers acknowledged in the text.

Matthew Richard Soman

18 March 2014

Dedication

To Mum, Dad and Charlotte.

Acknowledgements

I would like to acknowledge my gratitude to a number of people for their help and encouragement over the duration of my thesis.

Firstly, thanks to my supervisors David Hall, Andrew Holland, Bernd Schmitt and Thorsten Schmitt for their guidance and support.

Thanks to David Burt and Mark Robbins for imparting fractions of their vast knowledge and experiences on me.

Thanks to all the current and former members of the Centre for Electronic Imaging who provided friendship, entertainment and insight during the last three years: Edgar Allanwood, Simeon Barber, Ross Burgon, Andrew Clarke, Ben Dryer, James Endicott, Anthony Evagora, Jason Gow, Tom Greig, Karen Guyler, Richard Harriss, Nick Johnston, Salah Karout, Calum MacCormick, Neil Murray, Joseph Rushton, Phillipa Smith, Konstantin Stefanov, James Tutt and Daniel Weatherill.

Thanks to my friends and colleagues at the Open University who have all helped make the past three years an enjoyable and memorable experience. There are far too many of you to include here, but there are some names that come to mind: Jessica Barnes, Rob Farmer, James Holmes, Jonathon Keelan, Kathryn McDermott, Mohit Melwani Daswani, Pete Landsberg, Andreas Morlock, James Mortimer, Ziad el-Otell, Manish Patel, Samantha Rolfe, Ben Rozitis, Joshua Snape. A special mention must go to the Department of Physical Sciences football and cricket teams who have charitably included me in their activities.

I would like to thank my parents, Edward, Victoria and Claire for their invaluable support and encouragement to continue doing what I enjoy. Thanks also to Charlotte for her help, advice and motivation.

I would like to gratefully acknowledge the financial support and in-kind benefits received from the Open University, the Paul Scherrer Institut and e2v technologies plc. during my research studentship.

Finally I would like to thank the collaborators that I have had over the course of my studies for their help, support and expertise. They include Jörg Raabe and Benjamin Watts at the PolLux endstation, and Vladimir Strocov, Valentina Bisogni and Xiaoqiang Wang at the ADRESS beamline.

The PolLux endstation was financed by the German Minister für Bildung und Forschung (BMBF) through contracts 05KS4WE1/6 and 05KS7WE1. Some data contained in this thesis was obtained using the ADRESS beamline and the SAXES instrument jointly built by Paul Scherrer Institut, Switzerland and Politecnico di Milano, Italy.

List of Acronyms

ADRESS	ADvanced RESonant Spectroscopy
AIMO	Advanced Inverted Mode Operation
ARPES	Angle-Resolved PhotoEmission Spectroscopy
AXES	Advanced X-ray Emission Spectrometer
BBC	British Broadcasting Corporation
BW	Bandwidth
CCD	Charge-Coupled Device
CDS	Correlated Double Sampling
DC	Direct current
DOS	Density Of States
e2v	e2v technologies plc.
EM-CCD	Electron Multiplying Charge-Coupled Device
EPICS	Experimental Physics and Industrial Control System
ESRF	European Synchrotron Radiation Facility
FET	Field Effect Transistor
FIM	Fisher Information Matrix
FWC	Full Well Capacity
FWHM	Full Width at Half Maximum
FZP	Fresnel Zone Plate
IMO	Inverted Mode Operation
MCA	MATLAB Channel Access
MCP	Microchannel Plate
MOS	Metal-Oxide-Semiconductor
MOSFET	Metal-Oxide-Semiconductor Field Effect Transistor
NIMO	Non-Inverted Mode Operation
NXES	Normal/Non-resonant X-ray Emission Spectroscopy
OSA	Order Sampling Aperture
PCB	Printed Circuit Board
PES	Photoemission Spectroscopy
PGM	Plane-Grating Monochromator
PSF	Point Spread Function
PSI	Paul Scherrer Institut
PV	Process Variable
QE	Quantum Efficiency

RF	Radio Frequency
RIXS	Resonant Inelastic X-ray Scattering
RXES	Resonant X-ray Emission Spectroscopy
SAXES	Super Advanced X-ray Emission Spectrometer
SLS	Swiss Light Source
SXA	Soft X-ray Absorption
UPS	Ultraviolet Photoelectron Spectroscopy
UV	Ultraviolet
VLS	Variable Line Spacing
XES	X-ray Emission Spectroscopy
XPS	X-ray Photoelectron Spectroscopy

Contents

Chapter 1: Introduction

1.1 Background

A collection of techniques are used in soft X-ray spectroscopy to enable scientists to explore the links between a material's structure and properties. Resonant Inelastic X-ray Scattering (RIXS) is one technique that has become a vital contributor to this field through probing low energy charge, spin, orbital and lattice excitations in materials. For example, the first experimental observation of the electron's orbital degree of freedom being separated from its charge and spin degrees of freedom [1] as well as magnetic excitations in transition metal oxides [2,3] have recently been reported in prestigious journals. The emergence of RIXS as a powerful technique in the last few decades has been due to the development of high brilliance X-ray sources and improved instrumentation that compensate for both the photon-starved aspects and high resolution requirements of the technique.

The latest generations of soft X-ray RIXS spectrometers have been designed around a grating that disperses X-rays scattered from the sample of interest across a 2D position-sensitive detector (for example [4–7]). The detector image is converted into a single spectrum and combined with spectra at other scattering angles and incident X-ray energies and polarisations to build up a RIXS dataset for the sample of interest. To resolve excitations in the spectra smaller than 0.1 eV, an overall resolving power ($E/\Delta E$) of greater than 10 000 is required at 1000 eV. The Super Advanced X-ray Emission Spectrometer (SAXES) has a resolving power of greater than 12 000 at 930 eV, including contributions from the X-ray spot size on the sample, the grating slope error and the detector spatial resolution. To further extend the RIXS technique to observe lower energy excitations and narrower features in spectra, the instrumentation is undergoing continual development; detector resolution is currently a limiting factor therefore is a main priority.

1.2 Research goals

The research goal of this thesis is improve the science output of SAXES by enhancing the spatial resolution of its soft X-ray camera, whilst developing results and techniques applicable in many other fields of soft X-ray spectroscopy. The resolution is currently limited by diffuse spreading of charge in the detector which is larger than the pixel structure of the CCD: the charge cloud generated by a single X-ray photon spreads across several pixels reducing the spatial resolution. However, the distribution of signal amongst pixels in the observed X-ray event is known to depend on the photon's interaction position (e.g. [8,9]) and therefore to improve the spatial resolution of the detector at SAXES it is recognised that the camera could operate in a single

photon counting mode and the events could be processed to estimate each X-ray's interaction position to a sub-pixel resolution.

To achieve this goal, a study of the detection process in the camera system has been undertaken. Models of the diffusion-dominated charge spreading in the literature have been compared with a model derived here. All models have been compared to the pixel signal distributions observed in experimental data taken in later studies as described in this thesis. To further the study of charge spreading in the field-free regions of back-illuminated CCDs, the average charge cloud shape has been measured in the current and a new device (an Electron-Multiplying CCD) using experimental data, giving significant insight into the theoretical studies in the literature.

A second theme of study has been the development and testing of centroiding algorithms applied to events in CCDs. The most accurate model of the charge spreading has been implemented as part of a bespoke Monte Carlo simulation package, developed by the author as part of this research, to generate typical X-ray events observed in a CCD and allow the algorithms developed to be improved and fully compared. Populations of X-ray events have been used to investigate the accuracy and systematic errors of centroiding algorithms as a function of sub-pixel position. Non-linear corrections to linear centroiding algorithms have been investigated to compensate for inherent systematic biases and improve the overall accuracy and resolution. Experimental campaigns have been undertaken to record X-ray events for interactions occurring in a *known* sub-pixel location; the data collected allows the typical X-ray events and centroiding algorithm accuracy to be determined for X-rays interacting in any of the probed sub-pixel locations, whilst also providing vital data for other areas of this study.

The third theme of study towards achieving the research goal has been to apply the understanding and algorithms developed in the first two study themes to improve the camera at SAXES in the first instance, paving the way for applications on other RIXS facilities in the future (such as at the Advanced X-ray Emission Spectrometer (AXES) at the ID08 beamline of the European Synchrotron Radiation Facility (ESRF) and the new spectrometer at the I21 beamline currently under construction at Diamond [10]). The proof of principle experimental results achieved with a small area version (CCD42-10) of the current SAXES detector (CCD42-40) have been directly applicable to the current camera system, however the EM-CCD has been proposed as a more suitable detector for the photon-counting mode of operation required to apply centroiding algorithms at SAXES. Following this, a successful experimental campaign has been undertaken with a small area EM-CCD sensor (CCD97) demonstrating the feasibility of using an EM-CCD in a future camera at SAXES and other RIXS spectrometers. A final experimental campaign was undertaken to validate centroiding with single X-rays observed with a suitably large

area EM-CCD, the CCD207-40. To inform the decision-making process, the effect of two primary specifications of a future CCD207-40 based camera, the readout rate and X-ray angle of incidence, on performance of the camera at SAXES have been investigated.

The work carried out for this thesis was funded under collaboration between the Paul Scherrer Institut (PSI), the Open University and e2v technologies plc. (e2v), and data has been utilised from experiments undertaken at SAXES[1] and the PolLux spectromicroscope[2] at the Swiss Light Source.

1.3 Thesis organisation

This thesis is organised into nine chapters including this introduction. Background information and introductions to the topics relevant to the investigations in this thesis are contained in Chapters 2 and 3. Chapter 2 introduces dispersive soft X-ray spectroscopy in more detail, then describes the processes of the RIXS technique, its advantages and limitations, and the facilities at the Swiss Light Source (SLS) used to apply it. The resolution contributions to SAXES are described, along with the predicted improvements of the current upgrade plan (including the primary goal of an improved detector spatial resolution). Chapter 3 reviews the structure and operation of CCDs and EM-CCDs, and the noise sources dominant in the SAXES camera and the experimental setups used in later testing. The PolLux facility, a spectromicroscope at the SLS is introduced as a facility that can focus soft X-rays to a spot much smaller than the pixel size of a CCD.

Chapter 4 presents the model investigation and Monte Carlo package written to simulate soft X-ray events in CCDs. This software package is then applied in Chapter 5 to investigate the application of centroid algorithms to simulated single X-ray interaction events in CCDs and EM-CCDs.

Chapter 6 reviews the application of centroid algorithms to single photons experimentally observed by a standard CCD with the same architecture as the current CCD at SAXES. The X-rays are focussed to a sub-pixel location so the accuracy of centroiding algorithms can be measured. Following this proof of principle, the centroiding algorithms are applied to example images of spectra recorded at SAXES with the current camera.

Chapter 7 describes the results from another experimental campaign, where X-rays are focussed on sub-pixel areas of a standard EM-CCD (CCD97), as a proof of principle. In Chapter 8, a further test campaign is undertaken on a large area device (CCD207-40), to verify its suitability for a

[1] SAXES is a joint project of the PSI and of the Politecnico di Milano. The SAXES spectrometer is property of the Swiss Light Source at the PSI.

[2] The PolLux endstation was financed by the German Minister für Bildung und Forschung (BMBF) through contracts 05KS4WE1/6 and 05KS7WE1.

camera upgrade that has come about as a consequence from this study. Some suggested specifications of the future camera at SAXES based on the CCD207-40 are discussed. In the final chapter the work in this thesis is concluded and possible directions of future research are outlined.

1.4 Publications

Some of the results obtained by the author during the preparation of this thesis have been published within the following papers.

1) D. J. Hall, J. H. Tutt, **M. R. Soman**, A. D. Holland, N. J. Murray, B. Schmitt, and T. Schmitt, "High-resolution soft X-ray spectrometry using the Electron-Multiplying Charge-Coupled Device (EM-CCD)," *UV, X-Ray, and Gamma-Ray Space Instrumentation for Astronomy*, San Diego, SPIE 2013.
2) **M. R. Soman**, D. J. Hall, J. H. Tutt, N. J. Murray, A. D. Holland, T. Schmitt, J. Raabe, and B. Schmitt, "Developing a CCD camera with high spatial resolution for RIXS in the soft X-ray range," *Nuclear Instruments and Methods in Physics Research Section A: Accelerators, Spectrometers, Detectors and Associated Equipment*, pp. 1–6, May 2013.
3) **M. R. Soman**, D. J. Hall, J. H. Tutt, N. J. Murray, a D. Holland, T. Schmitt, J. Raabe, and B. Schmitt, "Improving the spatial resolution of soft X-ray detection using an Electron-Multiplying Charge-Coupled Device," *Journal of Instrumentation*, vol. 8, no. 01, p. C01046, Jan. 2013.
4) D. Hall, **M. Soman**, J. Tutt, N. Murray, A. Holland, T. Schmitt, J. Raabe, V. N. Strocov, and B. Schmitt, "Improving the resolution in soft X-ray emission spectrometers through photon-counting using an Electron Multiplying CCD," *Journal of Instrumentation*, vol. 7, no. 01, p. C01063, Jan. 2012.
5) J. Tutt, A. Holland, N. Murray, R. Harriss, D. Hall, and **M. Soman**, "Electron-multiplying CCDs for future soft X-ray spectrometers," *Journal of Instrumentation*, vol. 7, no. 02, p. C02031, Feb. 2012.
6) D. Hall, A. Holland, and **M. Soman**, "The influence of electron multiplication and internal X-ray fluorescence on the performance of a scintillator-based gamma camera," *Nuclear Instruments and Methods in Physics Research Section A: Accelerators, Spectrometers, Detectors and Associated Equipment*, 2012.
7) **M. R. Soman**, D. J. Hall, J. H. Tutt, N. J. Murray, A. D. Holland, T. Schmitt, J. Raabe, and B. Schmitt, "Improving the spatial resolution of a soft X-ray Charge Coupled Device used for

Resonant Inelastic X-ray Scattering," *Journal of Instrumentation*, vol. 6, no. 11, p. C11021, Nov. 2011.

8) J. H. Tutt, A. D. Holland, N. J. Murray, R. D. Harriss, D. J. Hall, **M. Soman**, R. L. McEntaffer and J. Endicott, "The use of EM-CCDs on high resolution soft x-ray spectrometers," *UV, X-Ray, and Gamma-Ray Space Instrumentation for Astronomy XVII, 21-24 Aug 2011, San Diego,* SPIE, vol. 44, 2011.

Chapter 2: Dispersive Soft X-ray Spectroscopy and RIXS

2.1 Introduction

A material's electron configuration controls the majority of its characteristics. Photons emitted when electrons decay to a lower energy shell whilst orbiting an atom are X-rays, typically with an energy between 150 eV and 10 000 eV for shells close to the nucleus, and therefore the X-ray spectrum of a material can be useful for understanding the structure of a material and explaining its characteristics. Non-dispersive instruments use the intrinsic energy resolution of a detector to measure an X-ray spectrum, for example a Si(Li) diode in an electron microscope, or the Swept Charge Device of the C1XS instrument on Chandrayaan-1 [11]. However for instruments with increased resolution requirements, a high resolving power can be achieved by dispersing the X-ray spectrum with a grating across a position sensitive detector such that the spatial position on the detector determines the energy of the X-ray. Energy dispersive X-ray spectrometers include the Reflection Grating Spectrometer on board XMM-Newton [12], and the Super Advanced X-ray Emission Spectrometer (SAXES) at the Swiss Light Source [7].

SAXES is designed to investigate exotic properties exhibited by materials using Resonant Inelastic X-ray Scattering (RIXS), an X-ray spectroscopy technique that has developed significantly in the last few decades due to the intensity of X-ray sources increasing dramatically together with improvements to the resolution of dispersive X-ray spectrometers. The work described in this thesis contributes to the continued development of instrumentation by focussing on resolution improvements, specifically for SAXES. However, results are also applicable to other soft X-ray dispersion spectrometers, e.g. AXES at ESRF [13], the RIXS facility currently under construction at Diamond's I21 beamline due for completion in 2016 [10], and future astronomical X-ray observatories.

2.2 X-ray spectroscopy

Spectroscopic techniques are powerful tools in modern physics used to understand the structure of, and excitations in, materials. RIXS is one such tool that has become more readily available due to the advancement in intense X-ray sources and improved resolution spectrometers. RIXS is introduced in this section in the context of a range of other spectroscopic techniques, whilst further details, the theory behind the observations and descriptions of notable results can be found in the review papers by Kotani and Shin [14], Hämäläinen and Manninen [15], Ament *et al*. [16], and references therein.

2.2.1 Spectroscopy

When an atomic, molecular or solid state material structure is in its ground state, electrons occupy the lowest energy states obeying the Pauli Exclusion Principle. An interaction of sufficient energy can excite an electron from its ground state to a higher energy state that was previously unoccupied. The system, now in its excited state, may relax (i.e. decay) back into the ground state through an electron from a higher energy state relaxing into the currently unoccupied low energy state. Different spectroscopy techniques investigate a range of electron excitation and decay pathways to determine the electronic structure of the material, from which some of the material's properties may be explained.

The bound electron energy states can be divided into core states – with the highest binding energies – and valence states which are least bound. The core states are spatially distributed closest to the nucleus and therefore are most affected by the quantity of charge in the nuclei of different elements. The valence states are most involved in the bonding and conduction between atoms in molecules or solids and therefore the distribution of electrons in the valence states is responsible for the majority of the physical and chemical material properties.

2.2.2 X-ray spectroscopy techniques

A wide range of X-ray spectroscopy techniques exist for investigating the energy and occupancy levels of electron orbitals of materials. Processes relevant to introducing and describing RIXS will be discussed here, and are illustrated in Figure 2.1.

When a photon excites a core electron, it becomes unbound from the atom if the photon energy is sufficiently high, otherwise the electron is excited to an unoccupied valence state. The now empty energy state in the core is termed a 'hole'. The hole is filled by an electron decaying from the valence band in a time period on the order of femtoseconds [17].

Tuning the incident photon energy to between approximately 20 eV and 5000 eV provides sufficient energy to excite a shallow core electron to an empty valence state. Observing the amount of absorption across a range of photon energies, known as Soft X-ray Absorption (SXA) spectroscopy [18], allows the energies of unoccupied valence states to be determined (Figure 2.1, SXA).

The decay of a valence band electron into the hole can occur by emission of a photon with energy equivalent to the gap between the two energy states (fluorescence) or by the emission of an Auger electron. In Auger emission, the energy gap between the two energy states of the decaying

electron is used to release an electron which is less bound to the atom (Figure 2.1, Auger electron emission). The kinetic energy of the Auger electron will be equal to the difference in the decaying electron's energy gap and the binding electron of Auger electron. Observation of Auger electrons is known as Auger spectroscopy and provides information about the occupied valence energy states [19].

The technique that measures the energy of electrons released when a sample is illuminated by photons can be called Photoemission Spectroscopy (PES). PES itself can be subdivided into two categories depending on the photon energy. The first, Ultraviolet Photoelectron Spectroscopy (UPS) uses lower energy photons in the Ultraviolet (UV) range; electrons are excited from the occupied valence band (Figure 2.1, UPS). In the second, X-ray Photoelectron Spectroscopy (XPS), photons have sufficient energy to excite electrons from the core energy states (Figure 2.1, XPS). UPS and XPS probe different regions of the occupied band structure in material and are sometimes referred to as Valence Band PES and Electron Spectroscopy for Chemical Analysis respectively.

PES is particularly sensitive to the surface region of a material due to the absorption length of the electrons. To investigate the bulk of a material, emitted X-rays are a more suitable probe because they are less attenuated by the surface layers of material than electrons. X-ray Emission Spectroscopy (XES) can be subdivided into either Normal/Non-resonant X-ray Emission Spectroscopy (NXES) or Resonant X-ray Emission Spectroscopy (RXES), depending on the excited state of the atom. When a core electron has been excited into the high energy continuum (ionising the atom), the decay process can be treated as a separate step to the excitation process, termed NXES (Figure 2.1, NXES) [14].

In RXES a core electron is excited into an empty valence state and the core hole is subsequently filled from a valence electron. If the decaying electron is the same as the excited one, the X-ray emitted has the same energy and the process is therefore elastic (Figure 2.1, RXES: Elastic contribution). Inelastic scattering occurs if a different electron decays from the valence band, as the emitted X-ray will have a different energy to the excitation photon. Inelastic scattering in RXES is known as Resonant Inelastic X-ray Scattering (Figure 2.1, RIXS).

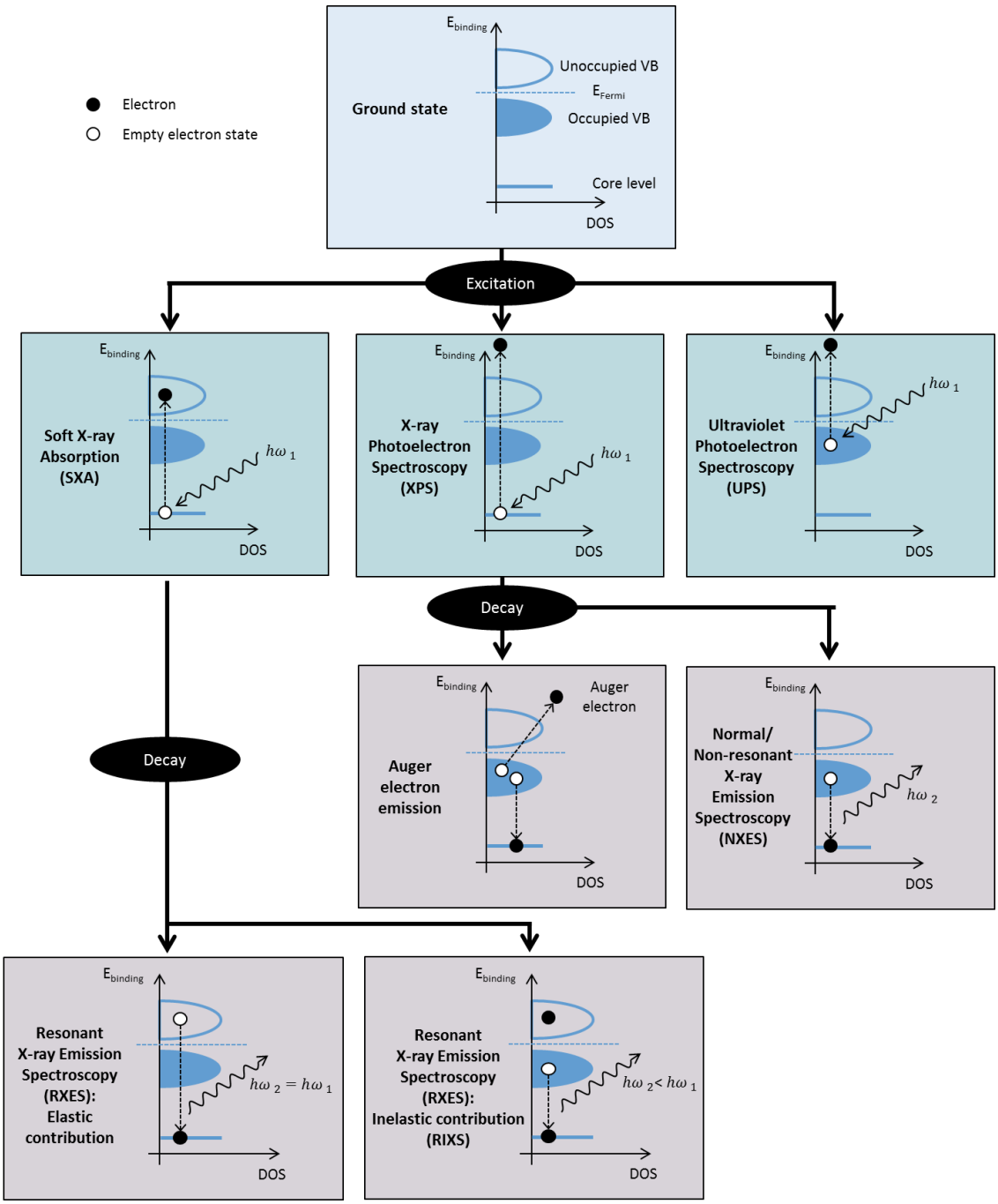

Figure 2.1. Illustrations of a selection of excitation and decay processes observed using the spectroscopic techniques described in the text.

2.2.3 The advantages of Resonant Inelastic X-ray Scattering

NXES and RXES are second-order optical processes as they include both excitation and decay steps; a greater level of information can be obtained by them than the first-order processes on their own [16]. Other advantages of RIXS are set out below;

- **Energy and momentum dependence**: The range of momenta that can be transferred by a scattering X-ray photon is greater than that of neutrons and electrons with a similar

wavelength, therefore a wider range of the scattering space can be probed using X-ray photons.

- **Polarisation dependence**: If the incident light can be polarised, or the polarisation of the emitted photon can be measured, the excitations allowed by angular momentum conservation during the scattering process can be investigated.
- **Bulk sensitivity**: The attenuation length of X-rays is sufficiently long to excite electrons at sites in the bulk of a sample, complementing more surface sensitive techniques.
- **Elemental and atomic site selectivity**: By tuning the incident photon energy to the absorption edge of a particular element, the technique can excite electrons from the core of that element allowing the environment of specific elements in the material to be investigated individually. When the absorption edges of the same element in different atomic sites are affected differently by their chemical bonding, atomic site selectivity can also be achieved.
- **Only small sample volumes required**: Compared to neutrons, X-rays interact more strongly, can be generated at higher intensities, and can easily be focussed therefore a smaller sample can be used. When the sample is a new experimental material that is currently difficult or impossible to produce in larger volumes, this is a significant advantage.
- **Extreme sample environments possible**: RIXS is a photon-in/photon-out technique so magnetic and electric fields or high pressure environments can be applied to samples during experimentation.

Other spectroscopic techniques such as Angle Resolved Photoelectron Spectroscopy (ARPES) and neutron scattering are commonly used instead of or to complement RIXS measurements. In ARPES, electrons excited from a material by a photon beam are measured to probe materials [20]. Electrons have a short attenuation length in solids, therefore ARPES is surface rather than bulk specific. Neutrons are electrically neutral and therefore are bulk sensitive as they penetrate further into materials but are also suitable probes for investigating magnetic excitations in materials as they have spin ½. However, the relatively low interaction cross-section of neutrons with matter means large samples are required, which can make manufacture of the sample as or more difficult than the scattering experiment itself [16].

2.2.4 Excitations probed with RIXS

The RIXS process is charge neutral as the same number of electrons remain in the material after the scattering process, therefore it can only be used to observe charge-neutral excitations. Excitations that may be observed in a RIXS spectrum are described in Table 2.1.

Table 2.1. Charge-neutral excitations observed by RIXS, and their typical energy scales.

Excitation	Description	Typical energy scale
Plasmon	Oscillations in the free electron density with respect to the ion lattice	10 eV
Charge transfer	Excitations that allow electrons to hop through the lattice structure (including exciton states)	2 eV to 5 eV
d-d	Crystal field transitions between different *d* orbitals	0.25 eV to 2 eV
Magnon	Collective magnetic excitations	0.3 eV
Phonon	Lattice vibrations	0.01 eV

Example RIXS spectra are shown in Figure 2.2 b, from [21]. The X-ray intensity is plotted relative to the energy lost during the scattering process and therefore the elastic scattering peak is identified at 0 eV energy loss. More complicated generation mechanisms are responsible for the other features in the spectra; X-ray fluorescence is observed at energy losses greater than 4.5 eV in a broad and intense feature; and the sharp features around an energy loss of 2 eV are due to *d-d* excitations. Further analysis can be found in the original paper [21].

RIXS has been limited until the last few decades due to the technique requiring a high intensity, tunable and monochromatic X-ray source typical of a synchrotron coupled with a spectrometer with an energy resolving power ($E/\Delta E$) in the order of 10^4. To record each RIXS spectrum in Figure 2.2 b, a state-of-the-art X-ray radiation source and spectrometer were used: the SAXES instrument at the Swiss Light Source, facilities further described in Sections 2.3.1 and 2.4. The spectrometer's energy resolution was 60 meV ($E/\Delta E > 8800$), and each spectrum was acquired over a period of 2 hours.

A highly brilliant X-ray source is required because RIXS has an intrinsically low cross-section. The yield of Auger electron emission is much higher than that of X-ray emission for lighter elements (Figure 2.3), and the cross-section of the second-order process is significantly smaller than for first-order processes (e.g. SXA or XES). Additionally, X-ray optics must be at glancing incidence

which results in low efficiencies and a small solid angle being collected by the detector. The X-ray source must have a tunable energy to adjust the incident X-ray energy to different portions of the absorption edges.

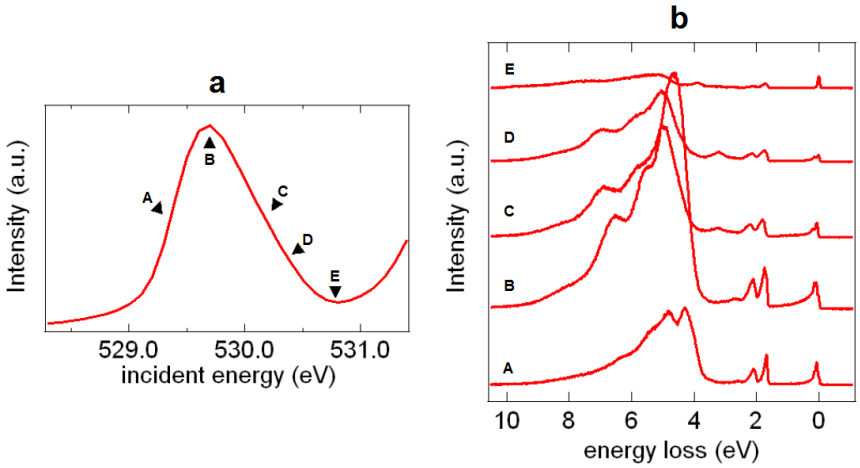

Figure 2.2. ***(a)*** *XAS and* ***(b)*** *RIXS spectra around the oxygen K-edge for a Li_2CuO_2 sample. The RIXS spectra are obtained using the incident photon energies A to E marked on the XAS and are shown with intensities normalised to the incident intensity, from* [21].

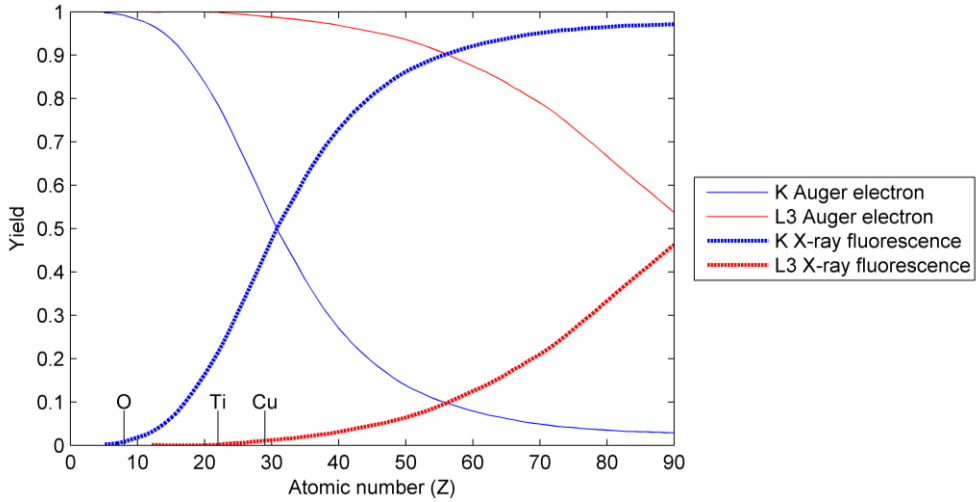

Figure 2.3. Lighter elements with lower atomic numbers have a significantly lower yield of X-ray fluorescence than the Auger electrons, data from [22]. *The atomic numbers of oxygen (O), titanium (Ti), and copper (Cu) have been marked for reference.*

2.3 Generation of soft X-rays for RIXS

Synchrotron facilities are used to generate highly intense beams of broad-band photons, through the emission of synchrotron radiation. Beamline optics focus and monochromate the light cones, commonly to a small area on a sample with a small width in energy space, and observations are made depending on the experimental procedure. The Advanced Resonant Spectroscopy (ADRESS) beamline at the Swiss Light Source (SLS) synchrotron facility has an endstation dedicated to RIXS. The following sections describe the generation of synchrotron radiation at the SLS, and how the light cone is monochromated and focussed by ADRESS.

2.3.1 Swiss Light Source

The SLS is a third generation synchrotron facility producing electromagnetic radiation that is focussed onto samples to investigate their structure and behaviour. The electromagnetic radiation is generated through synchrotron radiation, an effect where charged particles moving at relativistic velocities emit photons when accelerated [23]. Synchrotrons harness this effect by orbiting relativistic electrons in a ring structure and collecting the radiation emitted when the electrons are centripetally accelerated. The process at the SLS of accelerating the electrons to relativistic velocities and controlling their path is set out below.

Electrons, excited out of a cathode by applying a potential difference to the anode of 90 kV, are further accelerated to energies of 100 MeV by electromagnetic fields oscillating at a radio frequency (RF) of 3 GHz before being deposited into a booster ring with a diameter of 270 m. Magnets around the booster ring focus and control the path of the electron packets by adapting their field strengths as the electrons are accelerated close to the speed of light by more RF cavities. Electrons with the correct energy, usually 2.4 GeV at the SLS, are injected into packets that circulate around the storage ring of the synchrotron.

The storage ring is an evacuated vacuum system with 12 straight lengths and 12 bends, that define an approximately circular path with a diameter of 288 m. Vacuum with pressures lower than 10^{-9} mbar are maintained inside the storage ring to limit the number of electrons lost due to collisions with residual particles in the ring [24]. However, when the SLS is operating in top-up mode, the number of electrons in the bunches orbiting the storage ring is maintained by adding additional electrons from the booster ring [25]. The electron bunches are focussed into a beam using magnets in quadrupole and sextupole configurations arranged to account for chromatic aberrations [26], and are steered around the storage ring orbit by 12 sets of 3 dipole magnets. The desired side-effect of accelerating the electrons is the release of synchrotron radiation: the production of which is the purpose of the facility.

Synchrotron radiation is produced whenever charged particles (electrons at the SLS) that are travelling close to the speed of light are accelerated in a magnetic field. Narrow beams of electromagnetic radiation are emitted tangential to the electron path, meaning that the dipole bending magnets produce a narrow fan of radiation over a continuous energy spectrum. In addition to light production at the bends in the electron orbit, wigglers or undulators can be placed within the straight sections of the ring.

A wiggler is a series of *N* bending magnets that cause the electrons to travel along a sinusoidal path, emitting narrow fans of synchrotron radiation at each turn with a brilliance of approximately a factor *N* times the brilliance of a single bending magnet. The insertion devices at SLS are undulators. Similar to wigglers, the electron beam path through an undulator is sinusoidal but the photon emission is controlled to constructively interfere at particular photon energies. The radiation produced by an undulator is therefore emitted with a narrow spectral width at a given energy and its harmonics at higher energies, with a smaller angular divergence than wiggler radiation. The wavelength of synchrotron light emitted by an undulator, λ_s, is described by Equation 2.1, known as the Undulator Equation [27,28].

$$\lambda_s = \frac{\lambda_u}{2n\gamma^2}\left(1 + \frac{K^2}{2} + \gamma^2\theta^2\right) \qquad \textit{Equation 2.1}$$

$$K = \frac{qB\lambda_u}{2\pi \mathrm{cm}_0} \qquad \textit{Equation 2.2}$$

$$\gamma = 1/\sqrt{1 - \frac{v^2}{c^2}} \qquad \textit{Equation 2.3}$$

The Lorentz factor γ is given by the relationship between the velocity of the orbiting electrons, v, and the speed of light, c, in Equation 2.3 and K is the Undulator Constant (Equation 2.2). λ_u is the period of the magnet structure, n is the harmonic number ($n = 0,1,2,3 \ldots$), θ is the observed angle relative to the direction of motion, B is the magnetic flux density and q and m_0 are the charge and rest mass of an electron respectively. Importantly, the emitted photon energy can be tuned by changing the magnetic flux density, traditionally accomplished by adjusting the gap between the undulator magnet structures. Longitudinal movement is used to manipulate the polarization of the light. However, newer designs such as the UE-44 (used at the ADRESS beamline at the SLS) maintains a constant gap and uses longitudinal movement of the magnet structures to control both the photon energy and polarisation [29,30].

The synchrotron radiation emitted in bending magnets, wigglers and undulators travels tangentially away from the storage ring and selected parts of the electromagnetic spectrum are allowed to pass through ports out towards experimental stations at which the radiation is

required. Along the beamline the radiation is manipulated in both spatial and energy space before it reaches an endstation instrument where the desired radiation can be used for experimentation.

2.3.2 Advanced Resonant Spectroscopy beamline

Whilst a high intensity beam of X-rays is generated by the UE44 undulator source at the ADRESS beamline, the X-rays are divergent and chromatic. The beamline is designed to convert the cone of light into a highly focussed, monochromatic and intense beam of light focussed at the sample position of either the ARPES or RIXS endstation.

The optical configuration is a plane-grating monochromator (PGM) scheme that manipulates the light as follows (Figure 2.4):

- **Front-end baffles**: The central cone of light from the undulator is selected.
- **Collimating mirror**: The light is parallelised in the vertical direction.
- **Pre-mirror and grating**: A grating disperses the photons of different energies in the vertical plane.
- **Focussing mirror**: Photons of the desired energy are focussed in the vertical plane through the exit slits.
- **Slits**: These baffle the undesired energy photons, monochromating the beam.
- **Refocussing mirror**: Finally a refocusing mirror focusses the monochromatic beam onto a sample. If the RIXS endstation is in use, the first refocusing mirror is removed from the optical path.

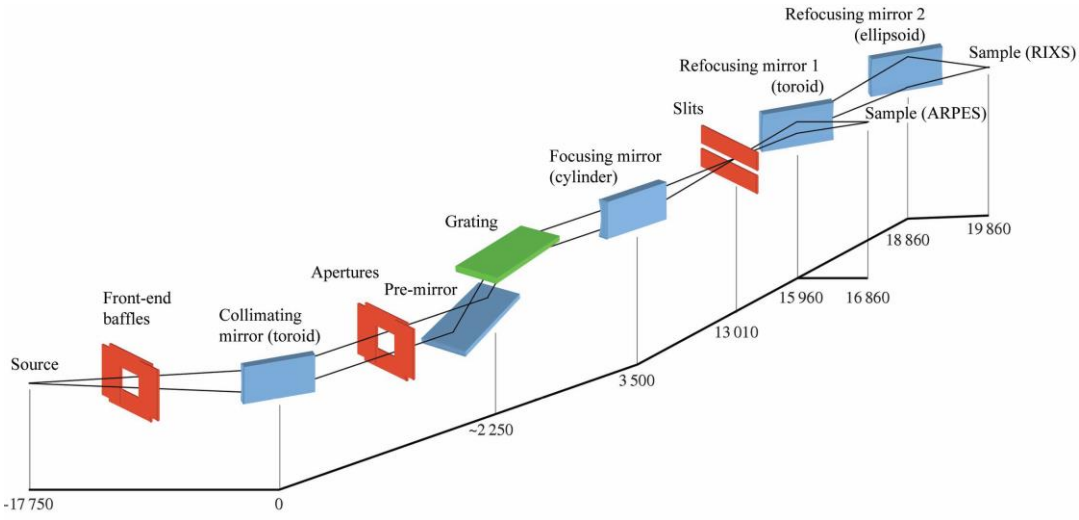

Figure 2.4. The optical components of the ADRESS beamline, from [31]*. The distance scale is shown in millimetres, with an overall length of approximately 37.6 m.*

The design and operation of the beamline optics have been optimised to improve the energy resolution, photon throughput and final spot size at the samples. When operating in a mode to optimise the energy resolution, a resolution of 33 000 (E/ΔE) is achievable at 1 keV, with a flux of approximately 10^{11} photons second^{-1}. Alternatively a high photon flux mode is capable of up to 10^{13} photons second^{-1} with a resolution of 10 000 (E/ΔE). The vertical spot size on the RIXS sample is important to improving the resolution of the RIXS spectrometer (Section 2.4.1), and is smaller than 4.7 µm.

2.4 The Super Advanced X-ray Emission Spectrometer

The RIXS spectrometer at the ADRESS beamline is the Super Advanced X-ray Emission Spectrometer (SAXES), shown in Figure 2.5 and Figure 2.6. Photons from ADRESS are focussed onto a sample of interest, and scattered photons are dispersed by a variable line spacing grating across a detector with 2D resolution. The energy dependence of the photon dispersion angle allows the energy of an X-ray that interacts at the detector to be determined by its position of interaction in the energy dispersive direction.

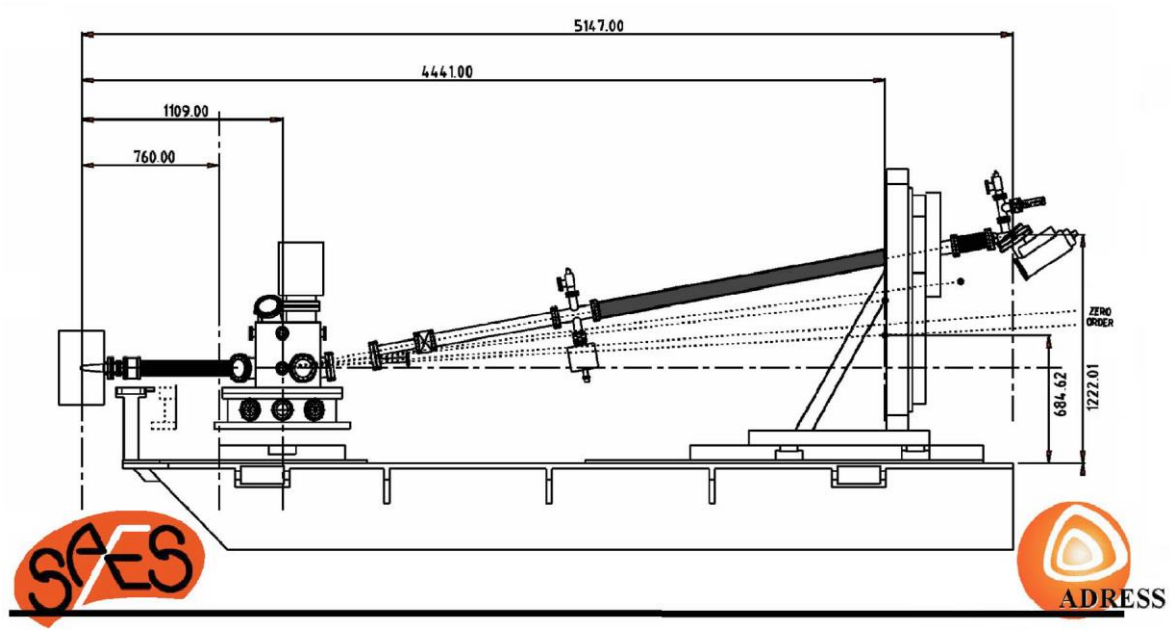

Figure 2.5. Scattered X-rays enter the spectrometer from the left in this schematic, and are dispersed by a grating (1109 mm from the entrance slits) across the detector (5147 mm from the entrance slits). The detector can be translated vertically, and the entire spectrometer can be rotated on its air bed about the sample. Distance scales are shown in millimetres, adapted from [7].

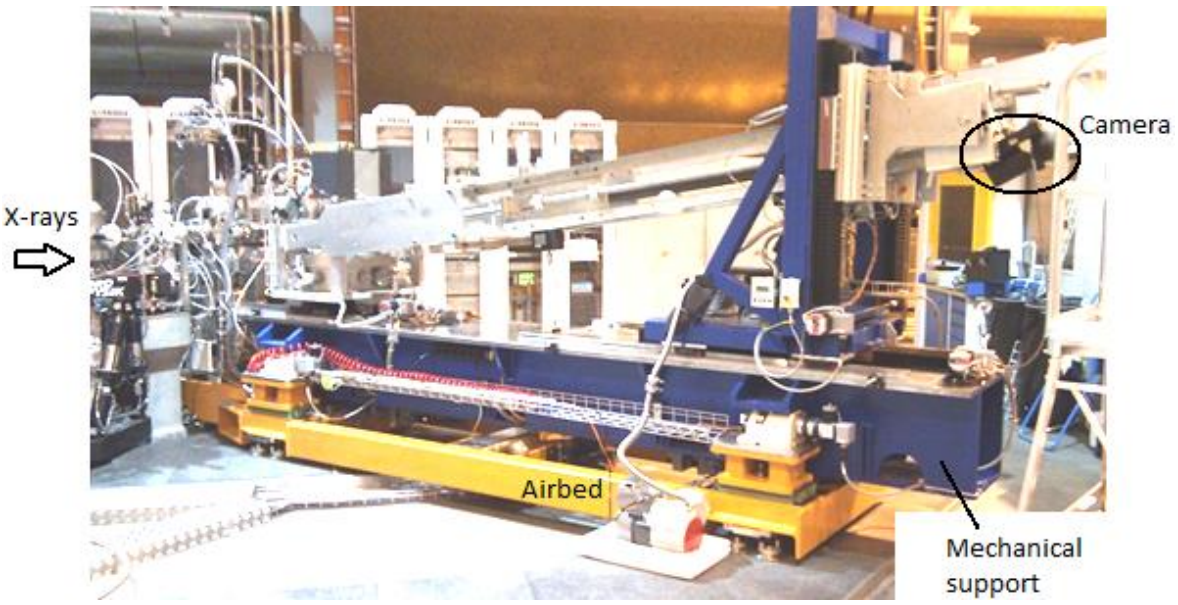

Figure 2.6. A photograph of SAXES shows the main spectrometer arm exiting the sample chamber (mid-left) extending up to the CCD camera that is encased in a black box (top-right). Mechanical support for the setup is provided by a girder (blue) on an air-bed (yellow) which allows the spectrometer to be rotated about the sample chamber to probe different scattering angles.

The source of X-rays for the spectrometer is the volume of sample from which X-rays are scattered, and is therefore controlled by the spot size produced by ADRESS. Slits can be used to reduce both the X-rays and stray light that enter the spectrometer from the sample chamber but current operation is slitless which means they are kept approximately 1 mm apart.

The grating is concave with laminar grooves spaced according to a quadratic equation to compensate for aberrations (for a vertical opening of 2 mrad), with an average of approximately 3200 lines mm^{-1}. A mask can be placed between the slit and grating to control the vertical aperture if needed. The spacing between lines on the grating, d, governs the diffraction angle for a given photon wavelength, λ, according to the grating equation (*Equation 2.4*).

$$d(\sin\theta_i + \sin\theta_m) = m\lambda \qquad \textit{Equation 2.4}$$

Here, θ_i is the photon incident angle and θ_m is the angle of dispersion for order m, where both angles are measured from the normal of the grating face. Dispersing the X-rays by a greater amount increases the spread on the detector, but manufacturing gratings with smaller line spacing is technically challenging, and therefore both expensive and prone to inaccuracies.

The detector is placed at a grazing incidence angle on the grating's focal cone approximately 4.1 m from the grating (Figure 2.5). Increasing the distance from the grating to the detector could result in an improved energy resolution as the spectrum would disperse more before detection.

However, the solid angle detected would be decreased so the photon count observed by the detector would be lower.

The detector of choice for soft X-ray spectrometers based on a dispersive grating and a 2D position sensitive detector was the microchannel plate (MCP) until the work by Dinardo *et al*. [32] in 2007 (following on from initial investigations by Sasaki *et al*. [33] in 2001), showed that back-illuminated CCDs could perform better both in terms of spatial resolution and detection efficiency. The CCDs tested exhibited detection efficiencies approximately 40 times greater than that of the MCP (Figure 2.7 a), and the spatial resolution for the MCP was measured to be approximately 100 µm, whilst the resolution of the two back-illuminated CCDs was shown to be approximately 25 µm to 28 µm (Figure 2.7 b). The resolution was shown to be largely independent of the CCD pixel sizes (20 µm and 13.5 µm), but dependent on the charge generated from the majority of X-ray interactions spreading into neighbouring pixels. This occurs due to isotropic diffusion of charge in the field-free region of the device, as will be explored in later chapters of this thesis.

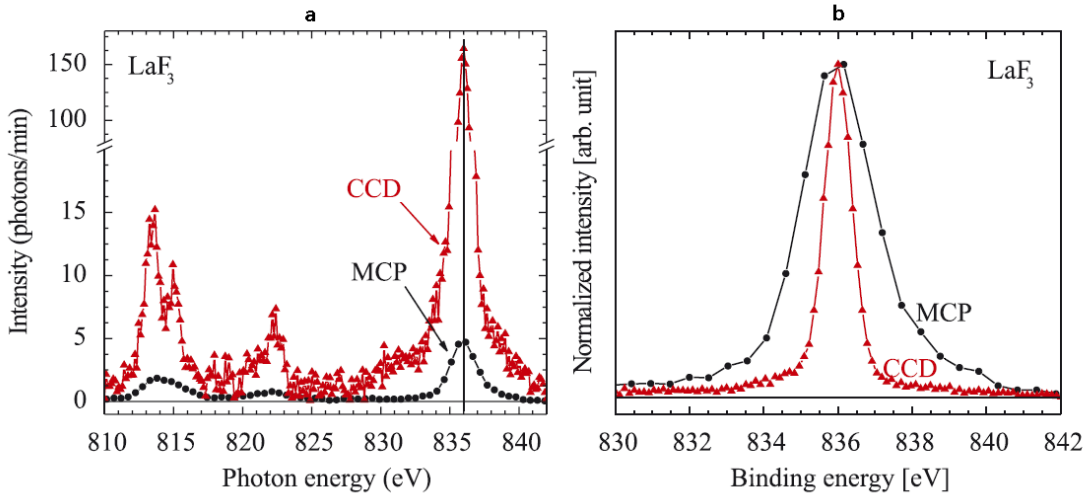

Figure 2.7. ***(a)*** *RIXS spectra obtained using similar conditions with a MCP and a back-illuminated CCD with 20 µm square pixels and* ***(b)*** *the 836 eV elastic feature shown with normalised intensity. The improved detection efficiency of the CCD (a) and spatial resolution (b) led to the CCD being adopted as the detector of choice for RIXS spectrometers, from* [32].

The detector used in SAXES is a back-illuminated CCD42-40 manufactured by e2v, in a camera system from Princeton Instruments (Roper Scientific). The CCD42-40 is described in more detail in Section 3.5.1. The spatial resolution of the detector is limited by charge spreading but to improve

the effective resolution, the detector plane is angled at approximately 20° to the incident X-rays. The effective pixel density in the energy dispersive plane is higher by a factor of approximately $\frac{1}{\sin 20°} \approx 2.9$, so the contribution of the detector spatial resolution to the overall energy resolution of the spectrometer is reduced by a factor of 2.9.

2.4.1 Contributors to the energy resolution of SAXES

There are three main contributions to the overall energy resolution of SAXES:

- **Source size**: X-rays are scattered from a non-zero volume of the sample which projects as a non-zero width in the energy plane when dispersed across the detector. A larger source size therefore degrades the resolution, but reducing it by closing the entrance slits to the spectrometer reduces the photon count.
- **Slope errors**: These derive from inaccuracies in the shape of the grating's surface. Slope errors can be in the form of random fluctuations across the surface or longer range deviations of the surface from the desired shape, but both forms of imperfection result in isoenergetic X-rays incident on different parts of the grating surface being dispersed to different points on the focal cone.
- **Detector resolution**: Once the X-rays have been dispersed across the detector, the spatial resolution of the detector controls how accurately the energy of an X-ray can be determined.

The alignment of the setup is important to ensure the CCD lies on the focal cone where the aberrations are compensated for. The vibration dampening and long term stability of the alignment is also vital as the detector is exposed to build up a spectrum typically for periods of 10 minutes. The distance between the grating and the detector, known as the throw of the spectrometer, could be increased to improve the energy resolution but the effective solid angle observed by the detector would then be smaller. At SAXES, increasing the throw is currently an undesirable solution to improving the spectrometer resolution as it would reduce the photon throughput and require changing the entire mechanics of the spectrometer arm. Additionally, there is insufficient space in the experimental hall around the sample chamber for a significantly larger throw.

2.5 Improvements to SAXES

To improve the science output and ensure that SAXES maintains its position as a leading instrument in the field of RIXS, it is desirable to continue improving its performance to increase

the quality and quantity of experiments that can be undertaken and to allow high impact research to continue, such as reference [1], as featured on BBC's Horizon programme. It is recognised that to improve the resolution of SAXES, the three main contributions can be focussed on: the source size, the CCD spatial resolution and the grating slope error. Their relative contributions to the total energy resolution of the spectrometer are shown in Figure 2.8 a. The CCD spatial resolution and grating's slope error dominate over the error from the source size, and so they are the current focus for improvement work.

An improvement in the detector spatial resolution will lead to the slope error of the grating, currently 0.67 µrad rms, dominating. With the progress in manufacturing technology, a grating with an improved slope error (0.2 µrad rms) can already be purchased, where the true shape of the grating will be a closer match to the desired concave shape. However, on its own, the grating improvement would currently have a limited impact on the resolution due to the dominance of the detector's spatial resolution.

The current detector resolution is governed by the charge spreading between pixels resulting in a resolution of 24 µm (Full Width at Half Maximum, FWHM) in the detector plane despite the smaller pixel size of 13.5 µm. When the 20° inclination of the detector is taken into account, the detector resolution is equivalent to 8.2 µm (FWHM) in the energy plane (normal to the incident photons). If the detector resolution was improved to 1.7 µm (FWHM) in the energy plane, and the improved grating was installed, the spectrometer energy resolution would be as shown in Figure 2.8 b.

The predicted energy resolution of the improved setup is dominated by the source size. The simplest method to reduce this contribution is by narrowing the entrance slits to the spectrometer; however this would reduce the photon flux from the sample lengthening the time required to collect sufficient photons to produce a spectrum and reducing the spectrometer throughput.

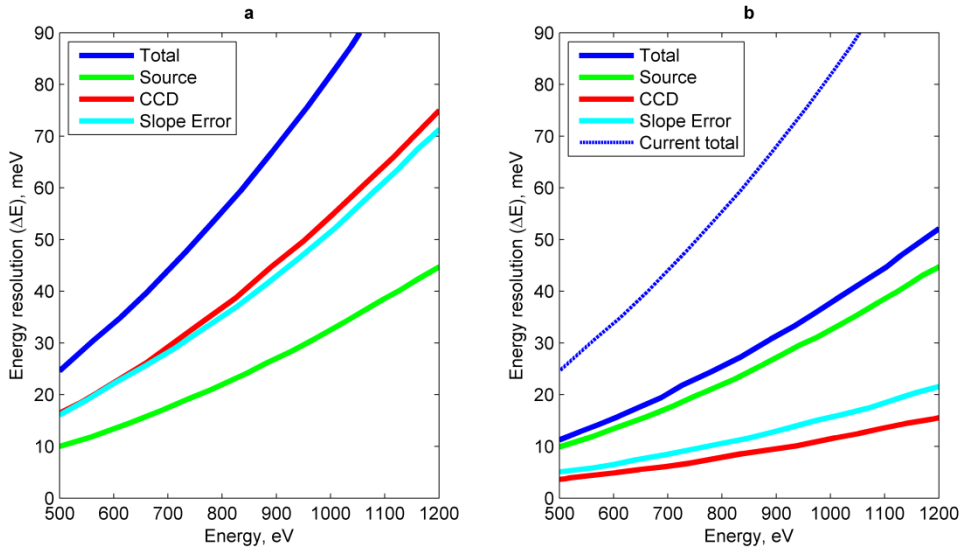

Figure 2.8. The current total energy resolution of SAXES increases as a function of energy due to the reduced dispersion of the grating. ***(a)*** *The relative contributions of the source size, CCD with 8.2 µm (FWHM) spatial resolution in the plane normal to the incident photons and the current grating with 0.67 µrad rms slope error are shown.* ***(b)*** *The predicted improvement from a detector with 1.7 µm (FWHM) spatial resolution and an upgraded grating with 0.2 µrad rms slope error, adapted from* [34].

2.6 Summary

X-ray spectroscopy techniques allow the electron energy states and excitations in a material to be investigated. One technique, RIXS, has an intrinsically low cross-section and requires a spectrometer with high resolving power and was therefore not practically viable until the last few decades. However, developments in synchrotron light sources and spectrometer instrumentation have allowed RIXS to emerge as a valuable spectroscopic technique for observing charge-neutral excitations in the bulk of materials. SAXES, a spectrometer at the ADRESS beamline at the SLS, is designed specifically for RIXS with an energy resolving power (E/ΔE) greater than 12 000 at 930 eV. Currently, the spatial resolution of the detector in SAXES is the dominant contributor to the overall energy resolution and so it has been prioritised as an area for improvement in the spectrometer development plans.

This thesis will focus on improving the spatial resolution of the detector at SAXES, to contribute to the improvement of the spectrometer, with results that will also be applicable to other RIXS beamlines and high spatial resolution soft X-ray applications. Currently the detector resolution is limited by the sharing of charge between pixels of the CCD. To begin exploring this effect and

understand how it can be used to improve the resolution, the detection of soft X-rays in a back-illuminated CCD is introduced in Chapter 3.

Chapter 3: CCDs for Soft X-ray Detection and the PolLux Facility

3.1 Introduction

A Charge-Coupled Device is used in the Super Advanced X-ray Emission Spectrometer (SAXES) to directly detect the dispersed X-rays. The spatial resolution of back-illuminated CCDs used for direct soft X-ray detection has been reported to be limited by the spreading of charge in the 'field-free' region of the detector, rather than the pixel size [7,32]. To understand why this is the case it is necessary to examine how X-rays interact in a CCD and how the structure and operation of the CCD allows it to be used as a 2D detector. Specific CCDs that are later referred to in this thesis will also be described and compared.

Experimental investigations into the interaction of X-rays in back-illuminated CCDs in later chapters of this thesis are carried out using data collected at the PolLux spectromicroscope at the Swiss Light Source. In Section 3.7, the PolLux facility and its standard operating setup is described.

3.2 Interaction of soft X-rays in silicon

The electromagnetic spectrum can be subdivided into segments according to the energy of the radiation. X-ray photons are emitted by electrons relaxing into a lower energy state, and have energies between approximately 100 eV and 100 000 eV. X-rays with energies below 5000 eV are generally known as 'soft' X-rays and are absorbed more by a given thickness of material due to their shorter attenuation lengths than higher energy X-rays.

3.2.1 Photon interaction depth

The probability of finding a photon at depth x into a material is described by the Beer-Lambert law, an exponential probability distribution characterised by an attenuation length, λ.

$$P(x) = \exp\left(-\frac{x}{\lambda}\right) \qquad \textit{Equation 3.1}$$

The attenuation length, λ, is defined as the distance into a material at which the intensity of a beam of particles has dropped to $1/e$ which is approximately 36.7% of the intensity at the material surface (Figure 3.1). The attenuation length for X-rays is dependent upon the photon energy and material type, e.g. Figure 3.2, [35].

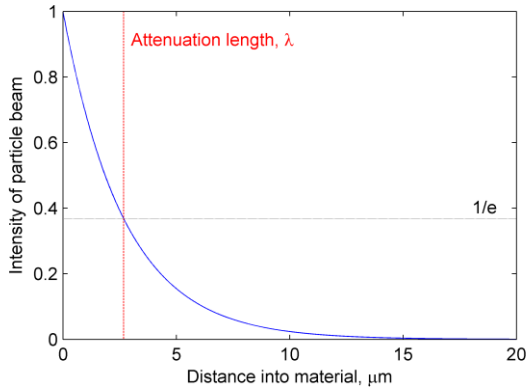

Figure 3.1. The Beer-Lambert law describes the intensity of a beam of photons incident into silicon. The attenuation length is defined as the depth at which the beam intensity drops to 1/e, which is at 2.68 μm for the case shown here (1000 eV photons in silicon).

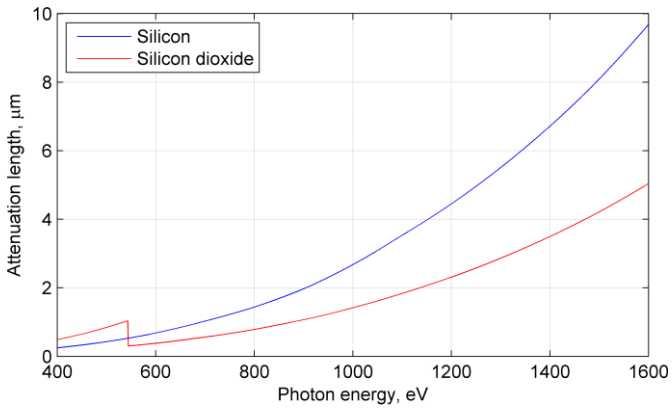

Figure 3.2. The attenuation length in silicon and silicon dioxide is shown for a range of soft X-ray energies. Data from [35].

3.2.2 Electron-hole pair generation

At soft X-ray energies, the dominant pathway of photon interactions with matter is the photoelectric effect (Figure 3.3) [36,37], where photons with sufficient energy are absorbed through the excitation of valence band electrons into higher energy states. In silicon, where the valence band is fully occupied, electrons are excited into the conduction band leaving an unoccupied state – a 'hole' – in the valence band. The electron and hole are independently mobile through the lattice and together are referred to as an electron-hole pair.

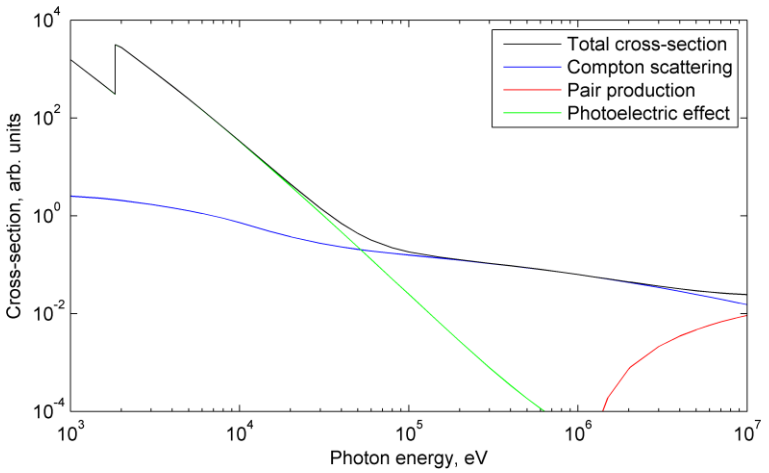

Figure 3.3. In the soft X-ray energy regime (below 5000 eV) of interest here, the photoelectric effect dominates over the Compton scattering and pair production cross-sections. Data from [38].

In silicon, electrons can be excited from the valence to the conduction band across indirect or direct band gaps (Figure 3.4), resulting in three ranges of photon energy, E_{ph}, that can interact in the lattice. The range values given here are for room temperature [39].

- **E_{ph} < 1.1 eV** (1127 nm, near-infrared): The photon energy is less than the indirect band gap of silicon and so insufficient to form electron-hole pairs. Silicon based detectors are therefore generally not suitable for observing photons in the far infra-red.
- **1.1 eV < E_{ph} < 3.1 eV** (400 nm to 1127 nm, UV to near-infrared): When coupled with a phonon, photons with this range of energies can generate single electron-hole pairs by exciting an electron across the indirect band gap.
- **E_{ph} > 3.1 eV** (400 nm, UV): Photons with energy greater than the direct band gap do not require a phonon to excite electrons across the direct band gap.

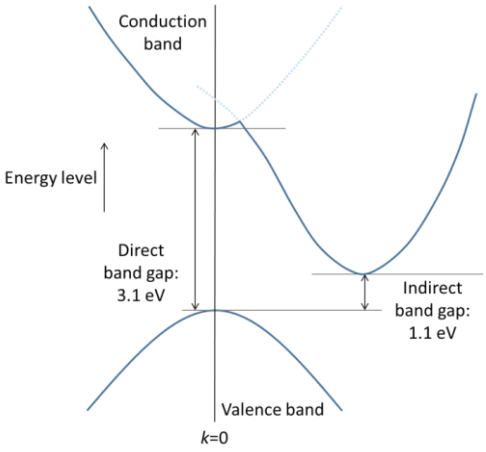

Figure 3.4. The silicon band structure allows both indirect and direct paths for exciting electrons from the valence to conduction band.

Extreme UV, X-ray and gamma-ray photons (E_{ph} > 10 eV) have sufficient energy to produce multiple electron-hole pairs through the process of impact ionisation [40]. On average, E_{ph}/3.65 eV electron-hole pairs are generated per photon at room temperature [41], but as the generation is a stochastic process, the number of charge-carrier pairs generated is distributed in a Poisson-like distribution with a variance ${\sigma_{n_e}}^2$ given in *Equation 3.2*. Here, f_{Si} is the Fano factor in silicon and is approximately equal to 0.12 [42].

$$ {\sigma_{n_e}}^2 = \frac{f_{Si} E_{ph}}{3.65\ eV} \qquad \textit{Equation 3.2} $$

The cloud of electron-hole pairs generated by an X-ray interaction occupies a volume of silicon dependent upon the initial photon energy. If assumed spherical, the radius of the volume is described by the relationship in *Equation 3.3* [43], valid across the energy range from 6 keV to 20 keV. At energies lower than 6 keV, the initial charge cloud radius will be smaller than 0.4 µm. The relationship of *Equation 3.3* is an average across many events, and therefore overestimates the diameter of the majority of charge clouds since the probability of a large scattering angle is small [44]. Individual charge clouds are better estimated as tear-drop shaped, but as their size is small relative to other dynamics of charge cloud spreading discussed later, they can be well estimated as spherical here.

$$ \text{radius} = 0.0171 \times \left(\frac{E_{ph}}{keV}\right)^{1.75} \qquad \textit{Equation 3.3} $$

A detector with position resolution is designed so that the clouds of electron-hole pairs are confined close to their generation point before the number of charge carriers is measured. The Charge-Coupled Device (CCD) uses potential wells in 1D or 2D arrays to provide this spatial resolution. The stored charge is then transferred along the potential wells to an output node where the number of electrons is measured. The charge storage, transfer and measurement processes in a CCD will be described in more detail in Section 3.3.

3.3 The scientific Charge-Coupled Device

Whilst working on a concept for semiconductor based bubble memory at AT&T Bell Labs, George E. Smith wrote the following in his laboratory notebook.

> *In collaboration with W.S. Boyle, a scheme for moving pockets of charge (or the absence of charge) along the surface of a semiconductor was devised.*
>
> Boyle and Smith's laboratory notebook entry, 19th October 1969 [39]

When reporting their findings in early 1970, Boyle and Smith made the important observation that the charge could be generated using radiation [45], demonstrating the initial concept of the CCD as an imaging device. Smith's colleagues soon demonstrated a 2D imaging device using the concept, and technological developments since have led to the CCD being used for a wide range of imaging applications where image quality, accuracy and sensitivity are crucial. These applications include professional digital cameras, medical imaging, both ground and space based astronomical observation and scientific imaging.

A CCD is built up of an array of metal-oxide-semiconductor (MOS) capacitors. Potentials applied to the gates form 'buckets' of low potential in the silicon where free charge is collected and stored. By clocking the gate potentials in a particular sequence, charge can be transferred across the array eventually reaching an output node. The voltage shift due to the additional charge stored on the output node capacitance is monitored to infer the amount of charge present.

3.3.1 Forming a potential well in silicon

3.3.1.1 Doping silicon

Silicon forms a tetrahedral crystalline structure with the four electrons in its outer valance shell forming highly covalent bonds with its neighbouring atoms. Phosphorus atoms have five electrons in their outer shells. When a phosphorus atom is substituted for a silicon atom in a silicon crystal lattice, one electron remains once four covalent bonds with the neighbouring silicon atoms have formed. This electron is loosely bound to the phosphorus atom and can be thermally excited ('donated') into the conduction band (Figure 3.5). Silicon doped with phosphorus is known as n-type, where the loosely bound electrons act as *negative* charge carriers in the conduction band and the phosphorus atoms are immobile positive charges that remain stationary in the lattice (Figure 3.6).

The effect of doping silicon with boron atoms can be thought of similarly: boron atoms have 3 electrons in their outer shell so therefore a boron atom in a silicon lattice leaves a hole that readily accepts an extra electron to form the last bond with the neighbouring silicon atoms. The hole can be filled by thermally exciting an electron from the valence band into the energy level of the hole (Figure 3.5). The resulting state is a mobile, charge-carrying hole in the valence band and static negative charges in the lattice. The majority mobile charge carrier is *positive*, so this material is referred to as p-type material (Figure 3.6).

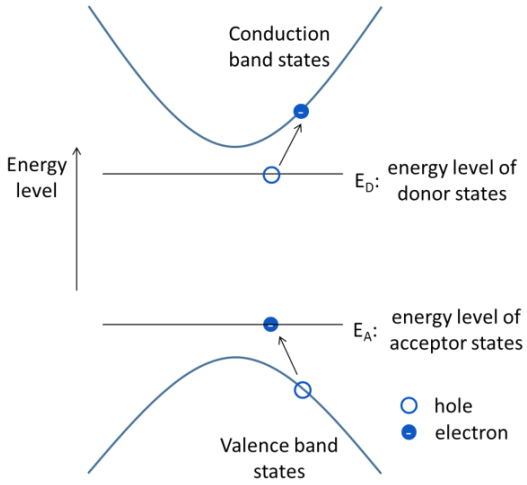

Figure 3.5. A schematic shows the acceptor and donor energy levels relative to the valence and conduction bands. An electron is excited from the donor energy level to the conduction band, where it is a negative charge carrier (n-type). An electron being excited from the valence band to the acceptor energy level is also shown, leaving a hole to act as a positive charge carrier in the valence band (p-type).

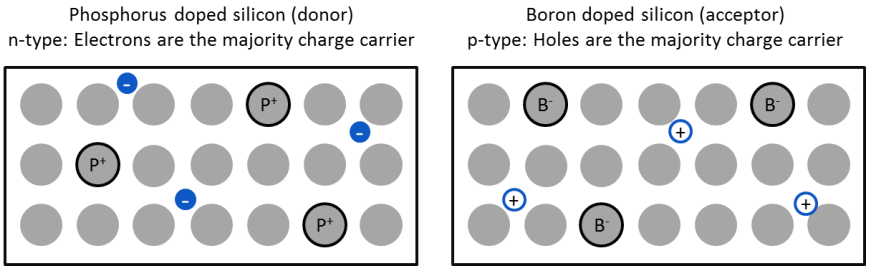

Figure 3.6. n-type material has a positive lattice charge with negative majority charge carriers. The opposite is observed in p-type material.

3.3.1.2 The p-n junction

Phosphorus and boron doping of silicon in CCD manufacture is used to form permanent potential structures within the material. When n-type and p-type material is brought into contact, electrons diffuse from the n-type material recombining with the holes diffusing from the p-type material. The lattice charges that remain form an electric field that opposes the diffusion until a state of equilibrium is reached. The volume at the boundary where mobile charge carriers are quickly swept away by the field is called the depletion region at a p-n junction, as shown in Figure 3.7. Any electron-hole pairs generated (e.g. thermally or by photon interactions) in the depletion region are separated by the electric field and swept in opposite directions.

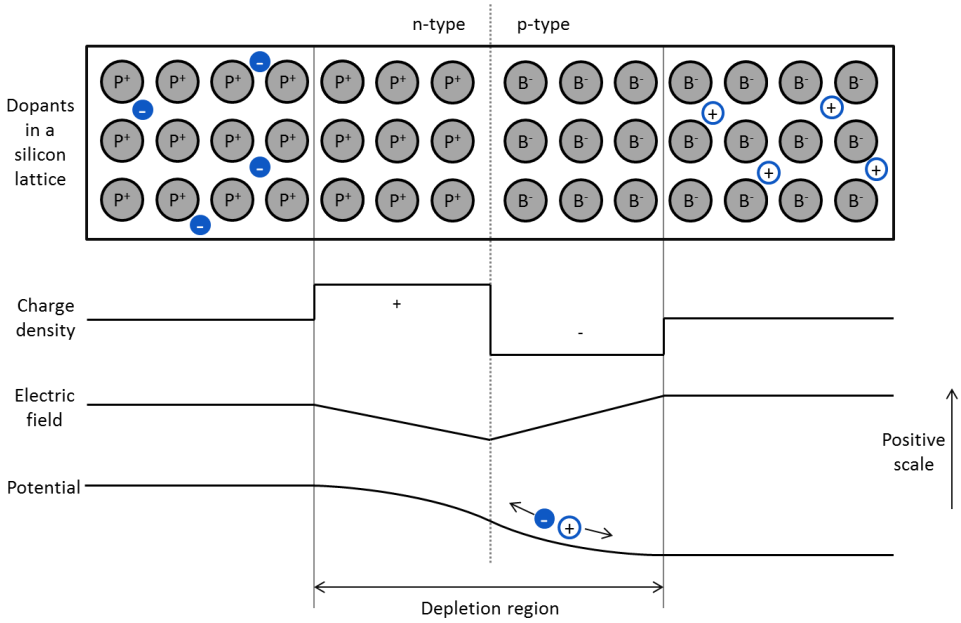

Figure 3.7. A depletion region forms when p-type material and n-type material are in contact (at a p-n junction). The charge density, electric field and potential profiles across the junction are shown.

3.3.1.3 The MOS capacitor

Whilst doping can provide a permanent potential structure in silicon, in a CCD dynamic control is required to allow charge to be transferred across the device. The building block of CCDs that provides the dynamic capability is the MOS capacitor, with a structure shown in Figure 3.8. When a positive gate potential is applied, mobile holes are repelled away from the gate structure forming a depletion region that extends away from the Si-SiO_2 interface. The depletion region extends until the electric field from the static negative ions in the lattice balances with the applied potential. The distance to the edge of the depletion region, where the potential is equal to zero, is referred to as the depletion depth. Any electron-hole pairs generated in the depletion region are separated by the field, with the electrons being collected at the Si-SiO_2 interface and the holes recombining at the substrate connection. Clocking the gate potentials on a series of adjacent MOS capacitors between high and low levels in a predefined sequence allows the potential along the surface of the silicon to be varied, where the electrons are always attracted towards the most positive potential. This dynamic capability of an array of MOS capacitors is Boyle and Smith's "scheme for moving pockets of charge along the surface of a semiconductor" [39].

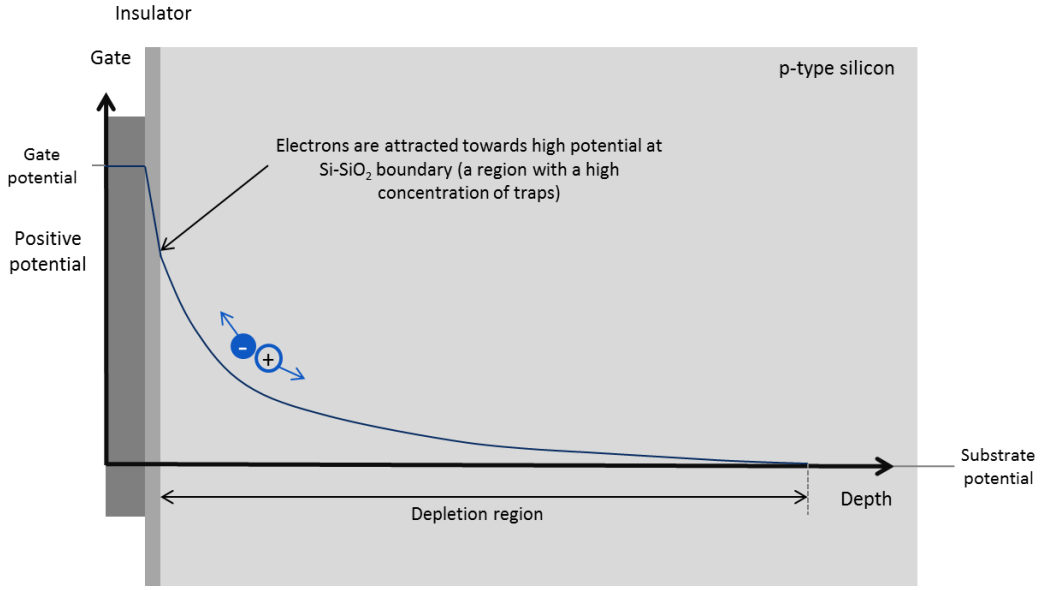

Figure 3.8. The structure and potential profile through a MOS capacitor of a surface-channel CCD.

3.3.1.4 The buried-channel MOS capacitor

Early CCDs used the MOS capacitor architecture, where the generated minority carriers are stored in a channel at the Si-SiO_2 interface - 'surface-channel' devices. There is a high concentration of traps at the Si-SiO_2 boundary, due to 'dangling bonds' where the Si and SiO_2 lattices meet. The traps inhibit the charge transfer efficiency of these surface-channel devices and the surface-channel architecture has been superseded by 'buried-channel' architecture for scientific applications, shown in Figure 3.9 [46].

An implant of n-type dopant is made to a depth of approximately 1 µm from the Si-SiO_2 boundary that reshapes the potential to form a maximum between the interface states at the oxide and the p-n junction. The n-type doping concentration is significantly higher than the p-type doping to ensure the depletion extends deep into the device. Once again, electron-hole pairs generated in the depletion region will separate, but the electrons will be stored in a potential well that is spatially separated from the traps at the Si-SiO_2 interface.

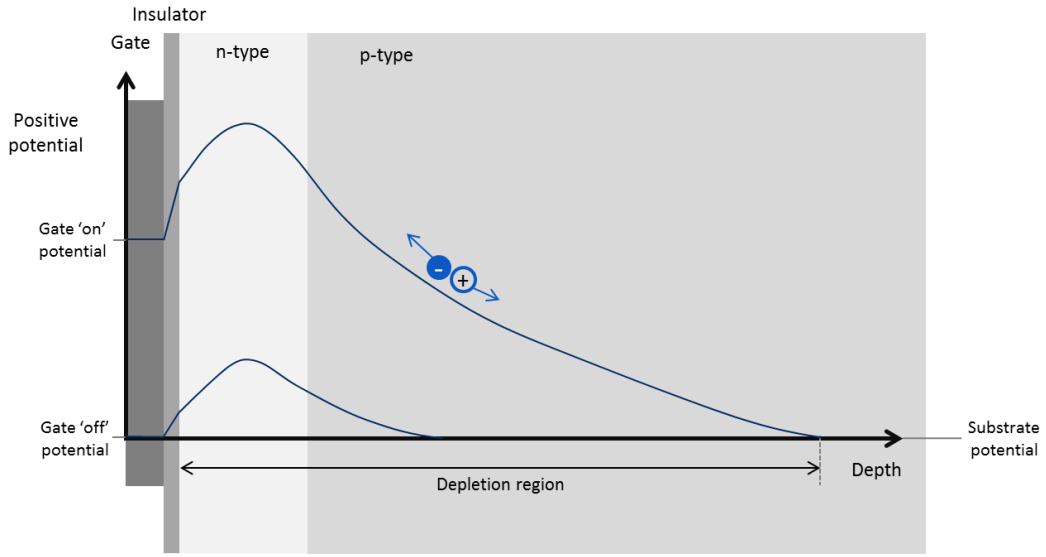

Figure 3.9. A structure and potential profile through a buried-channel CCD.

3.3.2 Charge transfer

3.3.2.1 3-phase clocking scheme

To transfer charge along a row of potential wells, the gate electrodes are switched between high and low voltage levels to sequentially clock the charge through the structure. An example clocking scheme (shown in the potential well format) is in Figure 3.10, where charge is transferred from under gate two (Ø2) to under gate three (Ø3). In this example, every third

gate is connected to the same phase (i.e. Ø1, Ø2 or Ø3) so that a large array can be clocked using only three waveforms. The unit cell is three electrodes wide, therefore it is referred to as 3-phase.

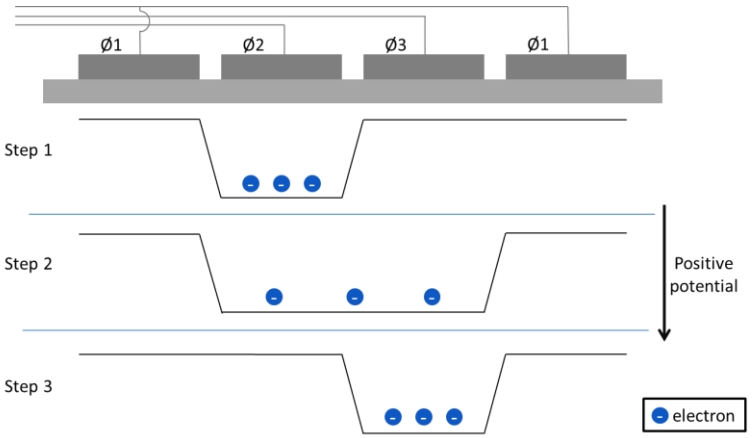

Figure 3.10. An example clocking scheme in a 3-phase (Ø1, Ø2 and Ø3) device shows the potential profile under the electrodes for 3 steps in time. These steps shift the charge from a potential well under the Ø2 electrode to under the Ø3 electrode. The horizontal axis of the potential profile aligns with the electrode structure at the top of the figure.

3.3.2.2 2-phase clocking scheme

From the 3-phase clocking scheme it is possible to imagine a clocking scheme for a four phase device but, to reduce the number of transfers required to clock a charge packet through the array, some devices use a 2-phase clocking scheme.

To allow a detector to be clocked in a 2-phase scheme, a boron implant is present under every other electrode (a p implant) to reduce the potential well depth (Figure 3.11). Adjacent pairs of electrodes are connected, and the relative location of the p implant controls the direction that charge is transferred. 2-phase clocking schemes allow a charge packet to be moved through the array using fewer transfers and so reduces the transfer time from one cell of electrodes to the next. However, the permanent implants reduce the flexibility of clocking schemes and only allow transport of charge in a single direction.

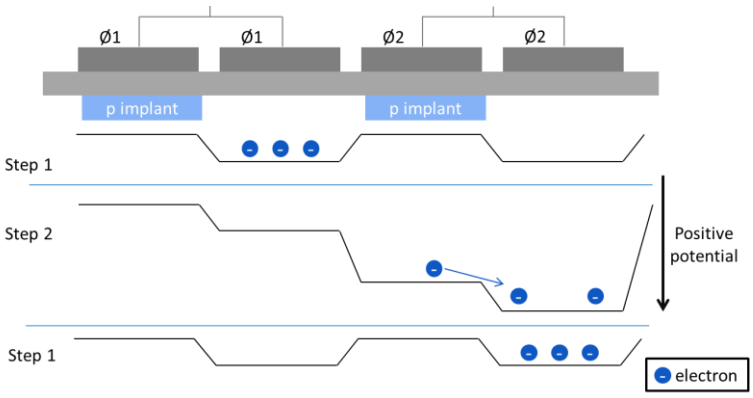

Figure 3.11. 2-phase clocking uses an additional p implant to introduce a permanent potential gradient, controlling the direction the electrons travel in. Here, 3 steps of the clocking sequence demonstrate how charge can be transferred from under Ø1 to under Ø2. The horizontal axis of the potential profile aligns with the electrode structure at the top of the figure.

3.3.3 CCD layout

In a CCD, electrodes and buried-channel structures are laid out to form an imaging area. Columns are defined by the n-type buried-channel implants, and electrodes divide the columns into pixel units (e.g. Figure 3.12). Charge collected under the 'on' electrode in the pixel unit is transferred down the column and then along a serial readout register to an output circuit to be read out.

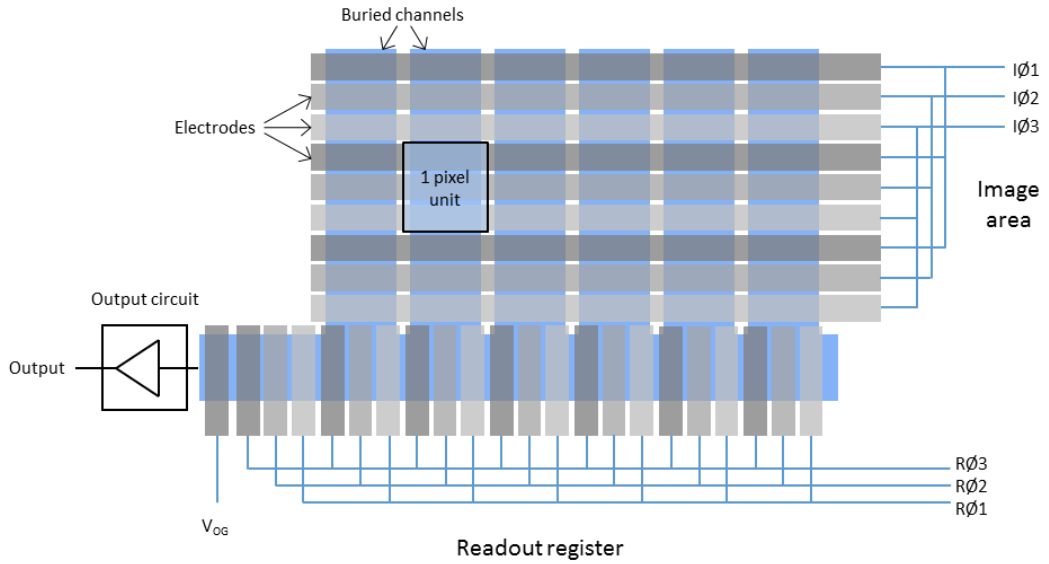

Figure 3.12. The layout of a 3-phase detector with a parallel imaging area and a single serial readout register that terminates at an output circuit.

3.3.4 Charge conversion

3.3.4.1 The single stage output circuit

To measure the number of electrons in a charge packet, the signal is converted from the charge domain into the voltage domain by an output circuit, at the end of a register of electrodes (Figure 3.12). A single-stage output circuit consists of an output node (a highly doped n-type region), an amplifier MOSFET and a reset MOSFET, as displayed in Figure 3.13. A charge packet is transferred along the register of potential wells and across an output gate (set at V_{OG}) to the output node. The total charge in the output node, qN_f, is the charge of an electron, q, multiplied by the number of electrons, N_f. The voltage, V, applied to the gate of the amplifier MOSFET then follows $qN_f = C_N V$, where C_N is the total capacitance of the output node. The voltage applied to the amplifier MOSFET gate controls the current flow from source to drain. The current flow results in a measurable potential drop across a load resistor on the output source, V_{OS}, that is proportional to the charge in the output node. Once V_{OS} has been measured, the charge in the output node can be reset to a zero level by switching the reset MOSFET on using ØR.

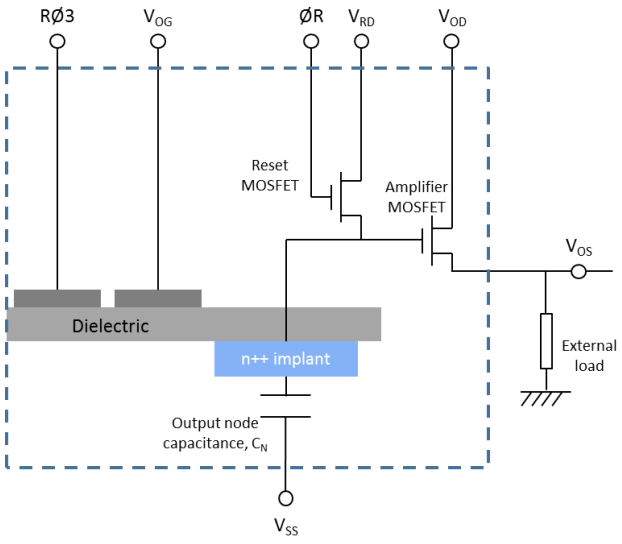

Figure 3.13. A single stage output circuit.

The change in the output source potential (V_{OS}) per electron added to the output node is defined as the output circuit responsivity. A high responsivity is desirable when one observes small signal levels, such as those resulting from a single soft X-ray photon. The responsivity can be tuned by varying the feature size of the output node (and therefore its capacitance) and the

feature size of the amplifier MOSFET. Higher responsivity therefore requires a lower node capacitance and a smaller transistor, however decreasing the capacitance of the output node reduces the maximum charge that can be contained and therefore the dynamic range is reduced. Decreasing the size of the amplifier MOSFET increases its impedance and in turn its response time, slowing the readout rate. A suitable solution to producing an output circuit with increased responsivity without reducing the response time or detector dynamic range is to use a multistage output circuit.

3.3.4.2 Two-stage output circuit

The layout of a two-stage output circuit used by e2v in some of its scientific CCDs is shown in Figure 3.14. The 2nd stage MOSFET amplifier is wider to reduce its impedance whilst it further amplifies the output from the first stage. As the floating capacitance between the amplification stages is significantly larger than the output node, it does not have to be reset as often and ØC is commonly tied to a parallel transfer clock.

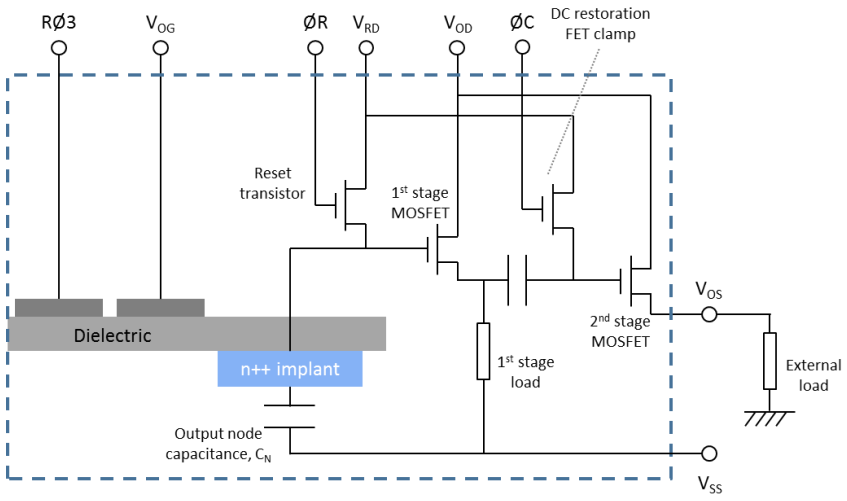

Figure 3.14. A standard scientific two-stage output circuit used by e2v.

3.3.5 CCD structure

In the potential well structure (described in Section 3.3.1.4) used to confine and transfer charge, four regions at the front face of a typical scientific CCD have been mentioned (Figure 3.9).

- **p-type bulk silicon**: All detectors described in this thesis are manufactured from p-type silicon, resulting in electrons being the minority carrier collected in the potential well.
- **n-type doped region**: A region of the bulk silicon, up to approximately 1 µm deep from the electrode structure, is phosphorus doped using an ion implantation process to produce an 'n-channel' in the p-type bulk.
- **Oxide and nitride layers**: The typical e2v manufacturing process is to produce an oxide and a nitride layer on the surface of the silicon, each approximately 85 nm thick. These layers act as a dielectric between the semiconductor and electrode structures. The nitride layer is resistant to the wet chemical etches used in later manufacture of the electrode structures and so protects the more vulnerable oxide layer beneath. The oxide layer aligns with the dangling bonds of the bulk silicon better than nitride, reducing the number of surface traps.
- **Gate electrode**: The electrode is polycrystalline silicon laid down using chemical vapour deposition. A sufficient doping of phosphorus (n-type dopant) is used to increase the conductivity of the material, whilst oxide layers insulate between the electrodes.

The dielectric and polycrystalline silicon layers are built up on the front face of a detector during manufacture. In front-illuminated standard devices, photons are incident onto these electrode structures and any photons that pass through the layers can generate charge in the bulk silicon to be detected.

3.3.6 Quantum Efficiency

At soft X-ray energies the photons have a short attenuation length (e.g. 1 µm at 700 eV) and if illumination is incident on a CCD's front face, the electrodes, oxide and nitride layers absorb a significant proportion of the photons, shielding the photosensitive bulk silicon. The proportion of photons incident on the detector that are detected is referred to as the Quantum Efficiency (QE).

One method of improving the QE of CCDs is to reduce the amount of shielding by manufacturing devices with thinner electrode and oxide structures [47] or an electrode shape that allows a large area of the pixel to remain uncovered [48]. However, a more effective method of improving the proportion of photons that are detected is to illuminate the CCD from the reverse side, where no electrode structure is present.

3.3.7 Backside illumination

CCDs are manufactured on a silicon substrate wafer that must be reduced in thickness for backside illumination to allow soft X-rays to penetrate and interact close to the potential wells in the silicon. Removing the majority of the silicon leaves a mechanically fragile structure that is often thinner than 50 µm. To provide support, e2v glues the CCD onto a silicon wafer (Figure 3.15), known as the 'whole wafer' approach. An alternative but more fragile method is 'picture framing', where a thick layer of silicon substrate is left around the edge of the device [49].

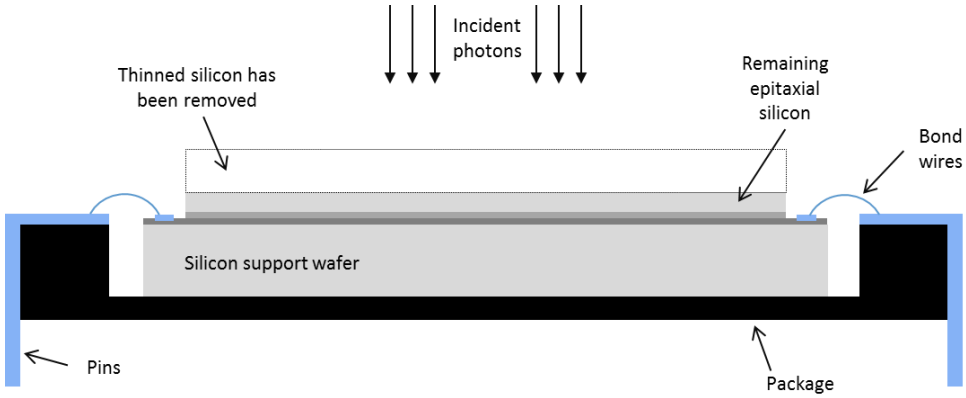

Figure 3.15. The 'whole wafer' approach to back-thinning used by e2v (showing a single packaged CCD).

The etched silicon surface naturally grows an oxide layer but the subsequent Si-SiO_2 interface contains many vacancy traps with energy states within the band gap, due to dangling bonds from the silicon atoms. The traps give the oxide layer an overall positive charge which depletes the silicon, attracting nearby electrons to the recombination centres at the interface. The recombination of photo-generated signal is prevented by generating a strong negative potential at the surface that repels any photo-electrons back into the bulk silicon; the back surface must be accumulated.

Accumulation has been achieved in a number of ways, which can be grouped as either 'passive' or 'active'. In passive accumulation, the oxide layer is negatively charged to attract holes to the Si-SiO_2 interface introducing a field and potential gradient. One method of achieving this is exposing the detector to UV (between 4.25 eV and 8 eV) photons in the presence of O_2. The irradiation excites electrons from the silicon valence band into the oxide conduction band. In the oxide, the electrons can be trapped at the oxide surface by forming acceptor states, adsorbing gaseous oxygen. A sufficient amount of negative charge at the oxide surface can offset the positive traps at the interface and bring about accumulation.

Unfortunately, the oxygen adsorption degrades in time, with a time constant of a few hours at room temperature or tens of months at approximately -90°C [39], so is not a suitable solution for the majority of applications.

e2v use an active accumulation method, where a permanent accumulation region is introduced using ion-implantation [50]. Boron is 'fired' into the back surface to build up a heavily doped p-type region up to approximately 100 nm from the back surface, resulting in the desired negative charge that repels electrons. The aggressive method of implanting the boron induces charge traps in the silicon lattice that cannot be annealed using high temperatures (~1000°C) as the metal bus lines on the front surface of the device would melt. Instead, a more localised method of laser annealing is used by e2v. Ion-implantation is a permanent back surface passivation treatment that improves the charge collection efficiency of the back-illuminated detector for its lifetime. The primary disadvantage of ion-implantation is that a region approximately 50 nm deep from the back surface can form that is not photo-sensitive. Delta-doping, a different active passivation method, does not suffer from this problem [39], but requires a large capital investment in equipment and is not suitable for large-scale manufacture processes.

Back-illuminated devices intended for optical applications are normally provided with an anti-reflection coating to maximise the QE, but this is not applied for X-ray applications as the coating layers would absorb photons.

3.3.8 Depletion depth

The short attenuation length of soft X-ray photons means the majority of interactions in a back-illuminated CCD occur close to the back surface. If a potential well's depletion depth does not extend fully to the back surface, a field-free region is present. With no field, charge does not experience a drift therefore a significant amount of diffusion can occur during the transit through a thick region of field-free silicon before collection in the potential well structures. The extent of the depletion region from the electrodes and thickness of the thinned silicon therefore strongly affects the spreading and splitting of signal from a single charge cloud between pixels.

An expression for the depletion depth, z_{dd}, in a buried-channel CCD is given in *Equation 3.5*, derived using a constant concentration of donor atoms, N_D, between the oxide and a known depth [51].

$$z_{dd} = \sqrt{\frac{2\varepsilon_{SI}\psi_{MAX}}{qN_A\left(1+\frac{N_A}{N_D}\right)}} \approx \sqrt{\frac{2\varepsilon_{SI}\psi_{MAX}}{qN_A}} \qquad \textit{Equation 3.4}$$

Here ε_{SI} is the silicon dielectric constant (1.0×10^{-12} F cm^{-1}), q is the elementary charge (1.6×10^{-19} F V) and N_A is the acceptor atom concentration in the silicon. The maximum potential in the well, ψ_{MAX}, is related to the voltage applied to the gate and substrate, V_G and V_{SS} respectively, and the intrinsic channel potential, ψ_{CH0}.

$$\psi_{MAX} = \psi_{CH0} + V_G - V_{SS} \qquad \textit{Equation 3.5}$$

The intrinsic channel potential of a device depends on the donor and acceptor concentrations. The n-type implant from ion-implantation in the manufacture of a real device is not constant as a function of depth into the silicon but is measured to be more Gaussian-like [52]. However, using the simplification $N_D \gg N_A$, *Equation 3.4* is a sufficient approximation to the real case.

The substrate doping concentration, in units of cm^{-3}, is regularly reported in terms of the resistivity of the material, R_R. The relationship between the two parameters is given in *Equation 3.6*, where μ_{SI} is the electron mobility for silicon.

$$R_R = \frac{1}{\mu_{SI} qN} \qquad \textit{Equation 3.6}$$

For a material with resistivity of 20 Ω cm, assuming a mobility of 500 cm^2 V^{-1} sec^{-1}, the doping concentration is approximately 6×10^{14} cm^{-3}. In most e2v devices, the channel potential is designed to be ϕ_{CHO}=11±1 V and so using *Equation 3.4* and *Equation 3.5*, the depletion depth for a gate potential of 11 V is approximately 6.6 µm. For a gate potential of 0 V, z_{dd} is approximately 4.7 µm (compared to a total device depth of approximately 13 µm, for example). In a real pixel, the depletion depth can be estimated using these two values, with fringing fields from the adjacent gates and channel-stop regions contributing to form a continuous boundary to the depletion region in the plane of the detector.

The charge clouds formed by X-ray interactions in the depletion region are quickly swept by the potential gradient into the closest potential well. Unless a charge cloud is generated on the boundary between potential wells in the depletion depth, all the charge will be collected in a single pixel and it is clear that the interaction took place somewhere within the region defined by the potential well. If the interaction occurs in the field-free region, between the depletion depth and the back surface passivation, electrons diffuse isotropically from their origin and may travel a significant distance in the plane of the CCD before crossing the depletion layer boundary and being attracted to the nearest potential well. Overall, the generated electrons

may be collected in a number of adjacent pixels. As the diffusion results in a Gaussian-like distribution of charge across the depletion boundary that is sampled by the potential well structures, the resulting pixel signals that are obtained when the detector is read out may be used to ascertain the interaction location in the plane of the detector to a finer scale than the potential well size. This method of event analysis is explored in Chapter 4.

3.3.9 Noise sources

In Section 3.2.2, the number of electrons produced by X-rays of the same energy was described to be distributed with a non-zero variance as governed by the Fano factor. Other stochastic processes are also sources of noise during detection. The sources that have the most impact in this thesis are dark signal generation and noise sources in the output circuit.

3.3.9.1 Dark current

Electron-hole pairs can be generated from thermal excitations. When they are generated in the silicon, the electrons are indistinguishably collected and measured with the photo-electrons. Traps with mid-band energy states significantly increase the rate of thermal generation therefore the dark signal generation at the Si-SiO_2 interface is dominant over the generation from the bulk silicon because of the relative trap densities in the two regions. The thermal generation of signal is a random process governed by Poisson statistics with a temperature-dependent average. To reduce the contribution of this noise source, CCDs are often cooled when operated. Alternatively, devices can operate in an inverted mode (see Section 3.3.10).

3.3.9.2 Noise sources in the output circuit

The two main sources of noise in an output circuit, reset noise and transistor noise, are caused by Johnson noise. Johnson noise [53] describes the noise in conductance/resistance due to thermal agitations of electrons. The root mean square voltage, V_n, across a resistor with resistance R is given by *Equation 3.7*, where k_B is Boltzmann's constant, T is temperature and Δf is the frequency bandwidth.

$$V_n = \sqrt{4k_B TR\Delta f} \qquad \textit{Equation 3.7}$$

Reset noise is caused by Johnson noise in the channel resistance of the reset transistor being in series with the reset voltage V_{RD}, so the potential at the output node after each reset varies. To

prevent the fluctuating reset level being interpreted as a varying level of charge in the node, correlated double sampling (CDS) is used. In CDS, the potential on the output node is measured after each reset before, and then after, charge has been placed on the node. The difference is calculated, removing the measurement's dependence on the reset level [54].

Johnson noise in the amplifier MOSFET channel leads to a fluctuation in the output source potential, directly affecting the measured charge level. The effect of this noise on the measured charge level can be reduced by sampling the output source multiple times or by averaging it over a period of time. The longer the averaging time period, or the more samples that are taken, the lower the effect the noise has on the measurement but the longer the pixel signal level takes to be measured. Therefore, readout noise increases as the pixel readout rate is increased.

3.3.10 Inverted Mode Operation

The dominant component of dark signal in CCDs is generated at the Si-SiO_2 interface traps at the front face of the device. An effective method of reducing surface dark current generation is to accumulate holes at the front surface by 'pinning', an effect exploited by inverted mode operation (IMO).

In standard buried-channel CCDs, holes generated close to the oxide in the potential well drift towards the more negative potential at the oxide, and along the Si-SiO_2 interface away from the buried-channel. Beyond the buried-channel, holes drift towards the back surface eventually recombining at the substrate connection. Increasing the substrate potential, V_{SS}, relative to the potential applied to the gate, V_G, generates a potential gradient that leads to holes accumulating at the Si-SiO_2 interface – known as inversion. When V_{SS} is approximately 6.5 V to 9.5 V greater than V_G, holes accumulating at the interface force the potential at the interface to depend on V_{SS} (rather than V_G) i.e. the surface potential is 'pinned' to V_{SS}. The holes at the interface suppress the surface dark signal generation, reducing the overall dark signal generation in the pixel by a factor of approximately 100 at room temperature.

Applying a high potential to a gate, as required to define the potential well, repels holes and takes the interface under the gate out of inversion so the surface dark current is no longer suppressed. Therefore, to define a potential well without applying a gate potential additional p-type implants are placed under an electrode phase to form potential barriers and define the pixel structure. Devices with this additional implant can collect charge whilst the entire surface

is pinned, and are referred to as IMO CCDs. Devices without the implant are referred to as Non-Inverted Mode Operation (NIMO).

A higher p-type implant concentration leads to a larger potential barrier, and therefore an increase in full well capacity (FWC) during integration. However, an increase in dopant concentration also results in a reduced FWC during charge transfer therefore a compromise must be made to ensure the device has the maximum overall FWC.

To help improve the FWC of inverted mode devices, e2v has developed an Advanced Inverted Mode Operation (AIMO) architecture, where the p-type doped region is implanted under only part of an electrode phase. The charge is stored in the pixel regions without the implant and is only transferred through the implant region rather than stored in it, therefore the doping concentration can be much higher than in IMO, leading to a higher overall FWC.

Operating in IMO or AIMO can greatly reduce the dark current. However operating a device inverted also reduces the depletion depth; the depletion region ends where the potential reaches the substrate potential V_{SS}, which is closer to the front face when V_{SS} is increased (*Equation 3.4* and *Equation 3.5*). Additionally, the implant will affect the extent of the depletion region. If a device is manufactured for IMO or AIMO, the implant will be present regardless of whether the device is pinned, and the field of the p-type implant will reduce the buried-channel potential reducing the depletion depth in its vicinity.

3.4 The Electron-Multiplying CCD

One method of minimising the effect of readout noise is to multiplying the signal before it is converted into a voltage. In an Electron-Multiplying CCD (EM-CCD), electrons are transferred through an additional avalanche multiplication register within which the signal can be significantly increased before it reaches the output circuit. The readout noise is not dependent on the signal level therefore the effective signal to readout noise ratio is significantly improved. The EM-CCD can therefore use its signal amplification feature to operate either at the same readout rate with a lower effective readout noise or at a faster readout rate with the same effective readout noise as a standard CCD. More commonly, EM-CCDs are utilised operating at faster readout rates and with a lower effective readout noise than possible with standard CCDs.

Avalanche multiplication is achieved in an additional serial register, which is between the standard serial register and the output node. The charge packet is accelerated through the silicon lattice in a register element using a voltage difference of approximately 30 V to 45 V,

giving an electron in the charge packet a small probability of generating a new electron-hole pair, through impact ionisation (Figure 3.16).

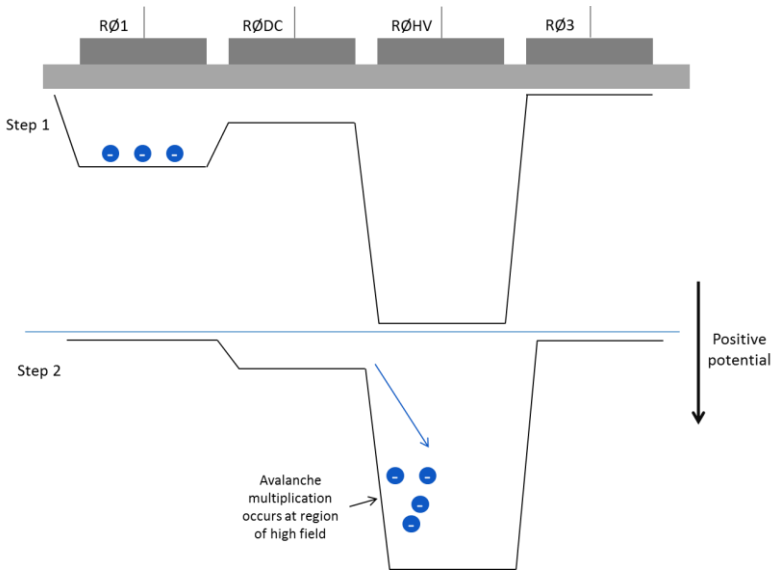

Figure 3.16. A potential well model diagram showing a charge packet, initially stored under phase RØ1, being accelerated from the potential set by RØDC to the potential set by RØHV. Impact ionisation results in an additional electron being generated.

During its transfer through the multiplication register a charge packet passes through many multiplication elements, resulting in a net gain of the number of electrons in the charge packet exiting the register. If the probability of an electron generating another electron in a multiplication element is p, and N_i electrons are passed into a register of n elements, the average number of electrons that exit the register, $\overline{N_f}$, is described in *Equation 3.8*.

$$\overline{N_f} = N_i(1+p)^n = N_i M \qquad \textit{Equation 3.8}$$

Here, M is the overall multiplication gain. A typical electron multiplication register in an e2v CCD contains 536 multiplication gain elements. When the potential between RØDC and RØHV is set to 40 V, p is approximately 0.01 so if N_i is 100, the charge packet at the end of the register will consist of approximately 20 700 electrons, i.e. $M \approx 207$. A readout noise level of, for example, 10 electrons rms would mask the original signal of 100 electrons but is insignificant when compared to the multiplied signal of 20 700 electrons.

The multiplication process can be modelled by the Binomial distribution as each element in the register is a Bernoulli trial with a small probability of generating another electron. When the

number of multiplication elements n is large (as is the case with e2v EM-CCDs), the distribution of N_f from successive trials of multiplying N_i electrons can be well approximated by the normal distribution with mean and variance equal to $\overline{N_f}$ (*Equation 3.8*).

3.4.1 The excess noise factor

When the noise introduced by the gain process is combined with the original shot noise on an optical signal that was detected in the EM-CCD, the increase in signal variance is described by the Excess Noise Factor, ENF. The ENF is defined as the ratio of the input and final signal variance (σ_i^2 and σ_f^2 respectively) [55].

$$ENF^2 = \frac{\sigma_f^2}{M^2\sigma_i^2} \qquad \textit{Equation 3.9}$$

In the case with no gain ($M = 1$), $ENF = 1$ since the initial and final variances are both equal to the noise on the input signal. When gain is applied, the excess noise factor is given by *Equation 3.10* [56], which is valid for optically or thermally generated photons.

$$ENF^2 = \frac{1}{M}\left(\frac{2M + p - 1}{p + 1}\right) = 2(M - 1)M^{-\left(\frac{n+1}{n}\right)} + \frac{1}{M} \qquad \textit{Equation 3.10}$$

Generally, for M larger than approximately 10, $ENF^2 \to 2$.

3.4.2 The modified Fano factor

When detecting X-ray photons, the variance in the detected signal is Fano limited rather than shot noise limited, so *Equation 3.10* is no longer valid and a different expression is needed. For charge packets generated with an average signal of N_i electrons, the variance following multiplication, σ_f^2, is described by the modified Fano factor, F_{mod} [57] where f_{Si} is the Fano factor in silicon (*Equation 3.2*).

$${F_{mod}}^2 = \frac{\sigma_f^2}{M^2 N_i} = f_{Si}ENF^2 \qquad \textit{Equation 3.11}$$

The modified Fano factor, derived and experimentally verified by Tutt *et al.* [57], is given in *Equation 3.12*.

$$F_{mod} = \frac{f_{Si}M(1 + p) - (1 - p)(1 - M)}{M(1 + p)} \qquad \textit{Equation 3.12}$$

F_{mod} is equivalent to the ENF in the optical case where $f_{Si} = 1$ but F_{mod} is a useful parameter for predicting the spectral resolution that can be obtained with an EM-CCD for X-

ray detection at different levels of gain. At high levels of gain the modified Fano factor tends to $1 + f_{Si}$ therefore the spectral resolution is worsened by applying gain, but this disadvantage may be outweighed by the reduction in effective readout noise and photon detectability.

3.5 Example CCDs

Four CCDs have been used to collect data during the preparation of this thesis (Table 3.1, Figure 3.17). All were manufactured by e2v, and are back-illuminated to improve their response to soft X-rays. They are described in the Sections 3.5.1 and 3.5.2.

Table 3.1. Details of the CCDs referred to in this thesis.

CCD type	CCD42-10	CCD42-40	CCD207-40	CCD97
Pixel size (square), µm²	13.5	13.5	16	16
Image area, pixels	512×2048	2048×2048	1632×1608	512×512
Image area, cm²	0.7×2.8	2.8×2.8	2.6×2.6	0.8×0.8
Electron Multiplying register?	No	No	Yes	Yes
AIMO or NIMO	AIMO	NIMO	AIMO	AIMO
Image area phases	3	3	2	2
Figure 3.17 label	a	b	c	d
Full Frame or Frame Transfer	Full Frame	Full Frame	Full Frame	Frame Transfer
Datasheet Reference	[58]	[59]	[60]	[61]

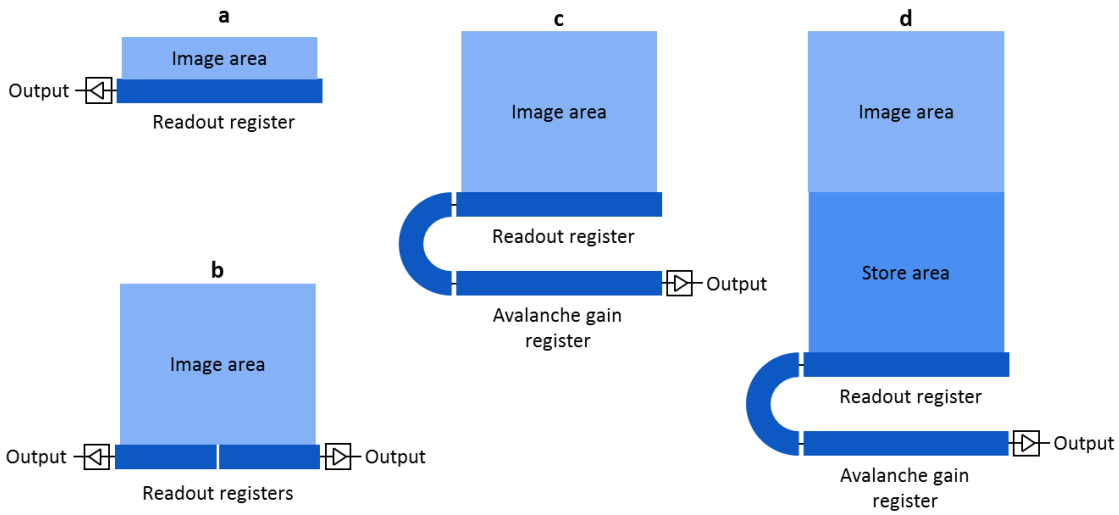

Figure 3.17. Schematic diagrams of the four CCDs discussed in this thesis: ***(a)*** *CCD42-10;* ***(b)*** *CCD42-40;* ***(c)*** *CCD207-40; and* ***(d)*** *CCD97. The diagrams are not to scale.*

3.5.1 CCD42-10 and CCD42-40

The CCD42-10 and CCD42-40 are two devices manufactured using the same mask set; therefore they have the same 3-phase pixel layout. The CCD42-40 has a large imaging area with approximately 4 MPixels and is the CCD used in the camera currently installed at SAXES. The device has two output nodes that each read out half the device area (Figure 3.17 b), which speeds up the frame rate of the large area by a factor of 2. The CCD42-10 has a quarter of the imaging area of the CCD42-40 with approximately 1 MPixels and a single output node (Figure 3.18).

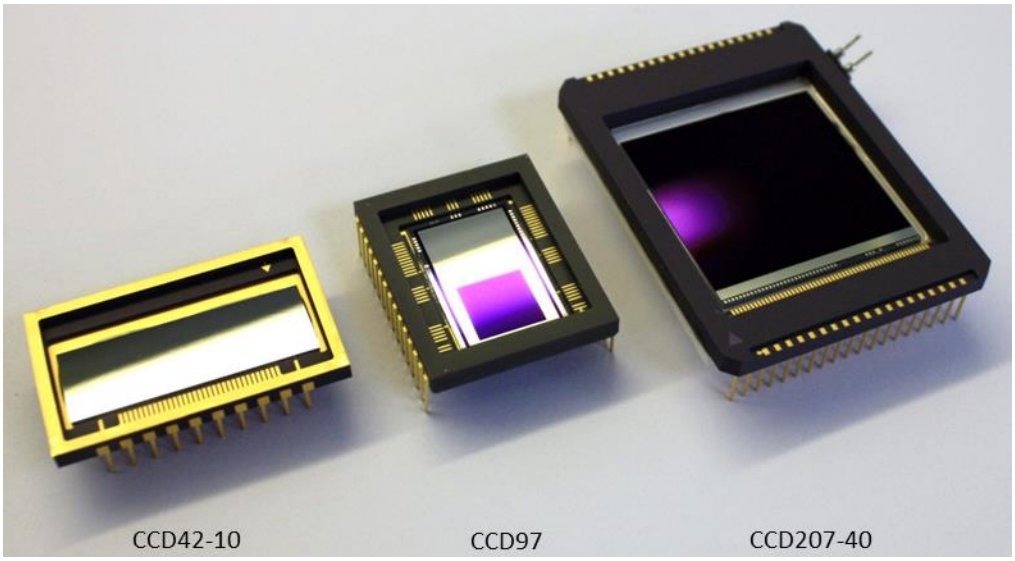

Figure 3.18. A CCD42-10 (left), CCD97 (centre) and CCD207-40 (right) manufactured by e2v. The pin pitch of the CCD42-10 packaging is 2.54 mm.

The CCD42-10 used in the experimental work in this thesis (serial number 09501-18-01) was back-illuminated and manufactured using 20 Ω cm material, with a nominal thickness of 13 µm, and implants that allow it to be operated in AIMO (Section 3.3.10). No coatings have been applied to the back surface, improving the soft X-ray response.

The current SAXES camera is a PI-SX: 2048-B-LN-CFT system delivered by Princeton Instruments (Roper Scientific) containing a CCD42-40 [62]. The ST-133-B camera controller system can read out the detector at 100 kHz or 1 MHz pixel rates, resulting in frame readout times of approximately 42 seconds or 4.2 seconds respectively. The read noise at these readout rates was measured before delivery to be 3.48 electrons rms and 10.8 electrons rms respectively. To minimise the dark signal generation, the detector is cooled using a liquid nitrogen dewar and operated at approximately -110°C. The dark current at this temperature is less than 1 electron pixel^{-1} hour^{-1} [7] therefore inversion is not required and the device is NIMO. NIMO detectors by e2v are manufactured with 100 Ω cm material so the depletion region tends to extend further into the thinned silicon than for AIMO devices (20 Ω cm).

3.5.2 CCD97 and CCD207-40

Apart from the CCD97, all devices discussed in this thesis are full-frame detectors that consist of a single parallel register of light-sensitive pixels that make up the image area and one or two serial registers. The CCD97 is a frame-transfer device with a second parallel register area which

is light shielded and sufficiently large to store the pixel signals from the image area (Figure 3.17 d). During operation as a frame-transfer device, the image area charge is quickly transferred into the shielded store region to be read out more slowly and whilst the store region is being read out, the exposed image area integrates the next image. The shielding of the store region is achieved using an aluminium coating that is laid on top of any anti-reflective coating. To improve its soft X-ray response, the CCD97 used in the experimental work described in this thesis (serial number 0641-21-7-3) is manufactured without any anti-reflective or aluminium coating on the back surface (unlike the one shown in Figure 3.18).

The second electron multiplying detector used is the CCD207-40 (Figure 3.17 c and Figure 3.18), which is a full-frame device with a similar image area size to the CCD42-40. The CCD207-40 used in the experimental work described here has serial number 04042-22-17. The CCD97 and CCD207-40 are manufactured with the same pixel and multiplication register architecture; their image areas contain p implants that allow the detector to be read out with a 2-phase scheme and operated in inverted mode.

3.6 The size and shape of the charge cloud

As discussed in Section 3.3.8, the charge cloud formed by an X-ray interaction diffuses in the silicon whilst drifting according to any field present. The majority of X-rays that are detected in the back-illuminated CCD42-40 at SAXES interact within the field-free region, between the depletion region and the back surface of the detector. Diffusion of the charge cloud in the field-free region can lead to the charge from a single photon interaction being detected across several adjacent pixels.

The average distribution of electrons from a charge cloud at the depletion region limits the resolution of the detector. To determine the resolution of the SAXES detector, an experiment was undertaken during commissioning by Ghiringhelli *et al.* illuminating the device with a uniform field of 930 eV X-rays [7]. The pixel signals of X-ray interaction events were plotted as a function of each pixel's displacement from the interaction location of the photon (Figure 3.19), estimated using a 'centre of gravity' style algorithm applied across a 3×3 pixel area around the event (Section 5.2.1). The resulting distribution shows the average X-ray charge cloud integrated over the pixel area, as a function of distance between the centre of the pixel and the interaction location. Note that the plot shows the charge cloud after it is integrated over by the pixel area, which is subtly different from the charge cloud shape after diffusion in the field-free region before sampling.

The distributions presented by Ghiringhelli *et al.* in Figure 3.19 therefore include the point spread function due to both the charge cloud spreading and the integration of the charge cloud across discrete pixel regions. A relatively insignificant contribution will also come from the method used to estimate the interaction position. The distributions' widths measure the detector spatial resolution when SAXES is operated in its current integrating mode, where it is limited by the charge cloud diffusion.

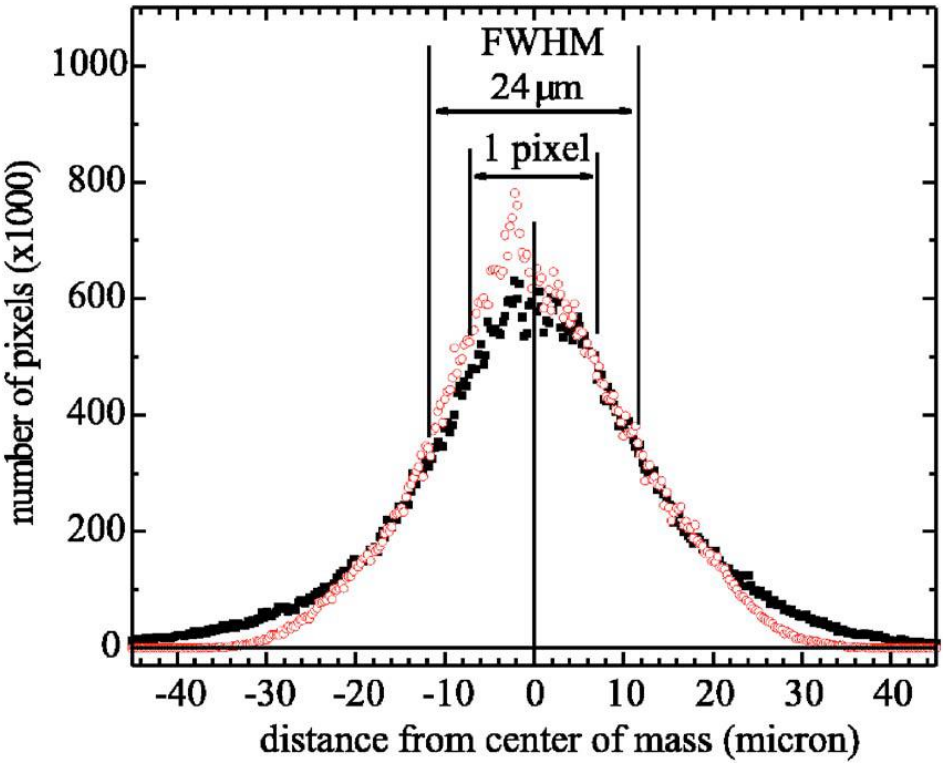

Figure 3.19. The charge cloud distribution of 930 eV X-rays detected using the SAXES CCD42-40, from [7]*. The distribution is shown along the rows in the x direction (red) and along the columns in the y direction (black).*

The diffusion and resulting charge distribution across the pixels from interactions in the field-free region of CCDs has been modelled in many forms and using various functions as reported in the literature, e.g. [63–66], and experimentally measured using a range of X-ray energies and CCDs, e.g. [67–69]. A discussion and comparison of the analytical models and experimental measurements is presented in later chapters of this thesis.

To investigate the diffusion and resulting charge cloud shape for an interaction in a given location in the 3D pixel, the interaction location within the pixel must be known. The depth of interaction of X-ray photons cannot be controlled as it is a random process, however the

interaction location in the 2D detector plane can be controlled by either shielding the majority of the pixel from a flat field of X-rays, as employed in the mesh experiment [70], or by focussing the X-rays into a sub-pixel region. An instrument capable of achieving the latter method is the PolLux spectromicroscope at the SLS.

3.7 The PolLux spectromicroscope

X-rays generated at a bend magnet at the Swiss Light Source, are monochromated and directed onto a Fresnel Zone Plate (FZP) in the PolLux endstation, focussing soft X-rays to a diffraction-limited spot size of 20 nm [71]. A thin sample of interest is placed at the 1st order diffraction focal point so that detectors behind the sample can observe the X-ray transmission and electrons emitted from the material's surface (Figure 3.20). The PolLux setup allows the sample to be scanned relative to the focussed X-ray spot and the incident photon energy and polarisation can be changed, therefore users can contruct maps of the sample in energy and two spatial dimensions. These capabilities have been used for investigations such as directly observing the magnetisation of thin samples [72], and for the spectroscopic characterisation of gas filled micro-balloons [73].

To attenuate the X-rays that are not diffracted in the 1st order, an Order Selecting Aperture (OSA) is placed between the FZP and the sample. The aperture is approximately 70 µm in diameter and is positioned so that, according to the geometry of the diffraction pattern, the 0th and higher than 2nd orders are attenuated (Figure 3.20 a).

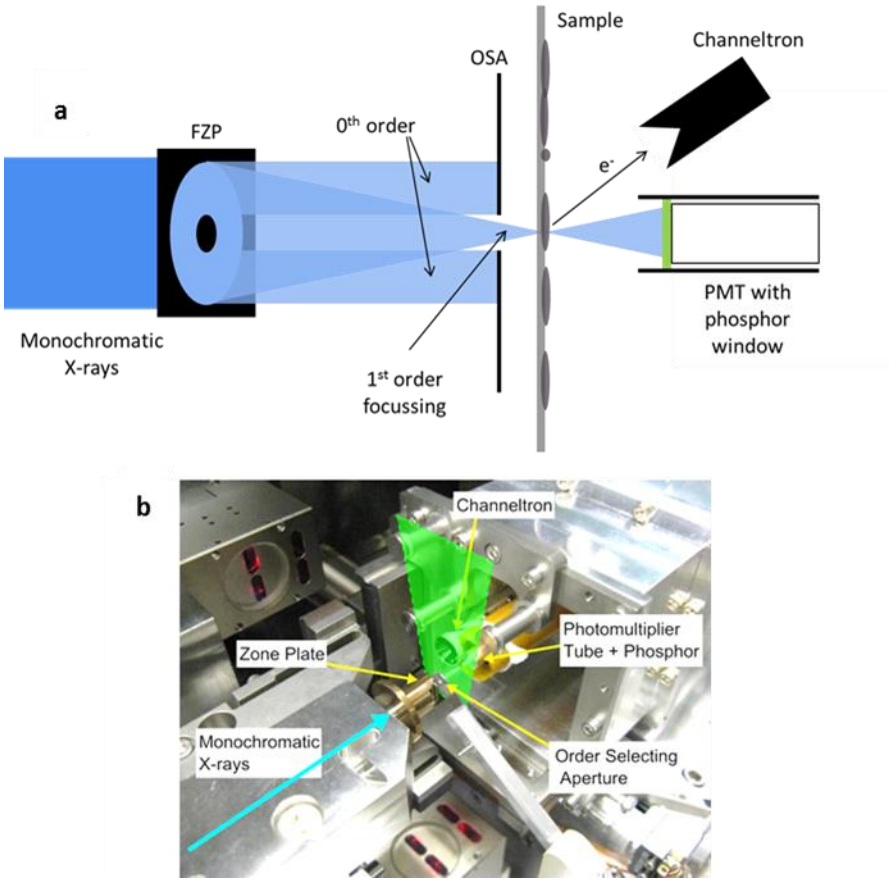

Figure 3.20. A schematic ***(a)*** *and photograph* ***(b)*** *of the standard setup at the PolLux endstation, adapted from* [74].

3.7.1 Focussing with the Fresnel Zone Plate

The focal distance, $F(E)$, of the FZP 1st order diffraction X-rays is energy dependent (*Equation 3.13*). When the incident X-ray energy is changed, the FZP *z*-stage position is tracked to maintain the focus on the sample [71].

$$F(E) = \frac{d_{FZP}\Delta r}{ch}E \qquad \textit{Equation 3.13}$$

Here, c is the speed of light and h is the Planck constant. At PolLux, the standard zone plates have an outer diameter, d_{FZP}, of 240 µm and a minimum slit width, Δr, of 35 nm (Figure 3.21) and therefore the focal distance is linear with energy, according to the empirical formula in *Equation 3.14*. Distances between the FZP and the sample are, for example, 2.7 mm and 8.1 mm for 400 eV and 1200 eV photons respectively.

$$F(E) \approx 6.77\ \left[\frac{\mu m}{eV}\right]E \qquad \textit{Equation 3.14}$$

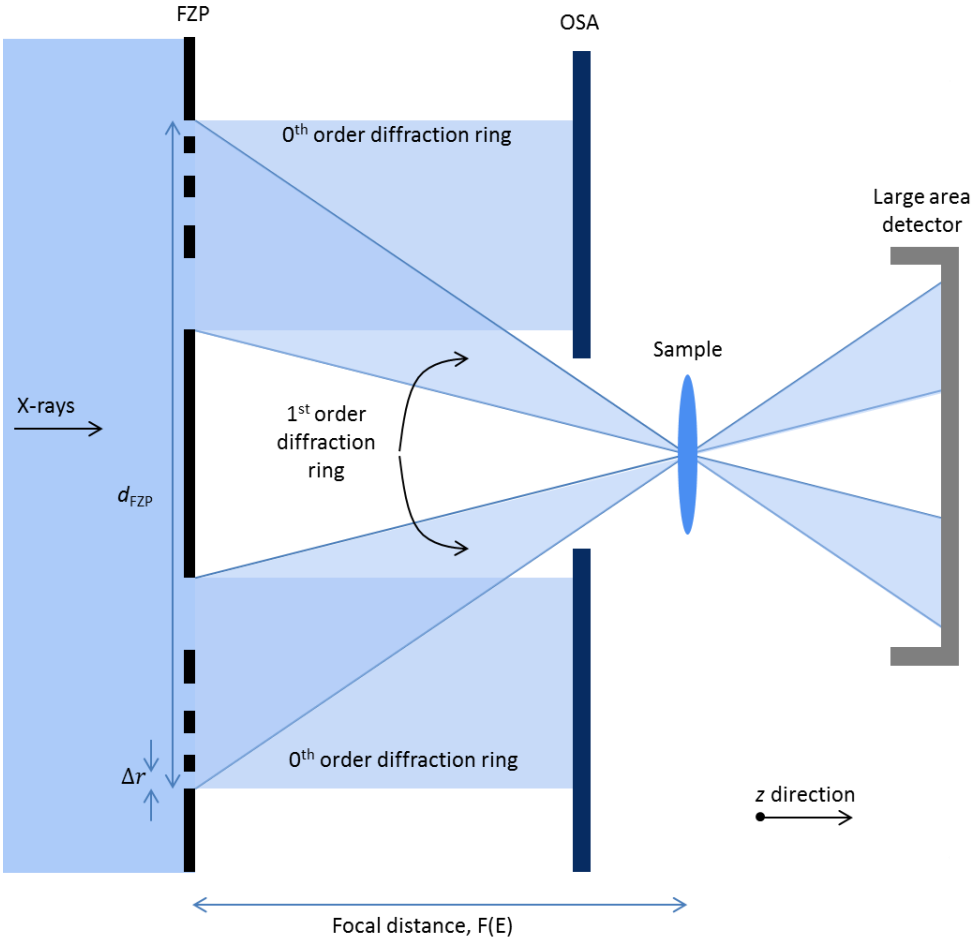

Figure 3.21. The X-ray focussing optics of PolLux uses a Fresnel Zone Plate (FZP). A detector counts the number of 1st order diffraction photons that were transmitted through a small region of the sample. Higher than 1st order diffraction orders are ignored for simplicity in this figure, but would also be attenuated by the OSA.

3.7.2 Sample environment

To prevent absorption of X-rays in the atmosphere, the FZP and sample stages are in a vacuum chamber held at pressures of approximately 10^{-5} mbar but flanges on the chamber provide capacity for electronics and cooling to monitor or control the sample, gauges and translational stages. Therefore, replacing the sample at the focal point with an operating and cryogenically cooled detector was a possibility for the work described in this thesis. However, to use the FZP optics at PolLux to focus an X-ray spot to a sub-pixel region of a CCD, the standard experimental setup must be adapted. The standard sample holder and OSA are not compatible with a CCD, so they have to be removed along with the standard detectors (channeltron and

photomultiplier tube or photodiode). In the space now available on the sample translational stages, a CCD can be located at the focal point of the soft X-rays. The adaptation of the PolLux experimental setup to focus the X-rays in the detector plane of a CCD is discussed in Sections 6.2 and 7.2.1.

3.8 Summary

The Super Advanced X-ray Emission Spectrometer disperses a spectrum across a CCD42-40, which directly detects the soft X-rays. A photon's interaction position on the detector in the energy dispersion direction is related to the energy of the photon, therefore the spatial resolution of the detector is significant to the overall energy resolution of the spectrometer. The CCD's spatial resolution has been measured to be limited by the sharing of the signal generated by single photon interactions across multiple pixels.

Following the description of the architecture and operation of back-illuminated buried-channel CCDs in this chapter, it is clear that the sharing of signal is due to charge diffusing laterally in the field-free region before collection in the potential wells. The short attenuation length of soft X-rays in silicon results in the majority of photons interacting in the field-free region of the silicon and so the charge clouds generated by the majority of photons are able to diffuse isotropically before being attracted towards a pixel's potential well in the depletion region. The thicker the field-free region, the further away the depletion region will be from the average soft X-ray interaction, and therefore the time that the charge cloud has to spread across a larger area increases. Therefore, the depth of depletion across the detector is an important parameter in the charge spreading, along with the overall thickness of the silicon. The depletion depth in CCDs is affected by the gate and substrate potentials, dopant concentrations and additional implants used for defining the potential well structure whilst the device is operated inverted.

IMO or AIMO devices and EM-CCDs have been described as evolutions of the standard CCD that allow noise contributions to be suppressed; operation in inverted mode allows the dark current of a device to be reduced by a factor of approximately 100 and in EM-CCDs, the signal is multiplied before readout, effectively reducing the readout noise. Of the four CCDs discussed in the chapters that follow, one is not manufactured as AIMO: the CCD42-40 currently installed at SAXES. However, the SAXES camera cools the detector so that dark current is negligible. The ability of the EM-CCD to suppress the effective readout noise to

sub-electron levels even at fast readout rates becomes an important benefit following the experimental testing described in later chapters.

The dynamics of the charge spreading in the field-free region of the CCD is a dominant factor in the resolution of SAXES, and the other back-illuminated CCDs investigated in this thesis. To investigate the sharing of charge between neighbouring pixels that results from a single photon interaction at a given interaction position in the pixel, an experimental setup is required that allows the interaction position to be defined or determined to an accuracy better than approximately 1 µm (c.f. CCD pixel size of 13.5 µm). An instrument capable of this is the PolLux spectromicroscope; an endstation at the Swiss Light Source that uses a Fresnel Zone Plate configuration to focus monochromatic X-rays to a minimum spot size of approximately 20 nm. However, the microscope chamber must be adapted in order to operate a CCD in place of the standard sample setup.

Chapter 4: X-ray Event Simulation

4.1 Introduction

The point spread function of X-ray events observed with the camera at SAXES is dominated by the lateral spread of charge clouds whilst diffusing in the field-free region of the CCD. The resulting X-ray events consist of signal split across multiple adjacent pixels. As the level of splitting is dependent on the interaction position and the dynamics of the charge cloud diffusion, the form of the X-ray event can be used to infer back the interaction position of the event to sub-pixel accuracy.

To explore charge spreading and possible centroiding algorithms, a simulation package was required that could output X-ray events that are consistent with experimental observations. The first section of this chapter describes the processes of a bespoke simulation package that has been developed by the author to generate X-ray events interacting at a given location in a back-illuminated CCD. The simulation is then calibrated using experimental data obtained in work described in Section 6.7.

4.2 Simulating the soft X-ray response of pixelated silicon detectors

The simulation package was developed to flow chronologically through the steps of an X-ray interaction and the subsequent charge collection process, resulting in an output of the pixel signals for an individual event. The simulation of detecting an X-ray photon is split into four steps, using the photon's energy as the most important initial parameter.

1) **Position of interaction within the 3D pixel structure:** An interaction depth is randomly generated from the energy-dependant probability distribution and the position in the plane of the detector can be a user defined or a randomly generated sub-pixel location.
2) **Number of electrons in the charge cloud**: This number is randomly generated from the Fano-limited distribution according to the X-ray energy.
3) **Assigning electrons to pixels**: The electrons in the charge cloud are assigned to pixels surrounding the position of interaction according to a probability distribution determined by a charge spreading model (resulting in Figure 4.1 a).
4) **Noise on the pixel signal outputs:** Noise is applied to the pixel signals to represent those that occur between electron storage in the pixels and the digitization of the signal in a real camera (Figure 4.1 b).

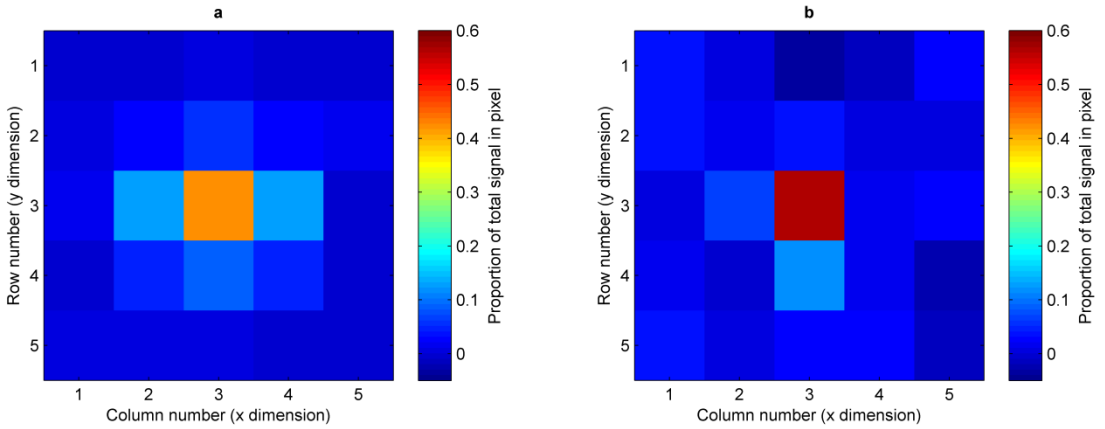

Figure 4.1. ***(a)*** *The simulation outputs an array of pixel signals formed due to the interaction of a soft X-ray photon.* ***(b)*** *Noise is added to the raw pixel signals to represent the various readout noise sources of a detector and camera system.*

The processes of 1 and 2 are well understood and can be carried out using normal and exponential distribution random number generators, if the Fano factor and the energy-dependent attenuation length for silicon are known. However, the distribution of charge at the interface between the field-free and the depletion regions following an interaction at a given location in the field-free region is a significantly more complicated process to model.

For the purpose of this simulation package, an analytical approach to determine the average charge-cloud distribution at the field-free and depletion region interface was desired to enable the generation of a large number of X-ray events at a wide range of sub-pixel interaction positions and photon energies. The derivation of an analytical model will be presented and compared to a selection of analytical models from the literature (Section 4.2.3). To compare the charge spreading models to experimental results obtained in work described in Chapters 6 and 7 of this thesis, noise is added to the pixel signals to closely match the noises observed in the experimental data, completing step 4 of the simulation. The steps will now be described in detail, following the chronological order of the detection process.

4.2.1 Initial X-ray interaction within the pixel structure

The simulation uses a simplified back-illuminated pixel structure with a depletion depth, z_{dd}, which is assumed constant across the pixel[§] and a field-free region with depth z_{ff} (Figure 4.2). A photon incident normal to the back surface interacts at a depth z_s, where z_s is randomly chosen

[§] As discussed in Section 3.3.8, the depletion depth is not constant in CCDs, but this approximation allows analytical models of the diffusion of charge clouds in the field-free depth of CCDs to be applied.

using the Beer-Lambert law (Section 3.2.1). Values for the attenuation length of photons in silicon are obtained from [35], although the empirical formula presented in [64] results in similar values across this range (Table 4.1). The interaction depth distributions for a selection of energies are shown in Figure 4.3.

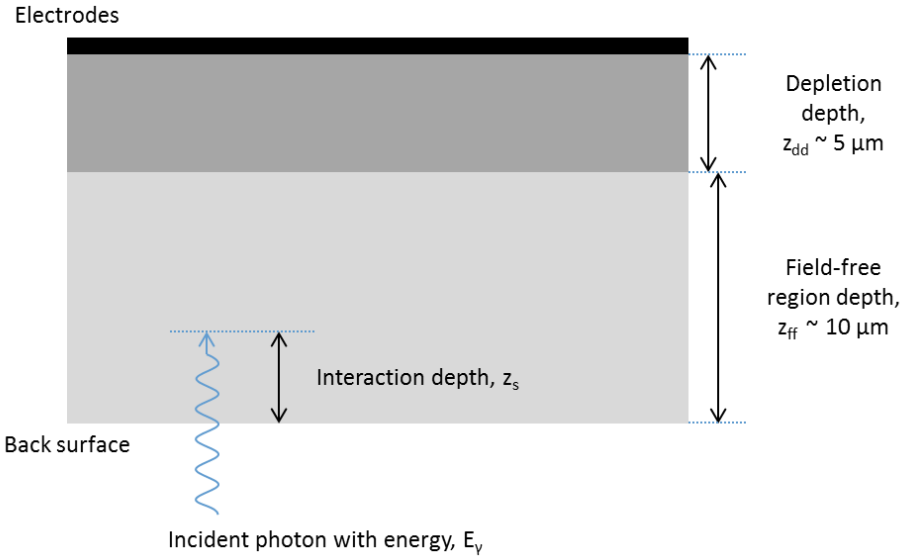

Figure 4.2. A cross-section of the device model shows the photon interacting at a random interaction depth, z_s, from the back surface.

Table 4.1. The X-ray attenuation length in silicon values used during this simulation are taken from [35]*, and are in close agreement with those obtained with the empirical formula in* [64]*.*

Energy, eV	Attenuation length values used in the following simulations [35], µm	Attenuation length values obtained using an empirical formula [64], µm
530	0.50	0.50
680	0.95	0.95
850	1.69	1.73
1000	2.68	2.69

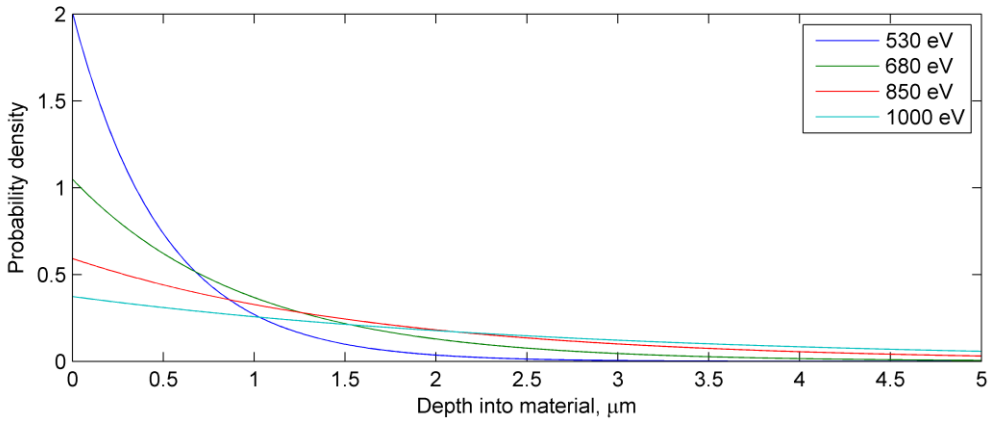

Figure 4.3. The probability distribution of interaction depths for 530 eV, 680 eV, 850 eV and 1000 eV energy photons with attenuation lengths of 0.50 µm, 0.95 µm, 1.69 µm and 2.68 µm respectively.

As described in Section 3.2.2, the number of electrons n_e produced by an X-ray photon with energy greater than 3.65 eV can be modelled using a Gaussian distribution with mean $\overline{n_e} = E_{ph}/\omega$ and variance, ${\sigma_{n_e}}^2 = f_{Si}E_{ph}/\omega$, given in *Equation 3.2*. E_{ph} is the photon energy, f_{Si} is the Fano factor for silicon [75] and is taken to be 0.12 [42] and ω, the average energy required to release an electron-hole pair, is taken to be 3.65 eV electron^{-1} [76].

4.2.2 Initial extent of the charge cloud

The charge cloud formed from an X-ray interaction is assumed to have an initial radius, r_i, given by the average electron range relationship for energies below 1000 eV from [77], where E is the photon energy in eV and r_i is measured in microns.

$$r_i = 0.03351\left(\frac{E}{1000}\right)^{1.4} \qquad \textit{Equation 4.1}$$

Evaluating *Equation 4.1* for photon energies between 530 eV and 1000 eV results in an initial charge cloud radius no larger than 0.034 µm. The contribution of r_i to the final charge cloud size is negligible when the drift and diffusion in the field-free and depletion regions are taken into account. However, the contribution of r_i is included in the model for completeness.

To progress the model from its current state of a number of electrons at a location within a 3D pixel to an array of pixel signals, the transport of the charge cloud from their initial positions to within the potential wells of the pixels must be modelled. A number of charge spreading models have been considered and evaluated on their ability to reproduce events experimentally detected

as accurately as possible whilst requiring minimum computational resources to enable the large number of events required to be simulated.

4.2.3 Diffusion in the field-free region

The splitting of charge from a single X-ray interaction between adjacent pixels is dominated by the diffusion process in the field-free region that occurs before charge enters the depletion region and drifts towards its closest potential well. Four analytical solutions will be presented that determine the charge cloud distribution to be sampled by the potential well structure at the depletion depth following diffusion from an interaction at depth z_s from the back surface. After the different distributions have been presented, they will be compared to each other and experimental data to determine which, if any, are accurate. The solutions are:

- a Gaussian distribution following Janesick *et al*. [64], Pavlov and Nousek [66] or Bootsma *et al*. [78];
- an analytical solution to the diffusion equation following Pavlov and Nousek [66];
- an empirical fit to the diffusion equation solution presented by Hopkinson [44]; and
- an analytical solution that models the electron diffusion paths as straight and isotropic from a point source, derived here.

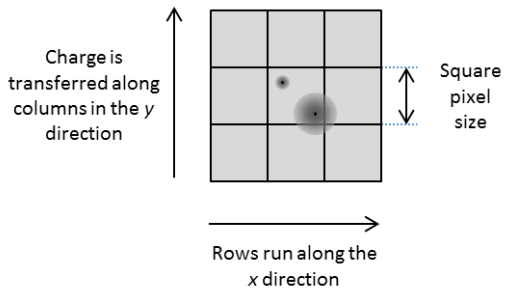

Figure 4.4. View of a 3×3 pixel area of the device structure. The column (charge transfer) and row directions are shown relative to the x and y direction vectors and two example events are shown interacting within the area of the central pixel. The charge cloud from one event is shown to have spread beyond the boundaries of the central pixel, sharing its charge with adjacent pixels. The other charge cloud does not extend beyond the pixel boundaries and therefore is an "isolated" event.

4.2.3.1 Assuming a Gaussian shape

The most straightforward charge cloud shape to apply is a Gaussian distribution; the spreading of the charge cloud in the different phases of its collection is elegantly handled by the ability to include the contribution of multiple Gaussians by adding their standard deviations in quadrature. A 2D Gaussian $G(x,y)$ with its peak at (x_0, y_0) and the same standard deviation of σ in both dimensions is defined in *Equation 3.5*, where A is some constant.

$$G(x,y) = A \exp\left(-\frac{(x-x_0)^2 + (y-y_0)^2}{2\sigma^2}\right) \qquad \textit{Equation 4.2}$$

To calculate the total charge collected in a rectangular potential well, the Gaussian error function, defined as $\mathrm{erf}(x) = \frac{2}{\sqrt{\pi}}\int_0^x e^{-t^2} dt$, can be used. The integral of $G(x,y)$ across a rectangular area with corners at (x_1, y_1) and (x_2, y_2) can be evaluated with relative ease due to the incorporation of the error function into many current-day software libraries. After normalisation, the integral of the 2D Gaussian across a rectangular pixel is in the form of *Equation 4.3*.

$$\mathbb{G} = \iint_{x_1,y_1}^{x_2,y_2} G(x,y)\, dx\, dy = \frac{Q_0}{4}\left[\mathrm{erf}\left(\frac{x_1 - x_0}{\sqrt{2}\sigma}\right) - \mathrm{erf}\left(\frac{x_2 - x_0}{\sqrt{2}\sigma}\right)\right] \left[\mathrm{erf}\left(\frac{y_1 - y_0}{\sqrt{2}\sigma}\right) - \mathrm{erf}\left(\frac{y_2 - y_0}{\sqrt{2}\sigma}\right)\right] \qquad \textit{Equation 4.3}$$

Janesick *et al*. [64] presented the following equation for a Gaussian standard deviation, σ_J, that empirically fitted to Monte Carlo random walk simulations of electrons generated at distance z_s from the reflective back face of a field-free region z_{ff} thick (therefore valid within the range $0 < z_s < z_{ff}$).

$$\sigma_J \backsimeq \frac{1}{2} z_{ff} \left[1 - \left(\frac{z_s}{z_{ff}}\right)^2\right]^{\frac{1}{2}} \qquad \textit{Equation 4.4}$$

The empirical equation fitted well for $z_{ff} = 0.05$ µm, 0.1 µm and 0.2 µm thick, but requires extrapolating and does not lend itself to being used with confidence in real devices with field-free regions in the order of 10 µm (e.g. 30 µm thick field-free region [65]).

An analytical method described by Pavlov and Nousek [66] indicates that the square root of the mean-squared radius of the charge distribution σ_{PN} in a device with a perfectly reflective back surface and neglecting recombination, is a factor of $2\sqrt{2}$ larger than the empirical fit of the random walk simulation by Janesick *et al*., *Equation 4.5*.

$$\sigma_{PN} = \sqrt{2}\, z_{ff} \left[1 - \left(\frac{z_s}{z_{ff}}\right)^2\right]^{\frac{1}{2}} \qquad \textit{Equation 4.5}$$

Alternatively, Bootsma *et al*. [78] initially use the expression of σ_J (*Equation 4.4*) for the spreading in the field-free region. Once added in quadrature with the Gaussian widths due to the initial charge cloud size (σ_{BI}) and spreading in the depletion region (σ_{BD}) the final Gaussian charge cloud standard deviation (σ_{BT}) is used as an energy-dependant fitting parameter in the simulation. The X-ray events observed in 38.1 µm thick back-illuminated CCDs lead to fitted parameters of $a_B = 0.21$ and $b_B = 3.8 \times 10^{-5}$ when E is measured in electron volts [78].

$$\sigma_{BT} = \sqrt{\sigma_J^2 + \sigma_{BI}^2 + \sigma_{BD}^2}\,(a_B + b_B E) \qquad \textit{Equation 4.6}$$

Three different standard deviations that have been used to model charge spreading in the field-free region of CCDs as a Gaussian profile have been presented. σ_J and σ_{PN} follow the same relationship with the field-free and depletion depth, where the standard deviation is proportional to the square root of the distance between the interaction point and field-free region. This form of a relationship is expected, as the further away the interaction occurs from the depletion depth, the longer time the charge cloud has to diffuse laterally before collection in the potential wells.

4.2.3.2 Solutions of the diffusion equation

A perhaps more accurate estimation than the Gaussian profile may be obtained by directly solving the diffusion equation. Hopkinson analytically derived the charge cloud shape at the depletion depth following diffusion from a point source in a slab of field-free material in the case of a fully reflective back surface and where the diffusion length is large relative to the field-free depth [79]. The derivation was repeated in a more general case by Pavlov and Nousek [66], and in specific cases again by Hopkinson [44] and others including Widenhorn *et al*. [80] and Groom *et al*. [81].

Pavlov and Nousek presented two generalised solutions of the diffusion equation determined by Fourier analysis and the method of images, resulting in two complementary equations that both describe the charge cloud density distribution as a function of radial distance, $q(r)$ at the boundary between the field-free region and depletion depth [66]. Assuming recombination does not occur and the back surface is completely reflective, the solutions simplify to the following expressions, where L is the diffusion length, K_0 is a zero order modified Bessel function of the second kind and $\alpha_n = (2n-1)\pi/2$.

$$q(r) = \frac{1}{2\pi} \sum_{m=-\infty}^{\infty} (-1)^m \frac{z_{ff}(1-2m) - z_s}{p_m^3} \left(1 + \frac{p_m}{L}\right) \exp\left(-\frac{p_m}{L}\right) \qquad \textit{Equation 4.7}$$

where $$p_m = \sqrt{r^2 + \left(z_{ff}(1-2m) - z_s\right)^2}$$

$$q(r) = \frac{1}{2z_{ff}^2}\sum_{n=1}^{\infty}\alpha_n \sin\left(\alpha_n\left(1-\frac{z_s}{z_{ff}}\right)\right) K_0\left(\frac{r}{z_{ff}}\sqrt{\alpha_n^2 + \frac{z_{ff}^2}{L^2}}\right) \qquad \textit{Equation 4.8}$$

Whilst both analytical solutions are equivalent, the method of images solution (*Equation 4.8*) converges with fewer terms, especially when $r < 0.1\, z_{ff}$, (observed in [66,82]) and so is most appropriate to use for evaluation.

Integrating the charge cloud across a rectangular pixel area is less trivial for this analytical solution than for the case of a Gaussian, but was presented by Pavlov and Nousek [66]. Under the conditions of a perfectly reflecting back surface and negligible recombination, the charge cloud integrated across the rectangular area with corners at (x_1, y_1) and (x_2, y_2) is given in *Equation 4.9*.

$$\iint_{x_1,y_1}^{x_2,y_2} q(r) = \frac{Q_0}{4\sqrt{\pi}}\int_0^{\infty}\frac{d\tau}{\tau^{3/2}} G_i(x,\tau)G_j(y,\tau)S(\tau)\exp\left[-\tau\left(\frac{z_{ff}}{2L}\right)^2\right] \qquad \textit{Equation 4.9}$$

where

$$G_i(x,\tau) = \operatorname{erf}\left(\frac{x_2 - x_0}{\sqrt{z_{ff}^2\tau + r_d^2 + r_i^2}}\right) - \operatorname{erf}\left(\frac{x_1 - x_0}{\sqrt{z_{ff}^2\tau + r_d^2 + r_i^2}}\right) \qquad \textit{Equation 4.10}$$

$$S(\tau) = \sum_{m=-\infty}^{\infty}(-1)^m\left(1 - \frac{z_s}{z_{ff}} - 2m\right)\exp\left[-\frac{\left(1 - \frac{z_s}{z_{ff}} - 2m\right)^2}{\tau}\right] \qquad \textit{Equation 4.11}$$

Hopkinson originally presented *Equation 4.12* as an empirical fit with 3% accuracy to his analytical solution (k_1 is a constant) [44]. Whilst being computationally simple and quick to implement, the superior accuracy of the analytical solution (*Equation 4.8*) outweighs the time benefits with current-day computational power. An integral could not be found analytically; therefore *Equation 4.12* must be integrated across a rectangular pixel area numerically.

$$q(r) = k_1\left(1 + \frac{r}{0.8\,(z_{ff} - z_s)}\right)^{-2.5} \qquad \textit{Equation 4.12}$$

4.2.3.3 Isotropic straight line diffusion model in 2D and 3D

An alternative solution to the charge cloud spreading may be derived by considering a situation where electrons generated at a point source travel on straight paths from the position of interaction to the depletion region, with an isotropic distribution. An analytical solution to this model is first presented for the 2D case [83] and then generalised to 3D.

An infinite slab of thickness L is considered, where one side is the back surface of a CCD and the other is the boundary between the field-free region and the depletion region. For an interaction occurring at the back surface, a point source is considered, from which electrons travel in straight lines isotropically into the device. As shown in the geometry and labelling of Figure 4.5, $d\theta$ is a small angle, θ is the angle of the path (where $\theta = 0$ is normal to the back surface), x is the distance scale across the field-free and depletion region boundary ($x = 0$ is directly opposite the interaction location) and $A(x)$ as the length along the boundary over which the small angle $d\theta$ sweeps.

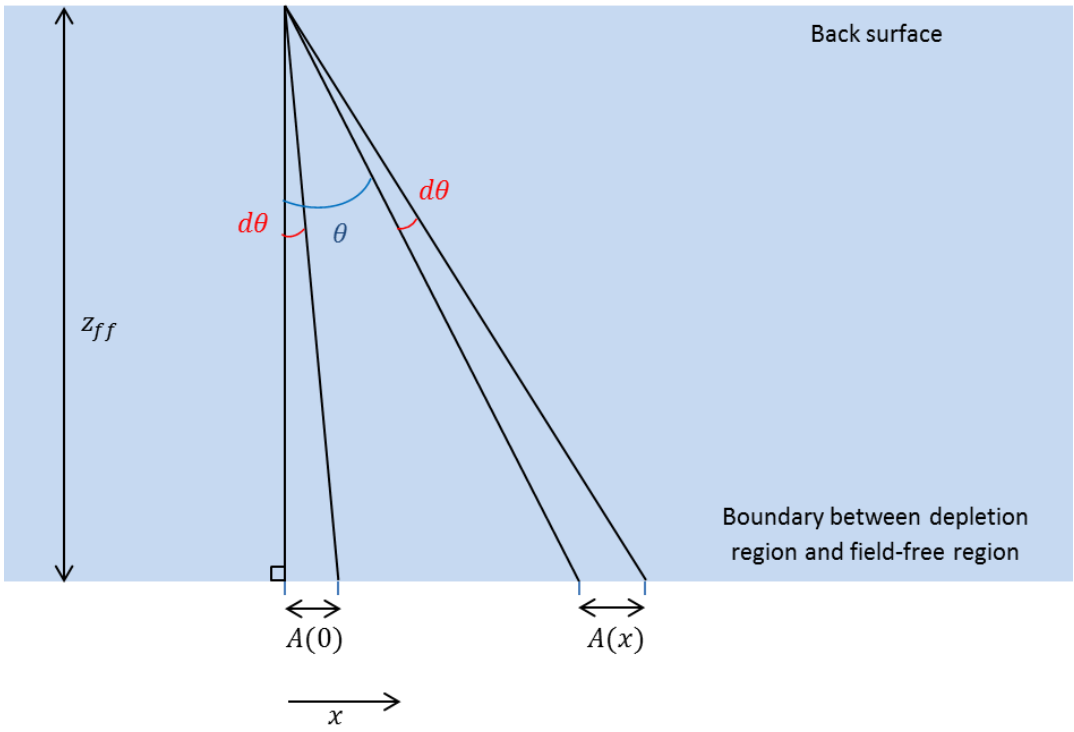

Figure 4.5. Geometry for the 2D proof, assuming an interaction at the back surface (top) and diffusion to the boundary of the field-free layer at the bottom.

Using the trigonometric addition formula, $\tan(\alpha+\beta) = \frac{\tan\alpha+\tan\beta}{1-\tan\alpha\tan\beta}$, and the relationships $\tan\theta = \frac{x}{z_{ff}}$ and $\tan(\theta+d\theta) = \frac{x+A(x)}{z_{ff}}$ observed in Figure 4.5, *Equation 4.13* can be written.

$$\frac{x + A(x)}{z_{ff}} = \frac{\frac{x}{z_{ff}} + \tan d\theta}{1 - \frac{x}{z_{ff}} \tan d\theta} \qquad \textit{Equation 4.13}$$

Rearranging *Equation 4.13* and dividing by $A(x = 0) = A(0)$ results in *Equation 4.14*.

$$\frac{A(x)}{A(0)} = \frac{z_{ff} + \frac{x^2}{z_{ff}}}{z_{ff} - x \tan d\theta} \qquad \textit{Equation 4.14}$$

Under the limit of $\mathrm{d}\theta \to 0$ (where $\tan d\theta \to \mathrm{d}\theta \to 0$) and noting that the electron intensity is inversely proportional to the length of the boundary that is swept by $d\theta$ ($I(x) \propto \frac{1}{dA(x)}$), an expression of the charge cloud shape for an interaction that occurs at the back surface, in a 2D system, is obtained (*Equation 4.15*).

$$I(x) = I(0) \frac{1}{1 + \frac{x^2}{{z_{ff}}^2}} \qquad \textit{Equation 4.15}$$

It can be shown that the FWHM of the distribution given by Equation 4.15 is $2z_{ff}$ i.e. doubling the thickness of the field-free region (z_{ff}) doubles the spread of the distribution. An equivalent relationship was observed in the diffusion equation solution by Hopkinson [79] for when z_{ff}/L is small, and utilised by Tutt *et al*. [84].

The derivation of *Equation 4.15* has been obtained from [83]. To expand the derivation to the 3D case, a similar geometry is defined for a 3D field-free slab, and a similar approach is made in the following proof to determine the charge cloud intensity at the boundary of the field-free region with the depletion region. In Figure 4.6, $d\Omega$ is a constant solid angle that projects across an area dA of the field-free-depletion layer boundary, where $\hat{\mathbf{n}}$ is the vector normal to the planes, therefore $d\Omega$ can be expressed as in *Equation 4.16*.

$$d\Omega = \frac{\hat{\mathbf{n}} \cdot \boldsymbol{dA}}{\rho^2} = \frac{\cos\theta \, dA}{\rho^2} \qquad \textit{Equation 4.16}$$

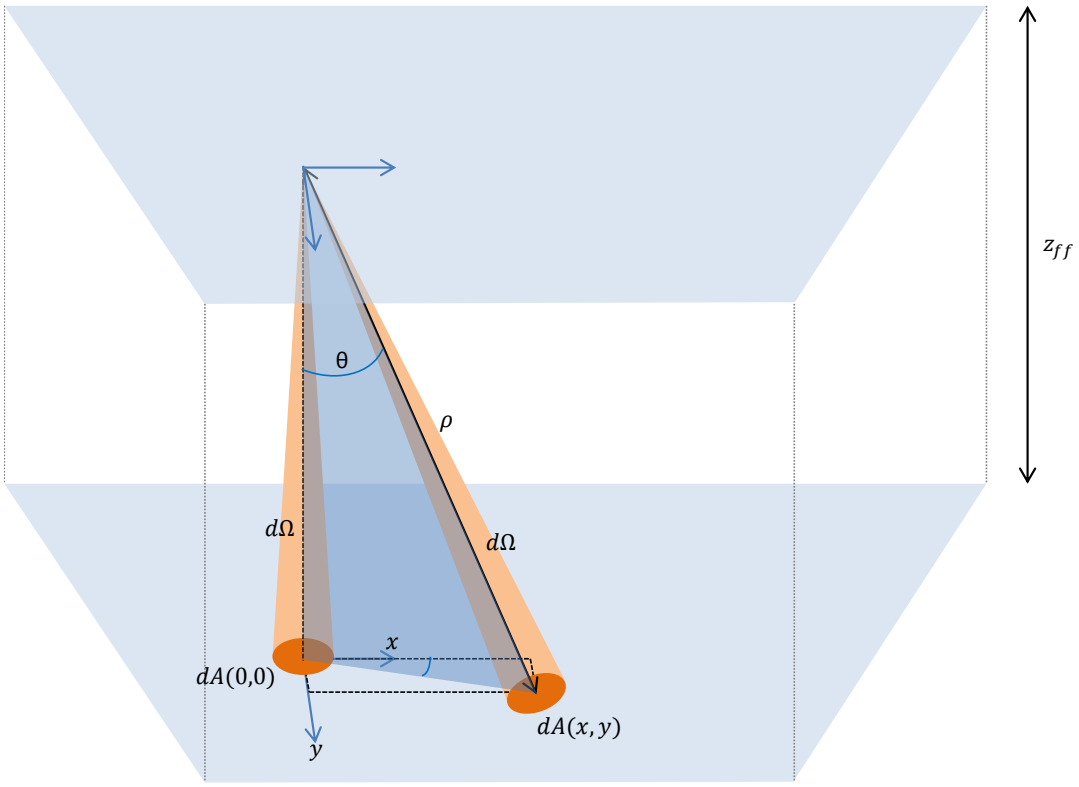

Figure 4.6. Geometry for the 3D proof, assuming an interaction at the back surface (top) and diffusion to the boundary of the field-free layer at the bottom.

Substituting the geometric relationship $\cos\theta = z_{ff}/\rho$, where $\rho^2 = x^2 + y^2 + {z_{ff}}^2$, leads to an expression (*Equation 4.17*) for dA as a function of the position on the plane (in x and y coordinates).

$$dA(x,y) = \frac{\rho^2}{\cos\theta}d\Omega = \frac{\rho^3}{z_{ff}}d\Omega = \frac{\left(x^2 + y^2 + {z_{ff}}^2\right)^{\frac{3}{2}}}{z_{ff}}d\Omega \qquad \textit{Equation 4.17}$$

Dividing by the area of the plane at $dA(x = 0, y = 0) = dA(0,0)$ allows the constant solid angle $d\Omega$ to be cancelled (*Equation 4.18*).

$$\frac{dA(x,y)}{dA(0,0)} = \frac{\left(x^2 + y^2 + {z_{ff}}^2\right)^{\frac{3}{2}}}{z_{ff}^3} \qquad \textit{Equation 4.18}$$

Using the fact that the density of the electron cloud is inversely proportional to the area of the plane swept out by the solid angle, $I(x,y) \propto \frac{1}{dA(x,y)}$, the charge cloud due to an interaction at the back surface of a 3D slab to be obtained. The result, *Equation 4.19*, is comparable to the result of Kirkpatrick [63], where the diffusion equation was solved for the special case of an absorbing back surface assuming no recombination.

$$I(x,y) = I(0,0)\frac{{z_{ff}}^3}{\left(x^2+y^2+{z_{ff}}^2\right)^{\frac{3}{2}}} \qquad \textit{Equation 4.19}$$

Extending this approach further, a perfectly reflective surface can be considered where electrons undergo specular reflection at the back surface. For an interaction at depth z_s, contributions from the component that travels directly to the boundary and the component that reflects at the back surface must be added together as in *Equation 4.20*.

$$I(x,y,z_s) = k_K\left[\frac{\left(z_{ff}-z_s\right)^3}{\left(x^2+y^2+\left(z_{ff}-z_s\right)^2\right)^{\frac{3}{2}}}+\frac{\left(z_{ff}+z_s\right)^3}{\left(x^2+y^2+\left(z_{ff}+z_s\right)^2\right)^{\frac{3}{2}}}\right] \qquad \textit{Equation 4.20}$$

To determine the value of the normalising constant k_K, *Equation 4.20* is integrated and equated to the total charge in the cloud, Q_0.

$$Q_0 = \iint_{-\infty,-\infty}^{\infty,\infty} I(x,y,z_s)\,dx\,dy = k_K 4\pi\left(z_{ff}^2+z_s^2\right) \qquad \textit{Equation 4.21}$$

Therefore the normalised charge cloud density at the field-free-depletion region boundary from an interaction at depth z_s from the back surface is given by *Equation 4.22*.

$$q(r,z_s) = \frac{Q_0}{4\pi\left(z_{ff}^2+z_s^2\right)}\left[\frac{\left(z_{ff}-z_s\right)^3}{\left(r^2+\left(z_{ff}-z_s\right)^2\right)^{\frac{3}{2}}}+\frac{\left(z_{ff}-z_s\right)^3}{\left(r^2+\left(z_{ff}+z_s\right)^2\right)^{\frac{3}{2}}}\right] \qquad \textit{Equation 4.22}$$

The symmetry in *Equation 4.22* is more easily observed by using $u_{nr} = z_{ff} - z_s$ and $u_r = z_{ff} + z_s$ for the non-reflected and reflected distances respectively.

$$q(r,z_s) = \frac{Q_0}{4\pi\left(z_{ff}^2+z_s^2\right)}\left[\left(\frac{u_{nr}}{\sqrt{r^2+{u_{nr}}^2}}\right)^3+\left(\frac{u_r}{\sqrt{r^2+{u_r}^2}}\right)^3\right] \qquad \textit{Equation 4.23}$$

Assuming the interaction occurs at the back surface ($z_s = 0$), the 3D models (*Equation 4.19* and *Equation 4.22*) have a FWHM of $2z_{ff}\sqrt{2^{2/3}-1} \approx 1.53z_{ff}$, thinner than the 2D case (FWHM of $2z_{ff}$). However, the charge cloud size still scales with the distance between the interaction and the field-free-depletion region boundary.

To integrate *Equation 4.23* across a rectangular pixel area with corners at (x_1,y_1) and (x_2,y_2), consider integrating the following.

$$P(u) = \iint_{x_1,y_1}^{x_2,y_2}\frac{u^3}{(x^2+y^2+u^2)^{\frac{3}{2}}}dx\,dy$$

$$= u^3 \int_{y_1}^{y_2} \left[\frac{x}{(y^2 + L^2)\sqrt{x^2 + y^2 + u^2}} \right]_{x_1}^{x_2} dy$$

$$= u^3 \left[\left[\frac{1}{u} \tan^{-1} \left(\frac{xy}{u\sqrt{x^2 + y^2 + u^2}} \right) \right]_{x_1}^{x_2} \right]_{y_1}^{y_2} \qquad \textit{Equation 4.24}$$

$$P(u) = u^2 \left[\tan^{-1} \left(\frac{x_2 y_2}{u\sqrt{x_2^2 + y_2^2 + u^2}} \right) - \tan^{-1} \left(\frac{x_1 y_2}{u\sqrt{x_1^2 + y_2^2 + u^2}} \right) - \tan^{-1} \left(\frac{x_2 y_1}{u\sqrt{x_2^2 + y_1^2 + u^2}} \right) + \tan^{-1} \left(\frac{x_1 y_1}{u\sqrt{x_1^2 + y_1^2 + u^2}} \right) \right] \qquad \textit{Equation 4.25}$$

Therefore the integral of $q(r, z_s)$ (*Equation 4.23*) over a rectangular region bounded by the corners at (x_1, y_1) and (x_2, y_2), is given by *Equation 4.26*.

$$\iint_{x_1, y_1}^{x_2, y_2} q(r, z_s)\, dx\, dy = \frac{Q_0}{4\pi\left(z_{ff}^2 + z_s^2\right)} \left(P(u_{nr}) + P(u_r) \right) \qquad \textit{Equation 4.26}$$

A solution has been obtained for the case where the diffusion of electrons is assumed to be isotropic in straight lines from a point source. The solution is comparable in form to a solution obtained by Kirkpatrick [63] when the interaction occurs at the back surface. From integrating the solution, the amount of charge expected to be collected in a rectangular pixel can be calculated using *Equation 4.25*, *Equation 4.26*, $u_{nr} = z_{ff} - z_s$ and $u_r = z_{ff} + z_s$. Diffusing electrons take a meandering path through silicon, rather than straight lines, so in the real case electrons are more likely to enter the depletion region and be collected closer to the interaction point. Therefore the solution derived here is expected to be wider than the real case.

4.2.4 Assumptions applied to determine the charge cloud shape models

Three models and an empirical fit have been presented in the previous sections:

1) a Gaussian distribution with a standard deviation derived from either a Monte Carlo simulation by Janesick *et al*. (*Equation 4.4*) [64], an analytical approach by Pavlov and Nousek (*Equation 4.5*) [66] or fitting to the data using an approach such as Bootsma *et al*. (*Equation 4.6*) [78];
2) an analytical solution to the diffusion equation which has been described most generally and completely by Pavlov and Nousek and is most accurately and quickly computed using *Equation 4.8* [66];
3) an empirical fit to the diffusion equation solution from Hopkinson (*Equation 4.12*) [44]; and

4) an analytical solution that models the electron diffusion paths as straight and isotropic with a perfectly reflective back surface and absorptive depletion layer boundary (*Equation 4.22*).

In calculating the analytical models, approximations have been made to simplify the derivation of a solution. The following approximations were made regarding the CCD structure:

- the back surface region has no thickness and all electrons incident are reflected;
- the boundary between the field-free region and the depletion region is a flat plane, normal to the back surface, with a definite boundary where one side is field-free, and the other has sufficient field to capture electrons;
- no charge is lost due to recombination; and
- the pixel collection area is rectangular.

The back surface treatment of back-illuminated detectors is highly reflective, and for modelling interactions in the field-free region, the back surface region can be considered a dead layer where no interactions occur. The second assumption is reasonable when the depletion depth is larger than the pixel size, but experimental data presented later shows that in devices such as the CCD42-10 there is a significant variation in the depletion depth across the pixel (Section 4.2.6.2). Not using this assumption significantly complicates the derivation of an analytical solution to the problem. The probability of electron-hole recombination is low in the time it takes for the electrons to be collected by the potential well, therefore it is reasonable to assume that no charge is lost due to recombination. Pixel collection areas are approximately rectangular, due to the grid-like layout of the electrodes and doping structures, and therefore this is also a reasonable assumption.

The charge collection process has also been simplified in the model. Effects caused by a charge cloud being formed with portions of charge in different CCD regions are ignored, i.e. although an interaction close to the depletion region boundary may result in some electrons being formed in the depletion region and therefore not party to the process of diffusion in the field-free region, all charge is assumed to be formed at the same point with the initial charge cloud size being added to the final spreading effect. Additionally, the changes to the field produced by the charge cloud itself are ignored. This includes field funnelling effects [79], reduction in depletion depth from charge already collected in pixels and interactions between holes and electrons generated within the cloud. For the majority of events, these effects are expected to only play a minor role in the allocation of charge between pixels, and so it is reasonable to overlook them in these models.

4.2.5 Charge cloud shape model comparison

Cross-sections of the charge cloud shape models are shown for four different interaction depths in Figure 4.7. The cross-sections have been calculated for a field-free depth of 8.3 µm, the maximum field-free depth predicted in Section 3.3.8 for a CCD42-10 when a 13 µm total thickness is assumed. The charge cloud widths vary dramatically between the models, getting narrower when the interaction occurs closer to the depletion depth, as expected.

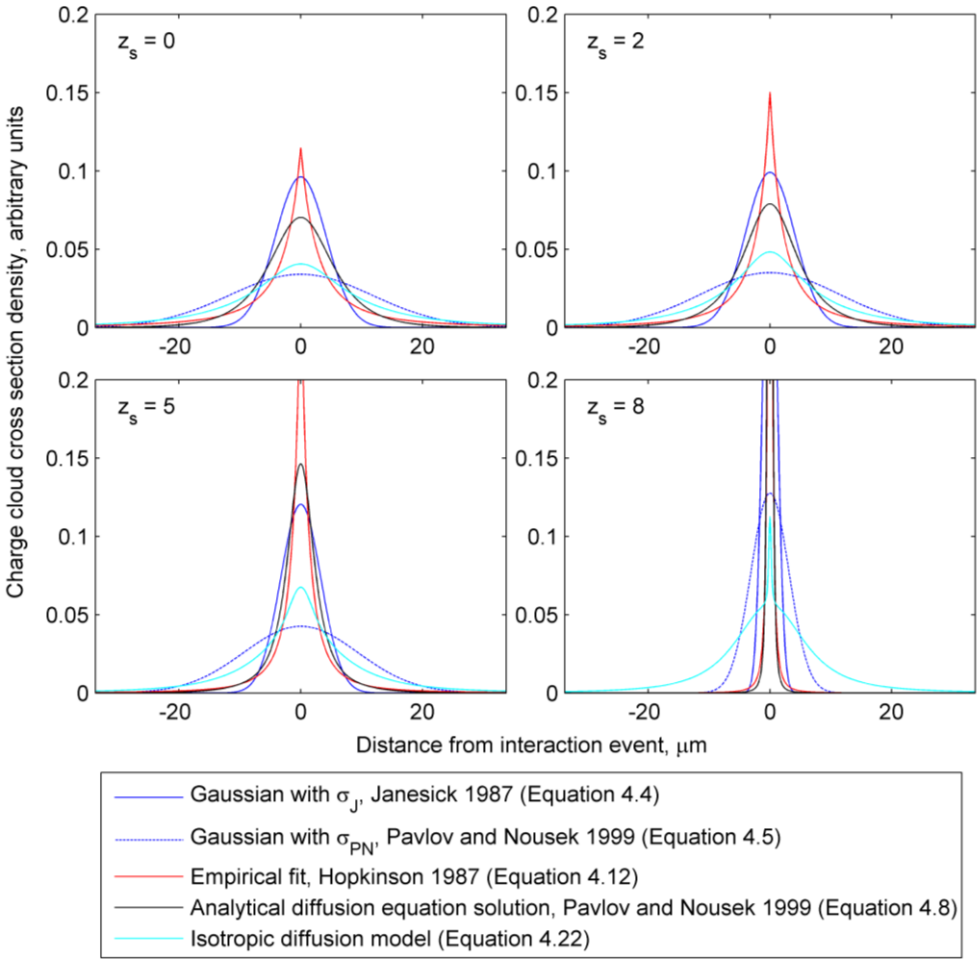

Figure 4.7. Charge cloud shapes from the models discussed in this section are displayed for four different interaction depths from the back surface, $z_s = 0$, 2, 5 and 8. The pixel used in these simulations had a field-free depth $z_{ff} = 8.3\ \mu m$.

The models must be compared to data taken with a CCD42-10 (Section 6.7), in order to determine which, if any, of the literature models are accurate and which is best to use in the simulation package. The experimental setup allowed 1000 eV X-rays, incident normal to the device, to be focussed to interact close to the centre of a pixel. During data analysis, a histogram has been

constructed for each pixel surrounding the interaction point that contains the pixel signals observed when a single photon is detected. The background signal and ADU offsets have been removed, and the signals calibrated using isolated events. The method of data collection and a full description of the data analysis that was undertaken for the CCD42-10 experimental data can be found in Section 6.3.2.

To match the experimental data, a simulation is constructed using the bespoke Monte Carlo package. Single, 1000 eV, photons are incident normally at the centre of a 5×5 pixel array, with an interaction depth given by the distribution described in Section 4.2.1. A field-free depth of 8.3 µm and depletion depth of 4.7 µm were chosen to match the expected dimensions of a CCD42-10 as calculated in Section 3.3.8 and the collection area of each pixel was assumed to be 13.5 µm square. A diffusion length of 100 µm was used [79] and, as will be discussed in 4.2.6, if the diffusion length is greater than the characteristic size of the pixel, it changes the charge cloud shape very little.

The electrons are randomly assigned according to the probability distribution defined by the model under investigation or, if the interaction occurs in the depletion region, all electrons are collected in the central pixel. To match the readout noise observed in the experimental data, a random value from a Gaussian distribution with standard deviation of 6.2 electrons rms is added to each pixel. A total of 50 000 photon events which interacted within the depletion region or field-free region were simulated for each model to produce the model pixel distributions.

The signal distributions for each pixel in the central 3×3 pixel area are shown for both the data and models in Figure 4.8. The outer pixels in the 5×5 are not shown as the experimental data is in good agreement with all the models, in Gaussian-like distributions centred at the zero signal level. In the central 3×3 pixels, closer to the interaction point, the distributions vary significantly more between models and when compared to the experimental data. The model and data distributions differ most for the central pixel within which the interaction occurred therefore these distributions have been reproduced at a larger scale in Figure 4.9.

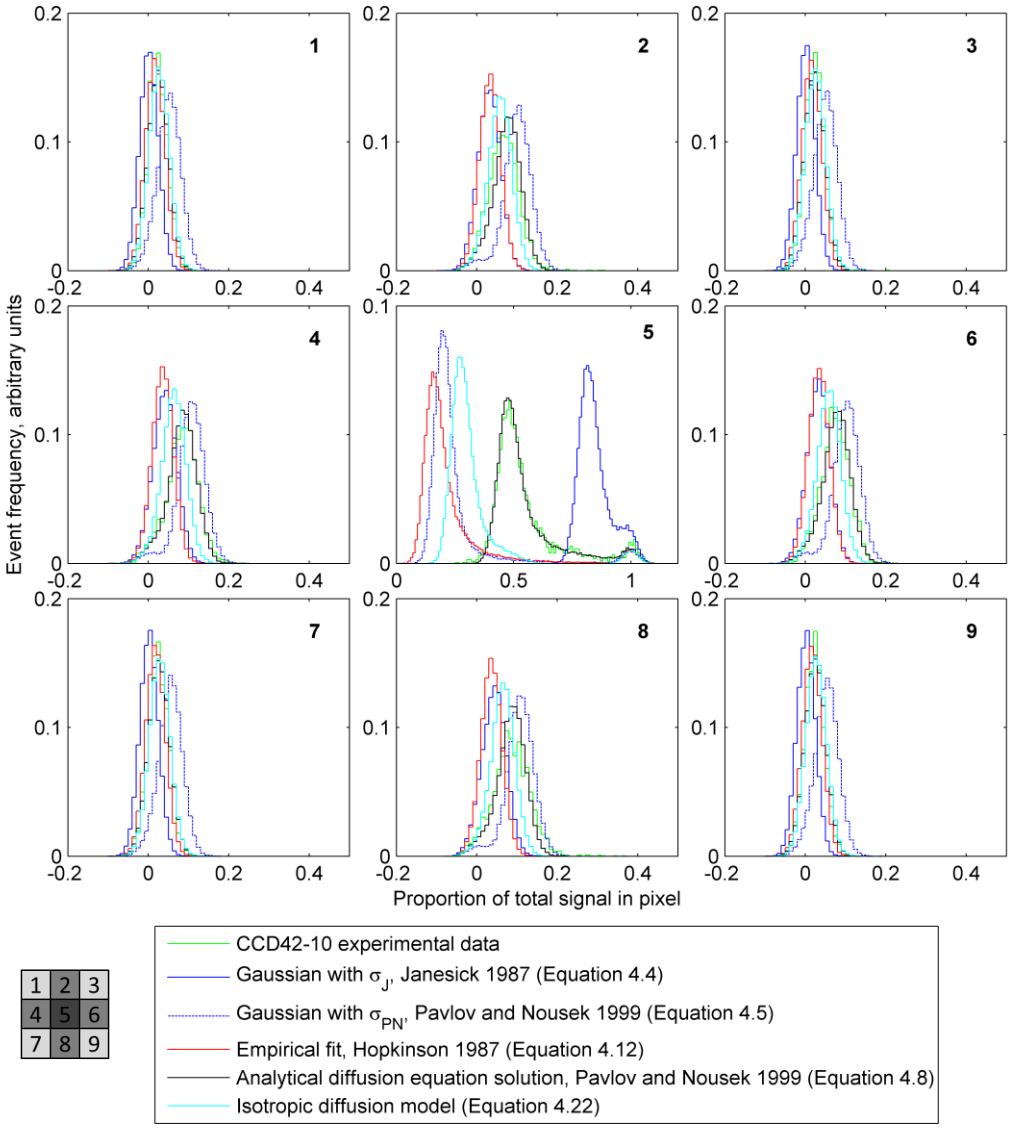

Figure 4.8. A histogram for each pixel in the 3×3 area is shown. The top-left histogram is the top-left pixel, which is closest to the output register. The parallel transfer direction of the CCD is vertically upwards along the columns, and the photons are incident in the centre of the central pixel whose signal distributions are shown in the central histogram.

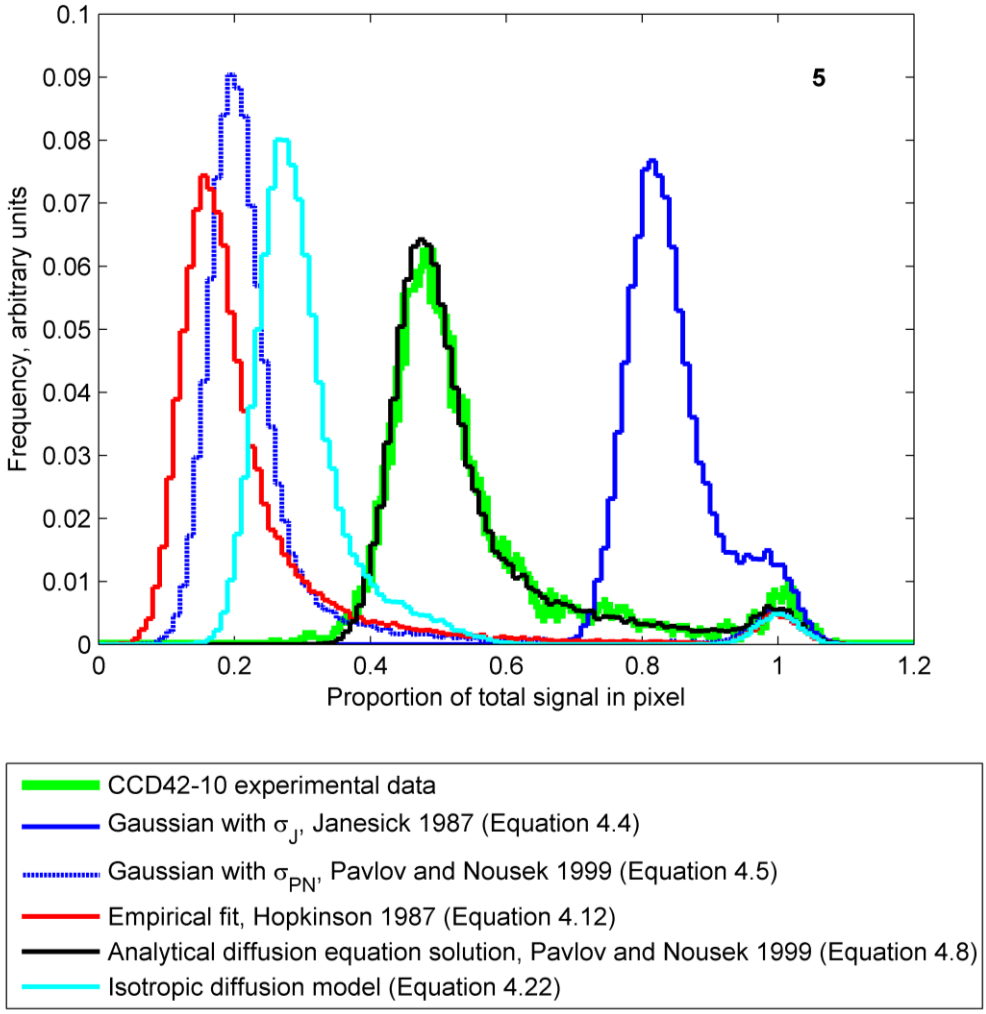

Figure 4.9. The distribution of signals detected in the central pixel of the 5×5 area (the central histogram of Figure 4.8). The Pavlov and Nousek analytical diffusion equation solution (Equation 4.8*) fits best with the experimental data set.*

The central pixel's signal distribution in the experimental data is dominated by a peak where around 50% of the total signal generated by an X-ray is collected in the central pixel. This peak is formed by the events that interact close to the back surface and dominates the distribution because the majority of events occur with a shallow interaction depth. The higher signal shoulder of the primary peak extends towards a smaller secondary peak centred at a total signal of approximately 1. In the modelled distributions, the extended shoulder is formed by the interactions that occur in the field-free region: when the interaction occurs further from the back surface, the charge cloud diffuses a shorter distance to the depletion region therefore it spreads over a smaller area and a larger proportion of the signal is present in the central pixel. The exponential-like decay of the shoulder corresponds to the exponential decay of the interaction depth probability distribution. The secondary peak at a signal level of 1 is formed by the events

that occur in the depletion region, where the entire charge cloud is collected in this central pixel (isolated events).

In addition to the distributions of signals in individual pixels (Figure 4.8), a distribution is calculated for the total signal in the central 3×3 pixel area for each event, displayed in Figure 4.10. The distribution from the experimental data is approximately Gaussian centred at a total signal of 1.

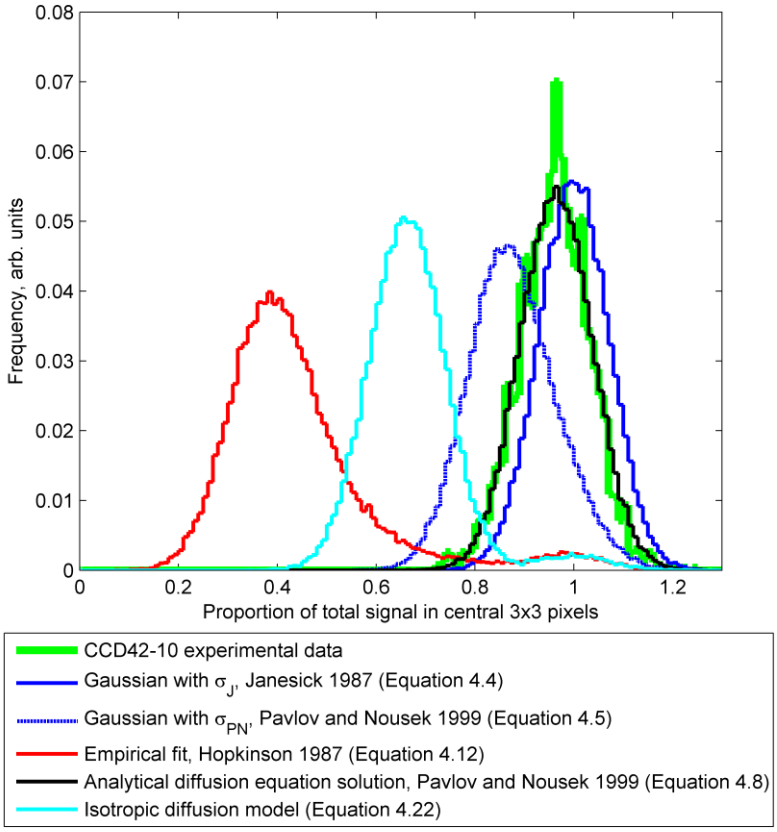

Figure 4.10. The signals detected in the central 3×3 pixel area are summed for each event in the distributions shown here. In the experimental distribution the events are distributed in an approximately Gaussian shape with a centre close to 1 indicating that virtually all the signal is detected within the central 3×3 pixels.

The ability of each model to reproduce the experimentally observed signal distributions can be compared easily using the distributions of the signal in the central pixel (Figure 4.9) and total signal in the 3×3 pixel area (Figure 4.10). The models result in very different distributions, with the starting conditions of a field-free depth of 8.3 µm, a depletion depth of 4.7 µm and a diffusion length of 100 µm. The analytical solution to the diffusion equation (*Equation 4.8*) derived by Pavlov and Nousek [66] performs best with these initial conditions, but the parameter space must

be explored to determine if other models can match the experimental data equally well or better when other parameters are used.

4.2.6 Model parameter sensitivity

With a field-free depth of 8.3 µm, a depletion depth of 4.7 µm and a diffusion length of 100 µm, the analytical solution to the diffusion equation by Pavlov and Nousek (*Equation 4.8*, [66]) is visibly the best-fitting model to the experimental data, in both the central pixel signal and the sum of the 3×3 pixel signals. However, the parameters of the simulation (depths of the depletion region and field-free region, and the diffusion length of electrons in silicon) must be varied to ensure a parameter set cannot be found where other models fit the experimental data set better, whilst keeping within the radius of probability in physics for the e2v manufactured device.

The diffusion length of electrons in silicon L is only used by the Pavlov and Nousek diffusion equation solution, which already fits the data well with an estimated value of $L = 100$ µm [79]. From *Equation 4.9*, if the diffusion length is significantly greater than the field-free region thickness, its value will have little effect on the evaluated solution. This has been verified in the simulation, where the distribution changes little for all values of L greater than approximately 50 µm. A diffusion length of 100 µm compared to a field-free depth between approximately 5 µm and 20 µm encompasses the assumption that recombination can be ignored, and agrees well with the experimental data so $L = 100$ µm is used for all simulations in this thesis.

Increasing the depth of the field-free region, z_{ff}, shifts the primary, charge-splitting peak in the modelled central pixel signal distribution (Figure 4.9) towards a lower value as the majority of events that occur close to the back surface must diffuse across a greater thickness of silicon to reach the depletion region. Additionally, the proportion of events occurring within the isolated event peak is reduced as photons are less likely to penetrate to the deeper field-free region to interact in the depletion region. For all models, the average signal detected within the 3×3 pixel area decreases as the field-free depth is increased.

Increasing the depth of the depletion region, z_{dd}, increases the proportion of events that interact within the depletion region. The result is an increase in the proportion of events in the isolated event peak that do not undergo any charge splitting. When the field-free region is thick relative to the attenuation length of the incident X-rays, small changes in the depletion region depth do not make a significant difference as very few X-rays penetrate to interact there.

4.2.6.1 Fitting the model parameters

The initial test of the charge spreading models shown in Figure 4.9 and Figure 4.10 used a field-free region thickness of 8.3 µm and a depletion region thickness of 4.7 µm. These initial values were chosen because they are predicted by the nominal thicknesses and doping levels of a CCD42-10 manufactured by e2v. Using these initial values, the Pavlov and Nousek model (*Equation 4.8*, [66]) is in good agreement with the experimental data.

For the charge-splitting peak of the Hopkinson empirical model in the central pixel's signal distribution (Figure 4.9) to align with the experimental data, the field-free region thickness in the simulation must be reduced to 2 µm. Similarly, the field-free depth must be reduced to approximately 4.8 µm to align the experimentally observed charge-splitting peak with the isotropic diffusion model. However, the thinner field-free region results in the total signal in the central 3×3 pixel distributions (Figure 4.10) not appearing Gaussian due to only approximately 80% of the charge being detected in the 3×3 pixels. This is not consistent with the experimental data. Coupled with the fact that the expected manufactured thickness of the devices is significantly thicker, it is concluded that the current forms of the Hopkinson empirical fit and isotropic diffusion model are not appropriate solutions to model the charge-sharing processes observed experimentally with the CCD42-10.

To align the charge-sharing peak of the Gaussian charge cloud models to the experimental data, the standard deviation of the Gaussian is multiplied by a constant fitting factor, in an approach similar to that of Bootsma *et al*. [78]. The standard deviation of the model proposed by Janesick *et al*. (*Equation 4.4*) fits best when multiplied by a factor of approximately 1.64 (not a factor of $2\sqrt{2} \approx 2.83$ proposed by Pavlov and Nousek [66]). However, when the charge cloud width is modified in this way, more signal is detected in the central 3×3 pixels for the Gaussian model than the experimental data. This observation implies that the experimentally observed charge cloud has wings that extend beyond the 3×3 pixel area.

The analytical solution to the diffusion equation from Pavlov and Nousek [66] (*Equation 4.9*) is in good agreement with the experimental data when the initial parameters are used (with thicknesses of 8.3 µm and 4.7 µm for the field-free and depletion regions respectively). The expected signal distribution sampled by an area of 5×5 pixels, for a single interaction position within a pixel takes approximately 0.1 seconds to evaluate and therefore is not too computationally intensive.

To summarise, a solution to an isotropic diffusion model has been derived in Section 4.2.3.3, and then reviewed alongside a selection of charge-sharing models from the literature. The models have been implemented and evaluated for 1000 eV photons incident at the centre of a pixel with

parameters expected for a CCD42-10. By comparing the pixel signal distributions simulated from single photon interactions to experimental data, it was determined that the analytical diffusion equation solution (*Equation 4.9*, [66]) was the model that best fit the data whilst using parameters that are physical and reasonable considering the nominal thickness and doping structure of the device. Therefore the full diffusion equation solution is chosen to be used in all simulations in this thesis.

4.2.6.2 Comparing the diffusion equation solution model to experimental data

A similar experimental data set was collected where 1000 eV photons were incident normal to the device in the corner of a CCD42-10 pixel (13.5 µm square). Of the 2889 single photons detected, insufficient isolated events are present to form a separate peak, so the experimental data cannot be calibrated to the isolated event peak as when the photons were incident at the centre of the pixel. Therefore, the corner data is calibrated using a Gaussian profile fit to the sum of the signals in the 3×3 pixel region. The overall noise in the experimental data is accounted for in the simulation by adding a random variable from a Gaussian distribution with a standard deviation of 6.34 electrons rms, matching the measured value in the experimental data.

The lack of isolated events compared to interactions for photons incident at the centre of the pixel suggests that the depletion depth is not as deep in the pixel corner and the charge clouds formed at all depths are split across multiple pixels. The assumption that the depletion depth is constant across the entire area of the pixel may therefore not be valid, but to compensate, a different effective depletion depth has been used when calculating the charge spreading in different areas of the pixel. This approximation provides a reasonable manner to deal with the varying depletion depth in a real device and allows the analytical model to be utilised.

In the experimental data, the X-ray photons have interacted across an approximately circular area in the plane of the pixel due the shape of the beam focussing optics (described in Section 3.7). The area and exact position of the X-ray interactions are not directly measureable but are used as additional fitting parameters within the model. At the corner of the pixel, the size and position of the X-ray photon beam has a more significant effect than at the centre of the pixel.

When setting the field-free depth to 9.5 µm and the depletion depth to 3.5 µm to maintain the total thickness at 13 µm, the best fitting beam size and position is at (-6.5, -5.5) µm relative to the centre of the main pixel, with the incident X-rays distributed evenly across a circle with radius 1.1 µm. The best fit is determined by minimising the sum of squared residuals for the four pixels surrounding the mean interaction position, shown in Figure 4.11. A reasonable fit is obtained but differences are observed that may be explained by the non-uniform depletion depth and/or

asymmetry of the pixel potential wells in the *x* and *y* directions. For example, the proportion of signal in the bottom-left pixel has a wider distribution in the experimental data than predicted by the simulation. This may be due to the potential structure in the column isolation leading to the charge splitting being more dependent on the interaction position than predicted by a constant depletion depth.

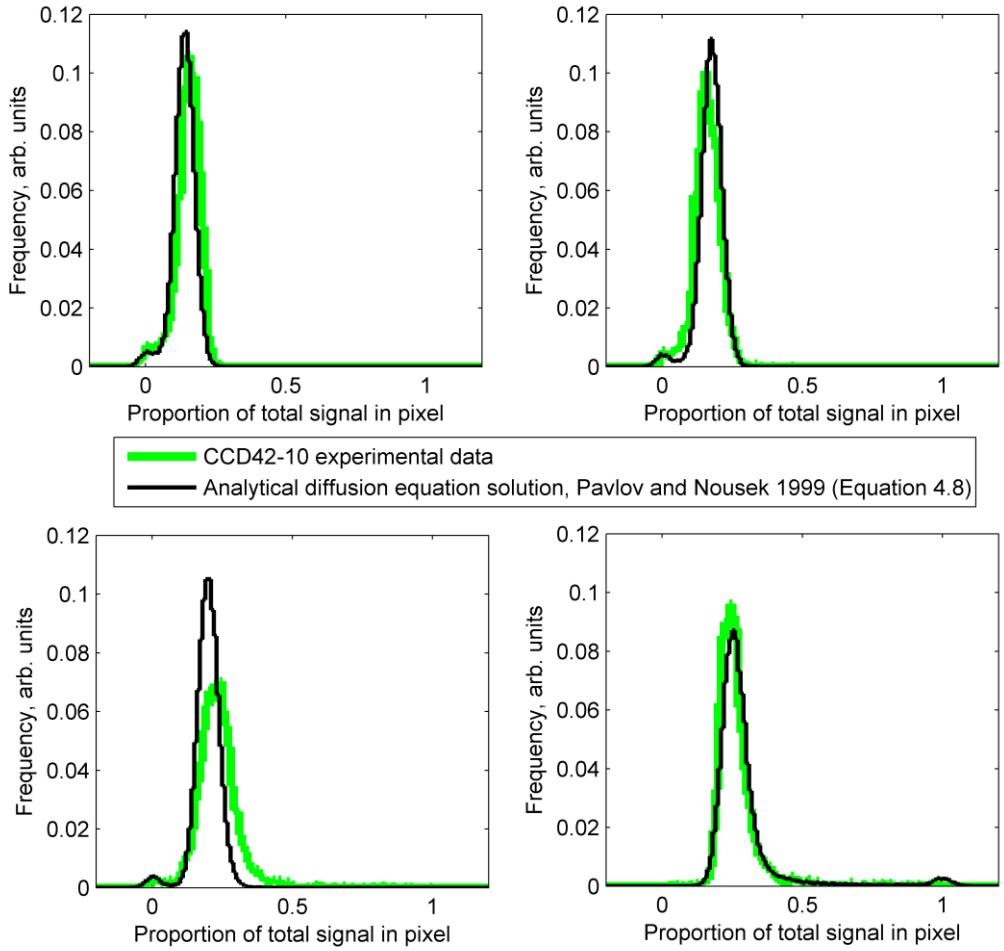

Figure 4.11. The experimental and simulated pixel signal distributions for the 4 pixels that contain the majority of the signal when the interactions occur at the corner between these 4 pixels.

4.3 Summary

When an X-ray interacts in the field-free region of a back-illuminated CCD, the initial charge cloud diffuses isotropically before collection in the potential wells. The diffusion process results in the charge being shared amongst several pixels for the majority of events, degrading the resolution of the CCD. This is the case in the CCD at SAXES, where the spatial resolution has been measured to be 24 µm (FWHM) relative to the pixel size of 13.5 µm [7].

Models for the distribution of charge after diffusion through the field-free region have been compared to each other and experimental data to identify an accurate and appropriate model for the charge spreading to be used in a Monte Carlo simulation of the process. An analytical solution to the diffusion equation (*Equation 4.9*) [66] most accurately represented experimental data and has been selected for use in the simulation package.

The processes of charge generation, collection and conversion have also been incorporated into the Monte Carlo simulation. The X-ray events generated by the model closely match experimentally observed events obtained with the CCD42-10 (Section 6.7), when physical device thicknesses close to the parameters expected from manufacture were used. Therefore, the simulation package developed here will be used to generate event populations in the simulations that follow in Chapter 5.

4.4 Conclusions

The charge spreading in a standard back-illuminated CCD is dominated by diffusion of the charge cloud in the field-free region, close to the back surface. Models and an empirical fit to describe the resulting charge cloud density sampled by the pixel structure after diffusion have been compared, and the analytical solution to the diffusion equation by Pavlov and Nousek (*Equation 4.9*, [66]) agrees best with experimental data when thicknesses expected from manufacturing tolerances were used. Recombination was ignored, the back surface was assumed to be perfectly reflecting, the pixel collection area was taken to be square and the depletion depth was assumed constant across the device. As the depletion depth varies across the pixel, the model must be evaluated with a different depletion depth in different areas of the pixel to conform to the experimental results. Other models present in the literature did not agree well with the experimental data and should not be used for generating realistic X-ray events in back-illuminated CCDs without further experimental verification.

Chapter 5: X-ray Event Centroiding

5.1 Introduction

Charge clouds spread whilst diffusing through the field-free region of the CCD42-40 at SAXES, degrading the spatial resolution to worse than the pixel size. The dynamics of this charge spreading have been modelled and calibrated to experimental data in Chapter 4, allowing populations of X-ray events with known interaction positions to be produced using the bespoke simulation package.

Centroiding has been proposed as a method of improving the spatial resolution at SAXES, potentially allowing the interaction position of X-rays to be determined at sub-pixel accuracy. To test this concept the performance of centroiding algorithms will be investigated by simulation in this chapter, determining the potential resolution performance that could be achieved. The investigations in this chapter will be undertaken utilising the Monte Carlo simulation package described in Chapter 4.

5.2 Linear sub-pixel event repositioning algorithms

5.2.1 A linear centroid algorithm

Since the charge cloud shape for the majority of interactions is larger than the CCD42-10 pixel size (13.5 µm), the average X-ray interaction is detected with charge distributed amongst several pixels. The distribution is approximately symmetrical and distributed around a point of maximum charge density at the x and y position of the photon interaction, so it follows that the interaction location may be estimated by performing a 'centre of gravity' style calculation on the signals in the pixels surrounding events (*Equation 5.1*). Here, x_{COG} is the estimated interaction location for a single photon interaction that resulted in signal S_i being observed in the i'th pixel (located at x_i in the x dimension). A similar calculation can be applied in the y dimension.

$$x_{COG} = \frac{\sum_i x_i S_i}{\sum_i S_i} \qquad \textit{Equation 5.1}$$

Equation 5.1 may be calculated across any number of pixels that surround a photon interaction. When designing an algorithm, an effort must be made to include as many pixels that contain signal as possible in order to capture the information, however including pixels where noise dominates the signal will introduce more error into the calculation. One scheme of defining the area of interest (the pixels included in calculating x_{COG}) is to include all pixels in a 3×3 pixel area centred on the pixel with maximum signal in the event (Figure 5.1).

Different methods of defining the area of interest could be used such as maximising the total signal that is within the area rather than keeping the signal in the central pixel as a maximum. Alternatively, instead of using a constant area of interest, the area could be defined to only include neighbouring pixels that contain signal over a predefined threshold.

The performance of the centre of gravity algorithm is measured by calculating x_{COG} for a population of events whose photon interaction occurred at known (x, y) positions in the pixel. The error in the algorithm is measured by fitting the distribution of the difference between the centroid locations and the assigned interaction (x, y) positions with a Gaussian profile; the FWHM of which gives the spatial resolution of the algorithm at that location within the pixel.

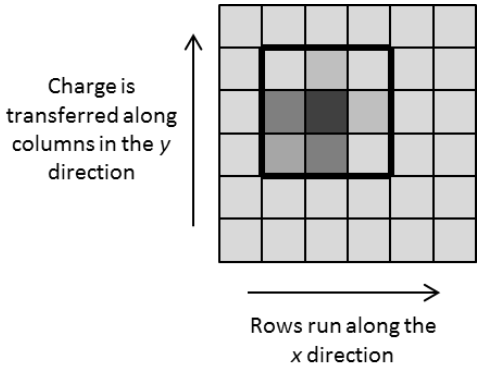

Figure 5.1. A single photon interaction may result in an array of pixel signals shown here, where a darker shade in the pixel represents more signal. A 3×3 pixel area can be defined around the pixel in which the maximum signal is observed (thick box).

5.2.2 Applying the centre of gravity algorithm across a 3×3 pixel area

To test the accuracy of the algorithm, the spatial resolution (FWHM) is determined for events with interaction locations across a range of sub-pixel areas. To generate the simulated events, a photon energy of 1000 eV has been used, with a pixel size of 13.5 µm square with a field-free depth of 8.3 µm and depletion depth of 4.7 µm (to match the CCD42-10 dimensions). To generate large numbers of events, a look-up table is first produced using Equation 4.9 to determine the pixel signals across a 5×5 pixel area expected for a grid of interaction locations within the central pixel.

The grid of interaction locations is defined to extend from the edges of the pixel (±6.75 µm) in the *x* and *y* dimensions and from the back surface ($z_s = 0$ µm) to the depletion depth ($z_s = 8.3$ µm). A uniform spacing of 0.08 µm was used for the grid resulting in 769184 positions, providing a lattice with a resolution much finer than the expected spatial resolution. For each interaction position on

the grid, Equation 4.9 is evaluated to determine the pixel signals across a 5×5 pixel area that results from the charge spreading, generating the 3D look-up table for reference in the simulations that follow; when the pixel signals are desired for a random interaction position in the field-free region, they are determined using linear interpolation from this pre-simulated data set.

To begin with, the centre of gravity algorithm is applied to a 3×3 area centred on the pixel with maximum signal. The algorithm is applied to three populations of events, where each population has interaction locations distributed across a different sub-pixel region (the centre, corner or edge of the pixel). An additional population, where events interact randomly across the area of the pixel has also been investigated, to realistically represent events distributed across a CCD.

In this initial simulation, no additional readout noise or electron multiplication noise is added, so events where multiple pixels contain the maximum signal frequently occur (especially when the interactions are occurring at the border of the pixel). In these cases, the central pixel used to define the position of the 3×3 pixel area is chosen randomly from the pixels with maximum signal.

The centroid distributions and accuracy for each interaction location population will be presented before the common features are discussed. The device entry point is the same for every photon in each interaction location population, but the distributions of centroid locations are not point-like due to the random allocation of electrons to the pixels during each X-ray event generation (number 3 in Section 4.2).

5.2.2.1 Interactions at the pixel centre

In the first population of events, all interactions occur at the centre of the pixel $(x = 0, y = 0)$, resulting in centroid locations that are distributed about the centre of the pixel (Figure 5.2 a). The pixel signals are in the discrete unit of electrons and therefore the centroid locations are in a grid-like structure (the ordered distribution of centroid locations is not due to the grid of interaction positions in the look-up table). A Gaussian profile fitted to the binned distributions of centroid errors results in a spatial resolution of 0.99 µm (FHWM) in both dimensions.

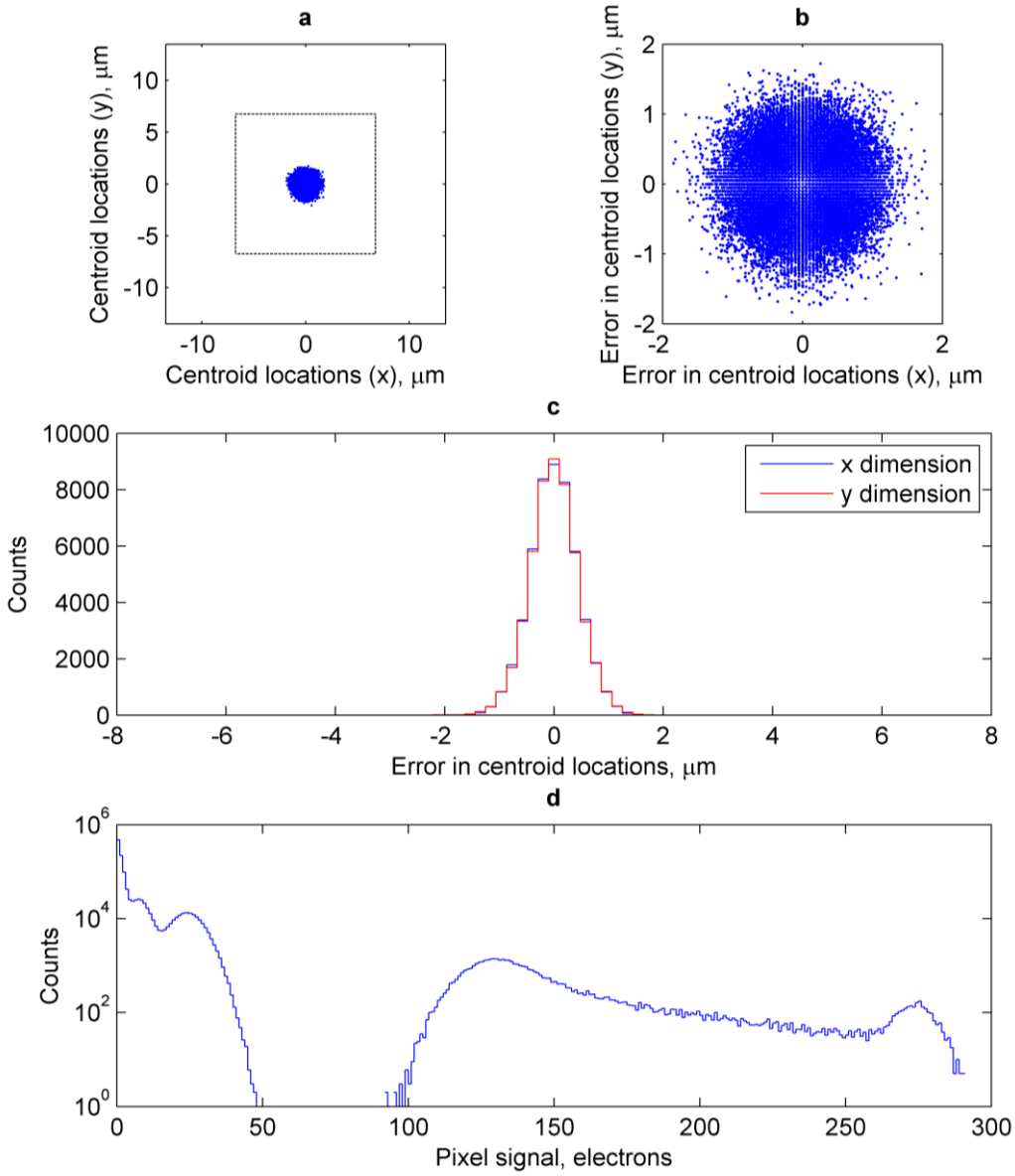

Figure 5.2. A 3×3 centre of gravity centroid algorithm is applied to simulated events where the interactions occur in the centre of a pixel. ***(a)*** *The centroid locations, relative to the pixel size and location (dashed line).* ***(b)*** *The distribution of centroid errors in x and y dimensions.* ***(c)*** *The centroid errors binned into the x and y dimensions.* ***(d)*** *The distribution of individual pixel signals from the 5×5 pixel area.*

5.2.2.2 Interactions at the centre of a pixel's edge

When all interactions occur at the central point on the edge of the pixel $(x = 6.75, y = 0)$ µm, the centroid locations are grouped in three distinct areas. Every interaction that occurs in the depletion region leads to all electrons being assigned into the central pixel, and therefore the resulting location from the centre of gravity centroid calculation is at the centre of the pixel. Although these events are not obvious in Figure 5.3 a and b as the point marking them is small,

they are visible in the *x* dimension binned distribution of centroid errors (Figure 5.3 c). The remainder of the centroid locations are in two Gaussian-like distributions, at either side of the pixel boundary close to where the interaction occurred. These two distributions mirror each other in the plane of the pixel boundary.

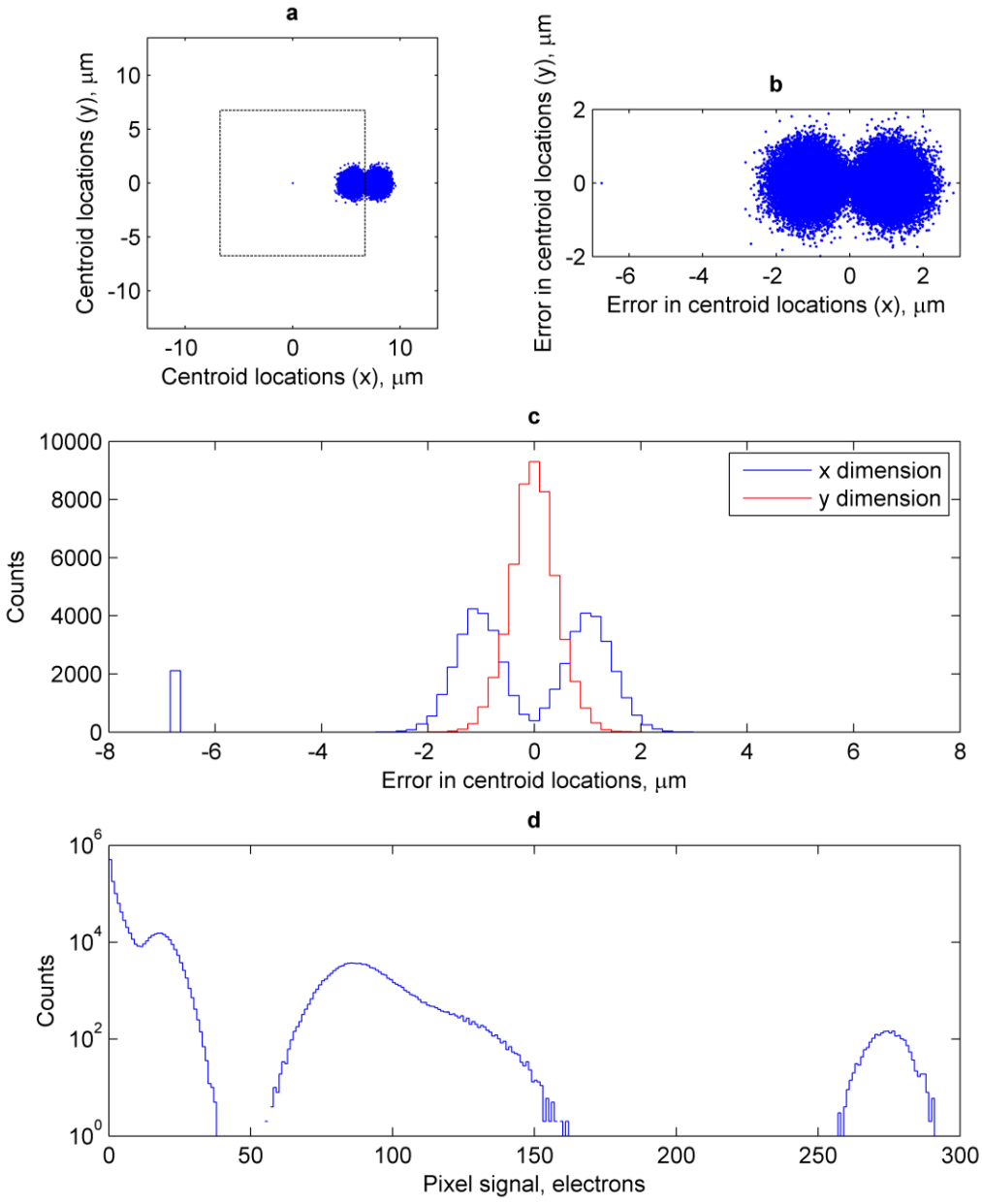

Figure 5.3. Same as Figure 5.2, for interactions that occur only at the centre of the edge of the pixel. ***(c)*** *The events with centroid locations in the histogram bin at -6.75 µm are from interactions that occur in the depleted region, as discussed in the text.*

5.2.2.3 Interactions at a pixel's corner

The centroid locations derived from interactions that occur at the corner of the pixel $(x = 6.75, y = 6.75)$ µm are arranged in a similar fashion (Figure 5.4). The interactions that occur in the depletion region result in centroid locations at the centre of the pixel. The remainder of the interaction events result in a pattern of four droplet-like shapes, with the tapered side pointing toward the interaction positions at the corner of the pixel.

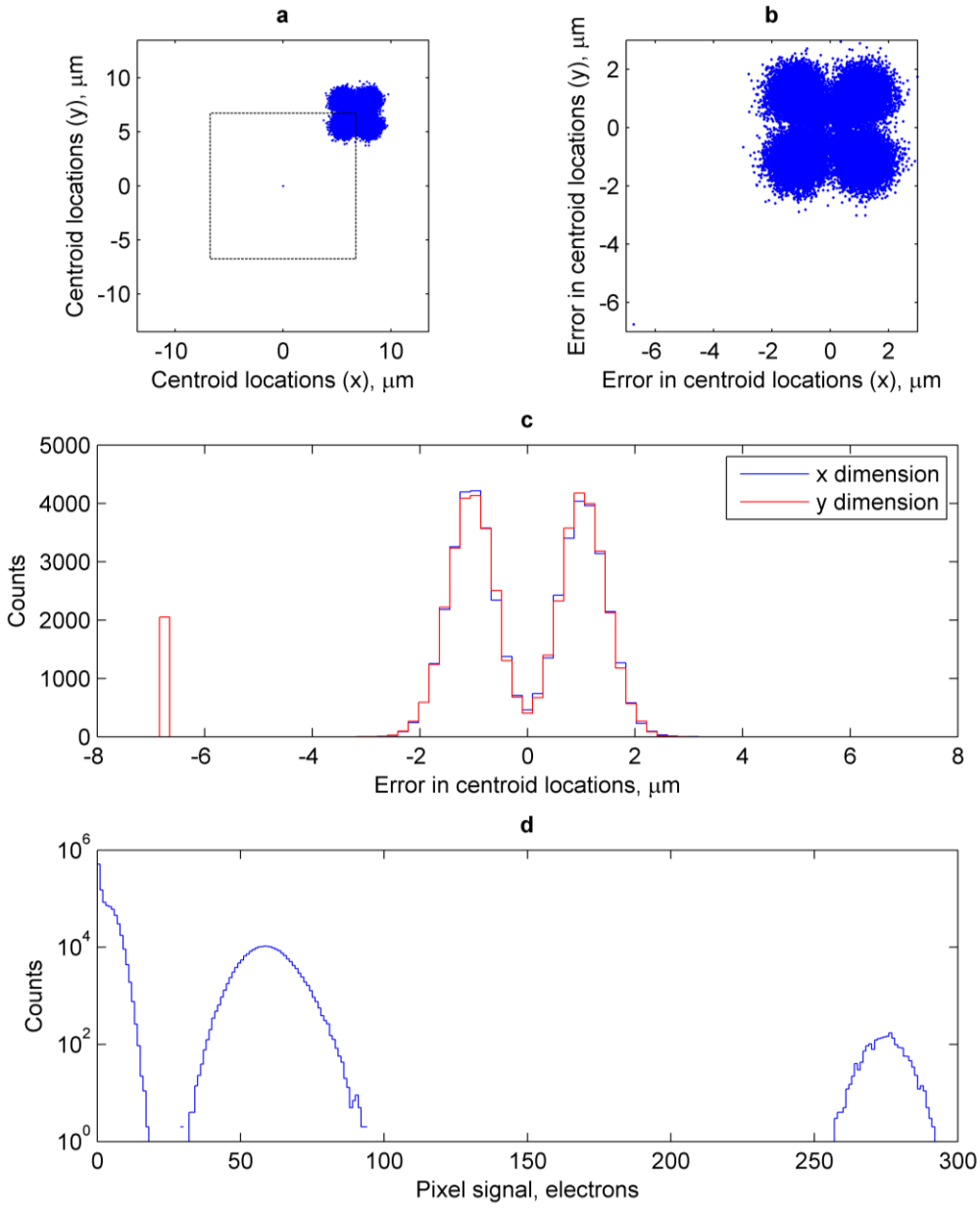

Figure 5.4. Same as Figure 5.2, for interactions that occur only at the corner of the pixel.

5.2.3 Systematic bias in the centre of gravity algorithm

In the centroid location distributions for interactions at the edge and corner of a pixel, the centroid locations are biased away from their interaction locations, towards the centre of pixels. Here, the direction of the bias comes from the only source of noise – the random allocation of electrons into pixels near the interaction location. The sampling of the Gaussian-like charge cloud by the pixels in the 3×3 area leads to the centroid location not necessarily being at the location of the interaction; especially when the charge cloud is narrow with respect to the pixel size, the centre of gravity of an event is biased away from the pixel edges, towards the centre. This biasing is termed the 'edge effect'.

The edge effect is most noticeable when events occur at the centre of the pixel edge, where the distribution of electrons is symmetric in the pixel boundary (e.g. Figure 5.5): the position of the pixel with maximum signal can change, and therefore the 3×3 pixel area over which the algorithm is applied changes position. When a population of events are generated at the pixel edge, the locations are therefore biased towards the centres of different pixels. The incorrect locating of the 3×3 pixel area leads to a further degradation of the spatial resolution when combined with the edge effect.

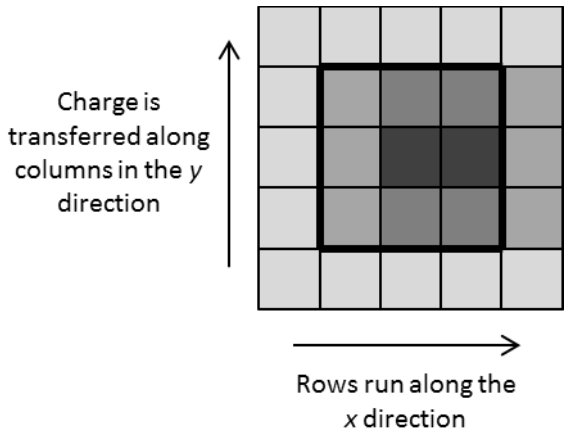

Figure 5.5. An example array of pixel signals formed from an X-ray interaction that occurred at the border of two pixels, resulting in the electrons being distributed symmetrically on each side of the pixel border. The 3×3 pixel area over which to apply the centroid algorithm has been centred on the left-hand pixel with maximum signal but could equally have been centred on the right-hand pixel with maximum signal.

5.2.4 Interactions distributed evenly across the pixel area

When interaction locations are evenly distributed across the pixel, the centroid locations are distributed across all of the pixel area apart from close to the pixel boundary, which is a clear example of the edge effect (Figure 5.6). Some centroid locations are in the adjacent pixels, and fewer are in the diagonally adjacent pixels. The error in the centroid algorithm for the majority of events is within a distribution which is approximately Gaussian with a flatted top; the FWHM in the *x* and *y* directions is measured to be 2.6 µm for a sample of 50 000 events. The main distribution sits on top of an approximately flat distribution that extends out to the size of the pixel, due to isolated events.

By comparing the energy spectrum for interactions occurring in the individual areas (Figure 5.2 d, Figure 5.3 d and Figure 5.4 d), the spectra for interactions occurring in random locations across the pixel (Figure 5.6 d) can be deconstructed. The peak centred at 274 electrons (1000 eV/3.65 eV electron^{-1}) is formed from the central pixel when the interaction occurs in the depletion region and is present in all the spectra. From the high energy peak, the floor extending up to the step at approximately 125 electrons is formed by the events interacting sufficiently close to the depletion region and close to the centre of the pixel such that the signal in the central pixel is greater than average. For the majority of events, the interaction occurs close to the back surface and the signal is split such that the signal in the central pixel is approximately 130 electrons (Figure 5.2 d). When the interaction approaches the edge of the pixel, the signal is shared more equally between the central pixel and the adjacent pixel, reducing the signal in the central pixel. However, the majority of events consist of a primary pixel with approximately 125 electrons, forming the shoulder observed. The peak at 0 electrons is formed by the pixels surrounding the event, primarily the outer pixels of the 5×5 area. Lastly, the continuum between the peaks at 0 electrons and 125 electrons is formed by the pixels surrounding the central pixel when the charge is split.

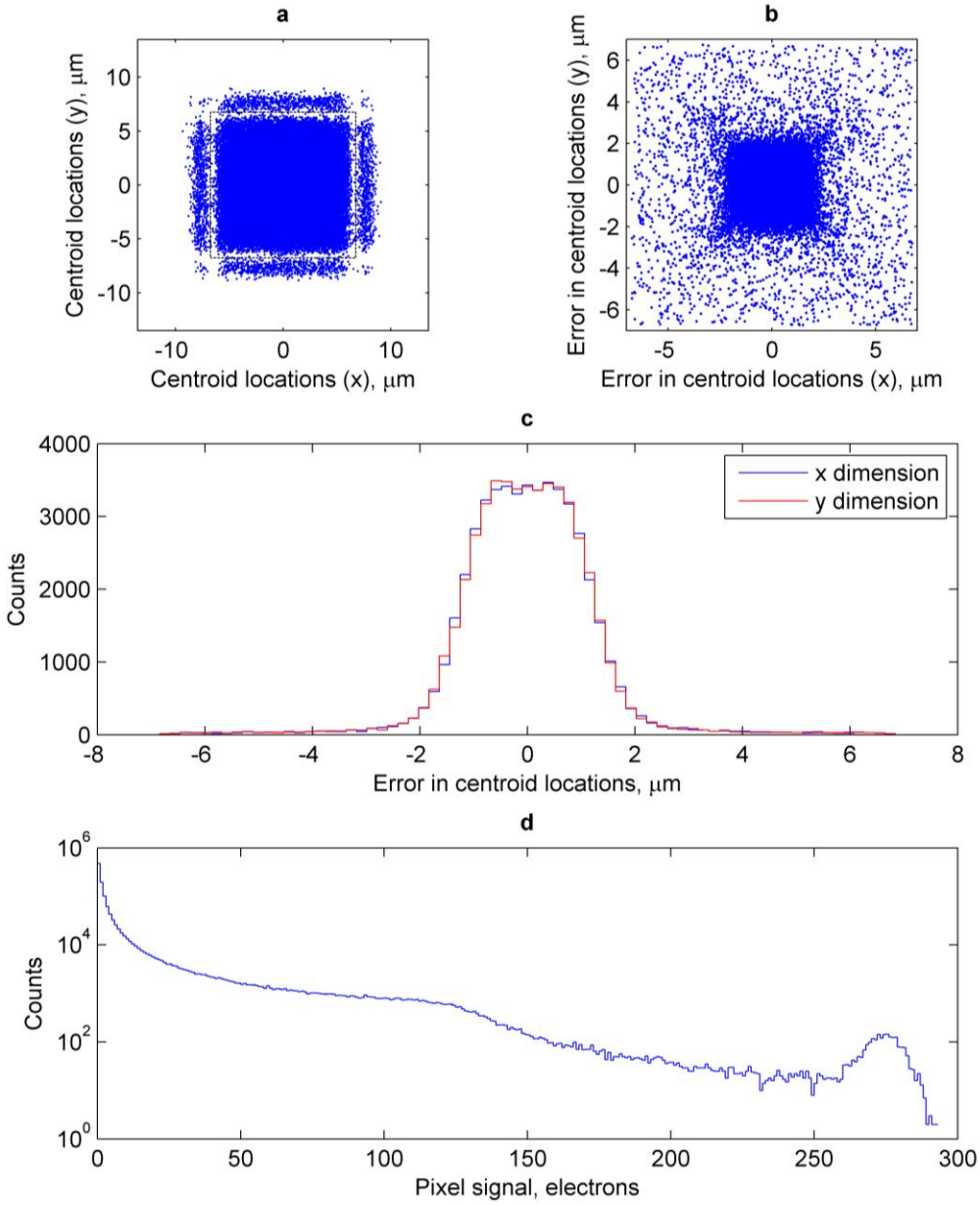

Figure 5.6. Same as Figure 5.2, for interactions that are distributed evenly across the entire area of the pixel.

5.2.5 Centroid algorithm performance with varying signal to noise ratios

In this section, the initial simulations are built on by interlinking the effects of varying the photon energy (i.e. signal) and the level of read noise using the simulation package. The centroid resolution deteriorates at higher noise levels for a given photon energy, due to the variation in the pixel signals increasing the error in the final centroid location (Figure 5.7 for 1000 eV photons). The difference between the resolution for interactions in the centre and interactions distributed evenly across the pixel is due to both edge effects and isolated events.

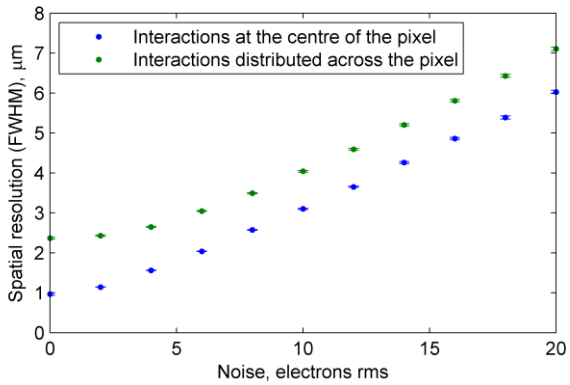

Figure 5.7. The simulated spatial resolution for a 13.5 µm square pixel with 8.3 µm thick field-free depth and 4.7 µm thick depletion depth for 1000 eV photons, using the 3×3 centre of gravity centroid algorithm. The errors shown are the 95% confidence limit of fitting the Gaussian distribution to the centroid location distribution.

The simulated spatial resolutions for 50 eV to 1500 eV photon energies are presented for a noise level of 2 electrons rms (Figure 5.8). The resolution for interactions at the centre of the pixel steadily improves at higher energies. When the interactions are distributed across the area of the pixel, the spatial resolution generally improves to a best resolution at approximately 750 eV, but then slowly degrades. This is due to the increase in proportion of events that are isolated, and are therefore centroided to a location close to the centre of the pixel regardless of their actual interaction position.

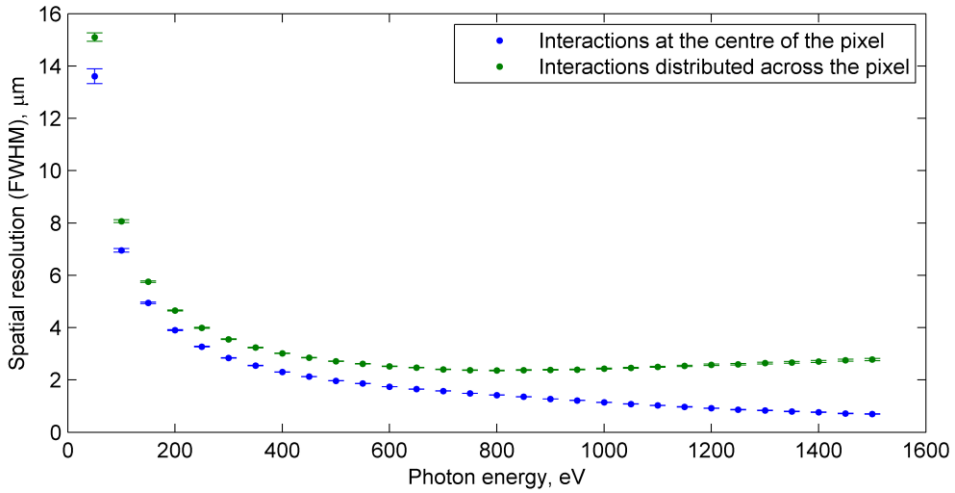

Figure 5.8. With a background noise of 2 electrons rms, the spatial resolution is shown for photon energies between 50 eV and 1500 eV. The errors shown are the 95% confidence limit of fitting the Gaussian distribution to the centroid location distribution.

Finally, the resolution is presented as a function of the signal to noise ratio, where the signal is given by the mean number of electrons produced by a photon with one of five energies between 200 eV and 1000 eV (Figure 5.9). The noise is given by the root mean square width of the Gaussian noise distribution, which notably excludes the noise associated with assigning the electrons into pixels given the probability distribution obtained from the charge spreading function.

At signal to noise ratios below approximately 8, the spatial resolution becomes worse than the pixel size, and in reality X-ray events would be difficult to identify from the noise background in an image but in these simulations the knowledge that an X-ray event occurred in the central pixel is assumed. In real images with low signal to noise ratios, individual X-ray events can become difficult or impossible to identify, so correct identification of X-ray events is the limiting factor rather than spatial resolution obtained with centroiding.

At higher signal to noise levels, the spatial resolution improves down to 3 µm (FWHM), but levels off at signal to noise ratios greater than 40. The resolution becomes limited by the binomial-style distribution of electrons into the charge spreading distribution that occurs during event generation. At energies approaching 1000 eV, the greater proportion of isolated events also leads to a degraded overall spatial resolution because isolated events are centroided to close to the centre of the pixel, regardless of the interaction position.

Results in this section show that centroiding algorithms can improve the resolution achieved when imaging X-rays in a single photon counting mode. The majority of soft X-ray events interacting in a back-illuminated CCD will result in an event with signal split across several neighbouring pixels. In systems with a very high signal to noise ratio, the simulations presented here show a centre of gravity algorithm applied across the 3×3 pixel area surrounding an event can locate the interaction position with an energy-dependent resolution of approximately 3 µm (FWHM). The point spread function of the detector can therefore be approximately a factor of 10 times better than the charge cloud limited case of approximately 24 µm (FWHM) [7].

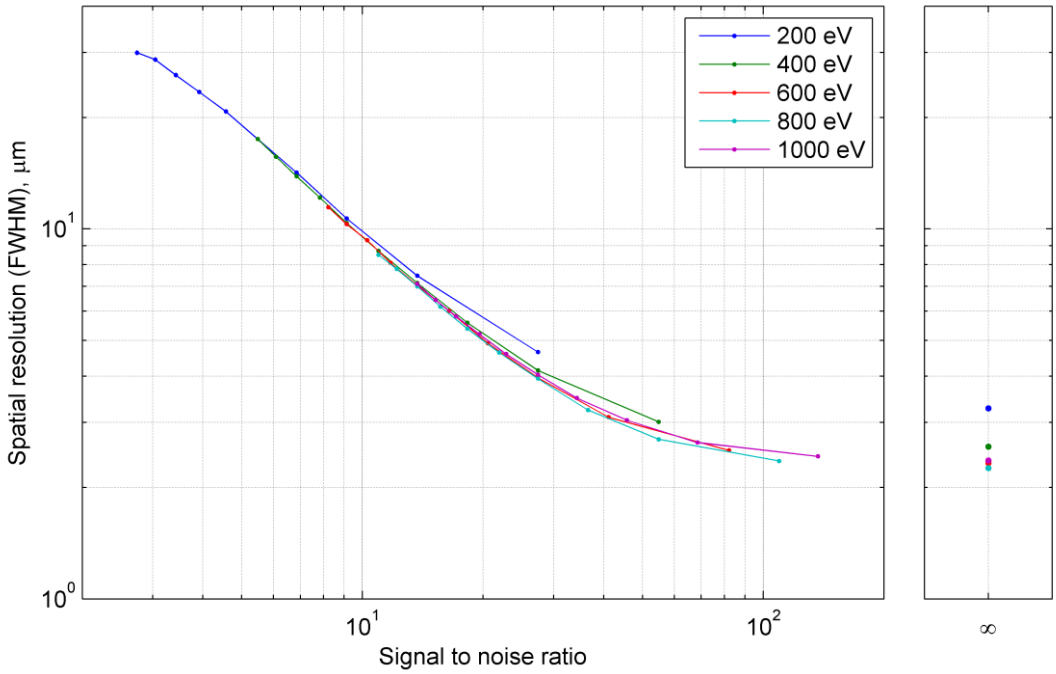

Figure 5.9. The spatial resolution is improved when the ratio of total signal generated to standard deviation of the noise distribution increases. The spatial resolution when no additional noise is added to the electron signal distribution is also shown, labelled with an infinite signal to noise ratio. Both axes use the same y *scale. Errors, calculated from the 95% confidence limit of fitting the Gaussian distribution to the centroid location distribution, are shown but are too small to be visible.*

5.3 Non-linear centroiding algorithms

A factor limiting the resolution achieved in the simulations with the linear centre of gravity algorithm is the bias of centroid locations away from the boundaries of pixels (the edge effect). To remove the bias, a correction must be introduced into the algorithm that varies as a function of the initial biased centroid position; a non-linear correction.

5.3.1 Correction of the systematic edge effect

To achieve the best resolution across the pixel, the systematic error of the observed edge effect must be corrected for. Using *Equation 5.1*, the systematic error in the centre of gravity centroid position $\delta_{x\,COG}$ for an interaction occurring at x_0 is given by *Equation 5.2*.

$$\delta_{x\,COG} = x_{COG} - x_0 = \frac{\sum_i x_i S_i}{\sum_i S_i} - x_0 \qquad \textit{Equation 5.2}$$

The values of S_i can be calculated using a chosen charge cloud shape model, and the sum over i is over all pixels used in the centroid calculation (e.g. a 3×3 pixel area). An expression for $\delta_{x\,COG}$ was derived by Alexander and Ng [85], where F_e is the Fourier transform of the charge cloud shape (centred at zero) that is sampled in every pixel. The systematic error was shown to be an effect of the sampling of the charge cloud.

$$\delta_{x\,COG} = \frac{\sum_{n=1}^{\infty} F_e'(n) \sin 2\pi x_0 n}{\pi[F_e(0) + \sum_{n=1}^{\infty} F_e(n) 2\cos 2\pi x_0 n]} \qquad \textit{Equation 5.3}$$

To simplify the derivation of this analytical solution, Alexander and Ng assume the charge cloud shape is a Gaussian profile with a standard deviation (σ, in pixel units) independent of interaction depth. Therefore the value of $\delta_{x\,COG}$ reduces to the expression in *Equation 5.4* [86].

$$\delta_{x\,COG} = \frac{1}{\pi}\sum_{n=1}^{\infty} \frac{(-1)^n \exp[-2(\pi\sigma n)^2] \sin(2\pi x_0 n)}{n} \qquad \textit{Equation 5.4}$$

Figure 5.10 shows the behaviour of *Equation 5.4* across the pixel for a selection of Gaussian charge cloud widths and the absolute systematic error is averaged across the pixel area for a range of charge cloud sizes in Figure 5.11. Assuming the charge cloud is well modelled by a Gaussian profile, the corrected centroid location, $\hat{x}_c$, is determined by solving *Equation 5.5* [85]. This method requires all events to use a Gaussian charge cloud width, σ, that has been estimated from previous experimental work.

$$\hat{x}_c - \frac{1}{\pi}\sum_{n=1}^{\infty} \frac{(-1)^n \exp[-2(\pi\sigma n)^2] \sin(2\pi \hat{x}_c n)}{n} = \frac{\sum_i x_i S_i}{\sum_i S_i} \qquad \textit{Equation 5.5}$$

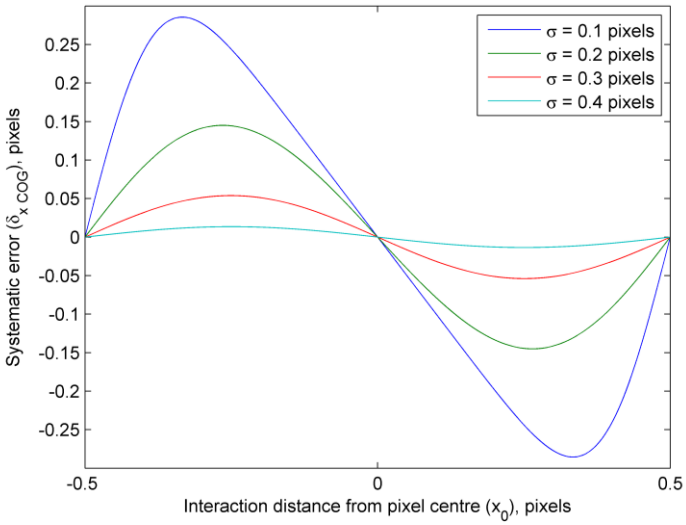

Figure 5.10. The systematic error in centroid location is plotted as a function of the interaction position in the x *dimension of the pixel.*

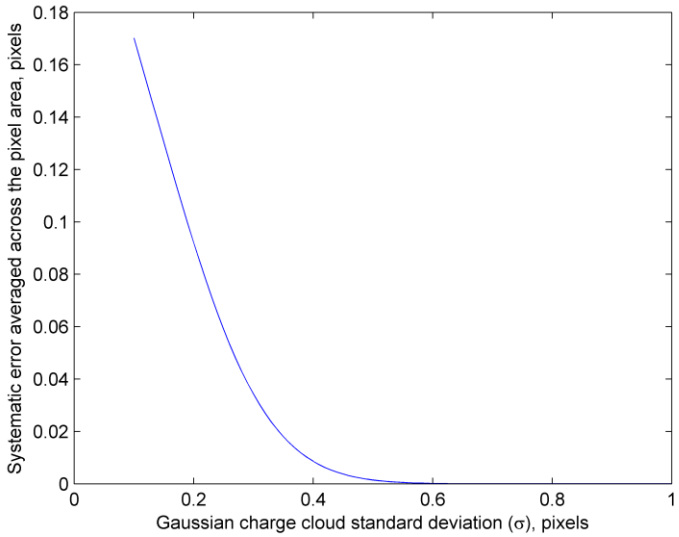

Figure 5.11. The absolute systematic error of the centre of gravity algorithm, averaged across the pixel area, tends to zero as the Gaussian charge cloud increases in width.

The corrected spatial resolution for simulated interaction events distributed across a pixel is shown in Figure 5.12, for 500 eV and 1000 eV photons, with no noise sources added to the pixel signals. The events are simulated using the Pavlov and Nousek analytical diffusion solution to best represent observed events, but the correction method assumes a constant Gaussian charge cloud shape, regardless of interaction depth. However, the correction still improves the resolution at values of σ that closely fit the charge cloud shape; for small values of σ, the systematic correction is too large and the spatial resolution is worse than the uncorrected resolution and at large values of σ, $\delta_{x\,COG}$ tends to zero due to the exponential decay term (*Equation 5.4*) and the corrected

algorithm resolution tends to the resolution of the uncorrected algorithm. The resolution of the corrected algorithm reaches a minimum for $\sigma = 0.3$ µm and $\sigma = 0.28$ µm for 500 eV and 1000 eV energy photons respectively; as expected, the higher energy photons are fitted with a smaller Gaussian charge cloud width due to their deeper interaction depth. However, this method is relatively easy to implement and for a set of monochromatic X-ray events, the σ value could be tuned to optimise the resolution of a detector, or chosen to approximately match the expected value.

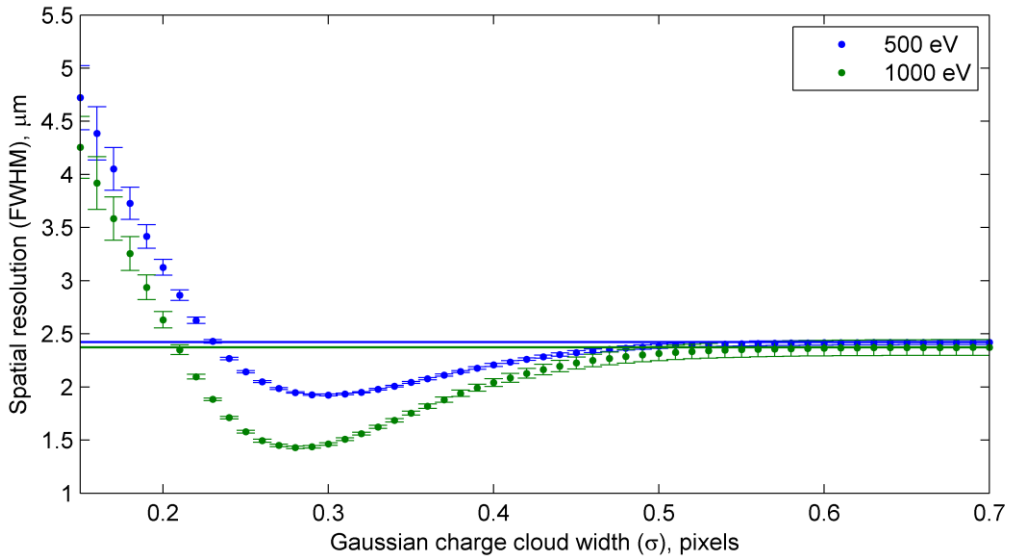

Figure 5.12. When correcting for the systematic error of the 3×3 centre of gravity algorithm using Equation 5.5, the achieved spatial resolution is a function of the chosen Gaussian charge cloud width. The resolution of the corrected algorithm tends to the uncorrected spatial resolution (horizontal lines) as the applied correction becomes small when σ is large. Error bars show the 95% confidence limit of the Gaussian profile fit to the distribution of centroid locations.

When compared to the original interaction locations, the corrected centroid locations are still clearly biased away from the edges of the pixels (Figure 5.13). In correcting the centroid locations for the systematic bias using Alexander and Ng's method [85], the X-ray event centroids are approximately mapped towards their real locations, but the mapping is not perfect. Even when the only noise contribution is from the binomial-like distribution of the electrons into the pixels following the charge cloud probability distribution, a significant number of events are centroided to locations in adjacent pixels. Alexander and Ng's correction method also does not account for more complex features of the charge collection in the pixel such as the non-Gaussian charge cloud shape and any non-uniform charge collection effects.

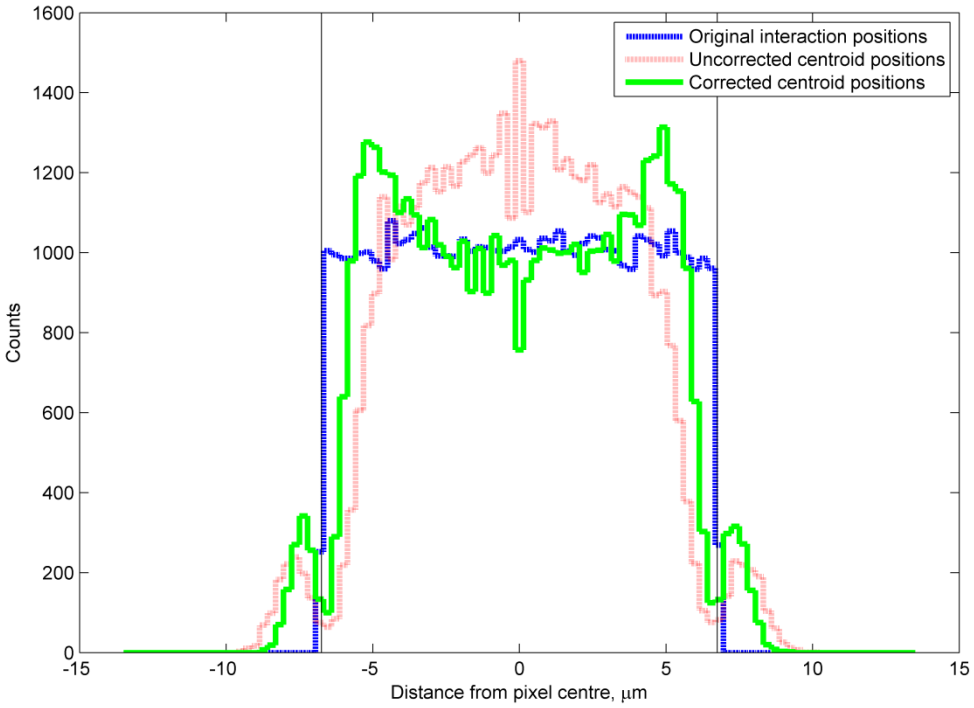

Figure 5.13. The original interaction locations and the uncorrected centroid locations are compared to the centroid locations that have been corrected for the systematic edge effects, for 500 eV photons using $\sigma = 0.3$ μm. The pixel boundaries are shown by vertical black lines (pixel size is 13.5 μm).

5.3.2 The η algorithm

Rather than correcting the systematic bias of a linear centroiding algorithm analytically as in the previous section, the η algorithm calibrates a correction using experimentally obtained X-ray events. By illuminating a detector with a low flux, flat field of monochromatic X-rays, a large number of single photon events can be observed whose interaction positions are distributed uniformly across the pixel area. A correction function can then be determined that maps the centroid locations calculated with a linear centroiding algorithm into a uniform distribution across the pixel.

Firstly, assume a function exists that can map a centre of gravity centroid location, x_{COG}, to a corrected centroid location that is the most probable real interaction position, x_η.

$$x_\eta = f_\eta(x_{COG}) = f_\eta \frac{\sum_i x_i S_i}{\sum_i S_i} \qquad \textit{Equation 5.6}$$

In a linear centroiding algorithm such as the centre of gravity (*Equation 5.1*), the mapping function is equal to 1 and $x_\eta = x_{COG}$. When the mapping function is non-linear, it can incorporate

corrections to the algorithm including the systematic edge effects corrected in Section 5.3.1, as well as accounting for any other geometric and electronic properties of the detector that affect the charge distribution and background levels between pixels.

The η non-linear centroiding algorithm has been applied with silicon microstrip detectors, for example in precise particle and photon detection in high energy collision experiments, X-ray Free Electron Lasers and in-orbit cosmic ray detection [87–89]. The centre of gravity centroid algorithm is applied to the adjacent two strips with maximum signal in an event, simplifying *Equation 5.1* to the ratio η in *Equation 5.7*, where S_L (S_R) is the left (right) strip signal observed when an event is detected (i.e. $x_L = 0$ and $x_R = 1$).

$$\eta = \frac{S_R}{S_L + S_R} \qquad \textit{Equation 5.7}$$

The mapping function, f_η, is obtained by illuminating the detector with a flat field and determining the value of the η ratio for a large number of events, resulting in a probability distribution for η for a flat field of centroid locations: $pdf(\eta)$. The cumulative sum of $pdf(\eta)$, normalised to run from the zero to one, is the mapping function f_η.

$$f_\eta(\eta) = \int_{-\infty}^{\eta} pdf(\eta')\ d\eta' \Big/ \int_{-\infty}^{\infty} pdf(\eta')\ d\eta' \qquad \textit{Equation 5.8}$$

The principle of *Equation 5.8* extends beyond the ratio of η to other linear centroiding functions, such as the centre of gravity centroid, x_{COG}, across a 3×3 pixel area. For 50 000 events simulating the interaction of 500 eV and 1000 eV energy photons distributed evenly across the pixel area, x_{COG} is calculated and its distribution is shown in Figure 5.14. The centroid locations are biased away from the edges of the pixel as expected by the edge effects. A peak is present around 0 in the 1000 eV photon energy distribution which is due to photons that interact in the depletion region. The reader should note that the x_{COG} values in Figure 5.14 have been constructed without the prior knowledge of which pixel the interaction is known to occur in, whereas the uncorrected centroid positions in Figure 5.13 are relative to the pixel in which the interaction occurred.

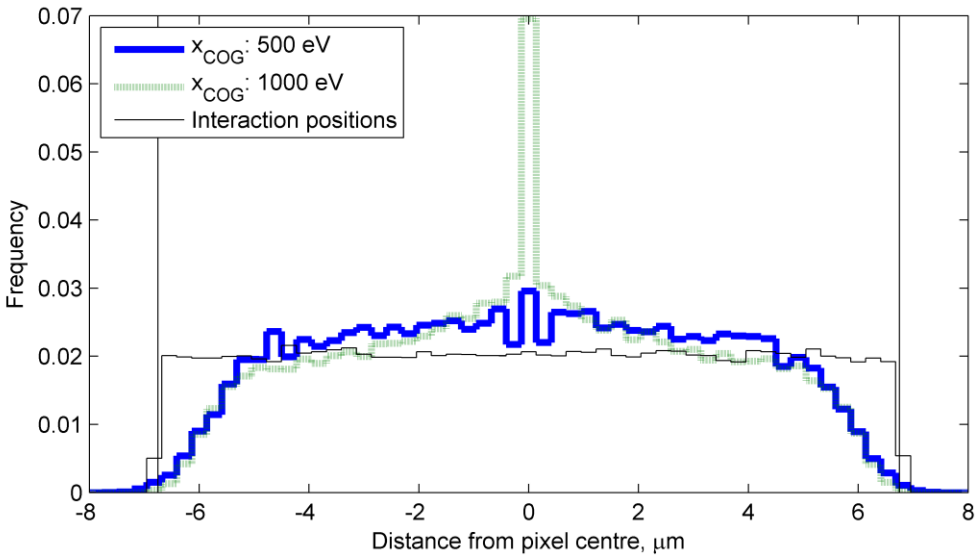

Figure 5.14. Simulated distribution of x_{COG} for a flat field illumination of 500 eV and 1000 eV photons. The dominant peak around 0 for the 1000 eV photon energy distribution is due to isolated events. The edges of the pixel (at ±6.75 μm) are marked by vertical black lines.

Using the distributions in Figure 5.14, the corrective mapping function f_η has been calculated for each energy (Figure 5.15) and used to correct the centre of gravity centroid positions, x_η. The distributions of corrected centroid locations (Figure 5.16) are flatter across the pixel area, as expected from the original flat field used to assign the interaction locations in the simulation. The deviation from a flat field in the centre of the pixel is due to isolated events: if events with greater than 95% of the total signal detected in the central pixel are removed from the analysis and f_η is reformulated, the peak is no longer present.

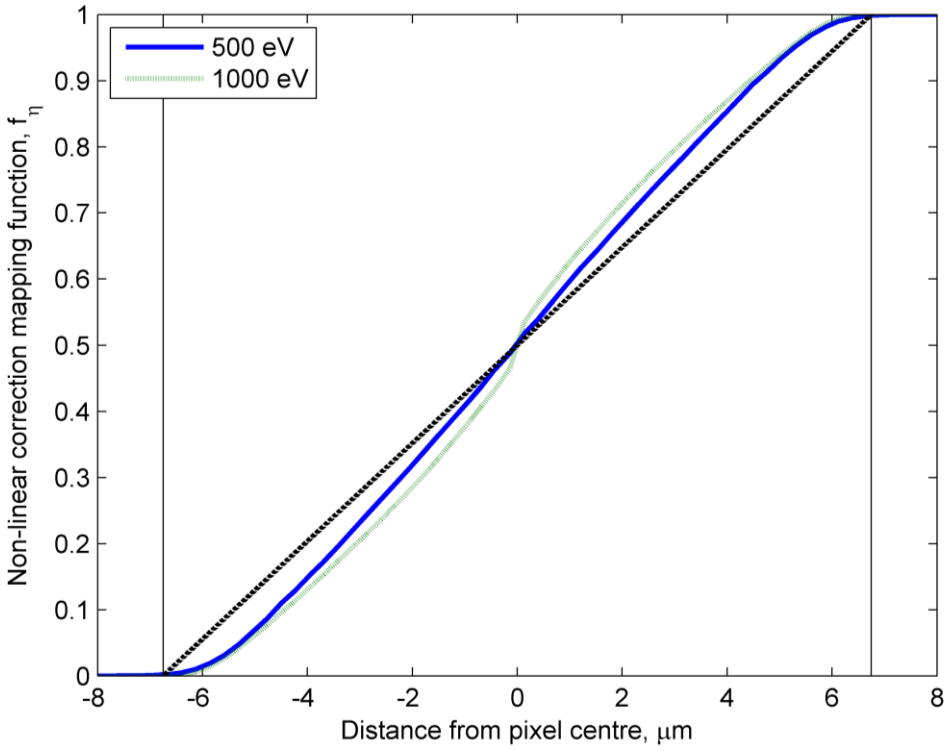

Figure 5.15. The corrective mapping function f_η calculated using Equation 5.8, from the distributions in Figure 5.14. The dotted black line shows the equivalent response of a linear centroiding algorithm.

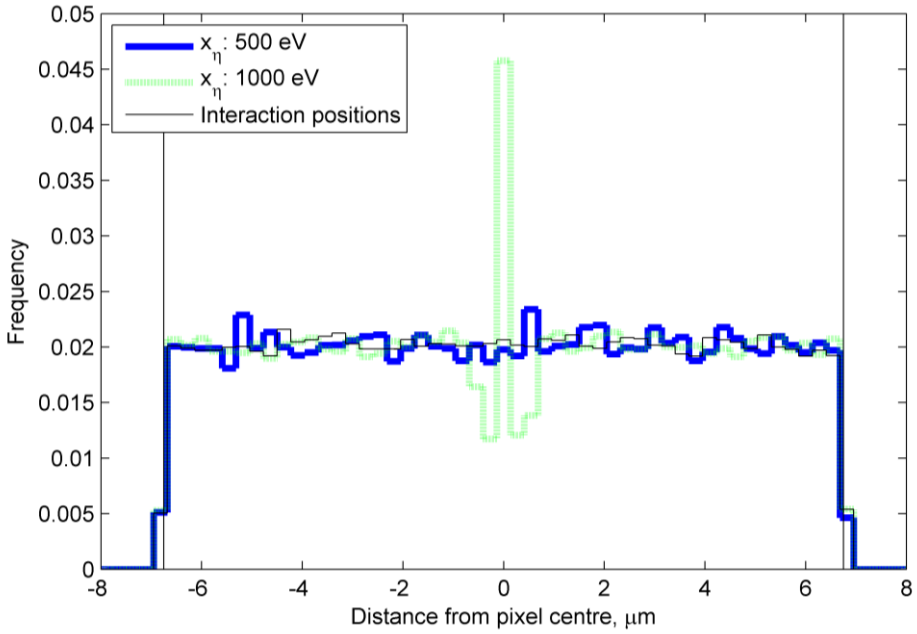

Figure 5.16. The distribution of centroid locations calculated using the non-linear η algorithm that corrects for the systematic errors of the linear centre of gravity algorithm. The distribution of locations is much more uniform than the uncorrected distribution (Figure 5.14). The peak close to 0 μm in the 1000 eV distribution is due to isolated events, as described in the text.

Ignoring isolated events, f_η is calculated and plotted when different noise levels are added to 1000 eV photon events (Figure 5.17). The removal of isolated events has removed the step in the function close to 0 µm from the centre of the pixel that is seen in Figure 5.15. The spatial resolution achieved with the η correction algorithm is measured across a range of signal to noise values and compared to the results of the uncorrected centre of gravity algorithm in Figure 5.18.

The results of the simulation show that the correction of the systematic error has the desired effect: across the energy and noise range investigated, the corrected algorithm achieves a better spatial resolution. The biggest disadvantage of the η correction is that the correction function, f_η, must be acquired using a commissioning phase before the algorithm can be used. A flat field must be imaged in a photon counting mode to build up a distribution that contains at least a few thousand photons. The camera operating conditions must be the same as that to be used in future experiments, and a distribution must be obtained for each photon energy to be observed. Whilst the η algorithm is commonly applied in silicon microstrip detectors, at the time of writing this is the first application to soft X-ray events in CCDs known to the author.

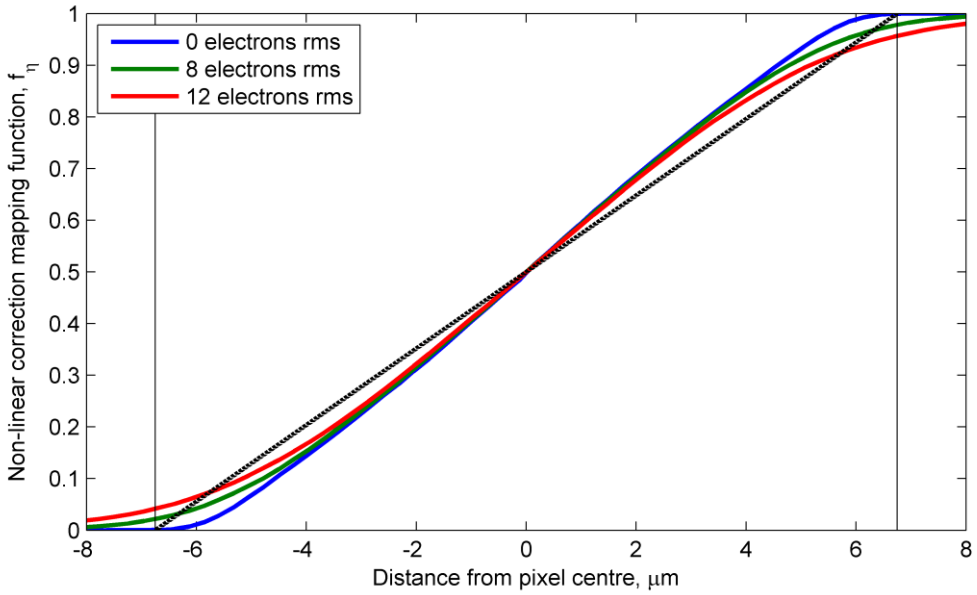

Figure 5.17. The corrective mapping function for 1000 eV photons, when isolated events have been ignored, for a range of noise levels.

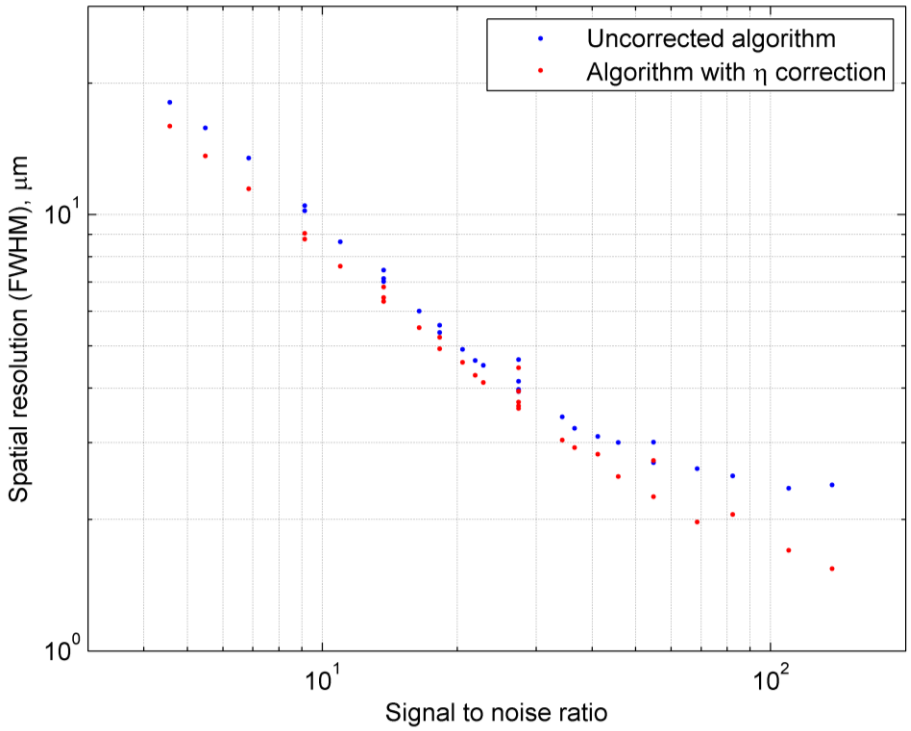

Figure 5.18. The centre of gravity algorithm applied across a 3×3 pixel area is improved across a range of signal to noise ratios. The data is simulated from photon energies of 200 eV, 400 eV, 600 eV, 800 eV and 1000 eV and random Gaussian noise levels with standard deviations of 2, 4, 6, 8, 10 and 12 electrons rms.

5.4 Applying the η algorithm to simulated events in an EM-CCD

The EM-CCD (described in Section 3.4) includes an additional gain register that allows the electron signal to be multiplied before readout noise is applied. Therefore, the effective readout noise can be reduced to sub-electron levels. According to the relationship shown in Figure 5.18, if the readout noise can be reduced, the spatial resolution achievable with centroid algorithms will approach a best-case level. However the situation is more complex as additional noise introduced during the gain process will degrade the spatial resolution. To determine if EM-CCD signal multiplication could lead to better spatial resolutions than predicted for CCDs, simulations have been undertaken that will be described in this section.

5.4.1 Incorporating signal multiplication into the simulation package

Signal multiplication occurs before readout noise is applied, in the device and simulation. At levels of high gain, the noise added to the signal is well modelled by the normal distribution with a variance equal to the signal in electrons. The pixel dimensions used in the previous simulations are modified to be representative of the EM-CCDs manufactured by e2v, such as the CCD97 and

CCD207-40 (Section 3.5.2), by increasing the pixel size to 16 µm from 13.5 µm. The total thickness and depletion depth are maintained at 13 µm and 4.7 µm respectively, as is representative for the devices.

5.4.2 Simulated spatial resolution achievable with an EM-CCD

Following the same procedures as described in Section 5.3.2, the η correction algorithm is applied to the centre of gravity centroid algorithm over a 3×3 pixel area for events simulated in an EM-CCD. The investigation has been repeated for gains of x100, x500 and x1000, but the results are similar across the energy and background noise levels used so only results for a gain of x100 have been presented here.

The spatial resolution achievable with the EM-CCD for readout noise levels between 2 and 20 electrons rms are shown in Figure 5.19 (1000 eV photons). With a gain of x100, the resolution remains constant over this range due to the multiplication noise dominating over the effective readout noise. For comparison, the resolution with a gain of x1 (no multiplication, and therefore no multiplication noise) is also shown. At low readout noise (below 4 electrons rms) the case of no gain (x1) performs better than with gain (x100), due to the multiplication noise becoming a larger source of error than the readout noise.

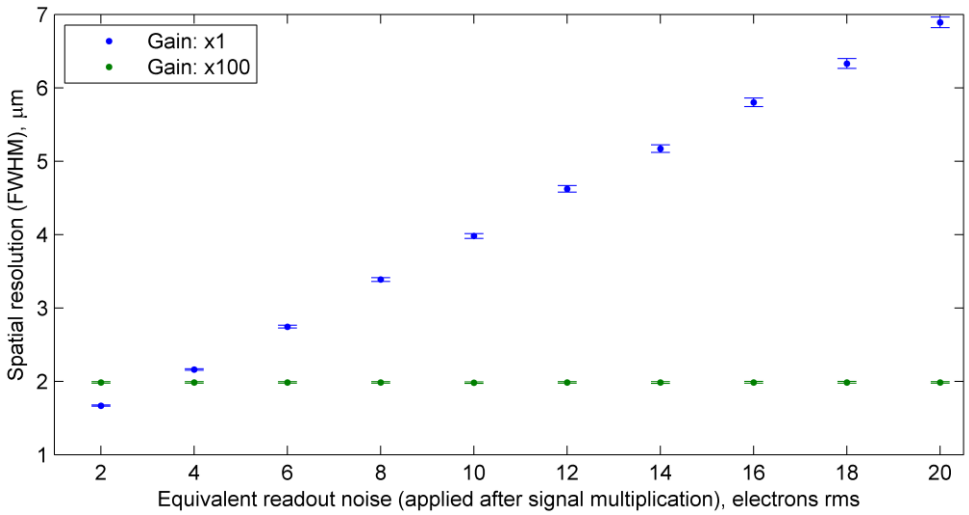

Figure 5.19. The spatial resolution achieved with an EM-CCD observing 1000 eV photons using a gain of x100 remains constant over the range of readout noise levels shown here. Error bars show the 95% confidence limit of the centroid location distribution fit.

At a gain of x100, the relationship between the spatial resolution and photon energy does not vary significantly for readout noise levels between 4 and 16 electrons rms, therefore only the

spatial resolution when a readout noise of 16 electrons rms is applied is shown in Figure 5.20. At high energies and/or low readout noise levels, the no gain case tends to a spatial resolution better than the case with gain, as observed in Figure 5.19 below 4 electrons rms. However, when operating with gain applied (x100), the spatial resolution is better than the no gain case (x1), tending towards approximately 2 µm (FWHM) at high energies.

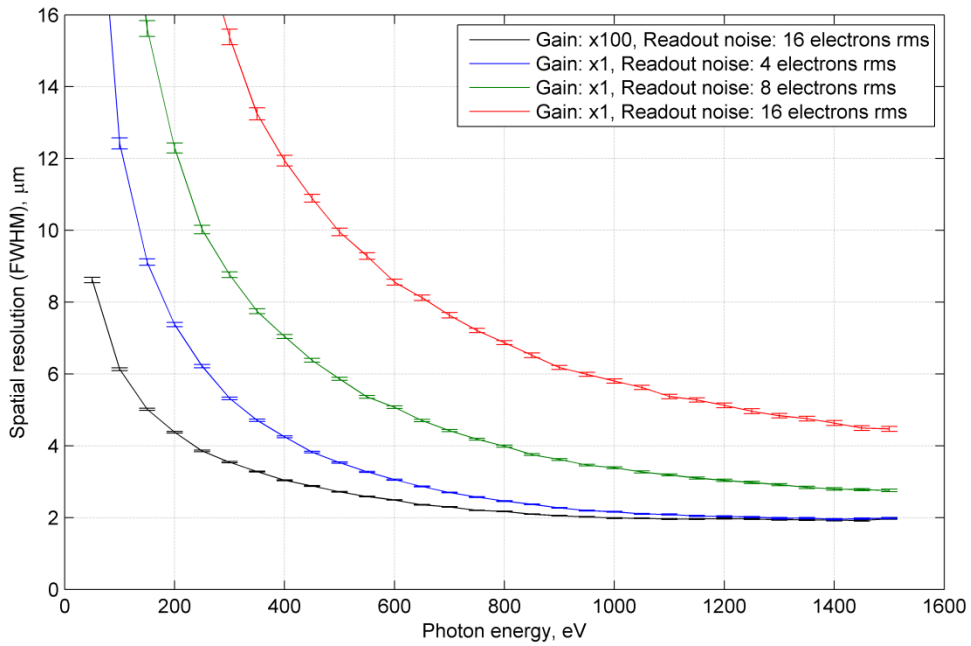

Figure 5.20. The spatial resolution improves for higher photon energies at levels of no (x1) and high (x100) multiplication gain. The relationships for x100 gain with 4 and 8 electrons rms readout noise applied are not shown here, but are equivalent to the 16 electrons rms curve, within errors.

To combine the relationship of the spatial resolution achieved with both the photon energy and the readout noise, the spatial resolution is shown as a function of signal (average number of electrons produced per photon) to readout noise ratio in Figure 5.21. In the case of no gain (x1), the same relationship is observed here as in the simulations for the standard CCD case (Figure 5.18) as expected. At a multiplication gain of x100, the spatial resolution remains constant at a given photon energy across the range of readout noise levels investigated. The minimum level is given by the error introduced by stochastic assignment of the electrons following the probability distribution from the charge sharing function, as well as the error introduced during the gain process. At low readout noise levels, the no gain case reaches a better spatial resolution than the high gain case, because the error from the multiplication noise dominates over the readout noise.

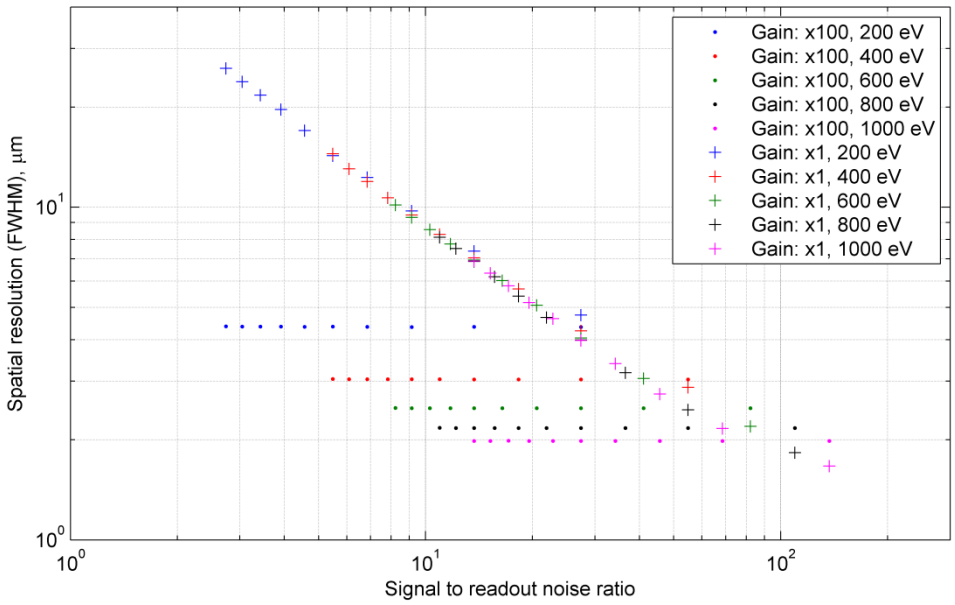

Figure 5.21. The simulated spatial resolution achieved with an EM-CCD (when applying the 3×3 centre of gravity centroid algorithm to single photon events) improves with higher photon energies, at the readout noise levels shown here (2, 4, 6, 8, 10, 12, 14, 16, 18 and 20 electrons rms). At high gain (x100), the resolution does not vary noticeably with readout noise, as when no gain is applied (x1).

Despite the large pixel size used to simulate the EM-CCD (16 µm rather than 13.5 µm) and the multiplication noise, the spatial resolution can be improved by using the EM-CCD gain feature over the majority of the readout noise and soft X-ray energy ranges investigated. The multiplication register has been demonstrated to be a significant benefit for improving the spatial resolution, with the simulation results showing that a resolution down to 2 µm (FWHM) can be achieved at 1000 eV and 3 µm (FWHM) at 400 eV.

5.5 Cramér-Rao inequality to calculate the best-case spatial resolution

The corrected centre of gravity algorithm applied across a 3×3 pixel area performs well on the X-ray events simulated here, but a different centroiding algorithm could perform even better. In optical applications of centroiding such as star-trackers, the best-case resolution of any centroiding algorithm can be determined analytically using the Cramér-Rao lower bound.

5.5.1 The Fisher Information Matrix

The Fisher Information Matrix (FIM), $\boldsymbol{I}(\theta)$ is a metric of the amount of information that observable random variables $\boldsymbol{R}$ carry about an unknown parameter, θ, upon which the random variables depend (e.g. pixel signals in an interaction event carry about the interaction position) [90]. $\boldsymbol{I}(\theta)$ is greater than zero and the larger its value, the higher the amount of information that is carried by $\boldsymbol{R}$ about θ. The Cramér-Rao inequality (*Equation 5.9*) states that an unbiased estimator of the parameter θ, $\hat{a}(\boldsymbol{R})$, has a variance greater than the inverse of the FIM [91].

$$Var[\hat{a}(\boldsymbol{R}) - \theta] \geq \big(\boldsymbol{I}(\theta)\big)^{-1} \qquad \textit{Equation 5.9}$$

In the application of estimating an interaction position, $\hat{a}$ is an unbiased centroiding algorithm that uses the observed pixel signals $\boldsymbol{R}$ to estimate the position of interaction of the photon detected θ. The lower bound from the Cramér-Rao inequality provides a bound to the best resolution that could be achieved with a centroiding algorithm. Although the Cramér-Rao lower bound (inverse of the FIM) does not necessarily provide the greatest lower bound (i.e. the best possible spatial resolution could be worse than the limit set), it is widely used as its application is mathematically straightforward in certain situations [92].

$p_{r|a}(\boldsymbol{R}|\theta)$ is the conditional probability of observing the pixel signals $\boldsymbol{R}$ given that the interaction occurred at position θ. If $\frac{\partial p_{r|a}(\boldsymbol{R}|A)}{\partial A}$ exists and is absolutely integrable, the FIM in the 1D case is given by *Equation 5.10*, where $E\{\dots\}$ is the expectation operation [91].

$$\boldsymbol{I}(\theta) = E\left\{\left[\frac{\partial \ln p_{r|a}(\boldsymbol{R}|A)}{\partial A}\right]^2\right\} \qquad \textit{Equation 5.10}$$

The calculation of the FIM applied to the centroiding of optical point sources observed in detectors can be found in the literature for applications such as star-tracking for spacecraft navigation [92], the observation of fluorescent molecules [93] and the array of spots produced on a detector of a Shack-Hartmann Wavefront Sensor used in adaptive optics systems [94]. The application by Ober *et al*. is relevant here [95], where the FIM is derived for a centroid algorithm applied to an optical spot observed in a pixelated detector.

5.5.2 The Fisher Information Matrix in the case of an optical spot

Ober *et al*. began by defining an image area with pixels $k = 1, \dots, K$, containing signals $\mathcal{I}_{\theta,1}, \dots, \mathcal{I}_{\theta,K}$ respectively. Electrons are generated at position (θ_i, θ_j) in the detector plane, resulting in an average of $v_\theta(k)$ signal electrons being present in pixel k in each image. When a Poisson distributed background electron count and a Gaussian distributed noise are added to the signal, the overall signal read out in a pixel, $\mathcal{I}_{\theta,k}$ is given in *Equation 5.11* [95].

$$\mathcal{I}_{\theta,k} = S_{\theta,k} + B_k + W_k \qquad \textit{Equation 5.11}$$

The three distributions making up the total signal are:

- **Photo-generated signal**, $S_{\theta,k}$: An average of $\mu_\theta(k)$ electrons are collected in pixel k that have been photo-generated at (θ_i, θ_j). The signal level is Poisson distributed due to shot noise of the optical light.
- **Background signal generation**: B_k is a Poisson random variable to represent background noise sources such as dark current generation. The distribution has an average of $b_k t$, where b_k is the background electron generation per pixel per unit time and t is the integration time.
- **Readout noise,** W_k: The noises applied to the signal during readout are modelled using a Gaussian random variable with mean η_k and standard deviation σ_k.

In this case the FIM is a 2×2 matrix given by *Equation 5.12*, using *Equation 5.13*, *Equation 5.14* and *Equation 5.15* [95].

$$[\boldsymbol{I}(\theta)]_{ij} = \sum_{k=1}^{K} \frac{\partial \mu_\theta(k)}{\partial \theta_i} \frac{\partial \mu_\theta(k)}{\partial \theta_j} \alpha_k \qquad \textit{Equation 5.12}$$

$$\alpha_k = \int_{-\infty}^{\infty} \frac{\left(\sum_{j=1}^{\infty} \frac{e^{-\nu_\theta(k)} [\nu_\theta(k)]^{j-1}}{(j-1)!} \mathrm{e}^{-0.5\left(\frac{z-j-\eta_k}{\sigma_k}\right)^2} \right)^2}{2\pi\sigma_k^2 p_{\theta,R}(z)} dz - 1 \qquad \textit{Equation 5.13}$$

$$p_{\theta,R}(z) = \frac{1}{\sqrt{2\pi}\sigma_k} \sum_{j=0}^{\infty} \frac{e^{-\nu_\theta(k)} [\nu_\theta(k)]^{j}}{j!} \mathrm{e}^{-0.5\left(\frac{z-j-\eta_k}{\sigma_k}\right)^2} \qquad \textit{Equation 5.14}$$

$$\nu_\theta(k) = \mu_\theta(k) + b_k t \qquad \textit{Equation 5.15}$$

No unbiased centroiding algorithm would have a variance error less than the inverse of $[\boldsymbol{I}(\theta)]_{11}$ or $[\boldsymbol{I}(\theta)]_{22}$, for determining the position in each dimension (θ_i, θ_j), respectively. Using this result, it is therefore possible to calculate and compare the resolution achieved with a centroiding algorithm to a theoretical best resolution in the case where the photon generated signal in each pixel is independent and shot noise limited.

5.5.3 Analytical centroiding accuracy limit for soft X-rays

Equation 5.12 is valid when the number of photons detected in each pixel is governed by shot-noise statistics and independent of the photons detected by the other pixels of the spot distribution. However, these assumptions are not valid for an X-ray generated charge cloud that is shared amongst neighbouring pixels. An X-ray will generate, for example, n photo-electrons that

are all collected in the event pixels, assuming recombination is negligible. It is very clear in the case of a detector with only two pixels that the number of electrons collected in one pixel is dependent on the number collected in the other; if a total of n_T electrons are generated and n_1 electrons are collected in the first pixel then the number of electrons collected in the other is $n_2 = n_T - n_1$.

Efforts to determine the FIM for X-ray interactions in CCDs and EM-CCDs are on-going. Until a solution has been determined, the expected spatial resolution obtainable by centroid algorithms applied to split X-ray events must be determined by developing a Monte Carlo simulation package, as has been described in Chapter 4.

5.6 Summary and Conclusions

A Monte Carlo simulation package incorporating the analytical diffusion equation solution (*Equation 4.9*, [66]) and other stochastic processes governing the detection of single X-ray photon interactions in a CCD has been used to generate large populations of X-ray events with known parameters to which centroid algorithms could be applied. X-ray events were generated within the volume of pixels with dimensions that match the CCD42-10 and CCD97.

A centre of gravity algorithm was applied to the simulated X-ray events, showing that the algorithm could determine the pre-defined interaction position to sub-pixel accuracy. This result was a proof-of-principle that if the SAXES camera were to operate in a single photon counting mode where individual X-ray events were observed, the resolution could be limited by the accuracy of the centroid algorithm, rather than charge spreading or pixel size. Best-case resolutions achievable were dependent on the photon energy and background noise in the image. At high signal to background noise ratios, the best-case resolutions were limited by the random assignment of electrons into the pixels.

A dominant source of error when applying the linear centre of gravity algorithm to a 3×3 pixel area was found to be a systematic bias, where centroid locations are biased towards the centre of the pixel (edge effects). The systematic bias deteriorated the achievable resolution therefore non-linear centroid algorithms were investigated to incorporate a correction. The analytical correction method described by Alexander and Ng [85] partially compensates for the systematic bias. However, the η correction proved a better solution, fully correcting for the systematic bias in the simulated events and significantly improving the spatial resolution, across a wide signal to background noise and soft X-ray photon energy range. The η correction will therefore be applied to correct the centroiding algorithms used with the experimental data in the following chapters.

The simulation package was extended to allow the simulation of events observed in EM-CCDs with levels of no or high gain. The η correction algorithm was applied, with the simulation results showing that a resolution down to 2 µm (FWHM) can be achieved at 1000 eV and 3 µm (FWHM) at 400 eV, for soft X-ray energies and readout noise levels below 20 electrons rms. These results suggest that an improved resolution could be achieved using the EM-CCD's multiplication register operating at high gain, at readout noise levels above 4 electrons rms for X-ray energies between 50 eV and 1500 eV. The EM-CCD is therefore a candidate detector for a future new camera as will be described in Chapters 7 and 8.

To set a lower bound on the resolution achievable with a centroid algorithm applied to soft X-ray events observed with a CCD, the Cramér-Rao lower bound was investigated. However as the pixel signals in a split soft X-ray event cannot be considered independently, an analytical solution could not be determined using the same processes as with optical spots in pixelated detectors.

In this chapter, a simulation package to accurately generate X-ray events in a back-illuminated CCD, developed in Chapter 4, has been used to investigate the accuracy of centroiding algorithms applied to soft X-ray events in CCDs. The investigations led to the application of non-linear centroiding algorithms, capable of achieving spatial resolutions of better than 2 µm (FWHM) at high signal to background noise ratios (Figure 5.18). The simulation results with the centroiding algorithms incorporating a non-linear η correction therefore suggest that the resolution of the CCD at SAXES could be improved from its current, charge cloud dominated, resolution of approximately 24 µm (FWHM) to a resolution better than 2 µm (FWHM) if a detector with a sufficiently low noise level was used.

Chapter 6: Improving the Current SAXES System

6.1 Introduction

Whilst centroiding has been shown through the simulation studies in Chapter 5 to improve the resolution of a photon counting CCD, experimental evidence is needed to prove the principle and calibrate the simulations. The PolLux spectromicroscope provides a facility with a tuneable X-ray energy range similar to the ADRESS beamline and its endstation's capability of focussing X-rays down to a minimum spot size of 20 nm (c.f. the 13.5 µm CCD42-40 pixel), makes it suitable for controlling the X-ray interaction location to a small sub-pixel area. Therefore, four experimental campaigns were undertaken at PolLux to collect data for testing the performance of a range of different centroid algorithm and the η correction function.

To undertake the experimental campaigns, mechanical, electrical and cooling interfaces between existing equipment available and the PolLux endstation were designed and constructed to enable detectors to be operated in the PolLux chamber, as described in Section 6.2. Analysis of the data collected with a CCD42-10 at PolLux, which has the same pixel structure as the CCD42-40 in SAXES, is described in this chapter: the data reduction pipeline and X-ray event grades are discussed in Section 6.3; Section 6.4 contains a detailed analysis of linear and non-linear centroid algorithms; and measurements of the charge cloud shape are described in Sections 6.5 and 6.6. The collection of data used to investigate charge cloud shape models and validate the simulation package in Chapter 4 is outlined in Section 6.7, and following the successful experimental demonstration of centroid algorithms in the CCD42-10, they are applied to images recorded at SAXES, as described in Section 6.8.

6.2 Experimentation at PolLux

To recap Section 3.7, the soft X-ray spectromicroscope at the Swiss Light Source, PolLux, has a tuneable X-ray source with energies between 200 eV and 1400 eV [71]. The endstation is designed to operate as a Scanning Transmission X-ray Microspectroscope, where focussed monochromatic X-ray photons are scanned across a sample, creating a map in the transmitted X-ray intensity as a function of incident X-ray energy and the two spatial dimensions of the sample.

The minimum size of the focussed X-ray photon spot is ~20 nm, significantly smaller than the 13.5×13.5 μm^2 square pixels of the CCD42-10. By interfacing the standard sample holder and stages with the mechanical supports for the cooling and electronics required by a CCD, it has been possible to operate a CCD whilst its sensitive region is at the X-ray focal point. Recording images

at locations during a scan of the X-ray spot across the pixel structure has allowed the typical events and the performance of centroid algorithms to be investigated for interactions in different sub-pixel areas.

6.2.1 Incorporating a CCD camera within the PolLux microscope

The experimental campaigns undertaken as part of the preparation of this thesis were the first time that the performance of a detector has been evaluated at the X-ray focal point in PolLux. Through examining computer aided design files and photographs, it was determined that if the microscope's sample holder mount, order selecting aperture and standard detectors were removed, the space available would be sufficient to incorporate the materials required for mechanical support, electronic control and cooling of a CCD. The mechanical setup was developed before and throughout experimental campaign 1, which was used primarily to calibrate the system and as a proof of concept. The results obtained are not presented here but can be found in reference [96]. The setup developed through this testing will now be described.

The primary mechanical interface was a plate mounted to the translational stages that allowed the detector to be translated relative to the X-ray beam (Figure 6.1). The plate was machined from G10 fibre glass to provide electrical and conductive thermal isolation of the camera to the microscope. The plate provided a standard method to interface all further iterations of setups when changes were made to the cooling system or detector of the camera.

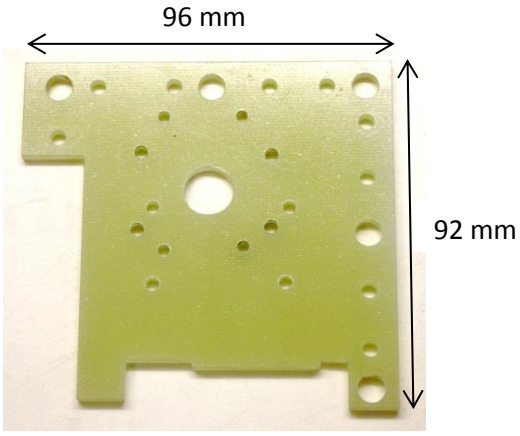

Figure 6.1. The G10 plate designed to interface between the PolLux microscope sample stages and the detector setup.

A copper cold-finger was bolted to the G10 plate and the ceramic package of the CCD was clamped onto the cold-finger using four studs and a clamping plate. Standard practice is to use 3 mm thick G10 sheet to create the clamping plate, but for the FZP to focus 530 eV X-rays in the

plane of the CCD, it must be located approximately 3.5 mm from the CCD surface. When the inset distance of the CCD within its ceramic package is also taken into account, a 3 mm clamping plate would be too thick. The clamping plate was made from 0.5 mm thick stainless steel sheet, in a compromise between thickness and rigidity (Figure 6.2).

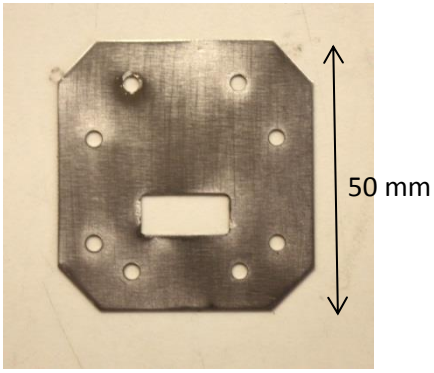

Figure 6.2. The stainless steel plate is designed with 8 holes for studs that are tightened to clamp the CCD's ceramic package to the cold-finger. A rectangular window allows X-rays to pass through to the photosensitive silicon.

An Order Selecting Aperture (OSA) is usually used at PolLux to block photons in diffraction orders other than the 1st order, which is focussed to a spot on the sample. However, the OSA cannot be located at its optimum distance of approximately 0.5 mm to 1 mm from the CCD detector surface due to the presence of the clamping plate and the inset of the CCD within its ceramic package. Therefore, photons from all diffraction orders are present in the data.

The thermal connection between the copper cold-finger head and ceramic package was maximised by ensuring the cold-finger was as flat as possible with a razor blade, or sandwiching a 0.2 mm thick layer of indium foil. Whilst the thermal conductivity of indium (82 W m^{-1} K^{-1} [97]) is significantly lower than that of copper (400 W m^{-1} K^{-1} [97]), its high malleability allows the contact area to be significantly increased, and point contacts to be avoided. To monitor the cooling, a platinum resistance thermometer (PT1000) was connected to the cold-finger or ceramic package during the experiment.

Methods for providing sufficient cooling power to the cold-finger evolved across the experimental campaigns (Table 6.1). A Polycold® Compressor and Cryotiger head from Megatech Ltd. [98] using the Standard PT-14 gas blend with a maximum cooling capacity of 10 W at -177°C, was used during the first two experimental campaigns. To lower the operating temperature, a Standard PT-30 gas blend was used with a maximum cooling power of 29 W at -144°C in the third test

campaign and in campaign 4, liquid nitrogen was flowed through a copper pipe that passed in and out of the vacuum chamber, providing a cold sink *in vacuo*.

Table 6.1. Four experimental campaigns were undertaken at PolLux to collect data with CCDs.

Campaign number	Date	Detector	Cooling system	Data collected
1	June 2011	CCD97	Cryotiger with Standard PT-14 gas blend. Copper sheets clamping to cold-finger	1D data scan with 1000 eV energy photons
2	August 2011	CCD42-10		1D data scans at four photon energies
3	December 2011	CCD97	Standard PT-30 gas blend. Copper braid attached to a single-piece cold-finger.	2D data scans using the automated MATLAB control at four photon energies
4	May 2012	CCD207-40	Liquid nitrogen.	2D data scans with four photon energies

The thermal connection between cold-sink and cold-finger was initially formed from copper sheets of the correct length, bent into shape to be clamped at the Cryotiger head and cold-finger ends. To improve the flexibility required for aligning the diffracted X-ray focal point in the plane of the detector and in the correct sub-pixel position, the copper sheets were later replaced with copper braids.

The pins from the CCD package were connected to a headboard held in place using the same studs that clamp the CCD to the cold-finger. The headboard provided initial output signal amplification, filters bias potentials, and acted as an interface for the CCD package. Electronic connections through the wall of the microscope vacuum chamber were developed using a custom ISO 63K interface flange, incorporating three Fischer connectors with 24, 7 and 4 pins. The bias and clock signals required for CCD operation were generated by an XCAM camera drive system [99] external to the vacuum chamber and passed in using the 24-pin connector to the headboard. In general, the cabling required was manufactured bespoke to the CCD to suit its requirements. The CCD output and wiring to monitor the resistance of the PT1000 and supply power to a resistive heater were also produced to interface at the flange.

6.2.2 Software control

The PolLux microscope and beamline is controlled using an implementation of the Experimental Physics and Industrial Control System (EPICS) [100], a software architecture that uses Channels to control access to pieces of data, known as Process Variables (PVs). A client machine at the user hutch of PolLux can view or set the values of PVs, to control or monitor the components of the beamline and microscope, such as the pressure gauges and translational stages using the PV associated to each variable, e.g. the observed pressure, set and read-back translational stage positions. The EPICS software on the client machine can access the PVs and either monitor the values, e.g. providing a warning and shutting valves if the observed pressure leaves a particular range, or assign values to the PVs which can, for example, move the translational stages.

During experimental campaigns 1 and 2, the CCDs were controlled using the software provided with the XCAM camera drive system, within which the voltages and timings can be set and images viewed and recorded. The translational stages used to raster the focussed X-rays across the plane of the CCD were controlled using the EPICS client software on the beamline machines. The collection of a data set containing images recorded where the X-ray spot was positioned at many locations in a pixel was possible and only user-intensive when the X-ray spot had to be moved to the next position. However, when scaling the number of sub-pixel locations up to an 18×18 grid (324 positions), it was appropriate to automate the image collection and translational stage movement to minimise the effective dead-time whilst the translational stages were moved and to reduce the required user input.

Therefore in experimental campaigns 3 and 4, the image capture and translational stages were both controlled using MATLAB [101]. The MATLAB Channel Access (MCA) toolbox [102] interfaced the Channel Access library of EPICS to allow access to PVs from the MATLAB command line and scripts, so the translational stages of the microscope could be controlled. The XCAM camera drive system was controlled in MATLAB by accessing the Dynamic Link Libraries directly. A MATLAB script was written to scan the translational stages across a set of predefined sub-pixel locations, recording images at each location. The integrated image capture and translational stage control system allowed raster scans to operate at all hours during a multi-day experimental campaign without additional man-power, making the most of the time and photons available.

6.3 Probing the sub-pixel of the CCD42-10

During the first experimental campaign undertaken at PolLux in the preparation of this thesis, a CCD97 was probed with the focussed X-ray spot. The campaign verified the interfacing setup and proved the principle of adapting the PolLux experimental chamber to allow a CCD to be operated

at the focal point of the X-rays. Data reduction and analysis methods were written to deal with the type of data collected, and initial results contributed to a publication [96]. Following the success of campaign 1, the electronics to operate a CCD42-10 were developed so that a device similar to the CCD42-40 in SAXES could be tested two and a half months later in campaign 2.

6.3.1 Experimental campaign

Results from an initial analysis of data collected during campaign 2 were published by Soman *et al*. [103], but a more complete analysis is presented here. The CCD42-10 was cooled using the Standard PT-14 cooling gas in the Cryotiger with a thermal connection to the cold-finger made from three copper sheets (Figure 6.3), resulting in temperatures measured on the cold-finger of between -20°C and -10°C.

The translational stages and CCD operation had not yet been integrated using MATLAB, and so performing raster scans of the focussed X-ray spot across many grid positions efficiently was not yet possible. However, experience from campaign 1 made the process faster and data sets containing single photons with energies 530 eV, 680 eV, 850 eV and 1000 eV were collected. This included 1D scans across pixels and extended observations of the X-rays focussed at the corner and centre of a pixel.

During setup, a full-frame image was recorded with a short integration time and with the X-ray beams incident on the detector (Figure 6.4). Serial pre-scan and over-scan, parallel over-scan and signal due to the X-rays are observed, confirming that the device was being read out and operating as expected. The high levels of background signal were due to the non-ideal operating temperature of between -20°C and -10°C, and stray light present in the vacuum chamber, primarily coming from the translation stages' laser interferometers. To reduce the stray light incident on the device, the laser interferometers were switched off and the stage position measured using the relative movement of the stages. This reduced the absolute position resolution but the relative position resolution was approximately 0.1 µm, which is still small compared to the pixel size. Additionally, matt black anodised aluminium foil was used to create a baffle around the detector to further block stray light.

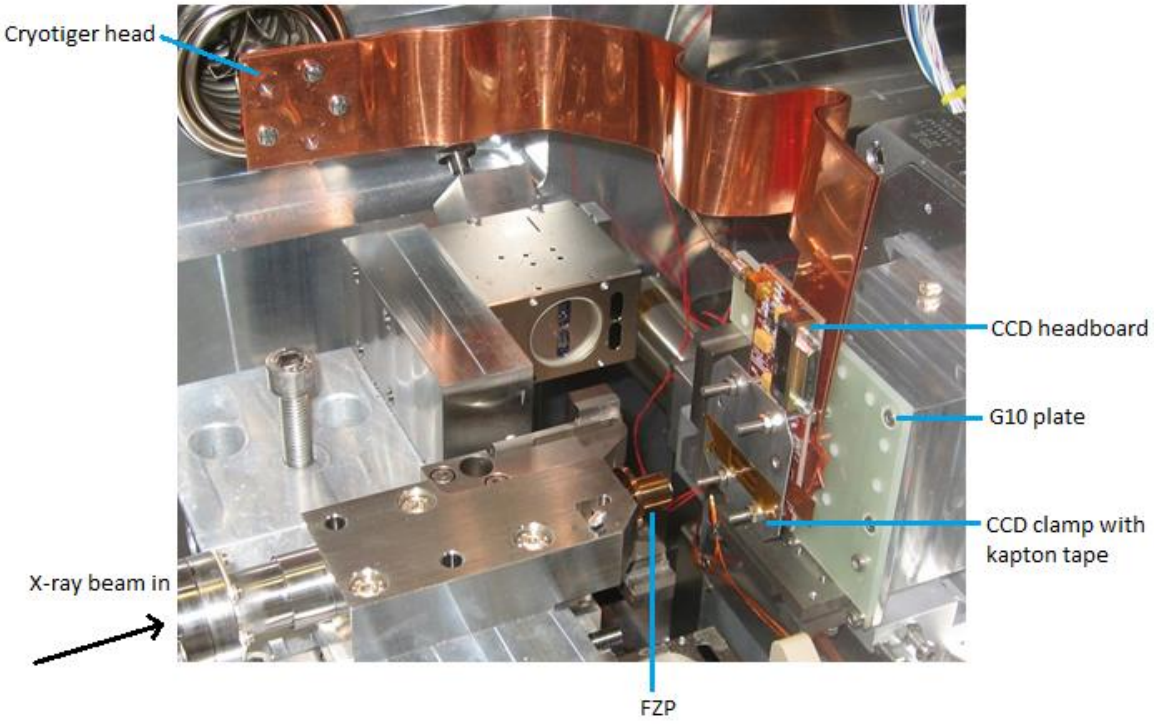

Figure 6.3. The inside of the PolLux vacuum chamber during the setup for observing X-ray events with the CCD42-10. The copper sheets are shown coupling the Cryotiger head (top-left) to the cold-finger, hidden by the headboard (red PCB). The CCD42-10 is hidden from view by the steel clamping sheet (in front of the PCB, with four studs extruding) and a strip of Kapton tape that is to be removed when the setup is complete. X-rays pass in through the beam pipe, entering at the bottom-left of the figure, and reach the FZP located in the top-hat-shaped golden object in front of the clamping plate.

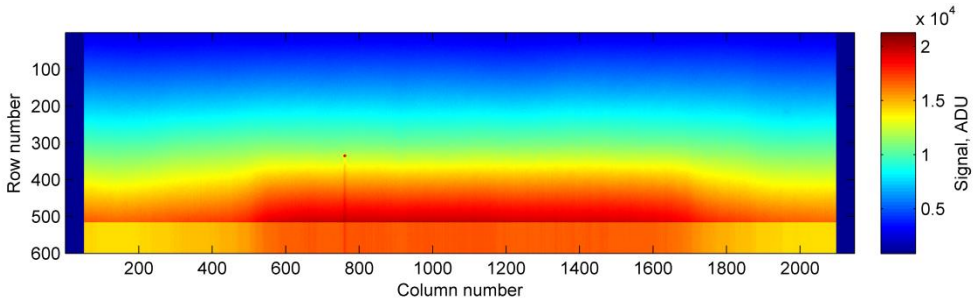

Figure 6.4. An initial full-frame image recorded at PolLux, showing serial pre-scan and over-scan, parallel over-scan, and a gradient of background signal in the image area. The gradient is due to pixels further from the output register (at column 1, row 1) having more time to accumulate background and dark signal. The spot and streak of signal at approximately column 750 is signal due to the unfocussed X-ray spot (approximately 20×20 pixel area).

To reduce the readout time, only a window of 20 rows by 24 columns surrounding the focussed X-ray spot was read out for each frame. The imaging area of 270 µm × 324 µm allowed the 0^{th} order diffraction ring to be observed and left capacity for scanning the spot across several columns. The pixel readout rate for the windowed region was approximately 60 kHz to reduce the readout noise, and the overall time per frame including integration and dumping was between 0.13 and 0.14 seconds. The beamline exit slits were opened to a width that maximised the proportion of frames for which a single photon is detected in the focussed X-ray spot (governed by Poisson statistics).

The X-ray spot, formed by photons diffracted at the 1^{st} order by the FZP, was focussed to the plane of the photosensitive silicon using a translational stage oriented in the direction of the incoming X-ray photons, upon which the CCD is mounted. During later campaigns, a more objective method is used for focussing (Section 7.2.1.2), but during campaign 2 the flux in the spot was increased to a few tens of photons per frame, and the CCD was translated to a position that visibly minimised the signal in the wings of the focussed spot. At the point when the charge sharing was minimised, it was assumed that the X-rays were most focussed.

From the 20×24 pixel window region, the first row and three columns are removed as they contain artefacts from the dumped signal, resulting in a region of 19 rows and 21 columns in each image. The distribution of X-rays diffracted from the FZP can be observed by displaying the average of a selection of frames where the focussed spot is kept at a constant location. In the example shown in Figure 6.5, the X-rays diffracted in the 1^{st} order by the FZP interact somewhere in or close to the pixel in the 10^{th} row and 11^{th} column. The 0^{th} order, and higher than 1^{st} order, photons are primarily observed in a surrounding ring which is approximately 18 pixels and 7 pixels (outer and inner diameter respectively) in the CCD42-10. These dimensions are expected for the FZP used which has outer and inner diameters of 240 µm and 90 µm respectively. The signal within the ring has some vertical structure, related to the distribution of X-rays incident on the FZP from the beamline.

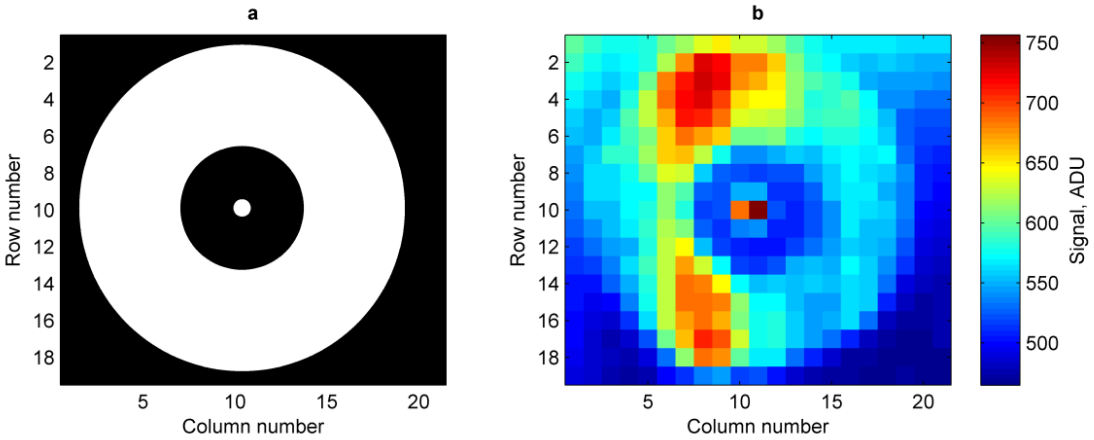

Figure 6.5. ***(a)*** *The vast majority of X-rays are incident on the device in the white areas of this schematic: a 0^{th} order diffraction ring with the same dimensions as the FZP, and a central spot where the 1^{st} order photons are focussed.* ***(b)*** *The mean of 2000 frames where 1000 eV photons are distributed in the diffraction pattern generated by the FZP.*

Example frames that contributed to the mean image in Figure 6.5 b are shown in Figure 6.6. The left two frames contain signal from interactions of X-rays of the focussed 1^{st} order diffraction spot, in the pixel at row 10 and column 11. The remaining photons in all the frames are from the 0^{th} order, and higher than 1^{st} orders. When analysing the events from photons interacting in the focussed 1^{st} order X-ray spot, care must be taken to exclude events where signal from other photons have been shared into neighbouring pixels.

The orientation of the two translation stages used for rastering the spot, relative to the orientation of the rows and columns of the CCD was examined. During a long integration time, the CCD was translated relative to the FZP and X-ray beam using the stage aligned approximately parallel to the row. The movement was in steps of 300 µm, pausing after each step. The X-ray beam shutter was opened for a short period to expose the device at step, forming the pattern shown in Figure 6.7. Signal from the X-ray ring and spot diffraction pattern is visible at each of the step locations, moving at an angle of approximately 1.5° relative to the rows of the detector. This angle is small, therefore for most analysis in this chapter, the stage movement and row axes can be considered parallel.

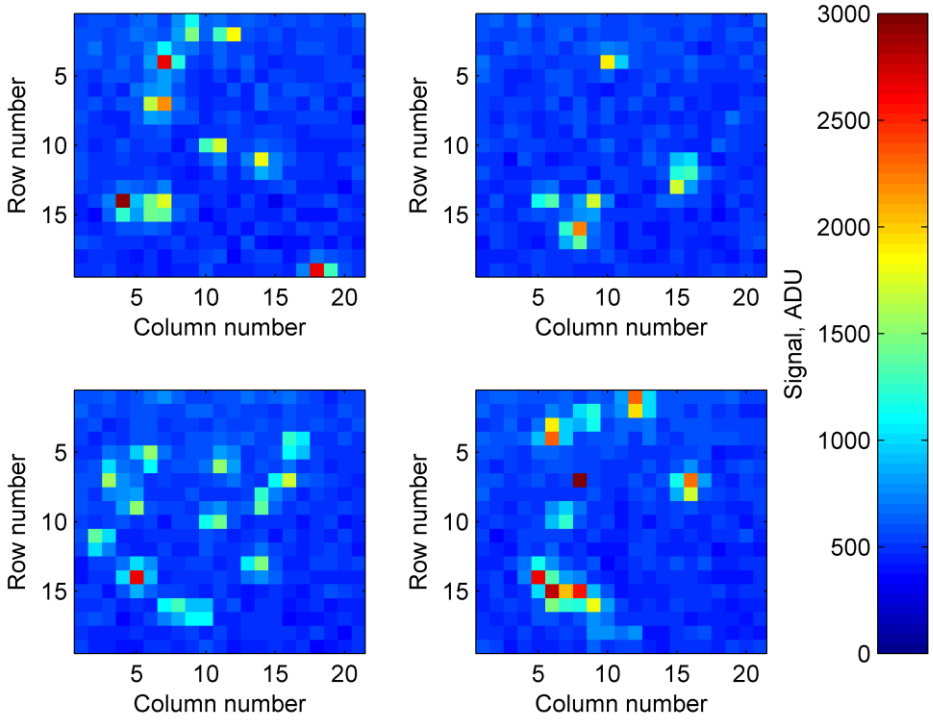

Figure 6.6. Four example frames containing signal from 1000 eV X-rays. The 1st order diffraction spot is centred within the pixel at row 10 and column 11. The frames on the left contain a photon in the central spot whilst those on the right do not.

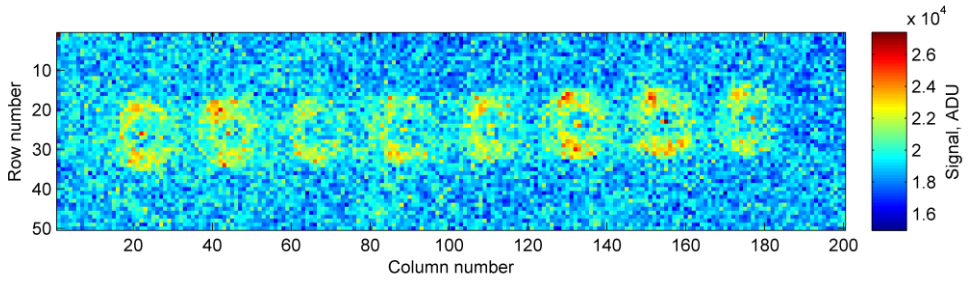

Figure 6.7. During a long integration time, the CCD is moved in 7 steps relative to the X-ray beam, using one of the translation stages. The X-ray beam shutter is closed during translation, and opened for a short period at each step.

6.3.2 Data reduction method

All windowed frames recorded with the detector at the same position relative to the FZP, with the same photon energy, are post-processed together. The following procedure is used:

- **Central pixel identification:** The 'mean central pixel' is identified as the pixel in the mean frame with maximum signal in the region where the 1st order X-rays are incident (e.g. pixel in row 10 and column 11 in Figure 6.5 b).

- **Background subtraction and noise measurement:** All the individual signals in the 5×5 pixel area centred on the 'mean central pixel' are binned into a histogram, and a Gaussian profile is fitted to the distribution (Figure 6.8 a). The offset of the Gaussian fit provides the zero signal offset level, which is subtracted from all the frames. The standard deviation of the Gaussian profile is the total background noise of the camera (currently in Analogue to Digital Units - ADUs).
- **Energy calibration and single photon signal thresholding:** The signals in the 3×3 pixel area centred on the 'mean central pixel' are summed and binned into a histogram (Figure 6.8 b). The peak in the histogram due to single photon interactions is fitted with a Gaussian profile whose offset provides information to calculate the energy per ADU calibration. Thresholds are set 3.5 standard deviations away from the mean – the 3×3 area thresholds.
- **Nearby event thresholding:** The signal in the 16 pixels neighbouring the 3×3 pixel area are summed and binned into a histogram, and a Gaussian profile is fitted to the peak (Figure 6.8 c). A threshold is set at 2.5 standard deviations above the mean – the 5×5 ring threshold.

Frames that do not have a total signal in the 3×3 pixel area between the 3×3 area thresholds are discarded, as are frames with signal greater than the 5×5 ring threshold. These discarded frames are not used in any further analysis. The remaining frames have had their offsets removed, and are expected to contain the signal from a single photon interaction which has been focussed in the 1^{st} diffraction order. The frames where photons in the 0^{th} or higher than 1^{st} diffraction orders have interacted close to the 1^{st} order diffraction spot have been discarded using the 5×5 ring threshold. Of the example frames in Figure 6.6, the right-hand two frames are discarded using this processing.

The background noise measured during this processing is converted to units of electrons using the calibration. During campaign 2, the overall background noise varied between 4 and 7 electrons rms due to the changing temperature of the device varying the dark signal generation.

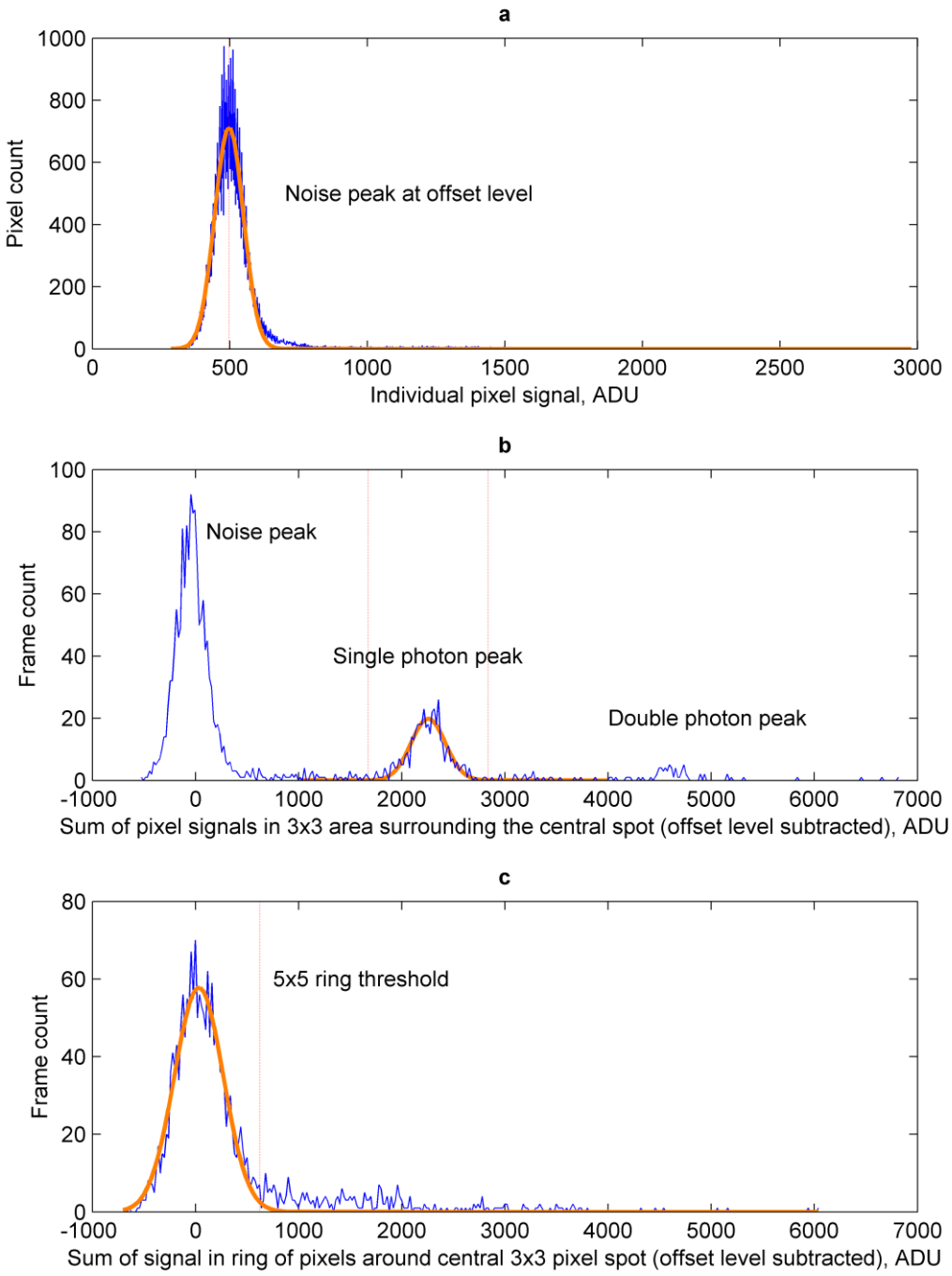

Figure 6.8. Data histograms are shown in blue, and the dashed red vertical lines show the offset and threshold levels derived from the Gaussian profile fits (orange). ***(a)*** *The individual pixels within the 5×5 area surrounding the 'mean central pixel'.* ***(b)*** *The total signal in the 3×3 area centred on the 'mean central pixel', with the single photon interaction thresholds shown.* ***(c)*** *The total signal in the 16 pixels surrounding the 3×3 area, with the 5×5 ring threshold.*

6.3.3 Pixel signal distributions

For a set of frames where the focussed X-ray spot was incident at the same location within the sub-pixel, i.e. the FZP was not moved relative to the CCD, the distribution of signals in the pixels of the event can be plotted. For a sub-pixel location, the signal distribution shows the likelihood of observing a given proportion of the charge cloud collected within that pixel's potential well. The distribution is dependent upon the interaction depth distribution (exponential decay) and the mean and variability of the charge cloud distribution. The Gaussian-like signal background and camera noise, and the fact that the X-ray interactions were distributed within the plane of the detector also contribute to the distributions.

The pixel signal distributions for the 5×5 pixel area centred on the 'mean central pixel' are shown in Figure 6.9, when the X-ray spot was focussed close to the centre of the pixel. Only images that passed the selection criteria (including a single X-ray photon) are included. The distributions were used to check the performance of charge cloud spreading models in Chapter 4 because they are dependent on the charge sharing process that follows a soft X-ray interaction in the field-free region.

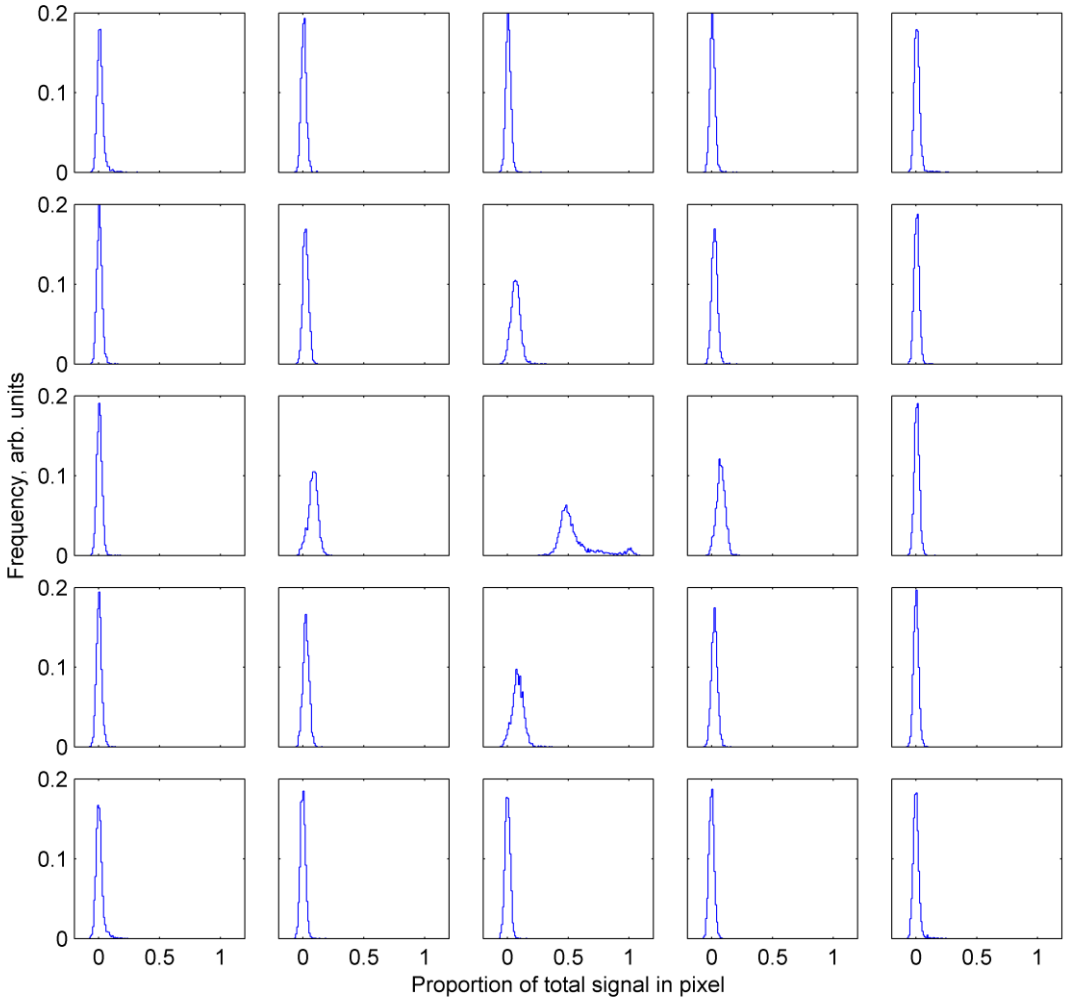

Figure 6.9. The pixel signal distributions for the 5×5 pixel area centred on the 'mean central pixel' (c.f. Figure 4.8). The X-rays were incident close to the centre of the central pixel. Signal in the outermost ring of pixels is negligible.

6.3.4 Centroid algorithm performance analysis

The X-ray events observed at the 'mean central pixel' are used to analyse the performance of the centroid algorithms. An algorithm is applied to all the events, to determine the centroid location in both the row and column dimensions where the location calculated as a displacement across columns is defined as being in the *x* direction, and is binned in the *y* direction (Figure 6.10). The result is a 1D distribution of centroid locations in the *x* direction. Similarly, the centroid location measuring the displacement of a centroid location across rows is defined as being in the *y* direction. The centroid locations are relative to the centre of the 'mean central pixel', where more negative values are closer to the CCD output.

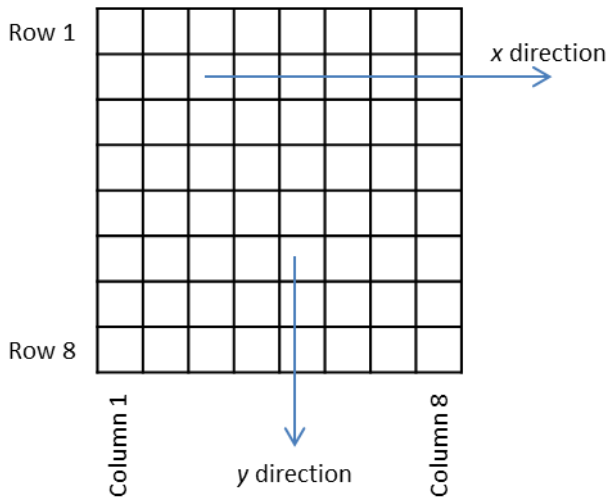

Figure 6.10. The relative orientation of rows, columns, and the x *and* y *directions.*

For each focussed X-ray spot location, the distribution of centroid locations can be plotted as two binned 1D distributions or a 2D map (Figure 6.11). The majority of centroid locations are in a small area of the sub-pixel, apart from a few evenly distributed outliers (from images wrongly identified by the single photon identification algorithm described in Section 6.3.2).

When binned into 1D, the distribution is fitted with a Gaussian profile, (e.g. Figure 6.11 c). The mean of the Gaussian fit can be used as the mean position of the centroid locations, and the width of the fit measures the spread of the distribution. The spread of the distribution contains contributions from the centroid accuracy and the X-ray spot size.

From the location shown in Figure 6.11, shifting the X-ray spot by 2.9 µm in the *x* direction (along the row), moves the X-ray distribution to the edge of a pixel (Figure 6.12). The distribution of centroid locations in the *x* direction is split across the pixel border (at 6.75 µm), and the locations are observably biased away from the pixel border, due to the edge effect in the uncorrected 3×3 centre of gravity algorithm applied here (c.f. Figure 5.3 a). The distributions of centroid locations show both that PolLux can be used to control the sub-pixel interaction location, and that centroiding algorithms can be used to determine the sub-pixel location of an X-ray interaction with an accuracy better than the pixel size.

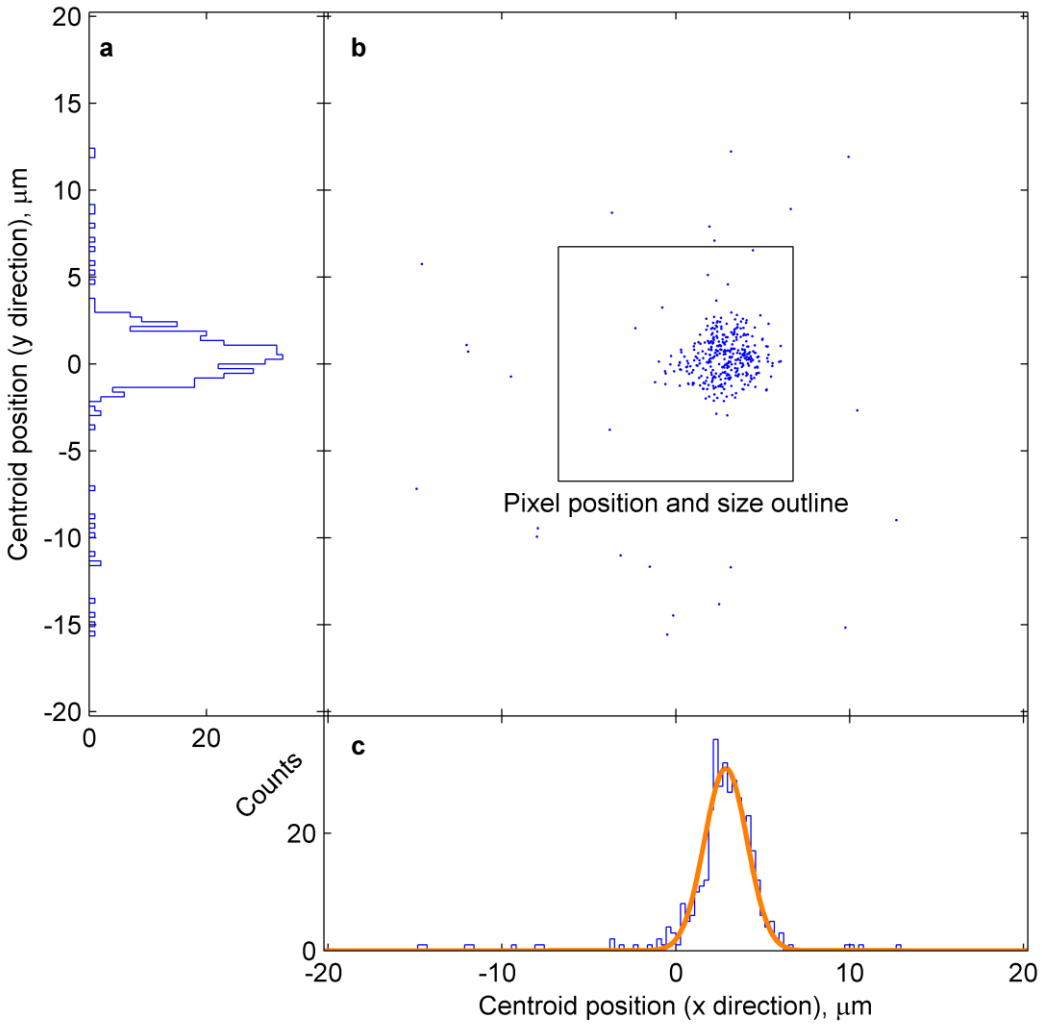

Figure 6.11. The centroid locations for an example set of 1000 eV photon events are determined using an uncorrected 3×3 centre of gravity algorithm in both the x *and* y *directions.* ***(a)*** *and* ***(c)*** *The centroids are binned into the single dimensions (blue), with a Gaussian profile fitted to the* x *direction centroid distribution (orange).* ***(b)*** *The centroid positions plotted in 2D, relative to the pixel position, shape and size.*

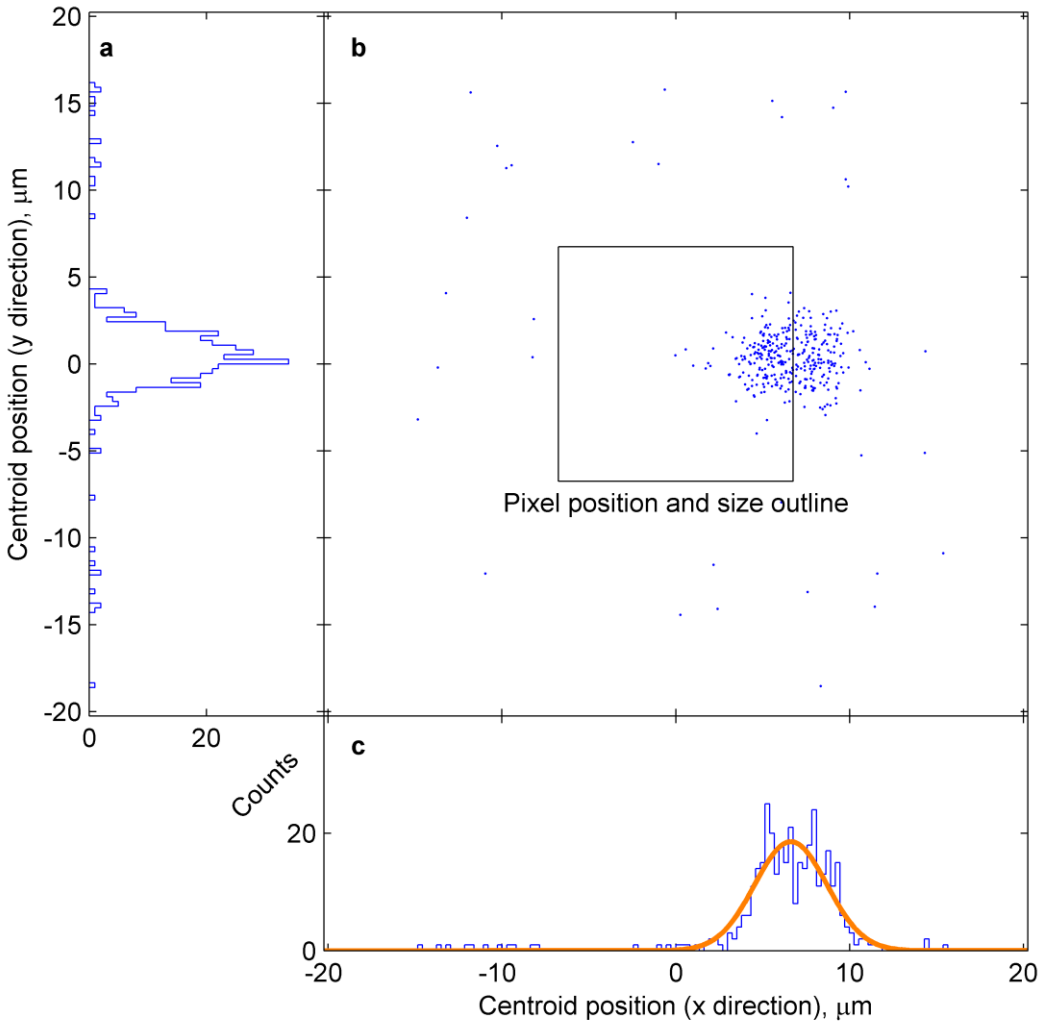

Figure 6.12. As Figure 6.11, with the focussed X-ray spot shifted in the x direction by 2.9 µm.

6.3.5 Raster scan analysis

To investigate the centroid resolution as a function of sub-pixel interaction location, the focussed 1st order diffraction X-ray spot was scanned along a set of locations, in a 1D scan. The relative location of the X-ray spot, known from the translation stage, is initially compared to the mean uncorrected 3×3 centre of gravity algorithm centroid location (Figure 6.13). The mean of the centroid distribution is displaced as the X-ray spot is scanned across the pixel: further experimental evidence that X-ray events can be post-processed to calculate the interaction location to a sub-pixel precision. The relationship between the assigned X-ray spot position and the mean centroid position is not linear: a reoccurrence of the 3×3 centre of gravity algorithm bias towards the centre of the pixel and away from the pixel boundaries.

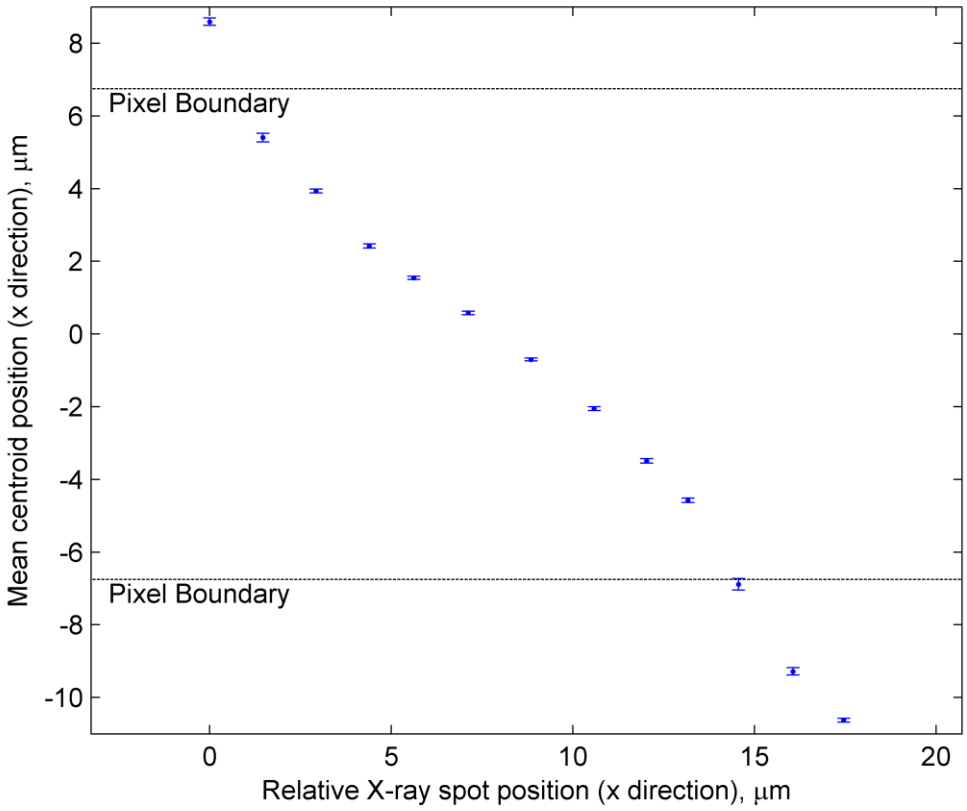

Figure 6.13. The mean centroid position, calculated using a Gaussian profile fit to 3×3 centre of gravity centroids, moves across the pixel in the x direction as the X-ray spot is scanned along the row. Error bars show the 95% confidence limit in the fit parameter.

The Gaussian profile fit width is measured as the focussed X-ray spot is scanned across the pixel to determine the resolution of the centroid algorithm at that position (Figure 6.14). The resolutions are all better than the pixel width and appear best at the centre of the pixel, and worst at the edges. However, it is not clear if this is due to the biasing of the 3×3 centre of gravity algorithm used (c.f. Figure 6.27).

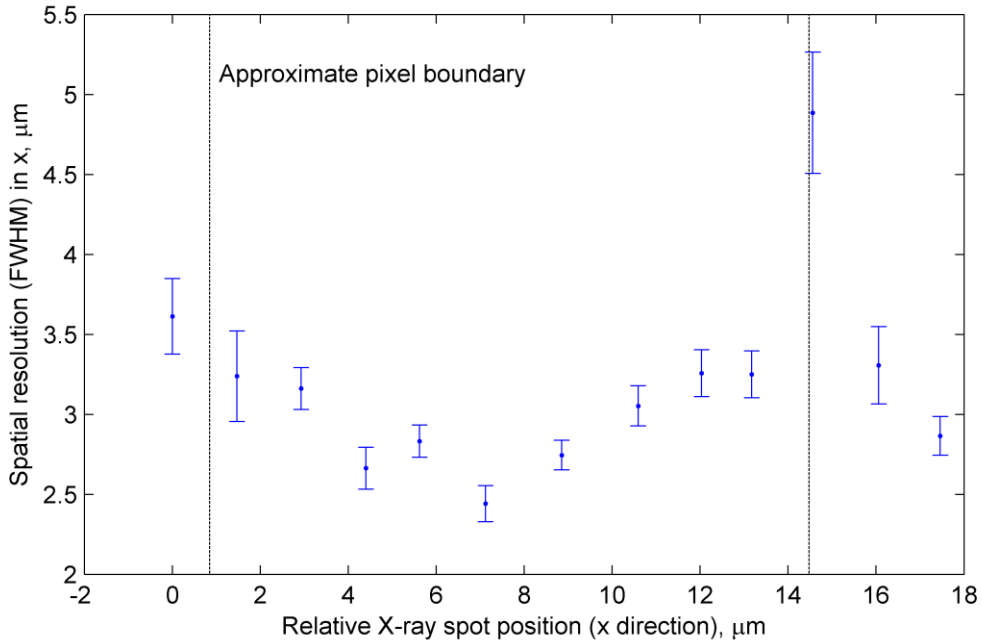

Figure 6.14. The worst-case resolution achieved with the 3×3 centre of gravity centroid algorithm, measured at 13 positions along the centre of a CCD42-10 row. The resolution errors show the 95% confidence limits in the Gaussian profile fitting parameter. The centre of the X-ray spot moves into the adjacent columns around the positions marked by the vertical lines.

6.3.6 X-ray event grading

The X-ray events detected can be classified into event grades, depending upon the number and locations of the pixels that contain signal greater than a threshold level. Figure 6.15 shows some event grades that an X-ray may form when detected in a CCD. The frequency of different event grades varies with the sub-pixel interaction position and is sensitive to the threshold level.

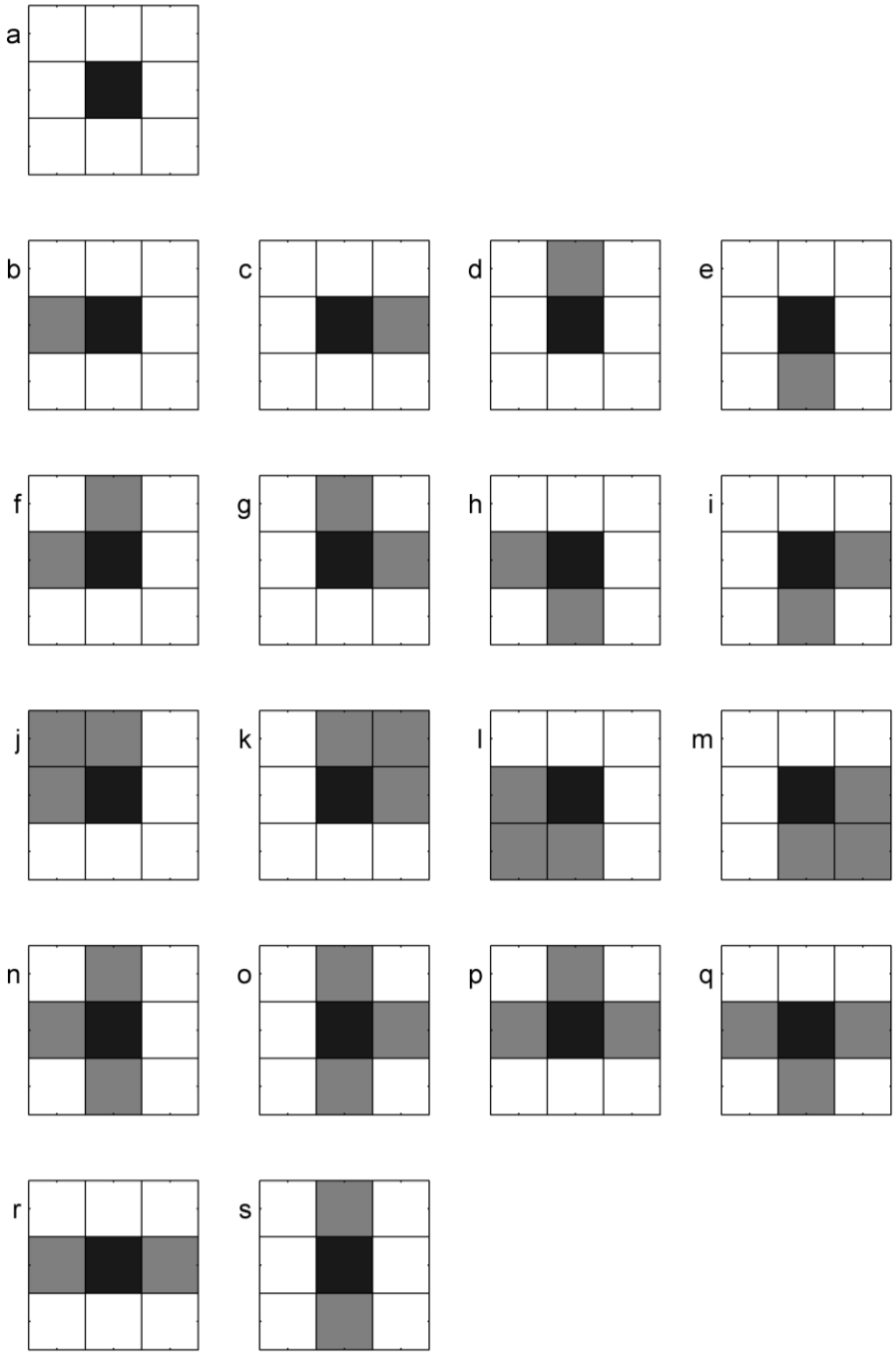

Figure 6.15. Typical event grades of soft X-rays detected with a CCD. The black pixels are the pixels with maximum signal in the 3×3 pixel region, the grey pixels have signal greater than the threshold level, and the white pixels have signal less than the threshold level.

The event grade in Figure 6.15 a is an isolated event, where only the pixel with maximum signal has a signal greater than the threshold level. The remaining event grades shown in Figure 6.15 are divided into groups: b to e are 2-pixel events, where two adjacent pixels contain signal above the threshold; f to i are 3-pixel corner events; j to m are 4-pixel corner events; n to q are T-shaped

events; and r and s show line-split events. Other event grades are observed, but Figure 6.15 illustrates the most common.

The frequency of observing different event grades is sensitive to the chosen threshold level, to which each pixel's signal level is compared to. The threshold must be set low enough to count pixels that contain signal, and high enough to ignore pixels with signal dominated by background noise. The frequency of the event grades in Figure 6.15 for the 1000 eV X-rays observed with the CCD42-10 are shown as a function of the stage position in Figure 6.16, using threshold levels of 4 and 5 times the standard deviation of the background noise peak. At background levels of approximately 6 electrons rms, the thresholds are approximately 24 and 30 electrons. The event grading therefore only identifies the pixels with a relatively large level of signal – c.f. 274 photoelectrons generated by the average 1000 eV photon. However, the mapping demonstrates which pixels the signal is primarily collected in, and which pixels have signal dominated by noise.

With a threshold level of 5 standard deviations (Figure 6.16 b), the majority of events are counted as a 2-pixel event, especially when close to the pixel boundary. The frequency of isolated events increases when close to the centre of the pixel, and the frequency of 3-pixel corner events is lower at both the pixel boundaries and the pixel centre. When a threshold level of 4 standard deviations (Figure 6.16 a) is used, the event grade frequency pattern across the pixel remains similar for the event types, but the relative frequency of the isolated events and 2-pixel events decrease, whilst the 3-pixel corner and line-split events increases. It is important to note that the majority of events are detected with signal over the threshold level in fewer than four pixels, at both these threshold levels, suggesting the majority of the signal is found in a 2×2 pixel area. Therefore, centroid algorithms applied over pixel areas smaller than 3×3 are worthy of investigation.

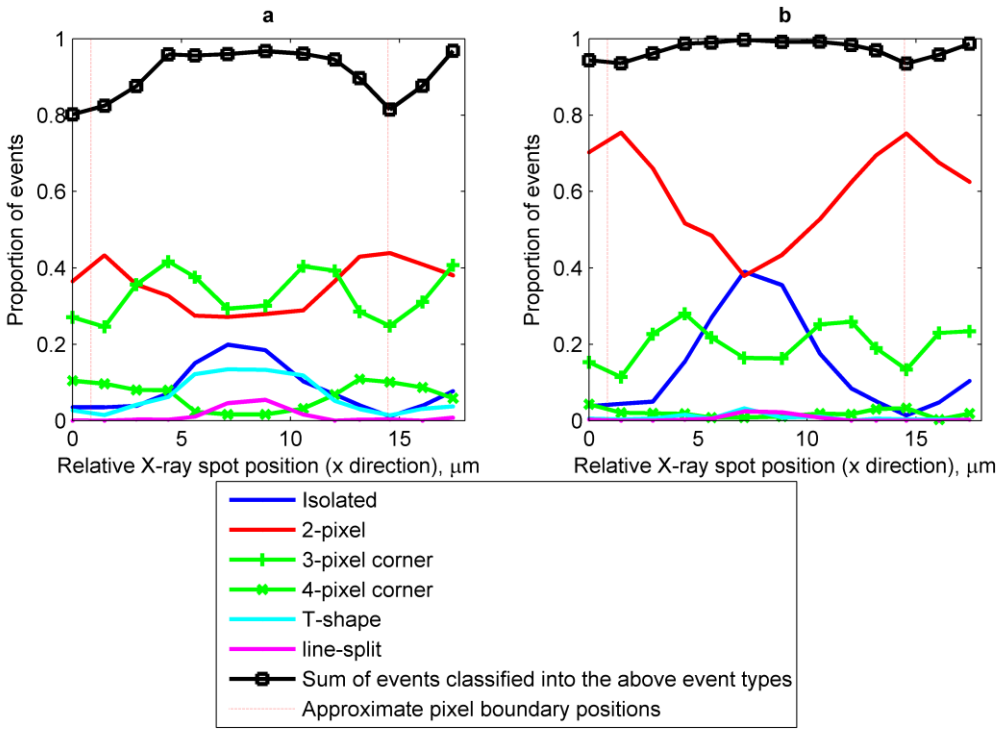

Figure 6.16. Frequency of event grades as the 1000 eV focussed X-ray spot position is scanned across the pixel. ***(a)*** *The signal threshold is 4 standard deviations from the background noise level.* ***(b)*** *The signal threshold is 5 standard deviations from the background noise level.*

6.4 Centroid algorithms

The algorithms described in Table 6.2 are centre of gravity algorithms applied to the signals from a range of pixel areas surrounding an event, used to estimate the interaction location in the *y* direction, i.e. across rows. The signal in the i^{th} row and j^{th} column of the 3×3 pixel area is denoted by S_{ij} (Figure 6.17) where the 3×3 pixel area is positioned around the X-ray event such that S_{22} is greatest.

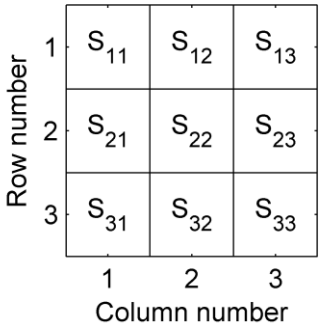

Figure 6.17. Diagram to show the notation of signals from pixels in the 3×3 area.

Table 6.2. Centroid algorithms names and descriptions, and figures to show which pixels' signals are utilised in the calculation (greyed pixels). The signals in the white pixels were ignored by the algorithm.

Algorithm name	**Signals observed in the greyed pixels were used by the centroid algorithm**	**Algorithm**
rows2x1_2var	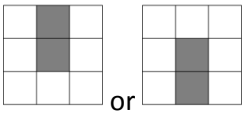 or	If $S_{12}>S_{32}$: $$y_c = \frac{S_{12}}{(S_{12}+S_{22})}$$ Else: $$y_c = \frac{S_{22}}{(S_{22}+S_{32})}$$
rows2x2	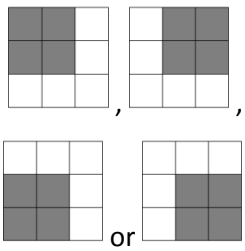 or	If the total signal in the 2×2 pixel areas is maximum for the area encompassing the pixel in row 1, column 1: $$y_c = \frac{S_{11}+S_{12}}{S_{11}+S_{12}+S_{21}+S_{22}}$$ Similarly, if the total signal is maximum in a different 2×2 pixel area.
rows2x3_2var	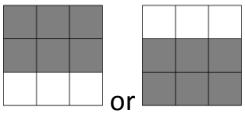 or	If $S_{11}+S_{12}+S_{13} > S_{31}+S_{32}+S_{33}$: $$y_c = \frac{S_{11}+S_{12}+S_{13}}{S_{11}+S_{12}+S_{13}+S_{21}+S_{22}+S_{23}}$$ Else: $$y_c = \frac{S_{21}+S_{22}+S_{23}}{S_{21}+S_{22}+S_{23}+S_{31}+S_{32}+S_{33}}$$

rows3x1_3var	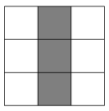	$y_c = \frac{S_{12} + 2S_{22} + 3S_{32}}{S_{12} + S_{22} + S_{32}} - 1.5$
rows3x2_3var	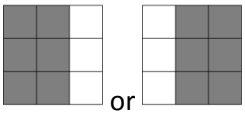 or	If $S_{11}+ S_{21}+ S_{31} > S_{13}+ S_{23}+ S_{33}$: $y_c = \frac{S_{11} + S_{12} + 2(S_{21} + S_{22}) + 3(S_{31} + S_{32})}{S_{11} + S_{12} + S_{21} + S_{22} + S_{31} + S_{32}} - 1.5$ Else: $y_c = \frac{S_{12} + S_{13} + 2(S_{22} + S_{23}) + 3(S_{32} + S_{33})}{S_{12} + S_{13} + S_{22} + S_{23} + S_{32} + S_{33}} - 1.5$
rows3x3	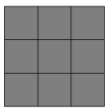	3×3 centre of gravity centroid (*Equation 6.1*)
rows2x1_outer	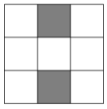	$y_c = \frac{S_{12}}{(S_{12} + S_{32})}$
rows2x2_outer	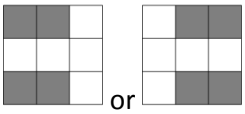 or	If $S_{11} + S_{31} > S_{13} + S_{33}$: $y_c = \frac{S_{11} + S_{12}}{S_{11} + S_{12} + S_{31} + S_{32}}$ Else: $y_c = \frac{S_{12} + S_{13}}{S_{12} + S_{13} + S_{32} + S_{33}}$
rows2x3_outer	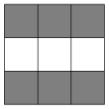	$y_c = \frac{S_{11} + S_{12} + S_{13}}{S_{11} + S_{12} + S_{13} + S_{31} + S_{32} + S_{33}}$

In the rare occasion that the signals in two compared areas are found to be equal, the event is ignored for simplicity. This occurs for no greater than 42 of the 38 495 events for any of the algorithms.

A similar set of algorithms can be defined to calculate the centroid in the *x* direction, across the columns: cols1x2_2var, cols2x2, cols3x2_2var, cols1x3_3var, cols2x3_3var, cols3x3, cols1x2_outer, cols2x2_outer, cols3x2_outer. The naming convention begins with ‘rows’ or ‘cols’ describing the dimension across which the algorithm acts, followed by a notation for the total pixel area used, for example ‘2x3’ is for an algorithm that is applied across a pixel area with two rows and three columns. An ending is applied to the name to aid the reader: ‘_2var’ (‘_3var’) stands for two (three) variables, used where the shape of the pixel area does not make it obvious whether an algorithm compares the sum of signals in two or three pixel areas; ‘_outer’ is used for the algorithms that do not incorporate the signal of the central pixel.

6.4.1 Applying non-linear centroiding algorithms: the η algorithm

The 3×3 centre of gravity centroid algorithm has been shown to be biased during the simulation investigation (Section 5.2.3) and algorithms applied across fewer pixels will be even more biased. The centroid bias was shown to be removed when applying the η algorithm to simulated events, but requires a flat field of X-ray events to determine the corrective mapping function f_η. A large enough number of events, with interaction locations distributed approximately equally across the pixel, can be extracted from the photons observed in the 0th order diffraction ring that surrounds the focussed 1st order diffraction X-ray spot.

Events are extracted using the same thresholds calculated for selecting events in the 1st order diffraction X-ray spot (Section 6.3.2): X-ray events are centred around a pixel with maximum signal; the sum of signal in the 3×3 pixel area centred on this pixel must be between the two thresholds extracting only signals of a single X-ray photon; the sum of signal in the 5×5 ring of pixels that surround the 3×3 pixel area must have a signal below a threshold, to exclude events where other events are observed nearby.

The centroid of isolated events always results in a position close to the centre of the pixel (Figure 6.18), therefore they are excluded in the calculation of the corrective mapping function, f_η. Isolated events are defined as events where greater than 90% of the total signal in the 3×3 pixel area is detected in the central pixel (Figure 6.18, Figure 6.19). This threshold level was chosen as a compromise between removing all isolated events, and incorrectly rejecting barely split events. In the frames analysed here (the scan of focussed 1000 eV X-ray photons along a row, in the centre of a pixel), 40 110 single photon events are discovered in the 0th order diffraction ring, 1615 of which are discarded for having a ratio above the isolated event threshold.

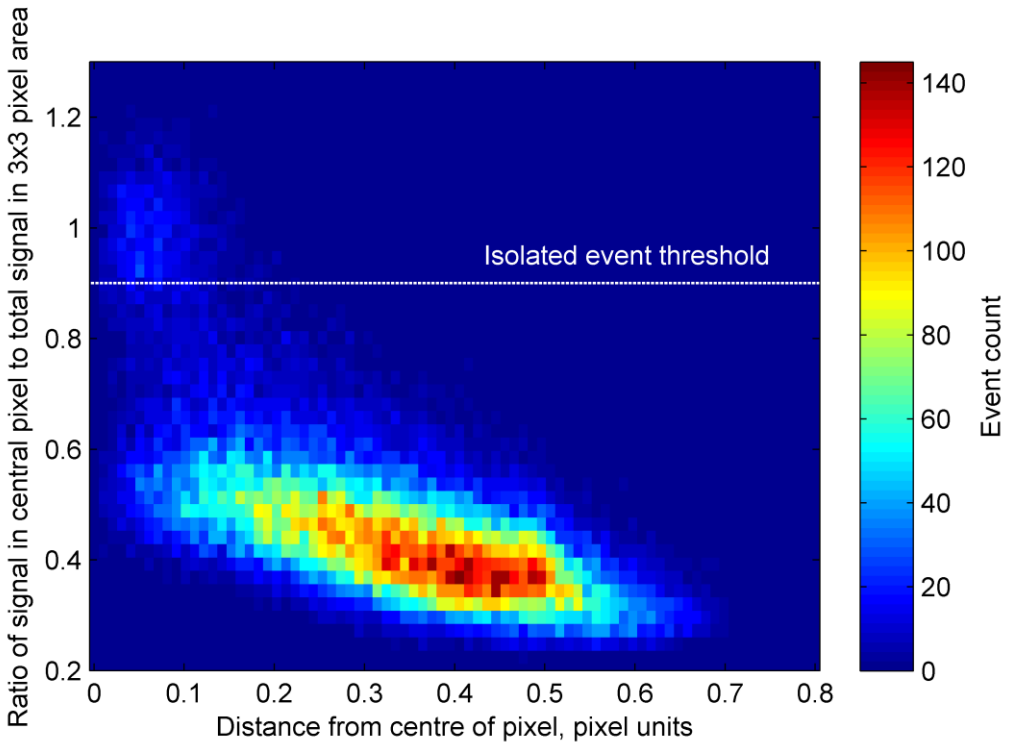

Figure 6.18. The distance of the centroid location from the centre of the pixel for the single photon interaction events selected from the 0th order diffraction ring. The events with a signal ratio above the isolated event threshold are in a separate population from the events with signal more split across the pixels.

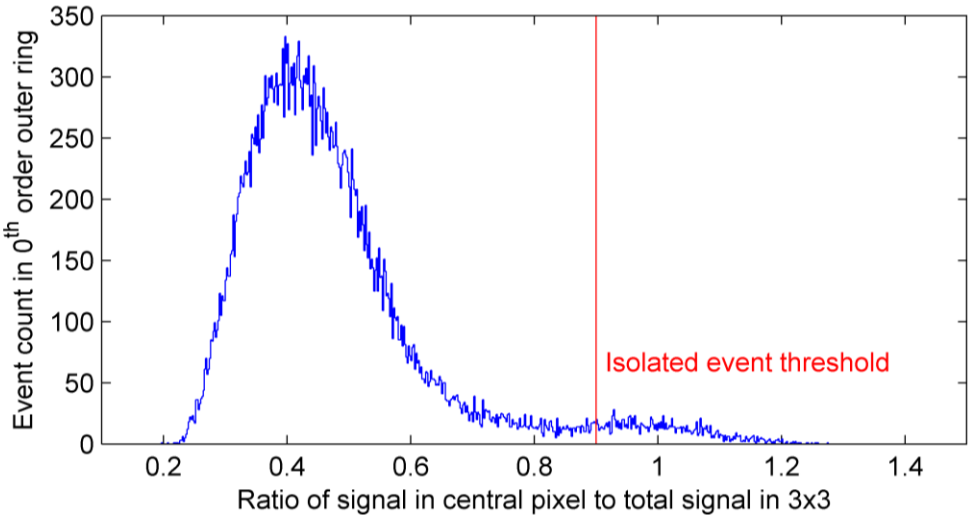

Figure 6.19. The majority of events selected in the 0th order diffraction region have less than 90% of the total signal from the 3×3 pixel area detected in the central pixel. Isolated events are selected using the threshold shown (vertical red line).

The distribution of centroid locations from events discovered in the 0^{th} order diffraction ring is shown in Figure 6.20, along with the average pixel signals, for comparison. More events are discovered in areas where there is a higher flux in the 0^{th} order diffraction ring, which is to be expected. The event locations are shown binned into a single pixel in Figure 6.21. When the isolated events are included, a high density of centroided locations is observed at the centre of the pixel, significantly changing the distribution. Excluding these isolated events shows the true distribution from the flat field illumination expected from centroiding a flat field with the biased 3×3 centre of gravity algorithm.

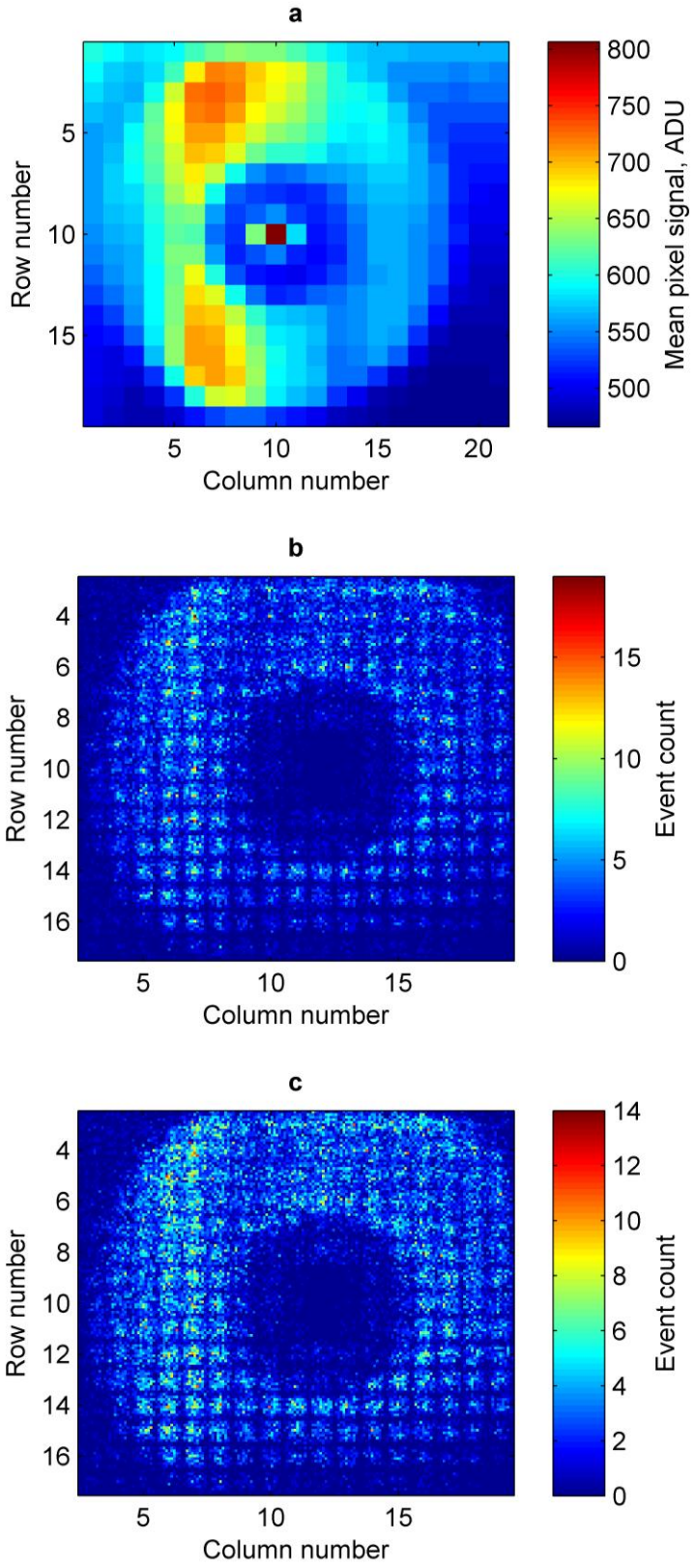

Figure 6.20. ***(a)*** *The pixel signals of the windowed area averaged across all frames during the scanning of the 1st order diffraction spot. The locations of the events selected from the 0th order diffraction ring are determined using the 3×3 centre of gravity centroid algorithm. The distribution of these event locations are shown including* ***(b)*** *and excluding* ***(c)*** *isolated events.*

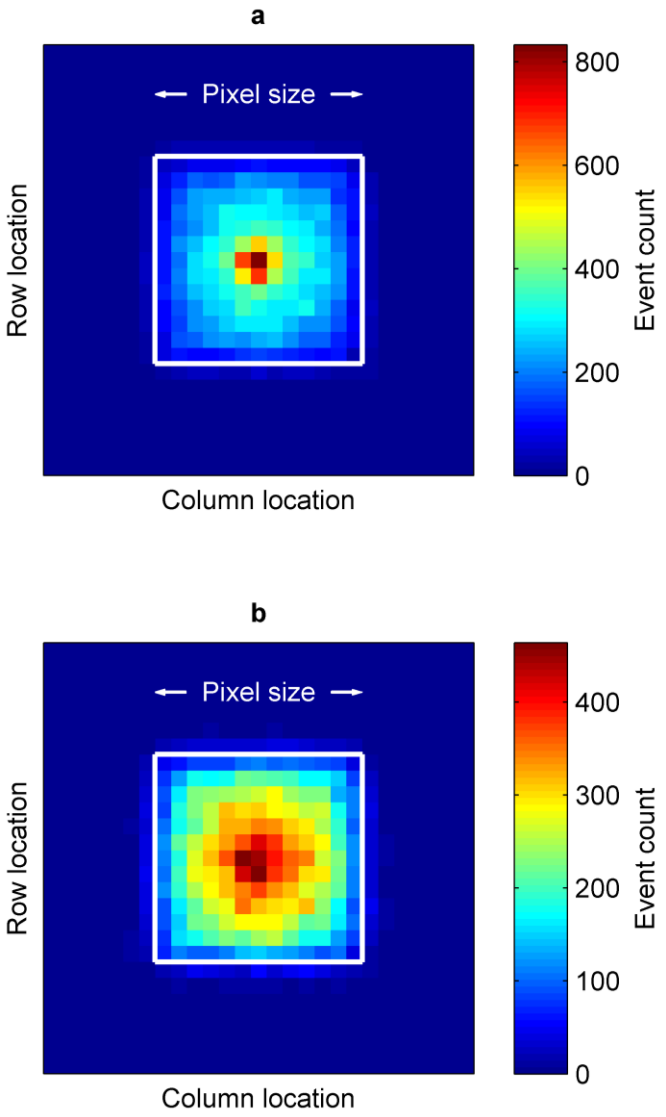

*Figure 6.21. The sub-pixel locations of single 1000 eV photon events observed in the 0th order diffraction ring, calculated using the 3×3 centre of gravity algorithm. The distributions are shown including **(a)** and excluding **(b)** the isolated events, relative to the pixel size and position (white rectangle).*

The corrective mapping functions, f_n, generated from the data for the different algorithms are shown in Figure 6.22. The algorithms that estimate the position using the signals from 3 pixel areas, such as the 3×3 centre of gravity algorithm (cols3x3 and rows3x3) show a correction closest to the unbiased linear case (a straight line from [0, 0] to [1, 1]). The corrective mapping functions are similar for certain algorithms – grouped by colour – and are similar for the same algorithms in both the column and row directions.

However, f_η across the row directions do not pass through [0.5, 0.5] as it does in the column direction, suggesting asymmetry in the distribution of charge between rows, with rows closer to the output node containing a larger amount of signal. This effect could possibly be related to asymmetry in the charge distribution from diffusion in the field-free region to the depletion region, but could also be due to the non-uniform background level observed in Figure 6.20 a. The η function's ability to include and correct for this effect is advantageous over other correction methods, for example the analytical systematic correction described in Section 5.3.1.

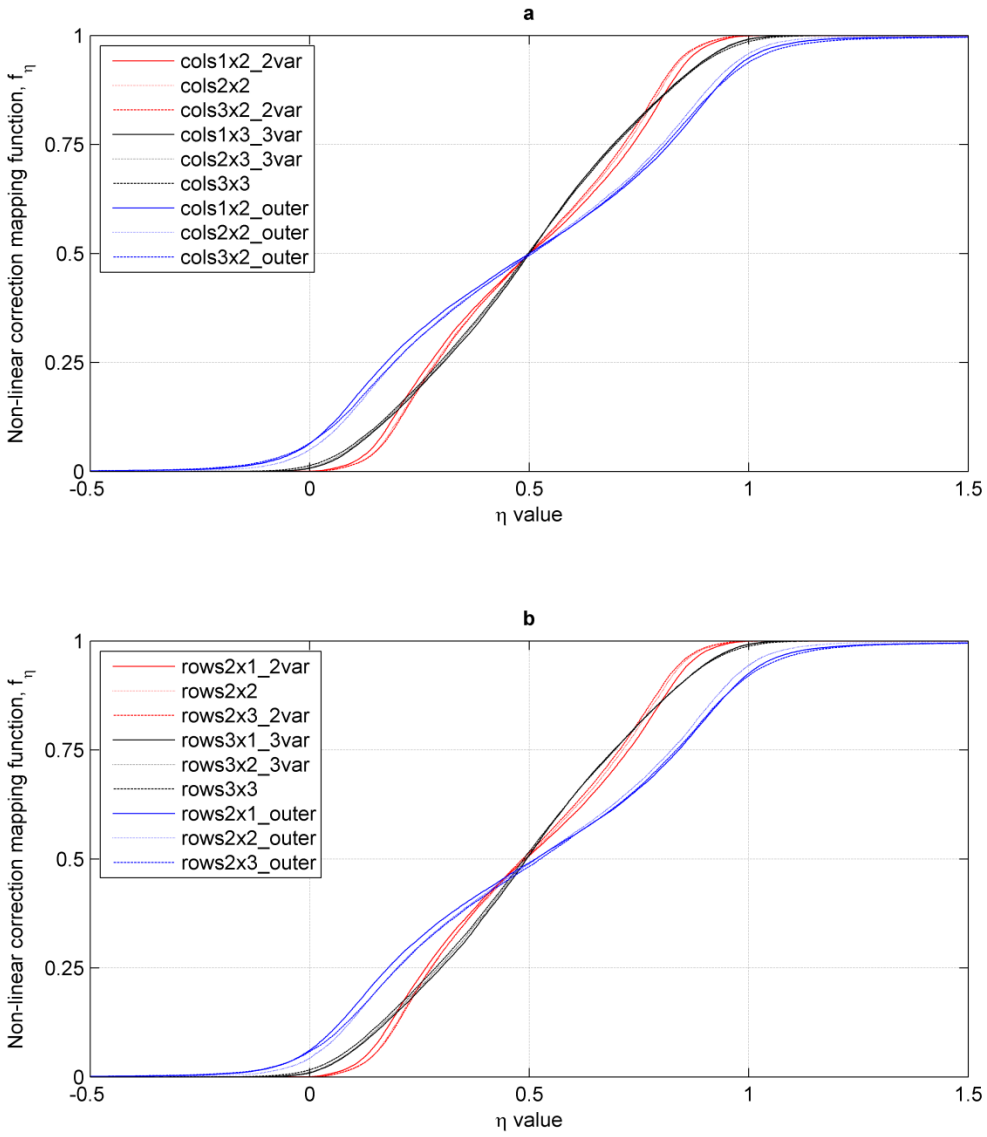

*Figure 6.22. The η algorithm corrective mapping functions for the linear algorithms that estimate the interaction location across the column **(a)** and row **(b)**, i.e. in the* x *direction **(a)** and* y *direction **(b)**.*

6.4.2 Performance of the η correction to a variety of centroid algorithms

The centroid algorithms are applied to the 1000 eV X-ray events observed when an X-ray spot is scanned in 13 positions across columns, in the centre of the row. Between 342 and 396 events were detected per X-ray spot position. The centroid locations across the column are binned into 50 bins per pixel (Figure 6.23) to show the distribution of centroid locations for each centroid algorithm, after applying the η correction. The distributions are fitted by a Gaussian profile, where the mean and spread of the distribution measure the mean centroid location and spatial resolution achieved with the algorithm.

The mean centroid locations, measured before and after the η correction is applied, are shown as a function of the relative positions of the focussed X-ray spot positions, measured by the translational stage positions, in Figure 6.24. A comparable characteristic bias can be seen before correction for the groups of similar centroid algorithms i.e. the '2 variable', '3 variable' and 'outer' algorithms, as expected from their similar corrective mapping functions in Figure 6.22.

The relationship between the stage position and the mean centroid position is virtually linear after the η correction has been applied for most of the algorithms tested. However the correction of the 'outer' algorithm has not performed as well: although it has improved, the relationship still deviates from a straight line more than the other algorithms when the interaction position is approximately 1 µm from the edge of the pixel. The bad performance of the correction at this sub-pixel location explains the division of the centroid location distributions obtained using the 'outer' algorithms at Position 3 in Figure 6.23. The removal of the majority systematic error from the '2 variable' and '3 variable' centroid algorithms is a positive result for these algorithms when used with the η correction procedure.

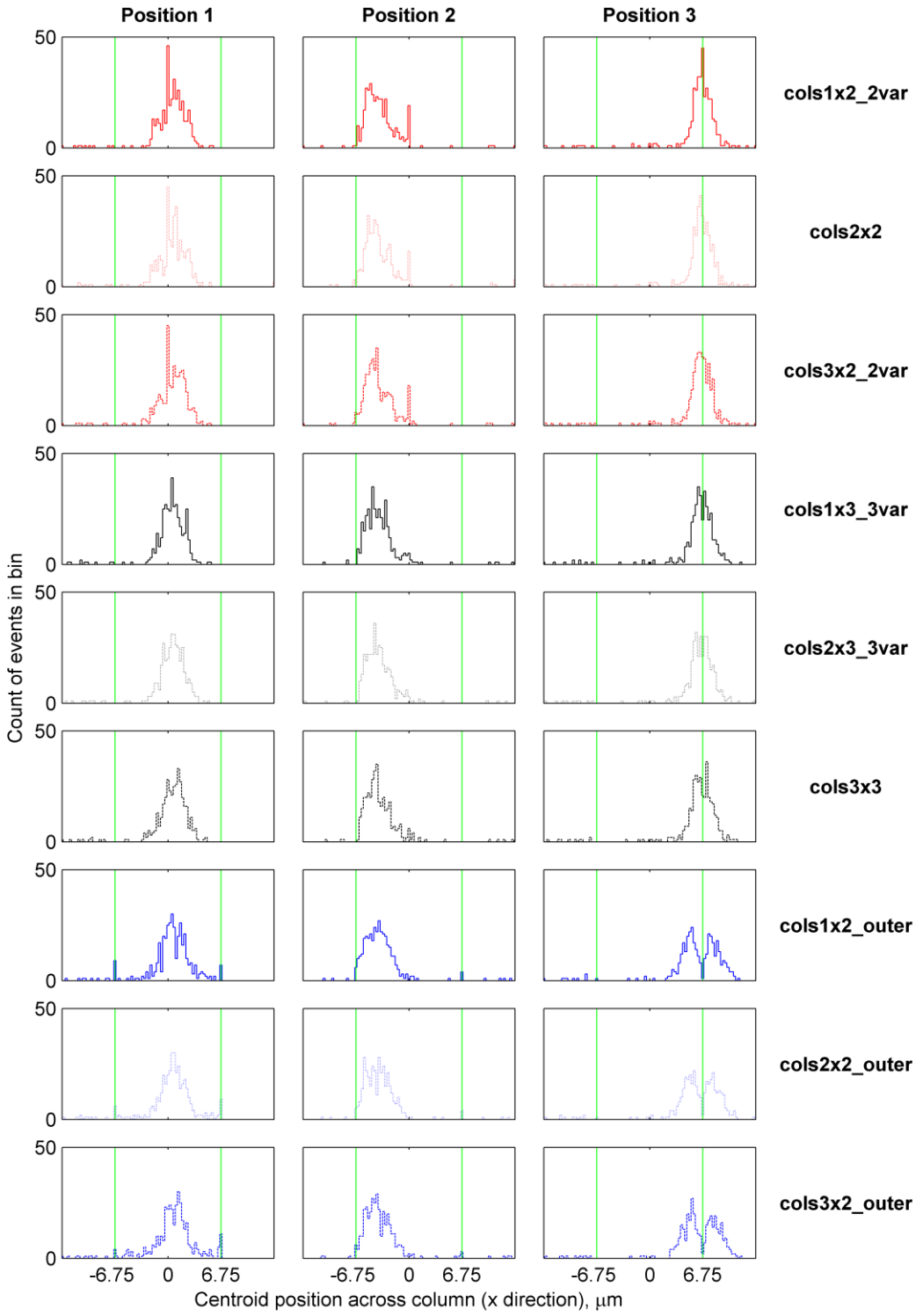

Figure 6.23. The distribution of centroid locations for 1000 eV energy photon events, captured when the X-ray spot was focussed at 3 example positions: Position 1 is close to the centre of the pixel; and Position 2 is between the edge and centre of the pixel; Position 3 is close to the edge of the pixel. Pixel boundaries are shown by the green vertical lines and edge effects, where locations are biased away from the pixel boundaries, are observed most in position 3 for algorithms 'cols2x2_outer' and 'cols3x2_outer'.

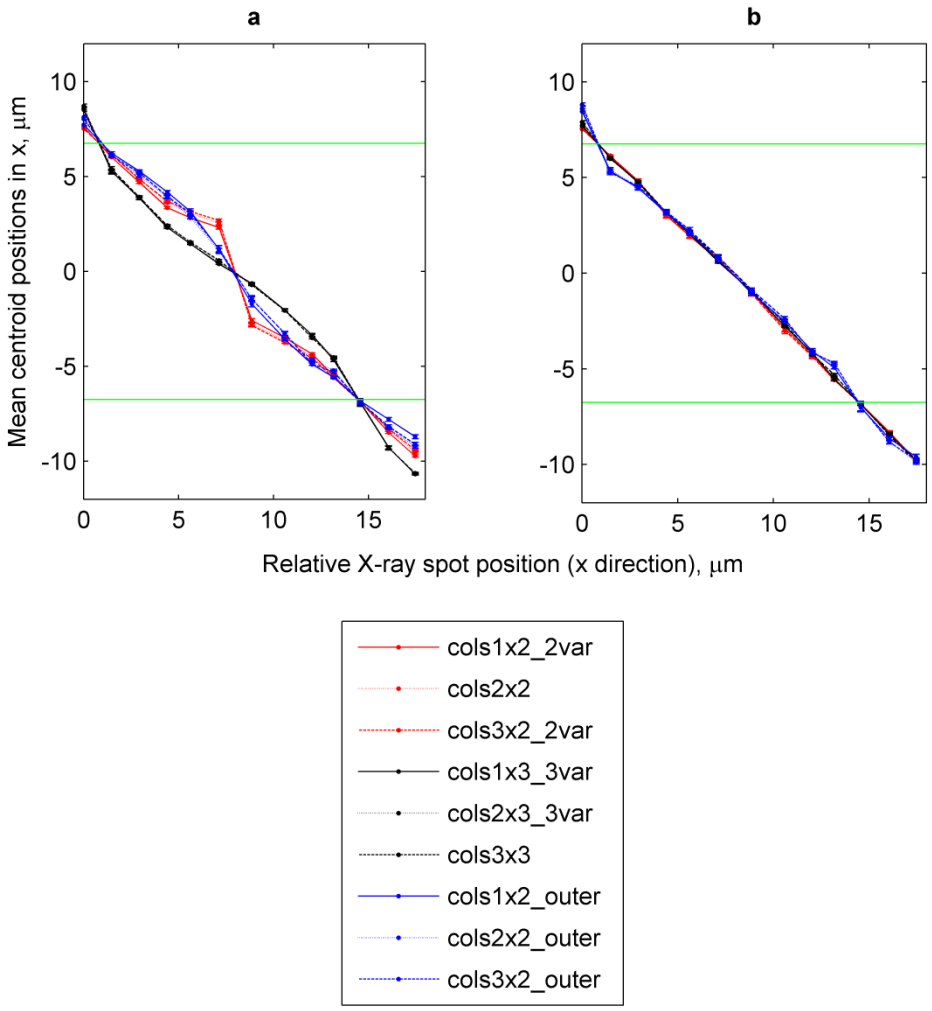

*Figure 6.24. The mean centroid location measured using a range of centroid algorithms **(a)** before, and **(b)** after, η correction. The pixel boundaries are shown by the green horizontal lines, and errors from the 95% confidence limit of the fit procedure are shown, but are too small to be visible on most data points.*

The performance of the algorithms is measured by the accuracy that the original interaction location can be determined. The spread of the centroid locations, determined by the standard deviation of the Gaussian profile fit, is converted into a FWHM measurement at each focussing position and for each algorithm (Figure 6.25). Before the systematic error has been removed, the '2 variable' algorithms may be appear to perform best. However, this is a characteristic of the strong systematic bias that effectively compresses the centroid locations into a smaller area. After η correction, the 'outer' algorithms perform worst across most of the pixel. At the relative X-ray spot position of 14.6 µm (Position 3 in Figure 6.23), where the interaction location is at the edge

of the pixel, the ‘outer’ algorithms result in a particularly bad resolution. In the Figure 6.23, the reason for this can be seen as, despite the attempt at correction, the distribution is split in two and biased away from the pixel edge.

The ‘2 variable’ and ‘3 variable’ algorithms perform similarly across the pixel. However, although the difference is small, the ‘2 variable’ algorithms show a better resolution achieved at locations close to the pixel boundaries and the ‘3 variable’ algorithms achieve a better resolution at locations closer to the centre of the pixel. Within each group of the algorithms, where the pixel areas compared consist of 1, 2 or 3 pixels, the spatial resolutions differ by less than the 0.27 µm bin width used in the centroid location distributions, and so can be considered to be within the errors of the fitting. A larger number of interaction events are required if the bin widths are to be reduced whilst maintaining a significant number of events per bin.

These resolution measurements include unknown contributions from the size of the X-ray spot, and any vibrations or drift that occurred during the capture of frames, which is estimated to be up to 2 µm. Therefore, the performance of the algorithms can be compared but only worst-case measurements can be reported.

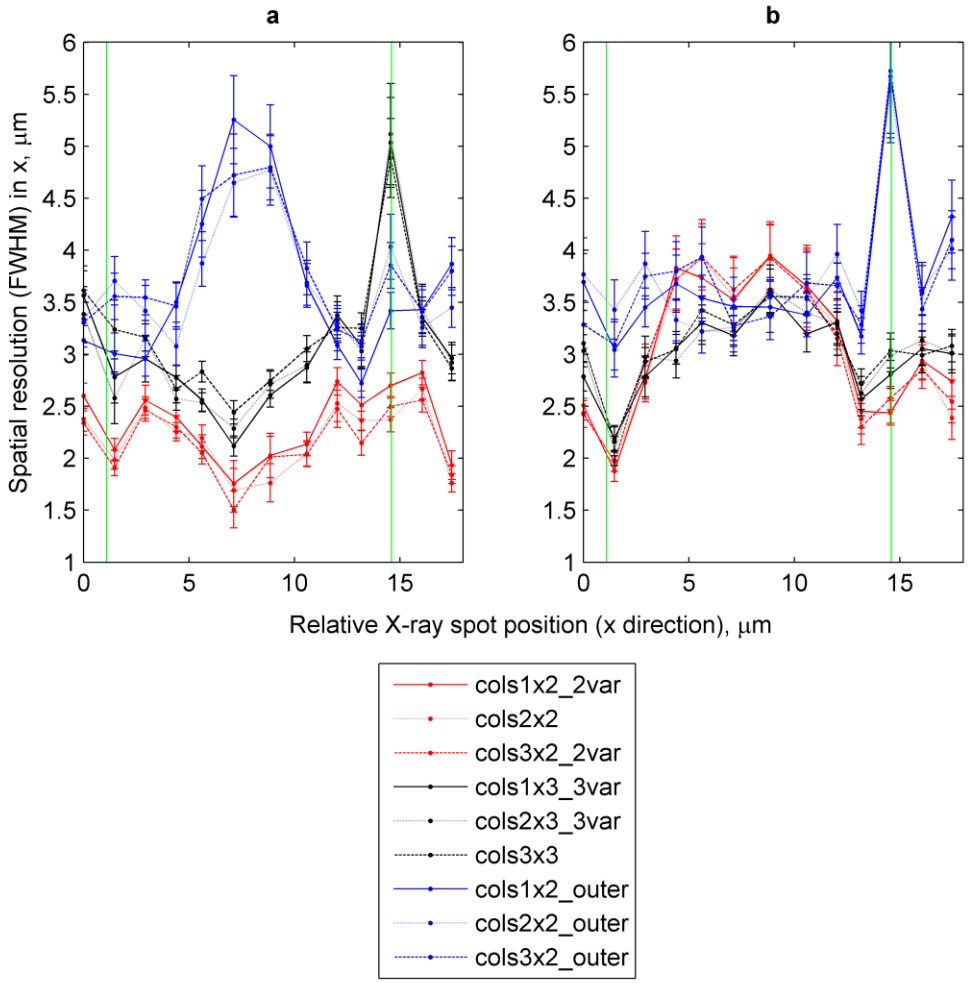

*Figure 6.25. The spatial resolution achieved at each position that the 1000 eV X-ray spot was focussed is shown for the algorithms **(a)** before and **(b)** after the η correction has been applied to remove the systematic error of the algorithms. The vertical green lines show the approximate pixel boundaries.*

6.4.3 Performance at other energies

The X-ray spot was scanned across the pixel, with the X-ray energy tuned to 530 eV, 680 eV and 850 eV, as well as the 1000 eV already shown. The images recorded were processed as described in Section 6.3.2 to extract single photon events that interacted in a sub-pixel area for each position that the 1st order diffracted X-rays was focussed and η correction functions were obtained from the events in the surrounding 0th order diffraction ring, to correct for bias in the centroid locations.

The mean η corrected centroid locations show the sub-pixel positions that the X-rays in the 1st order diffraction spot were focussed (Figure 6.26). At 530 eV, 680 eV and 1000 eV the spot was

scanned across the columns, in the centre of a row. The scan direction was the same for 850 eV, but the spot was located much closer to the edge of the pixel, towards the boundary between rows.

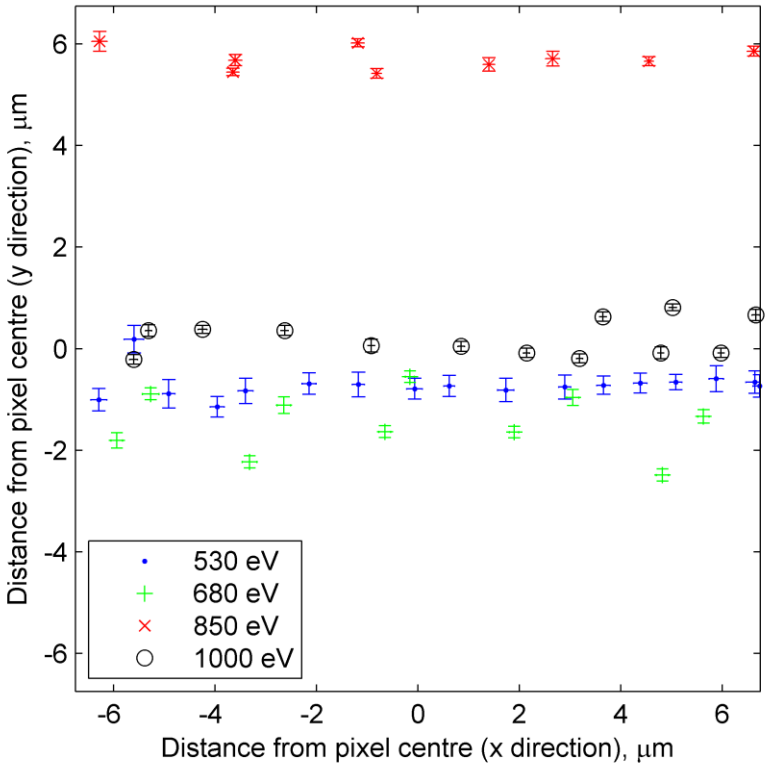

Figure 6.26. The mean centroid location for each sub-pixel position that the X-ray spot was focussed, obtained using the corrected 3×3 centre of gravity algorithm. The locations have been binned into the area of 1 pixel. Error bars shown in both dimensions are the 95% confidence limits of the parameters from the fitting procedure.

The performance of the centroid algorithms incorporating the η correction can be compared for the four energies (Figure 6.27), where the centroid algorithms are applied across the columns to result in a location in the *x* dimension. The measurements are plotted as a function of the mean centroid position across the column, binned into a single pixel width. In general the spatial resolution is worse at lower energies, due to the lower signal to noise ratio. The 'outer' algorithms perform worst at all energies, whilst the '2 variable' and '3 variable' algorithms have similar performance distributions across the pixel. The resolution tends to be degraded at locations where the sharing process results in the pixels used in the centroid algorithm containing lower levels of signal, such as the centre of the pixel using the '2 variable' algorithm.

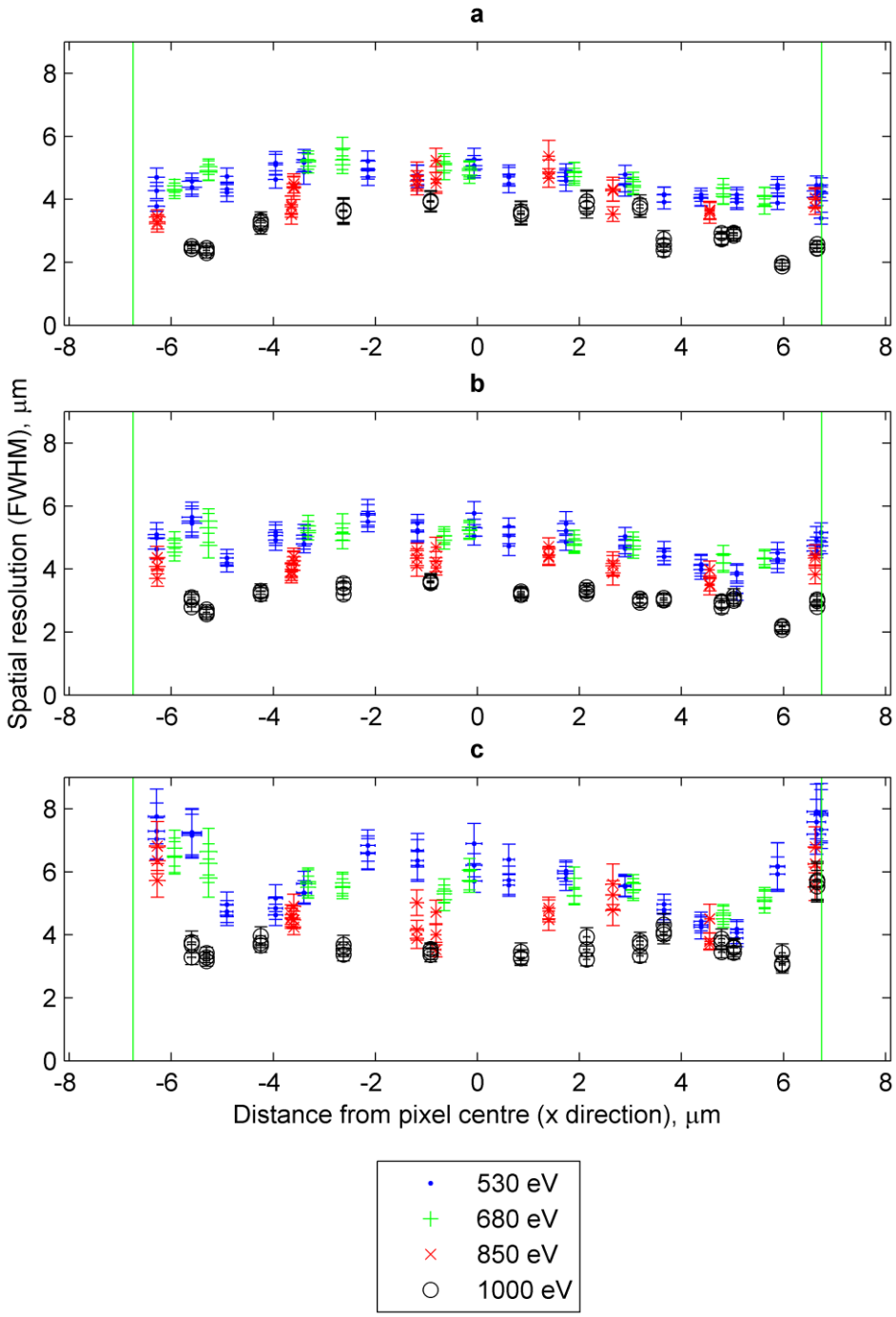

Figure 6.27. The spatial resolution achieved with the centroid algorithms, with respect to the mean centroid location with the pixel: ***(a)*** *'2 variable' algorithms;* ***(b)*** *'3 variable' algorithms; and* ***(c)*** *'outer' algorithms. The pixel boundaries are shown by the vertical green lines and error bars show the 95% confidence limits from the fitting procedure.*

To determine an average performance across the centre and outer halves of the pixel (in the dimension the centroid algorithms are applied), the spatial resolutions are averaged across the sub-pixel locations within and beyond a quarter of the pixel width from the centre of the pixel, as shown in Figure 6.28. The 'outer' algorithms are not shown due to their comparably poor performance across all the locations and energies. It should be noted that the 850 eV data set, where the X-ray interaction locations in the *y* direction were close to the boundary between two pixel rows, may not be directly comparable with the other energy data sets where the interaction locations in the y-direction were close to the centre of a row.

For each energy and pixel half, the best performing algorithm type can be identified from Figure 6.28. At the pixel centres, the '2 variable' algorithms perform best at 530 eV and 680 eV but when the energy is increased to 1000 eV, the '3 variable' algorithm results in the best spatial resolution. Towards the edges of the pixel, the '2 variable' algorithms result in the best spatial resolution at all energies, except for 850 eV, where there is no significant difference between the '2 variable' and '3 variable' algorithms.

At 1000 eV, the average resolutions achieved at each area of the pixel are well separated for the algorithms. The best case is for interactions at the edge of the pixel that are centroided using the '2 variable' algorithms. This is an ideal situation for centroiding since the signal is expected to be well split for the majority of events between few pixels, which are used to calculate the centroid. The '3 variable' algorithms perform worse for interactions at the edge of the pixel as the additional pixels are further from the interaction position and have low signal to noise ratios. For interactions closer to the centre of the pixel events are less split and more likely to be isolated so centroiding generally becomes less accurate. The additional pixels in the '3 variable' algorithms contain higher levels of signal useful to the calculation, so their performance is better than the '2 variable' algorithms.

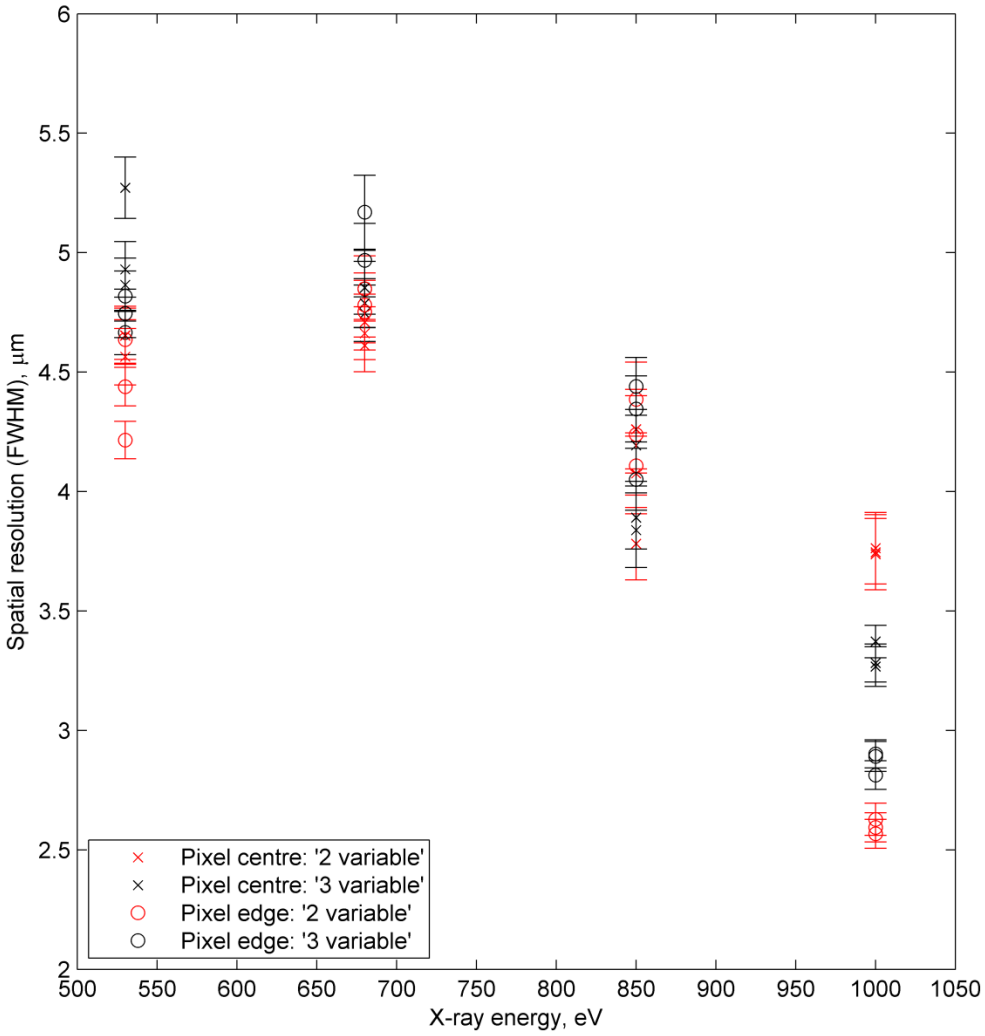

Figure 6.28. Average performance of the '2 variable' and '3 variable' centroid algorithms applied across the rows, for interactions in the central and outer halves of the pixel. Error bars show the 95% confidence limits propagated from the parameter fitting.

6.4.4 Summary of spatial resolution measurements with the CCD42-10

In the last two sections, the collection and reduction of the data during campaign 2 at PolLux has been presented. A typical 1000 eV X-ray event observed in the CCD42-10 consists of 1 to 4 pixels with a signal level that is four or five standard deviations above the background level, so nine centroid algorithms have been described that calculate the centroid position from the pixel signals within a 3×3 pixel area.

The η correction function for these nine centre of gravity style centroid algorithms have been determined for 530 eV, 680 eV, 850 eV and 1000 eV photons from events recorded in the 0^{th} order diffraction ring that are not defined as isolated. Using the correction, the spatial resolution achieved at each sub-pixel location in a 1D scan across the pixel has been presented for each

energy and centroid algorithm. The performance of the corrected algorithms is shown in Figure 6.25 b for 1000 eV, and compared across the energy range and sub-pixel locations in Figure 6.27. The energy dependent performance of the '2 variable' and '3 variable' style algorithms is shown in Figure 6.28, with the best measurements given in Table 6.3.

Table 6.3. The best spatial resolution measurements at each photon energy and pixel area, as seen in Figure 6.28, are summarised here alongside the measured background noise levels.

Energy, eV	**Best spatial resolution measurement, µm (algorithm)**		**Total background noise, electrons rms**	**Signal to background noise ratio**
	Pixel centre	**Pixel edge**		
530	4.56±0.12 (2x2)	4.22±0.08 (1x2_2var)	6.72±0.07	21.6
680	4.61±0.11 (1x2_2var)	4.75±0.13 (2x2)	6.64±0.13	28.1
850	3.78±0.15 (2x2)	4.05±0.13 (2x3_3var)	6.37±0.12	36.6
1000	3.27±0.06 (1x3_3var)	2.57±0.06 (2x2)	6.36±0.09	43.1

The experimental measurements are compared to the resolutions predicted by the simulations described in Chapter 5 in Figure 6.29. The experimentally measured results agree well with the trend predicted by the simulation, and no experimental measurements are better than simulations. The differences between the experimental and simulated resolutions could be due to the assumptions in the simulation being inaccurate, such as the constant depletion depth, or the fact the experimental data has been averaged across a group of 1D sub-pixel locations rather than interactions spread equally across the pixel area.

The non-zero size of the focussed X-ray spot also contributes to the experimental resolution measurement, but the best resolutions achieved are better than the 5 µm (FWHM) goal set for an improved detector at SAXES (using a detector at 20° to incident photons). Therefore centroid algorithms will be applied to SAXES images in Section 6.8.

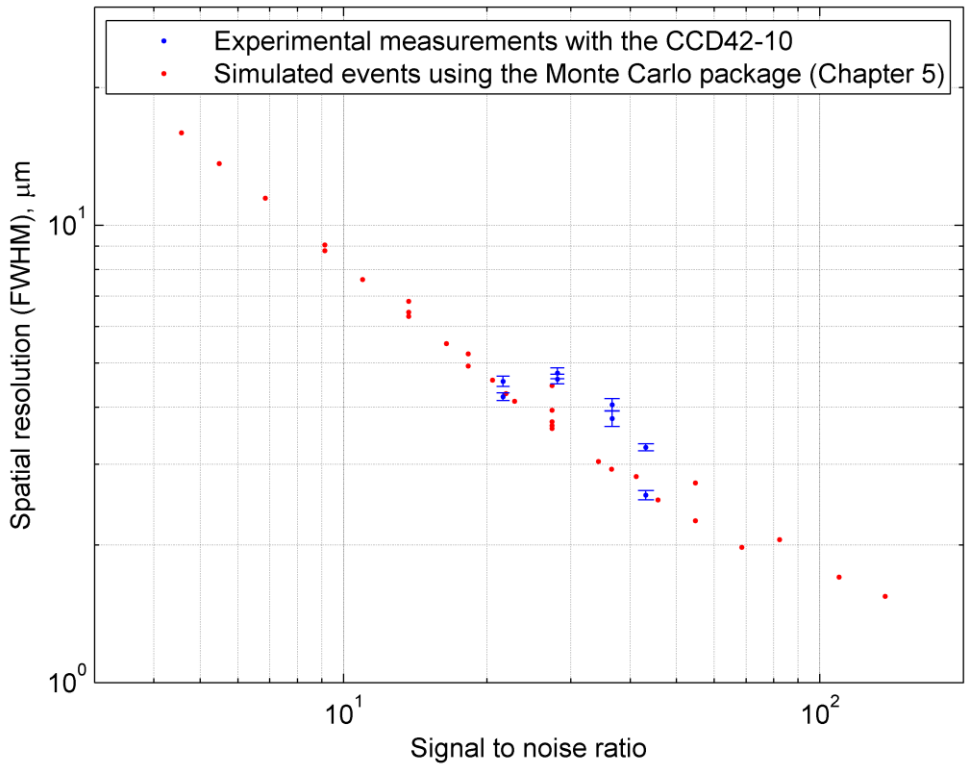

Figure 6.29. The best spatial resolution results experimentally measured at each photon energy and sub-pixel region are shown against the resolutions predicted using the corrected 3×3 centre of gravity algorithm applied to events simulated in Chapter 5 (Figure 5.18).

6.5 Charge cloud shape

Centroiding takes advantage of the fact that the majority of X-ray interactions generate charge that is collected in a number of adjacent pixels. As discussed in Chapter 4, the sharing of the charge between pixels is dominated by the diffusion of charge in the field-free region. An analytical solution to the diffusion equation [66] was shown to agree best with X-ray events observed with the CCD42-10 during campaign 2 (Chapter 4) but in the following section, methods to measure the average charge cloud shape or width using the experimental data are presented.

6.5.1 Methods for determining the charge cloud shape experimentally

Two methods were presented by Hiraga *et al*. [67] and Yoshita *et al*. [104] to measure the average charge cloud size and shape formed from X-ray interactions detected in a CCD, using a large number of single photon events with known sub-pixel interaction location. The interaction location of events was determined using a setup called the mesh experiment, where a grid of small holes is made in a material opaque to the X-rays and placed in front of the sensor. Upon

illumination with an approximately parallel beam of X-rays, the regularity of the grid superimposed upon the pixels allows the sub-pixel location for events to be determined, within a few microns.

The method presented by Hiraga *et al*. [67] used the average event observed from interactions in a grid of sub-pixel locations to construct a map of the average sampled pixel signal, as a function of interaction position. The authors showed that the charge cloud shape could be found by differentiating the sampled pixel signals map in both the row and column dimensions.

Yoshita *et al*. [104] assumed the charge cloud was a certain shape – a top-hat or a Gaussian profile – but with unknown width. The signal in two adjacent pixels of observed X-ray events were used to calculate uncorrected centre of gravity centroid positions to compare with the known interaction locations. The resulting distribution was fitted with the function expected from the behaviour of the assumed charge cloud shape by varying the width.

6.5.2 Determining the charge cloud shape using the differential method

Firstly, the differential method shall be explained. The average pixel output for interactions occurring at a location in the CCD plane is equal to an integral across the pixel area of the average charge cloud from the events. The pixel integrates across a different area of the charge cloud, therefore as the interaction location moves across the detection plane, the integral of the charge cloud can be mapped out using a grid of sub-pixel interaction locations. For example, if the charge cloud is much smaller than the pixel size, when the interaction occurs in the centre of a pixel all electrons would be detected in that pixel. If the interaction shifts towards the pixel edge, the number of electrons would decrease until, on the boundary between two pixels, each pixel would be expected to detect 50% of the signal.

For a given sub-pixel position that the focussed X-ray spot is incident, the interaction locations can be written as $H(x, y)$. The average pixel output of the n^{th} pixel can then be written as *Equation 6.1*, where the average charge cloud shape when the beam spot is focussed at (X_{in}, Y_{in}) is described by f, and $f \otimes H$ represents the convolution between f and H [67].

$$D_n(X_{in}, Y_{in}) = \int_{x_n}^{x_{n+1}} dx \int_{y_n}^{y_{n+1}} dy\, f \otimes H(x - X_{in}, y - Y_{in}) \qquad \textit{Equation 6.1}$$

Differentiating $D_n(X_{in}, Y_{in})$ yields a distribution with four occurrences of the averaged charge cloud shape convoluted with the X-ray distribution from the focussed spot.

$$\frac{\partial^2 D_n(X_{in},Y_{in})}{\partial X_{in}\partial Y_{in}} = f \otimes H(X_{n+1}-X_{in},Y_{n+1}-Y_{in}) + f \otimes H(X_n-X_{in},Y_n-Y_{in}) \\ -f \otimes H(X_{n+1}-X_{in},Y_n-Y_{in}) - f \otimes H(X_n-X_{in},Y_n-Y_{in})$$

Equation 6.2

When the average charge cloud is not large relative to the pixel size, the occurrences are separable and can be combined to present the average charge cloud distribution [67]. For the 1D scans described in this chapter, the interaction locations are aligned in a strip across the pixel in the *x* direction. In this case, the charge cloud binned along the *y* direction can be measured. *Equation 6.2* can be adapted to *Equation 6.3* in this 1D case.

$$\frac{\partial D_n(X_{in})}{\partial X_{in}} = f \otimes H(X_{n+1}-X_{in}) - f \otimes H(X_n-X_{in}) \qquad \textit{Equation 6.3}$$

If the interaction locations were at the same location in the x-y plane, $H(x,y)$ could be approximated to a delta function and therefore *Equation 6.3* would simplify to *Equation 6.4*.

$$\frac{\partial D_n(X_{in})}{\partial X_{in}} = f(X_{n+1}-X_{in}) - f(X_n-X_{in}) \qquad \textit{Equation 6.4}$$

6.5.3 Estimating the charge cloud width through assuming a certain shape

The second method to measure the charge cloud shape was presented by Yoshita *et al*. [104] and uses the systematic error in centre of gravity centroiding to infer back the shape of the charge cloud. Firstly, assume the charge cloud shape as detected by the pixels, f, can be written as a product of its two dimensions $f(x,y) = S(\sigma_x,x)S(\sigma_y,y)$, and that the integral over all of f has been normalised to 1. Next, assume the charge cloud is entirely collected in two pixels, n and $n+1$ which have boundaries along $[x_{n-1},x_n]$ and $[x_n,x_{n+1}]$. The signal detected in pixel n from an interaction at $X_{in}$is the following.

$$D_n(X_{in}) = \int_{x_{n-1}}^{x_n} dx\, S(\sigma_x,x) \qquad \textit{Equation 6.5}$$

A similar expression can be written for pixel $n+1$. A centre of gravity centroid calculation applied across these two areas results in a centroid location X_{CG} that is given in *Equation 6.6*, and simplifies to *Equation 6.7* by using *Equation 6.5*.

$$X_{CG}(X_{in}) = D_n(X_{in})x_n + D_{n+1}(X_{in})x_{n+1} \qquad \textit{Equation 6.6}$$

$$X_{CG}(X_{in}) = (x_{n+1} - x_n)\left(\frac{1}{2} - \int_{-\infty}^{-X_{in}} dx\, S(\sigma_x, x)\right) \qquad \textit{Equation 6.7}$$

Yoshita *et al*. [67] then assumed the charge cloud was either a Gaussian or top-hat profile and therefore could fit their experimental data using *Equation 6.7* to determine the best fitting widths for these given charge cloud shapes.

6.5.4 The charge cloud shape in the CCD42-10: differential method

The pixel scans of the CCD42-10 are analysed to measure the observed charge cloud, as a function of photon energy. Both methods of measuring the charge cloud will be applied and then compared in Section 6.5.6.

The average pixel signals surrounding 1000 eV photon interaction events are determined, and shown as a function of the interaction location relative to the central pixel location in Figure 6.30 a. The pixel signal is greatest when the interaction location coincides with the location of the central pixel (where the pixel position is in approximately the location shown by the rectangular box). By summing the signal in the central three rows, the charge cloud sampled by the pixels is binned into 1D (Figure 6.30 b). The differential of this distribution (Figure 6.30 c) shows positive (blue) and negative (green) peaks that are the charge cloud shape convoluted with the beam shape, $f \otimes H$. The negative and positive peaks are overlaid and fitted with Gaussian profiles in Figure 6.30 d. Their shape appears Gaussian-like, with the extended wings expected from the simulation work presented in Chapter 4. A similar analysis has been repeated to measure the charge cloud shape for the 850 eV (Figure 6.31), 680 eV (Figure 6.32) and 530 eV (Figure 6.33) data sets. The FWHM of the profile fits are shown in Figure 6.36 and discussed in Section 6.5.6.

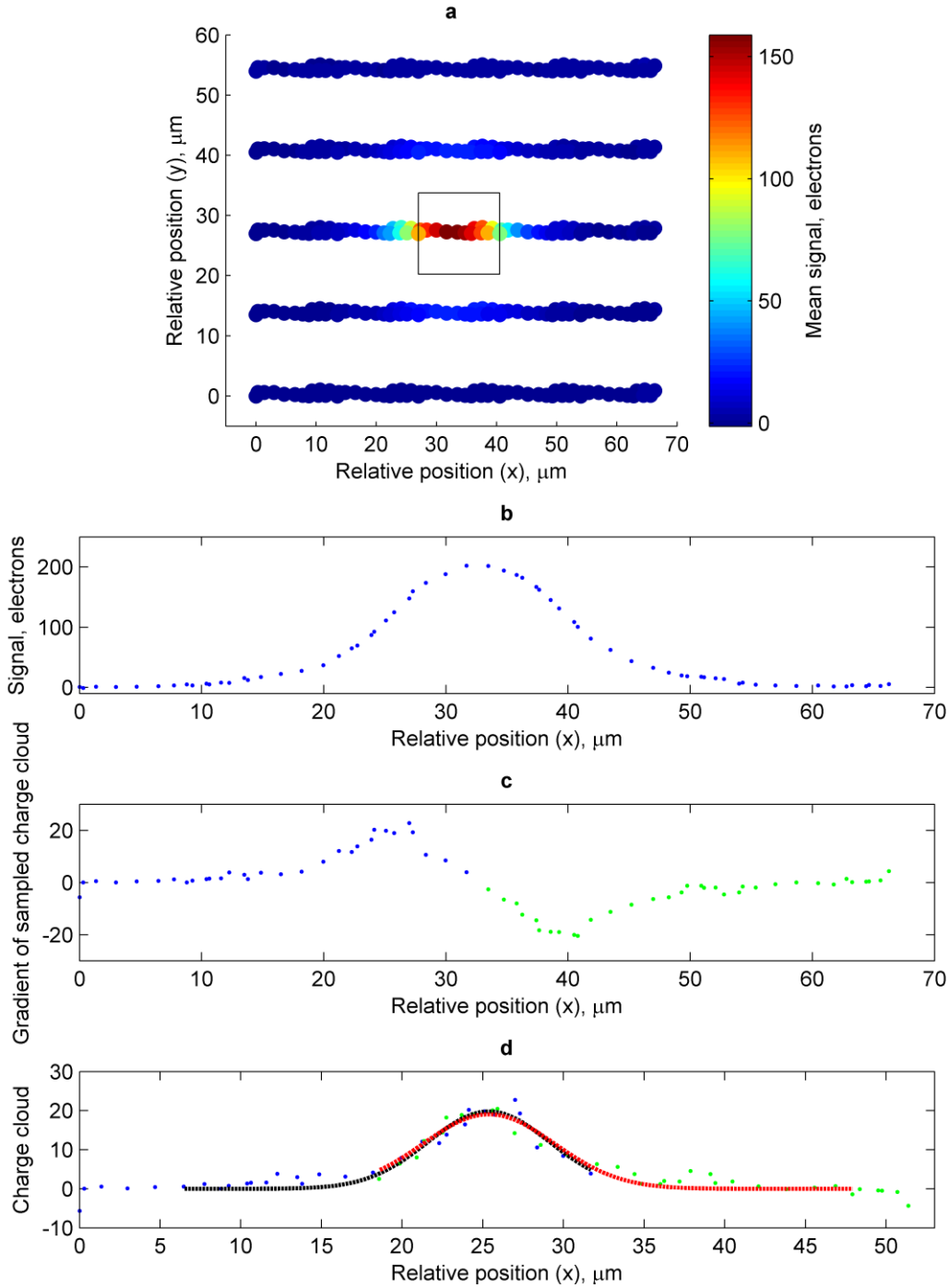

Figure 6.30. ***(a)*** *The mean signal in each pixel surrounding a single photon interaction event is averaged for each sub-pixel position of the focussed 1000 eV X-ray spot scan. The average signals for the 5×5 pixel area are shown in their locations relative to the interaction position, with the pixel size shown for reference.* ***(b)*** *The signal from the central three rows is summed to show the average total signal detected in these rows relative to the interaction position.* ***(c)*** *The differential of (b) results in a positive (blue) and negative (green) occurrence of the charge cloud shape.* ***(d)*** *The charge cloud shapes are overlaid and fitted with Gaussian profiles (black and red dashed lines) to measure their width.*

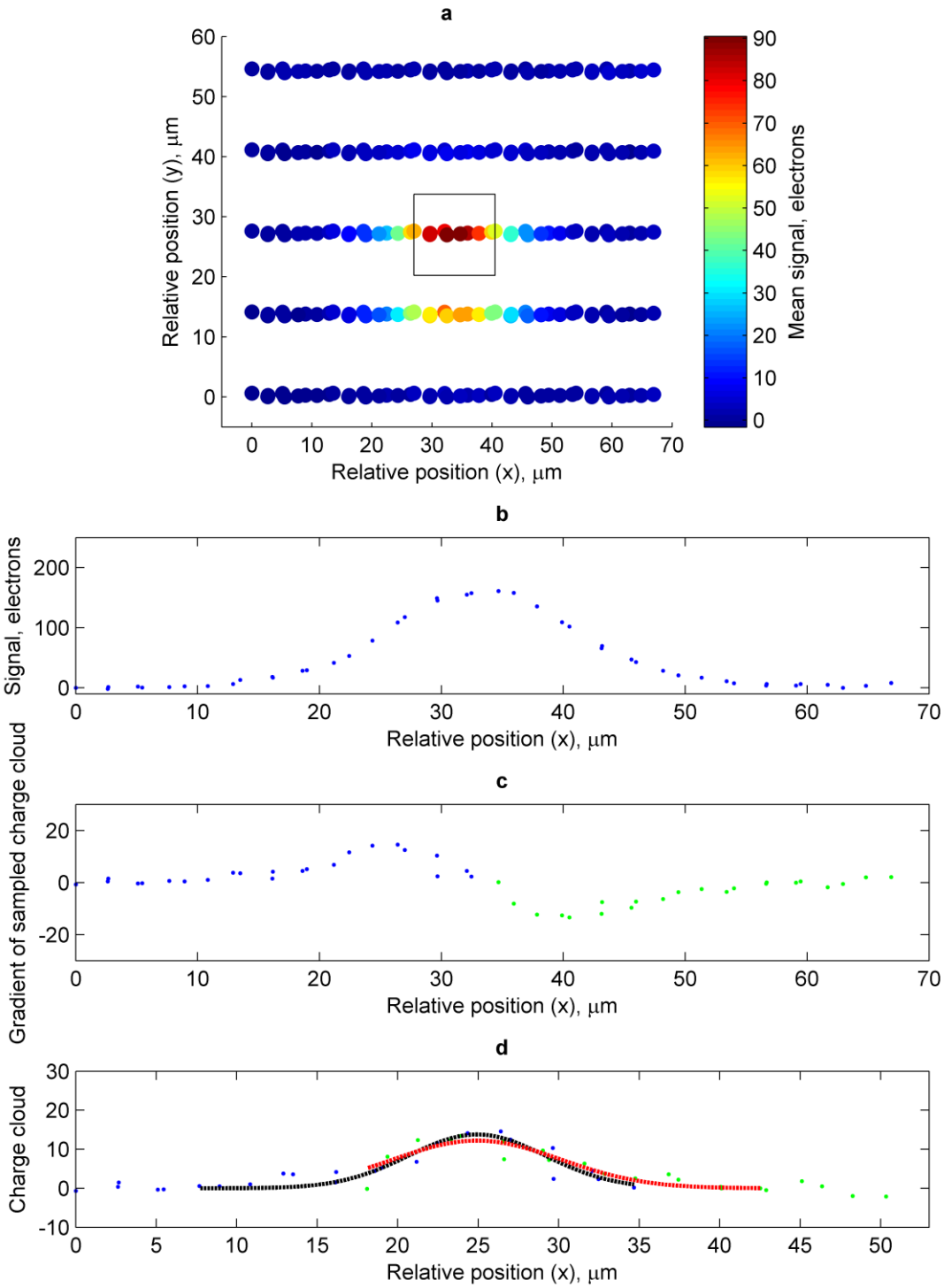

Figure 6.31. As Figure 6.30, for 850 eV photons.

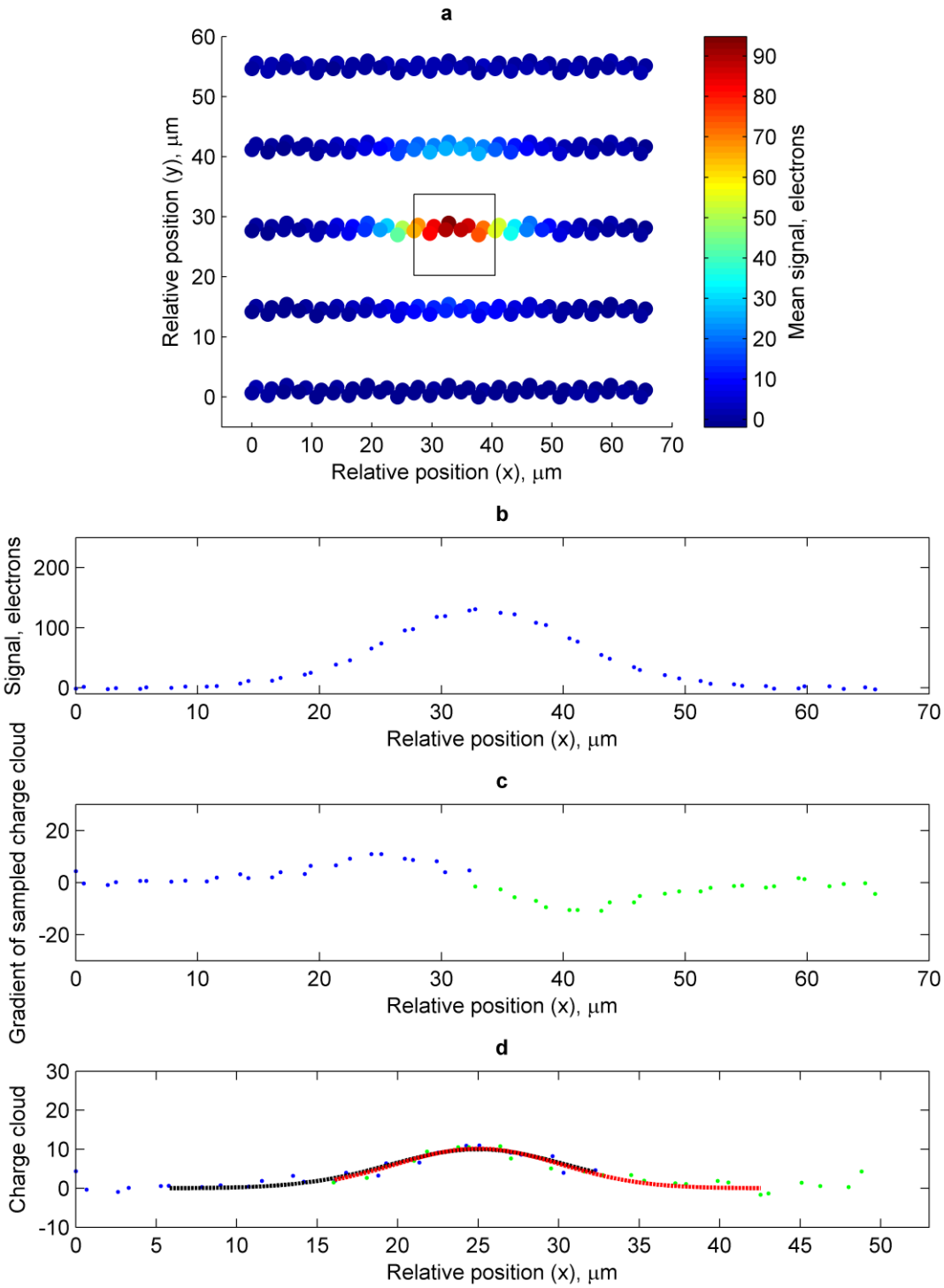

Figure 6.32. As Figure 6.30, for 680 eV photons.

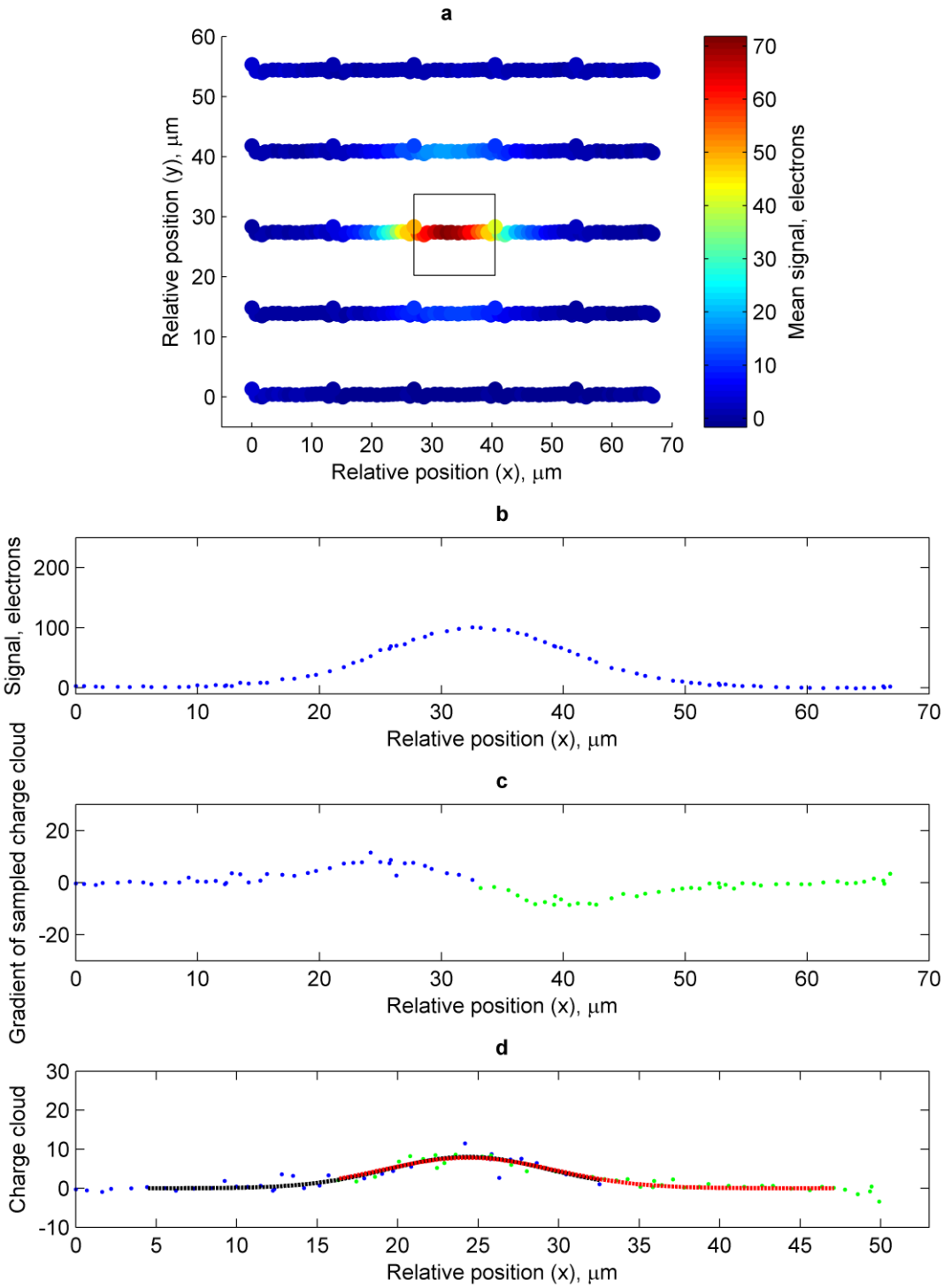

Figure 6.33. As Figure 6.30, for 530 eV photons.

6.5.5 The charge cloud shape measured using the systematic error

The method of measuring the charge cloud width by using *Equation 6.7* requires the centre of gravity calculation to be applied to two areas within which all the event signal is collected. To match the approach of Yoshita *et al.*, the areas are each chosen to be 3 pixels high and 1 pixel wide meaning the centroid locations X_{CG} were determined using the uncorrected '2 variable'

algorithm named 'cols3x2_2var'. The centroid locations have been converted to units of µm, and offset such that the origin is aligned at the pixel edge. The photon interaction positions, X_{in}, are the relative translational stage positions, which have been offset such that the origin is approximately aligned with the edge of the pixel.

To display the centroid locations $X_{CG}(X_{in})$ effectively, 2D histograms have been produced (Figure 6.34). A Gaussian and a top-hat shape have been fitted as the charge cloud shape, where $S(\sigma_x, x)$ is defined by *Equation 6.8* and *Equation 6.9* respectively.

Gaussian: $$S(\sigma_x, x) = \frac{1}{\sqrt{2\pi}\sigma_x} \exp\left(-\frac{X^2}{2\sigma_x^2}\right) \qquad \textit{Equation 6.8}$$

Top-hat: $$S(\sigma_x, x) = \begin{cases} \frac{1}{2\sqrt{3}\sigma_x}, & (|X| < \sqrt{3}\sigma_x) \\ 0, & (|X| > \sqrt{3}\sigma_x) \end{cases} \qquad \textit{Equation 6.9}$$

The least square residual fits of the distributions using *Equation 6.7* and varying σ_x, are shown in Figure 6.34. The fits do not appear to agree with the distributions well, and resulting charge cloud widths (σ_x) are significantly larger than those measured using the differential method in the previous section, Figure 6.36. The most probable reason for this is that the pixel area over which the centroid is calculated does not contain all the signal, which is assumed by the model.

To increase the area, the method has been adapted to operate across a 3×3 pixel area using the 'cols3x3' algorithm. The resulting distributions are shown in Figure 6.35 and fitted with the expected function that assumes a Gaussian profile charge cloud shape. The measured widths are in agreement with those determined using the differential method, and are also shown in Figure 6.36.

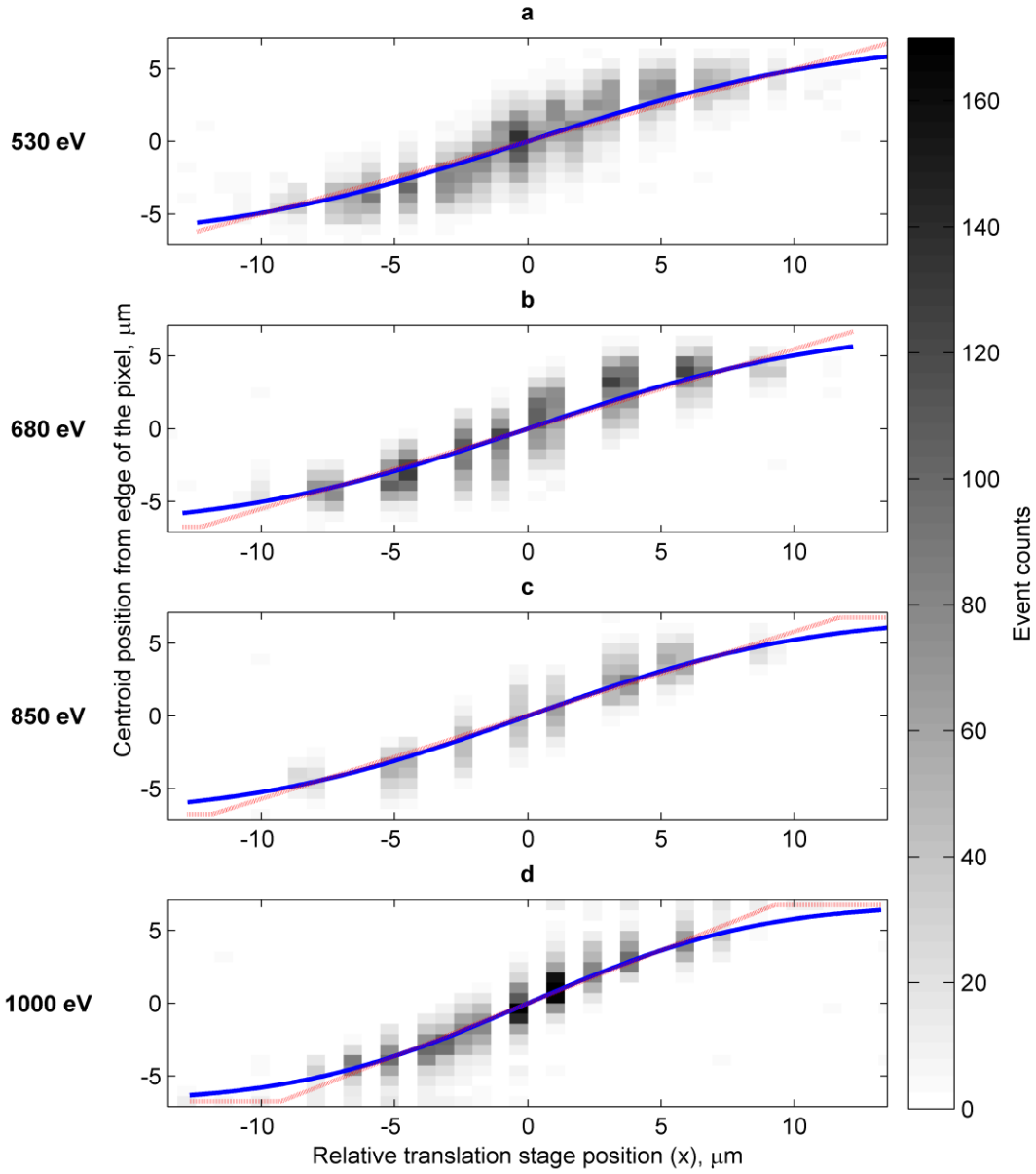

Figure 6.34. The distribution of centroid locations, calculated using the 'cols3x2_2var' algorithm, is shown in a histogram as a function of the interaction location which is given by the relative stage location. The distribution for each energy data set is fitted using a Gaussian (blue line) and top-hat (red dashed line) charge cloud shape.

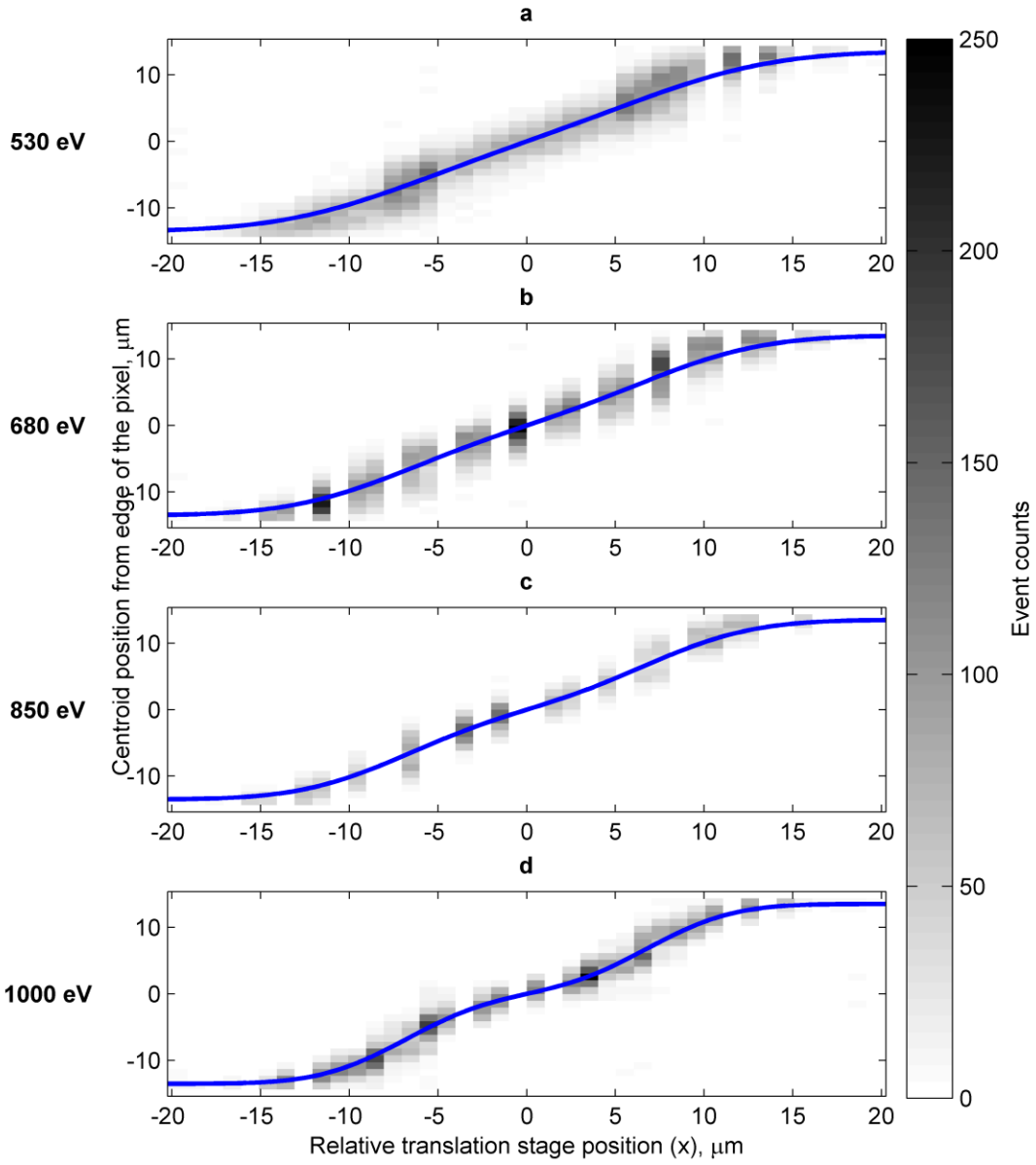

Figure 6.35. The distribution of centroid locations for each energy data set, determined using the uncorrected 'cols3x3' algorithm, is fitted with the distribution expected from a Gaussian-shaped charge cloud (blue line).

6.5.6 The average charge cloud width

The charge cloud shape of the average event that is sampled by the pixels has been measured using two methods (described in Sections 6.5.4 and 6.5.5) with the results presented in Figure 6.36. The measured widths determined by both methods agree with a general trend where the charge cloud width decreases with increasing photon energy. The trend is expected because

higher energy photons will, on average, interact further from the back surface and closer to the depletion region and therefore will have a shorter distance within which to diffuse in the plane of the detector.

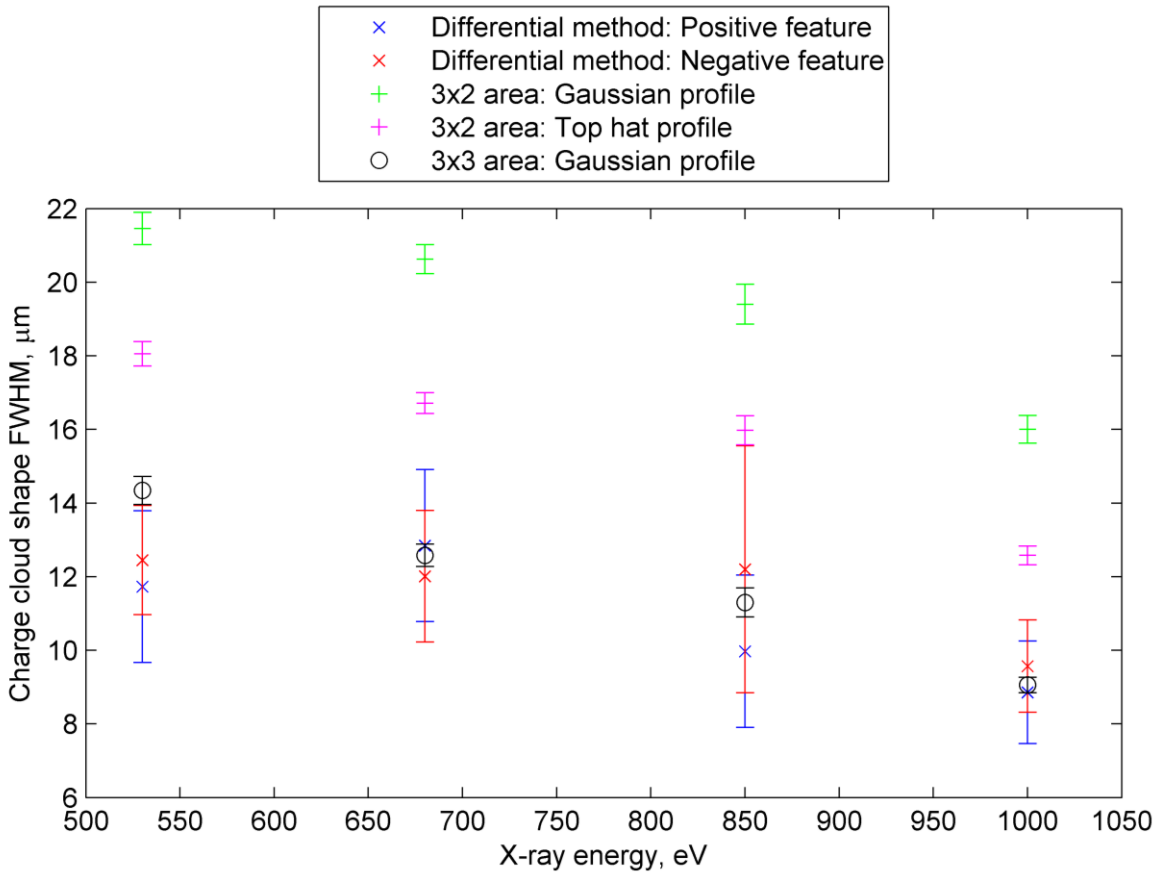

Figure 6.36. The change in charge cloud widths with photon energy as measured by the differential method Gaussian profile fits, and Gaussian and top-hat profile fits to the $X_{CG}(X_{in})$ distributions. The general trend of decreasing charge cloud width with increasing energy is visible. Errors shown are 95% confidence limits from the fitting procedures.

In the CCD42-10, the charge cloud is larger with respect to the pixel size than those investigated by Yoshita *et al*. [104], which meant the original approach of using a centre of gravity algorithm applied to an area two pixels wide had to be adapted and the '3x2 area' measurements in Figure 6.36 overestimate the charge cloud shape. The implementation that uses the systematic error of the 'col3x3' centroid algorithm requires a more complicated fitting equation, but results in charge cloud widths that are in better agreement with those determined using the differential method (Figure 6.36).

The differential method and the systematic error method that uses a 3×3 pixel area produce similar results but the errors of the differential method are larger. This may be due to the magnification of errors in the integrated charge cloud distributions that occurs during differentiation in the differential method, and the fact that the distribution fitted in the systematic error method includes significantly more points.

The charge cloud widths measured here for the CCD42-10 are much narrower than the value quoted by Ghiringhelli *et al*. [7] of 24 µm (FWHM). This is because the measurement quoted by Ghiringhelli *et al*. is not the actual charge cloud width, but is the oversampled charge cloud integrated in the pixel areas, convoluted with the accuracy of the centre of gravity algorithm used to determine the centroid position. The sampling of the pixel has the effect of significantly increasing the width of the distribution, measured by Ghiringhelli *et al*. Therefore, despite the charge cloud having a width of approximately 10 µm as measured here, the actual effective spatial resolution of the detector is widened by the pixel sampling to approximately 24 µm [7].

6.6 Other CCD operating modes

The diffusion of charge in the field-free region is the dominant contributor to charge splitting between pixels. By increasing the level of charge spreading, the average signal to noise in the pixels used to calculate a centroid can be increased, which results in a better spatial resolution. It is predicted that the level of charge spreading can be varied by adjusting the potentials applied to the CCD, which will in turn affect the depletion depth.

To test this prediction, X-ray events were also recorded whilst the CCD42-10 was operating in alternative modes. In the standard mode presented up until this section, the device has been operated with two of the three image phase electrodes held at 0 V during integration. A potential of 11.8 V was applied to the other electrode, IØ2, to form the potential well confining the charge from spreading up and down the column (the buried n-channel confines charge from spreading along the rows). The implant that is present to define potential wells when all phases are at 0 V for advanced inverted mode operation also helps define the potential well. The change in depletion depth when the electrode is held at its high or low potentials is illustrated in Figure 6.37.

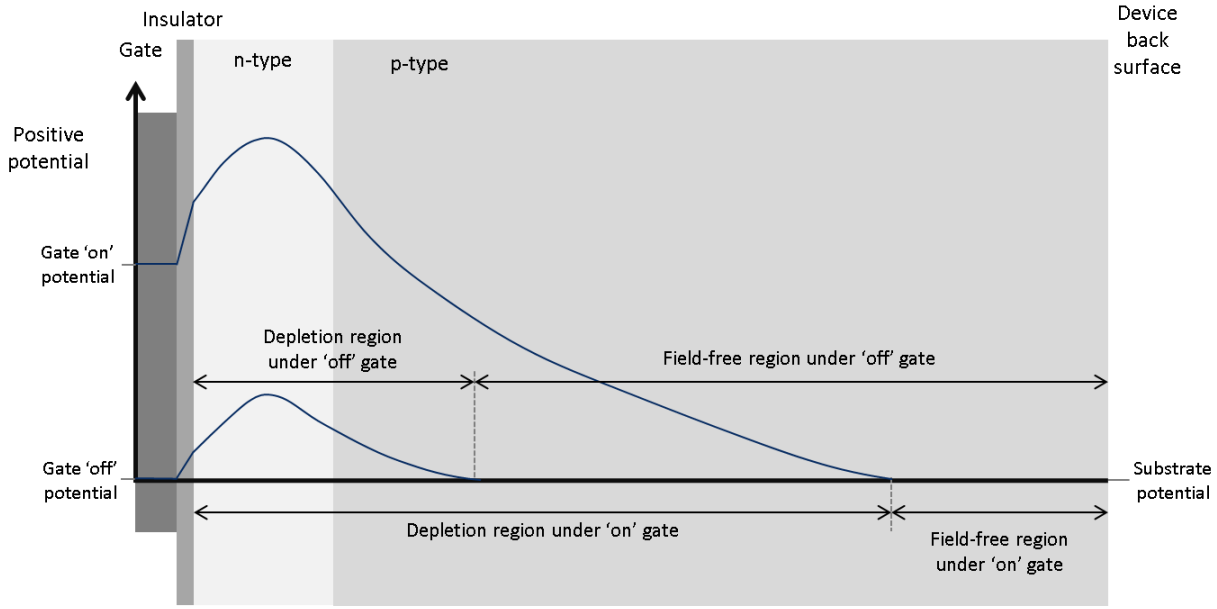

Figure 6.37. The depletion depth under the gate extends further into the silicon when the gate is set to a high potential ('on'), resulting in a thinner field-free region. This diagram is not to scale, but illustrates the effect of varying the gate potential on the depletion and field-free depths.

By changing the number of electrodes that 11.8 V is applied to, the shape of the potential wells can be changed: if two adjacent electrodes are held at the higher voltage the potential well will physically extend further in the column direction; and if all three electrode phases are held low (at 0 V) the potential well will only be defined by the AIMO implant and so the depth of depletion will penetrate less deep into the silicon (Figure 6.38). The operating modes will be referred to as '0 phase', '1 phase' and '2 phase', defined as integrating with no image clocks high, only IØ2 high, and both IØ2 and IØ3 high respectively.

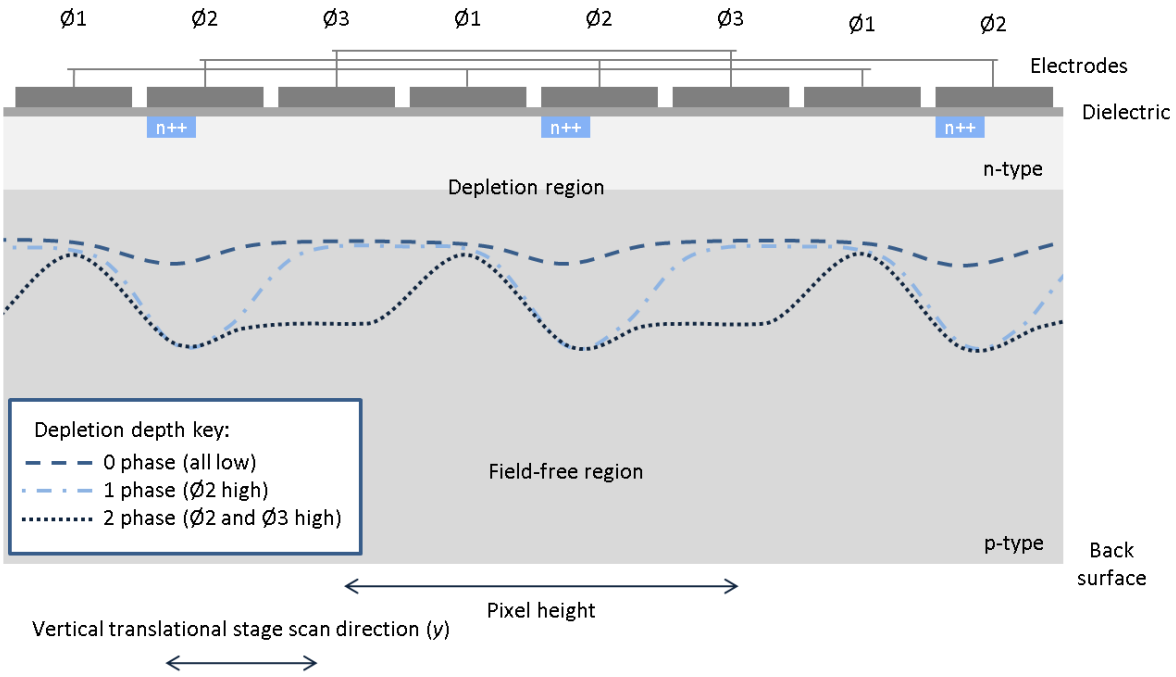

Figure 6.38. The depletion depth varies down the column of the CCD42-10, as illustrated here (not to scale). When an electrode is held at a high potential, the depletion depth is increased under it.

6.6.1 The charge cloud width in other operating modes

In addition to the horizontal scans of the 1 phase data already presented 7 other scans were made, including a scan vertically through the pixel (Table 6.4). The majority of the scans passed close to the centre of the pixel, as seen in Figure 6.39, however the 0 phase scans were close to the top of the pixel.

Table 6.4. Raster scans across the CCD42-10 pixel, excluding the horizontal 1 phase scans whose data has been presented earlier in this chapter.

Operating mode	Horizontal (h) or vertical scan (v)	Photon Energy, eV	Number of points in scan
0 phase	h	530	14
0 phase	h	1000	6
0 phase	h	1000	9
2 phase	h	530	14
2 phase	h	680	10
2 phase	h	1000	9
1 phase	v	1000	15

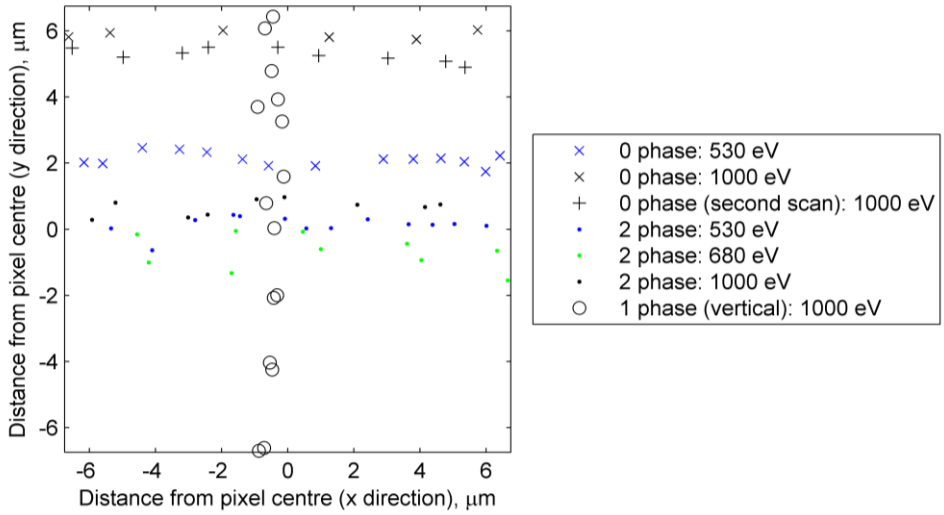

Figure 6.39. The spot locations across the pixel area sampled during the scans with different operating modes.

It should be noted that the boundary of the pixel has been defined by the location at which the charge cloud is collected equally between the adjacent pixels, and has been assumed to be square. This has allowed the pixel boundary to be defined by the data collected. However, the potential well is changed by the different image clock configurations and therefore the position of the pixel moves to be centred over the electrodes that are at a high potential.

The charge cloud width has been measured for each of the scans using both the methods described in Section 6.5.1 and shown relative to the results of the 1 phase data in Figure 6.40. At 1000 eV, both methods measure the horizontal charge cloud width to be approximately 1 µm larger when the CCD is operated in 0 phase (black) than in 1 or 2 phase modes (blue and red respectively). Possibly, this is due to the depletion depth being significantly further from the back surface, such that electrons diffusing from interaction events close to the back surface have a significantly longer time to diffuse in the plane of the detector (as shown in Figure 6.38). However, it is also possible that the measured wider average charge cloud width is from the scan being run at the top of the pixel, rather than at the centre (Figure 6.39).

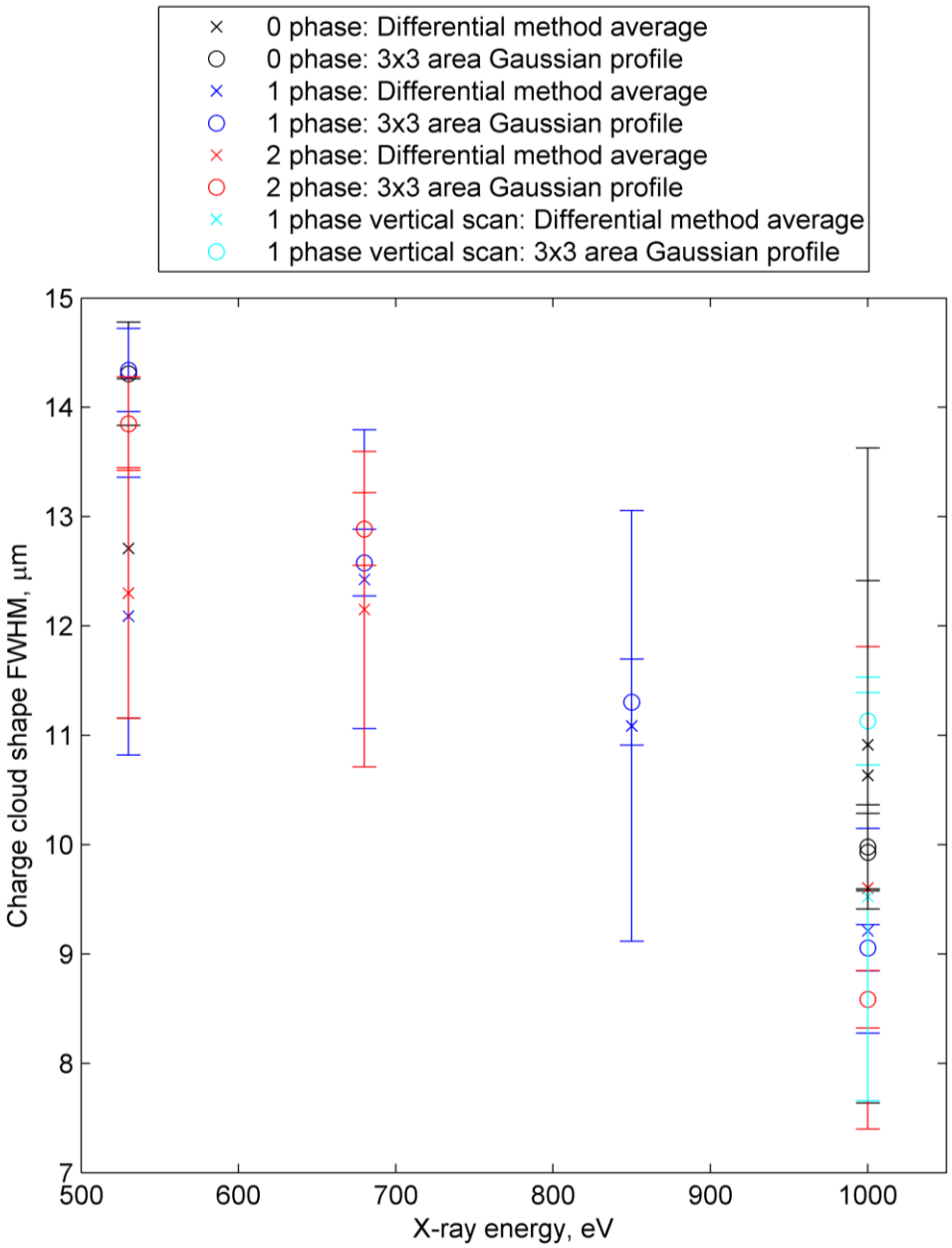

Figure 6.40. The charge cloud width, measured using the two methods, is shown for the scans across the pixel for different operating modes. Error bars show the 95% confidence limits of the fitting procedure.

The measurement of the charge cloud width from the vertical scan of the pixel (cyan) is wider than the horizontal scan measurements attained using the systematic error method. This suggests the charge cloud may be asymmetric in the CCD42-10, perhaps because of the different structures of the pixel in the two dimensions resulting in a region of deeper depletion in a rectangular region of the pixel. In the vertical cross-section (Figure 6.38), the 1 phase mode results in a region of deeper depletion running across approximately one third of the pixel, whereas in the horizontal

cross-section (Figure 6.41). The region of deeper depletion extends across closer to 70% of the pixel, as the depletion depth is reduced during the column isolation region where there is no n-type buried-channel implant. The region of deeper depletion is wider in the horizontal direction, so a charge cloud generated in the field-free region is likely to diffuse a shorter distance in the horizontal direction than the vertical direction before entering the depletion region.

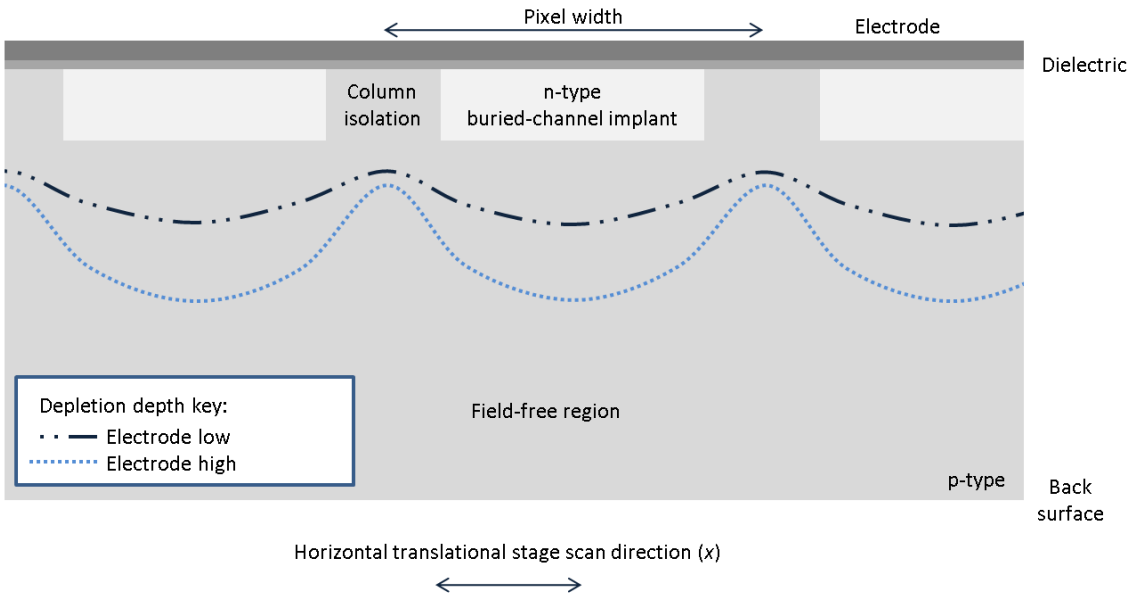

Figure 6.41. An illustration of the depletion depth in a section across the column of a CCD42-10 shows the shallower depth of depletion in the column isolation region, between buried-channel implants.

Scans were also made with the substrate voltage set to 0 V, rather than 8.4 V. Unfortunately, due to drifting of the device temperature and increased dark current, the background noise was at 14.0±0.3 electrons rms and 11.5±0.1 electrons rms for scans with 530 eV and 1000 eV energy photons respectively. At these noise levels, the identification of single photons becomes difficult, and these data sets have not been included in this analysis.

If the charge cloud is wider in a given mode, more signal may be found in the pixels that surrounding the main central pixel. Higher levels of signal in the neighbouring pixels will improve their signal to noise, and result in an improved accuracy for X-ray event centroiding. The errors in the measurements here, especially using the differential method, are too large to draw any significant conclusions however the results suggest that there could be a different level of spreading in the column- and row-wise directions, and that operating with all image clocks off during integration may increase the spreading.

6.7 Focus on corner/centre of pixel

During long experimental breaks of the synchrotron campaign, the X-ray spot was focussed at a single sub-pixel location and a large number of frames were collected to build up a data set containing many images with a single photon recorded in the focussed 1st order diffraction spot. The number of frames collected at each photon energy and sub-pixel location is shown in Table 6.5. The images recorded with 1000 eV photos have been used to calibrate the charge spreading model in Chapter 4, after they were reduced and analysed using the same methods as described in Sections 6.3.2 and 6.3.3.

Table 6.5. The number of frames collected during long focusses at sub-pixel locations.

	Photon energy, eV		
	530	**680**	**1000**
Corner of pixel	10 000	14 000	32 000
Centre of pixel	12 000	-	14 000

6.8 Centroiding algorithms in the SAXES data pipeline

The best resolutions achieved with the centroid algorithms across the energy range tested at PolLux (Figure 6.28) with the CCD42-10 are better than 5 µm (FWHM), the target spatial resolution for an upgraded detector at SAXES. Therefore, application of a centroid algorithm to X-ray events observed with the CCD42-40 detector currently in SAXES could be a solution to achieving the desired resolution. However, when proposing any changes to the operating mode of the camera, such as operating in a photon counting mode, any loss of beamline throughput must be considered.

6.8.1 Beamline throughput

RIXS is a photon-starved experiment, and obtaining a single spectrum that contains sufficient photons can take up to 30 minutes integration time. Time to use SAXES, a world-class facility, is valuable and highly oversubscribed, therefore users wish to make the most of beam time that has been competitively obtained. In the majority of experiments, it would not be acceptable to reduce

the photon count rate significantly and any proposition to change the camera operating mode to apply centroiding must also maintain (or improve) the throughput of the beamline.

6.8.2 The SAXES spectrum extraction algorithm

A schematic of a typical spectrum recorded by the CCD42-40 at SAXES is shown in Figure 6.42. Isoenergetic photons are detected in lines across the device as dispersed by the grating. The current detector is operated with long integration times (typically 10 minutes) to build up an image containing many photons leading to a significant amount of pile-up. An algorithm first determines the slope of the isoenergetic lines in the image, approximating it as linear, before constructing a spectrum by adding the pixel signals to bins, with each column offset by the gradient of the slope.

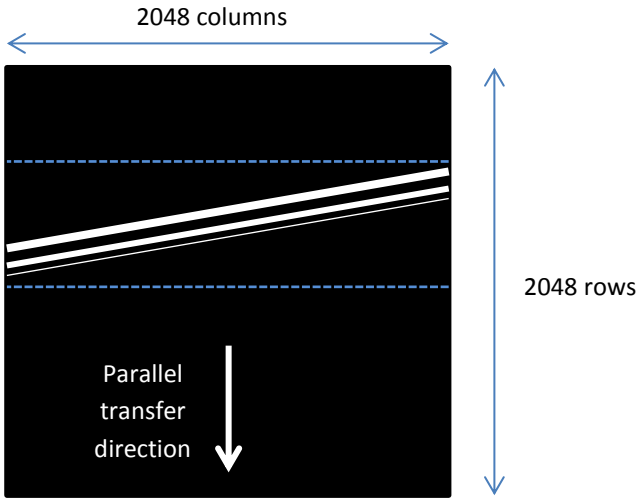

Figure 6.42. A sketched spectrum is shown as detected by the CCD42-40 at SAXES. Photons of the same energy are detected in diagonal lines across the device.

To apply centroid algorithms, the detector must be operated in a photon counting mode taking many images, each with a small collection of photons. The photons in the images can be centroided if they are isolated from other photons, to create a catalogue of photon centroid locations. The catalogue can be used to determine the slope of the isoenergetic line, and the centroid locations can be corrected using the gradient, aligning them into energy space. An appropriate bin width can be chosen to histogram the corrected locations into a spectrum.

The algorithms investigated in this thesis can only be applied to single photons, therefore pile-up must be avoided by reducing the integration time. However pile-up is most likely to occur within higher flux regions of the spectrum. Ignoring these events completely when constructing a spectrum may result a systematic error in the relative count rates in high and low flux peaks. Including the events in the spectrum in their pile-up state would degrade the resolution to the PSF width measured during the commissioning of SAXES, 24 µm [7].

Isolated events are not centroidable due to no signal being present in adjacent pixels that can inform an algorithm on the interaction location. If included in the spectrum, isolated events would also make the resolution worse, but the error can be no larger than half a pixel width in each dimension (6.75 µm in a CCD42-40).

To achieve the best possible resolution, both pile-up and isolated events would be rejected and the spectrum would be made up of events detected as split events. The relative count rates in peaks could be adjusted using the number of rejected events, but the overall count rate would be reduced. The systematic changes would have to be very well understood to avoid introducing systematic errors into the final spectrum that could be misinterpreted. RIXS is a photon-starved technique and experimental time at the spectrometer is limited, therefore certain users may choose to compromise resolution for a higher count rate by including all the photons.

6.8.3 Applying centroid algorithms to example images

Images were recorded by Thorsten Schmitt for this investigation using 930 eV photons incident on a carbon tape ('C-tape') sample. The characteristic feature in the spectrum is a sharp elastic line with high signal strength that is used to define the experimental spectral function of the spectrometer. Five images were recorded with the current CCD42-40 detector at each of the following integration times: 10, 20, 30, 40, 50 and 60 seconds.

Firstly the background offset level, which was obtained by fitting the distribution of pixel signals in the entire image (Figure 6.43 a), is subtracted from the image. Single photon events are then identified and extracted from the image by one of two methods, depending on if the centroid algorithm will be applied to a 2×2 or 3×3 pixel area. The methods must identify single photon events that are sufficiently isolated from nearby interaction events.

In the 3×3 centroid algorithm, 3×3 pixel areas across the image are identified where the central pixel has maximum signal. The total signal of these 3×3 pixel areas are added to a distribution (Figure 6.43 b), forming a peak at approximately 105 ADU due to the signal from single photon interactions. A Gaussian profile is fitted to the peak, and thresholds are defined at 3.5 standard deviations above ($t_{U:\,3\times3}$) and below ($t_{L:\,3\times3}$) from its mean, where 3.5 has been chosen so that

the thresholds include the vast majority of single photon interaction events, whilst excluding the regions with too much or too little signal. The background noise is also measured from these peak fits, at an average of 4.00±0.03 electrons rms across the 30 images.

X-ray interaction events are defined as the 3×3 pixel areas where the central pixel contains the maximum signal, and the total signal is greater than $t_{L:\,3\times3}$. The subset of X-ray interaction events that are classed as '3x3 centroidable' are defined as the X-ray events where the total signal in the 3×3 pixel area is also less than $t_{U:\,3\times3}$ (excluding events containing too much signal to be a single photon), and where another X-ray event's 3×3 pixel area does not overlap (excluding pile-up of events).

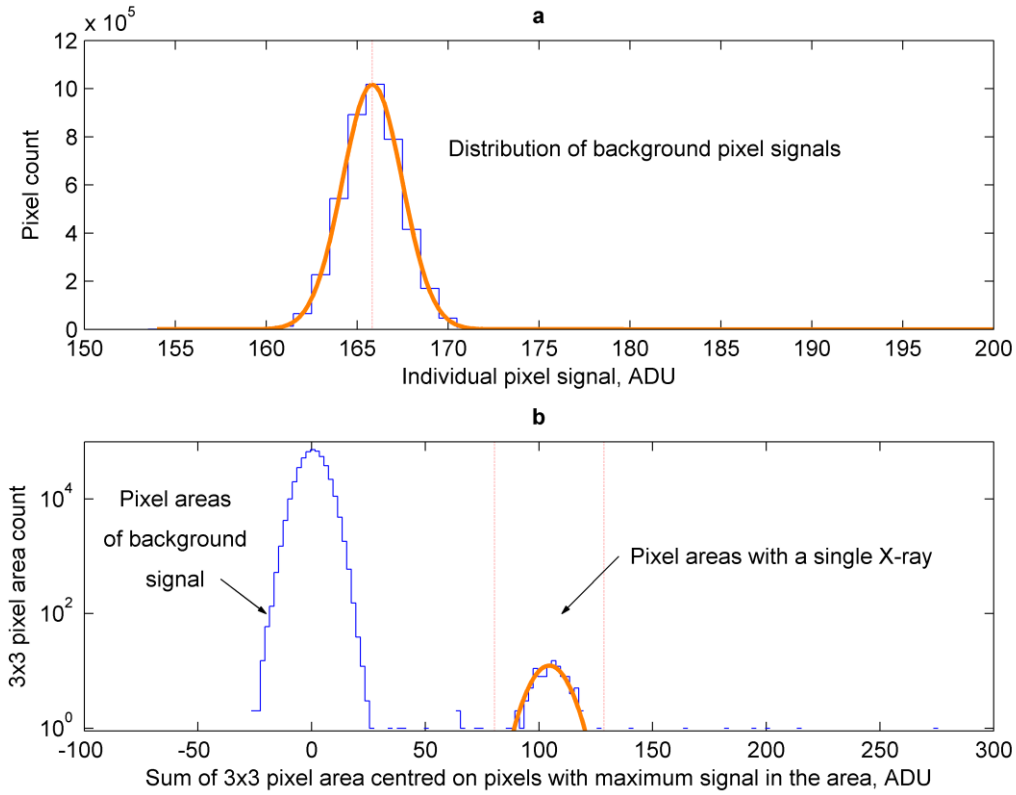

Figure 6.43. ***(a)*** *Distribution of pixel signals from the 2048×2048 image area. A Gaussian profile fit measures the ADU offset level (vertical red dashed line).* ***(b)*** *3×3 pixel areas where the central pixel contains the maximum signal are selected, and the total signal in the 3×3 pixel areas are added to this distribution. The peak due to single photon interactions is fitted by a Gaussian profile, to determine lower ($t_{L:\,3\times3}$) and upper ($t_{U:\,3\times3}$) thresholds (vertical red dashed lines).*

The method to extract '2×2 centroidable' events is similar, but as the event area is no longer centred on a pixel with maximum signal, there are added complications in its application. The '2×2 centroidable' areas are determined by initially using the set of 3×3 pixel areas discovered as X-ray interaction events and removing those unsuitable. For each 3×3 pixel area, the 2×2 quadrant with maximum signal is determined and pile-up events are eliminated by removing events with overlapping 2×2 areas. The primary peak in the distribution of total signal in the remaining 2×2 pixel areas is fitted with a Gaussian profile and a threshold ($t_{U:\,2\times2}$) set at 2.5 standard deviations above the mean, where the value of 2.5 has been chosen to include 2×2 pixel regions with signal from only one photon (Figure 6.44). 2×2 pixel regions with a total signal greater than $t_{U:\,2\times2}$ are removed unless greater than 90% of the signal in the 2×2 area is contained in a single pixel, to allow for isolated events which may be less split and may have a higher level of signal. As with the 3×3 algorithm, the events with signal greater than $t_{U:\,3\times3}$ in the 3×3 pixel area are removed to eliminate pile-up events. The remaining 2×2 pixel areas are classed as '2×2 centroidable'. Every event classed as '3×3 centroidable' will also be classed as '2×2 centroidable', but additional events will be discovered by the 2×2 method as events are allowed to occur closer together without being eliminated for having overlapping pixels areas.

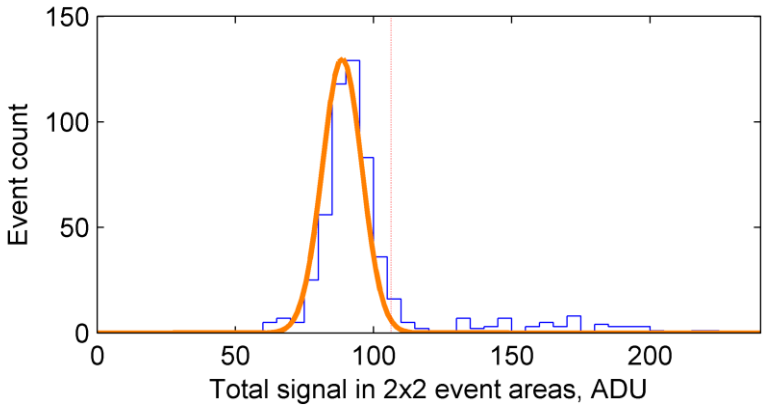

Figure 6.44. An example distribution of the total signal in the 2×2 pixel event areas which is fitted with a Gaussian profile. The threshold, $t_{U:\,2\times2}$, is shown by the vertical red dashed line.

The number of events expected to be found by the methods is equal to the total signal in the image, divided by the average signal per photon, equivalent to the number of events that contribute to a spectrum when it is extracted using the current software. With this integration method, the number of photons observed remains constant with integration time, where the average has been calculated across the 5 images per integration time, Figure 6.45. The number of 3×3 centroidable and 2×2 centroidable events identified decreases as the integration time

increases as a larger number of events are lost due to pile-up. However, as expected, fewer events are disregarded due to pile-up when using the 2×2 algorithm. The number of centroidable events does not tend towards the number of events determined by the integration method at short integration times because partial events, where the majority of charge is lost at the back surface of the detector, are not identified as centroidable.

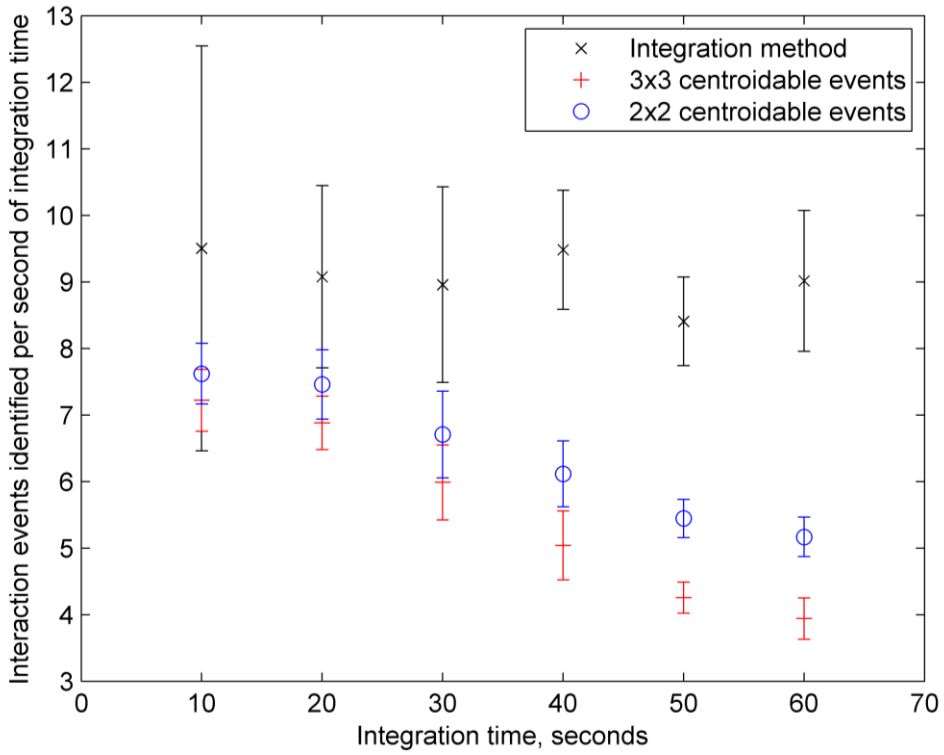

Figure 6.45. The number of photons observed per second of integration time is calculated by measuring the total signal in the image (integration method), and by extracting events classed as '2×2 centroidable' and '3×3 centroidable'. The values and errors shown are the mean and standard deviation from the 5 images per integration time.

The centroid locations are calculated for the '2×2 centroidable' and '3×3 centroidable' events using the centre of gravity algorithms, and an η correction function is determined from their sub-pixel uncorrected locations to compensate for the systematic bias in the centroid algorithms. The majority of the centroidable events detected in the images are observed in the elastic line, in a 'slope region' (defined below) between rows 740 and 795 in this case. The 2×2 centroidable event locations within the 'slope region' from all the 30 images are shown in Figure 6.46 a and fitted using a linear profile, as used in the current SAXES spectrum extraction software, and a quadratic profile (green and red respectively). The 'slope region' is defined as the area within 10 rows from the quadratic fit, and all events outside this region are ignored. The row locations are

corrected using the profile fits, to place photons with the same energy into the same effective row location (Figure 6.46 b and d). The location distributions are then binned into 5 bins per pixel (Figure 6.46 c and e), and a Gaussian profile is fitted using least square regression. The resulting spectral line feature suggests that the isoenergetic line should be fitted with a quadratic profile as the FWHM of the spectral feature is reduced from 83.5±2.4 µm to 75.7±2.1 µm (a 9.3% improvement in this case). The level of this improvement will vary with the level of deviation from linear that the spectral line is when projected onto the CCD, a function of the relative locations of the grating and detector, and the photon energy.

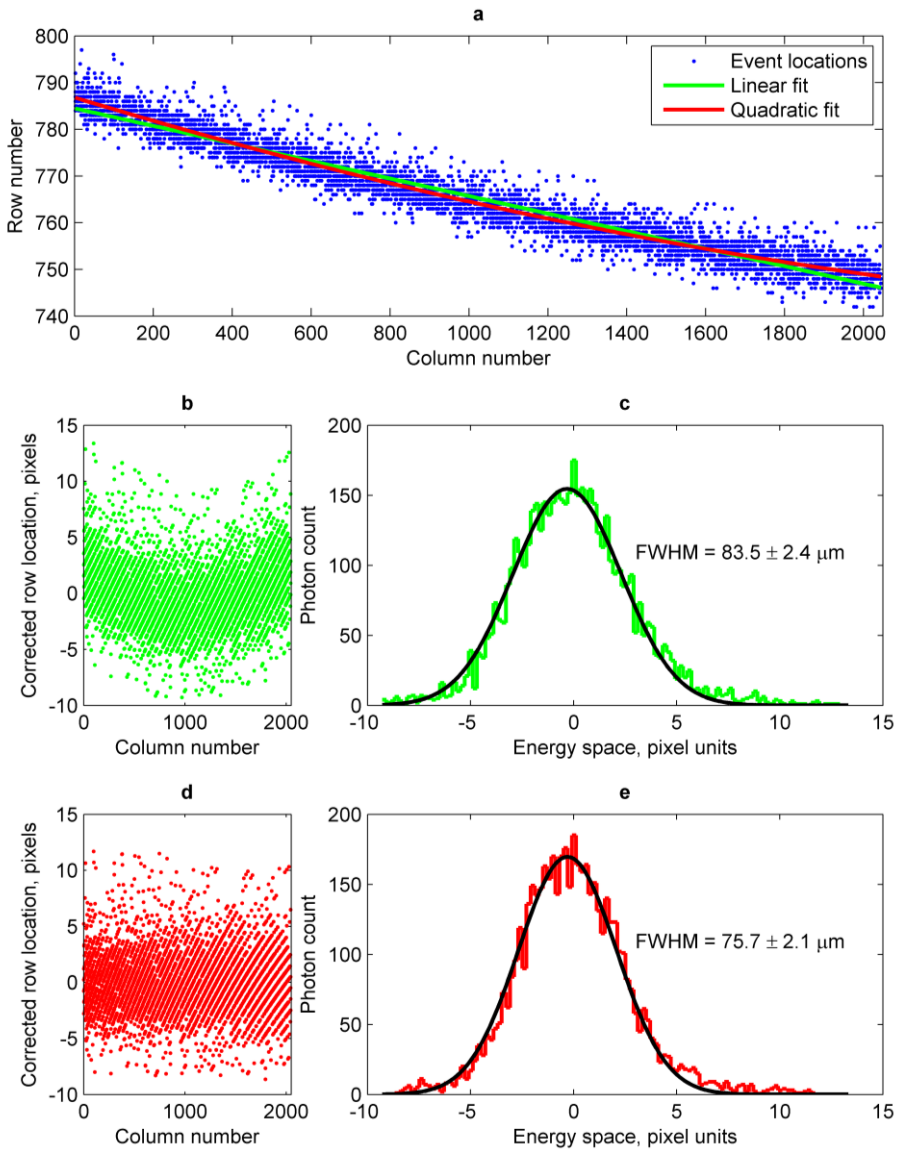

Figure 6.46. ***(a)*** *The locations of centroidable events in the slope region, shown fitted by a linear and a quadratic equation.* ***(b)*** *The row location distribution is corrected using the linear fit.* ***(c)*** *The row location distribution corrected using the linear fit is now binned and fitted by a Gaussian profile.* ***(d)*** *Like (b), for the quadratic fit.* ***(e)*** *Like (c), for the quadratic fit.*

The current spectrum extraction software can be applied to the sum of all the images, with an equivalent integration time of 1050 seconds. The elastic line feature from the 930 eV photons is clearly visible at approximately 1300 pixels across the spectrum (Figure 6.47 a), with an increasing background level from the pixel bin at 2000 to the pixel bin at 0. The elastic line is shown in greater detail in Figure 6.47 b, with a width of 6.60±0.07 pixels or 89.1±0.9 µm (FWHM) measured using a Gaussian profile fit.

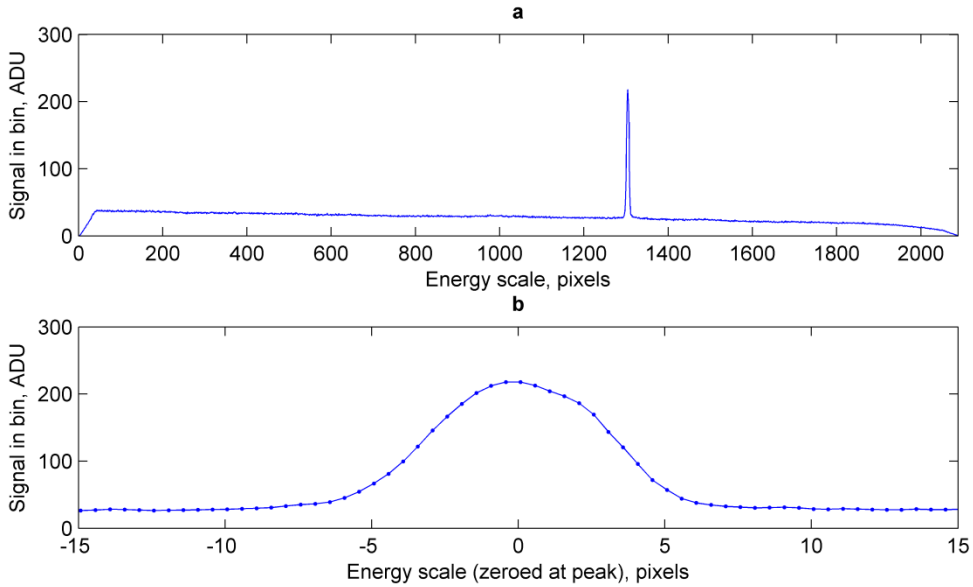

Figure 6.47. ***(a)*** *The spectrum of 'C-tape' extracted from the 30 sample images using the current software.* ***(b)*** *A closer look at the elastic line from (a).*

The spectrum is extracted from the centroid locations using both the linear and quadratic fit to the isoenergetic lines, where the linear fit used the gradient determined by the current SAXES software of -0.0187 rows per column. A total of 5193 3×3 centroidable events and 5993 2×2 centroidable events were identified in the images. The resulting spectral features are shown in Figure 6.48 a, with their respective widths (FWHM) in Figure 6.48 b, alongside the feature and width determined using the current software (which uses the linear fit). Each feature determined using the linear fit shows a small shoulder on the positive energy side, due to the linear approximation of the isoenergetic lines. The features determined using the centroid locations have flatter peaks, due to pile-up events being lost preferentially in the higher flux centre of the feature. The 2×2 centroidable events result in a feature width approximately 0.2 pixels narrower than the 3×3 centroidable events. The majority of this difference is related to the different

proportion of events rejected due to pile-up in the centre of the feature, rather than the resolution performance of the algorithms.

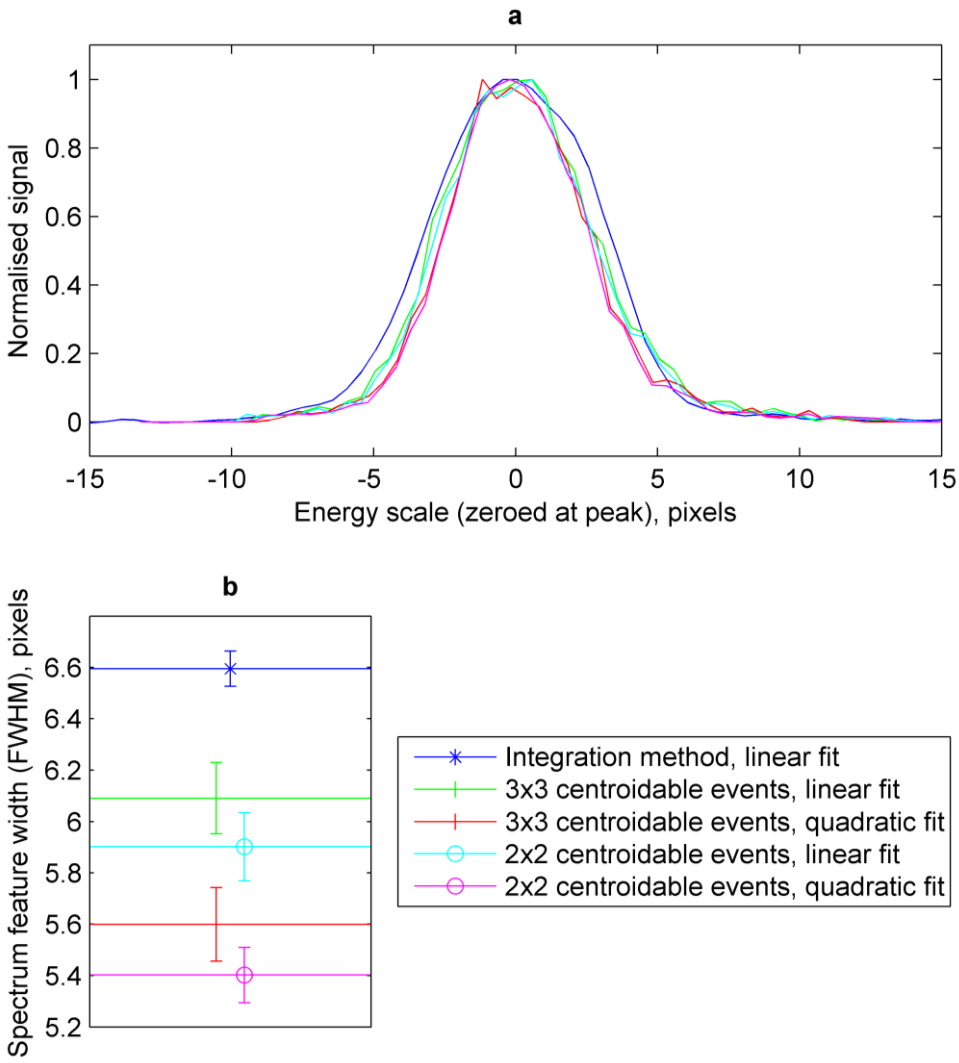

Figure 6.48. ***(a)*** *The feature width determined using the different methods is shown, each zeroed to the mean of a Gaussian profile fit. The widths of the Gaussian profile fits are shown in* ***(b)****.*

Some improvement of the resolution due to centroiding is masked by preferential loss of pile-up photons from the higher flux areas of the spectrum as losing more photons in the centre of the spectrum effectively widens the spectral feature. Despite this, centroiding using the 2×2 centroiding algorithm still improves from the resolution of the spectral line from 6.60±0.07 pixels using the integration mode to 5.90±0.13 pixels in these measurements. Using a shorter integration time would reduce the pile-up and decrease this effect.

Using the energy calibration of 27.658 meV per pixel, determined by varying the incident energy and measuring the change in position of the elastic feature on the detector, the improvement is

from 77.5±0.8 meV to 69.3±1.6 meV (1 standard deviation width of the spectral feature) when using the 2×2 centroiding algorithm.

The achievable resolution of the CCD42-40 expected from simulations described in Chapter 5 (Figure 5.18) is approximately 2.5 µm for a background noise of 4.00±0.03 electrons rms and photon energy of 930 eV, whilst the measured resolution without centroiding applied is 24 µm [7]. Therefore, the CCD's resolution should have been improved by approximately a factor of 10, but this level is *not observed* here as the CCD resolution is not improved to this extent due to the preferential rejection of pile-up photons at the centre of spectral lines, and the grating's slope error and the source size also contributing to the overall spectrometer resolution. Given the relative contributions to the overall energy resolution, shown in Figure 6.49, it is estimated that the CCD resolution has been improved by approximately 33% (from 24 µm to 18 µm), to achieve the overall improvement in energy resolution of 77.5±0.8 meV to 69.3±1.6 meV.

To achieve the full resolution improvement expected from centroiding, pile-up must be reduced significantly by operating with shorter integration times. However, reducing the integration time degrades the throughput of the spectrometer as a larger proportion of time is spent during readout. A possible method of compensating for a reduced integration time is to read out the SAXES detector faster, for example at its 1 MHz pixel readout rate rather than its current 100 kHz readout rate, as will be explored in Section 6.8.4.

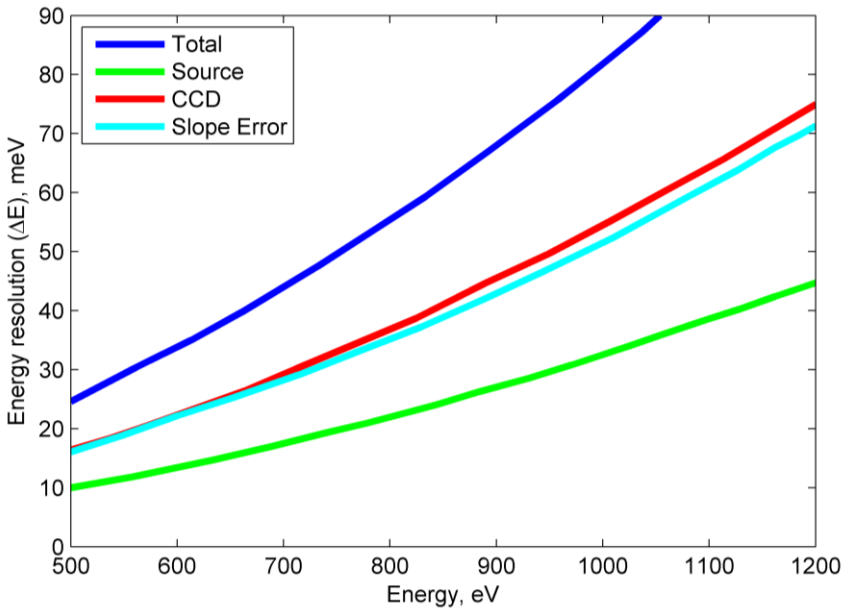

Figure 6.49. The overall resolution of SAXES is a combination of the source size, CCD spatial resolution and the slope error of the grating (c.f. Figure 2.8).

6.8.4 Applying centroiding algorithms to higher flux lines

To minimise the effect of pile-up when observing features with a similar or higher flux as the 'C-tape' elastic line, integration times must be as short as possible. However, the time spent during readout is wasted as no photons can be collected to contribute to the spectrum, therefore a compromise must also ensure a high throughput for the spectrometer. This is especially important for SAXES as a reduction in photon throughput will lead to experiments taking longer, reducing the science output of the beamline (Section 6.8.1). The available experimental time at the ADRESS beamline is already heavily oversubscribed so whilst a low throughput centroiding mode for the spectrometer may be useful for specific high resolution measurements, it is not an ideal solution.

The current camera typically operates with an integration time of 600 seconds and a pixel readout rate of 100 kHz, reading out a frame of 2048×2048 pixels in approximately 42 seconds. The throughput, i.e. the proportion of photons incident on the detector during the integration time, is therefore 93.5%. The camera can also operate in a higher frequency mode with a 1 MHz pixel readout rate which would allow the integration time to be reduced to 60 seconds whilst maintaining the throughput of the spectrometer at 93.5%. 6 test images using 930 eV photons and an exposure time of 10 seconds were collected using the 100 kHz and 1 MHz readout rates at each of the low, medium and high gain settings available. These images were analysed to check if the performance of the camera is sufficient to allow centroiding algorithms to be applied at the faster readout rate.

For the readout rate of 100 kHz, the gain calibration and background noise measured in the images is shown in Table 6.6. The high gain setting results in the lowest background noise. With the readout set to 1 MHz, the background noise level is significantly higher such that a reliable gain calibration is difficult to obtain, and so the background noise cannot be measured. The increased noise level can be seen in the example images, Figure 6.50. Single photon interaction events are difficult to identify when using the 1 MHz readout rate, but the noise level was estimated to be between 18 and 22 electrons rms, approximately double the value quoted by the manufacturer's initial camera testing (10.8 electrons rms). If single photon events could be identified accurately, the simulations described in Chapter 5 (Figure 5.18) predict that 930 eV photons could be centroided with a resolution of between 4 µm and 7 µm (FWHM) for background noise levels between 10 electrons rms and 20 electrons rms. At lower energies, the resolution degrades further, making the 1 MHz mode unsuitable for achieving the 5 µm (FWHM) goal.

Table 6.6. The gain calibration and background noise for the 6 images collected at 100 kHz, for each gain setting.

Gain setting	Gain calibration, electrons per ADU	Background noise measured in images, electrons rms
High	1.44±0.02	4.12±0.05
Medium	2.90±0.03	4.85±0.05
Low	5.85±0.09	6.78±0.12

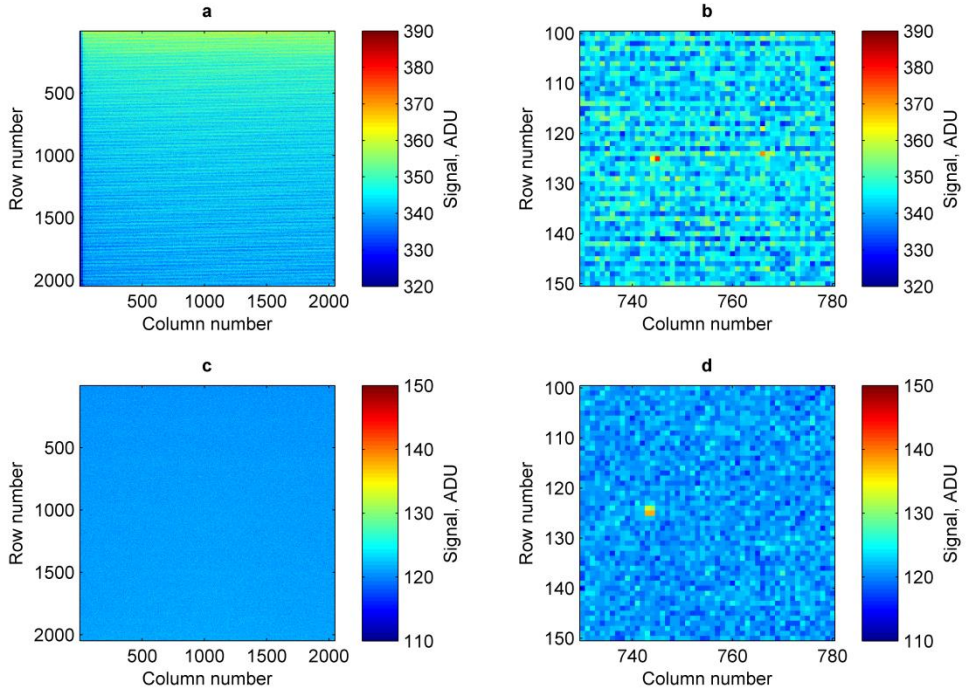

*Figure 6.50. A full-frame test image **(a)** and a region of interest **(b)** captured using the 1 MHz and medium gain readout mode. A full-frame test image **(c)** and a region of interest **(d)** captured using the 100 kHz and medium gain readout mode.*

6.9 Moving forward

Although centroid algorithms can improve the resolution of the spectrometer, the integration time of the camera at SAXES would have to be significantly reduced to apply them. The reduced throughput to the spectrometer would only be acceptable for very specific experiments where a low flux line is being observed, and the improved resolution is desired. Therefore, for the majority of experiments a camera that can single photon count to centroid whilst maintaining a high throughput is required.

Increasing the readout rate of a CCD increases the readout noise and which makes identifying photon interactions within the images obtained using the 1 MHz pixel readout rate of the SAXES camera difficult or impossible (Section 6.8.4). The increased readout noise also reduces the accuracy of the centroid algorithms. Importantly, the principle of applying centroid algorithms to improve the spatial resolution of a CCD has been shown, but to apply centroid algorithms to SAXES, a camera system operating at faster frame rates with lower than 10 electrons rms effective readout noise is desired.

6.10 Summary

An experimental campaign was carried out at the PolLux spectromicroscope at the Paul Scherrer Institut, which was adapted to allow a CCD to be placed at the focal point of the X-ray beam focussed by a Fresnel Zone Plate. The X-ray spot was scanned across a line of sub-pixel positions in a CCD42-10, a similar device to that operated in the SAXES camera, for a range of photon energies and CCD operating conditions.

The single photon X-ray events formed from interactions in the same sub-pixel position have been used to measure the performance of centroid algorithms whose bias has been successfully corrected for using the η function. The resolution of a range of corrected centroid algorithms have been compared, and the 'outer' algorithms were shown to be the least accurate. On average across the pixel the '2 variable' and '3 variable' algorithms performed approximately equally, but the former performed better close to the edges of the pixel and the latter performed better at the centre of the pixel.

The data from the 1D scans has been used to estimate the charge cloud shape and width using two methods. The first method measures the charge cloud shape by differentiating the signals in the pixels, i.e. the oversampled charge cloud integrated across the pixel area [67] whilst the second method uses the systematic bias of uncorrected centroid algorithms [104]. The bias is fitted by the relationship expected from a charge cloud of a given shape by varying the width. The charge cloud width was not significantly smaller than the pixel size, as was the case for Yoshita *et al*. [104], therefore the method was adapted to use the signals in pixels across a wider area.

The majority of measurements were taken using scans along the rows of the device, in the direction of the electrode structure. The charge cloud widths in this direction, when a single electrode phase was kept at a high potential during integration, were measured for 530 eV, 680 eV, 850 eV and 1000 eV. The expected relationship was observed, where the low energy photons resulted in a wider charge cloud width. When 2 phases were kept high during integration the charge cloud width did not change significantly, but two scans using 1000 eV photons were

made when no phases were on during integration. These scans measured a significantly wider charge width but it is not known if the increased charge cloud width is due to the scan location being at the top of the pixel, or the different operating integration scheme. The vertical scan using 1000 eV photons also showed a wider charge cloud width, suggesting that in the CCD42-10, the charge is more confined by the potentials of the channel-stop regions than the potentials formed by the channel-stop, electrode and doped region that allows for Inverted Mode Operation (IMO).

The charge cloud widths measured here for the CCD42-10 differ significantly from the value quoted by Ghiringhelli *et al*. [7] of 24 µm (FWHM), as the measurement quoted by Ghiringhelli *et al*. is the charge cloud width sampled by the pixel structure. The sampling effect degrades the resolution of the detector further than the diffusion of the charge cloud in the field-free region alone.

When operating in the 100 kHz readout rate, the current SAXES camera can take images with a low background noise that allows reliable detection of single photon interaction events that centroiding algorithms can be applied to. However to single photon count, the integration time must be reduced significantly, which decreases the throughput of the spectrometer. The resolution is improved, but limited by the preferential loss of photons to pile-up events in higher flux areas of spectral features. Centroid algorithms applied to a 2×2 pixel area are therefore preferred over algorithms applied to a 3×3 pixel area as the number of photons rejected due to pile-up can be reduced, and the difference in resolution between the algorithms is small. Shortening the integration time further would reduce the issues caused by pile-up.

Whilst investigating the example images from SAXES, it was also shown that fitting the isoenergetic line across the detector with a quadratic function rather than a linear one would improve the resolution, in this case, by 9.3%. Any future spectrum extraction algorithm should use a quadratic function to take advantage of this relatively straightforward route to resolution improvement.

The overall improvement from extracting the spectrum from the sample images using centroiding is clear, but currently relatively small. In addition to the reduced improvement due to the rejection of pile-up events because of the integration time being too long, the slope error and source size of the spectrometer begin to dominate in the overall resolution of the spectrometer.

Another source of error is the distribution of interaction depths in the detector. As the plane of the SAXES detector is at approximately 20° relative to the incident photons, the exponential distribution of interaction depths spreads isoenergetic photons in the plane of the detector. This source of error will be more significant higher in the energy range of SAXES, where the attenuation length is longer, and is investigated further in Section 8.4.

In this chapter the performance of the current detector in the SAXES camera, the CCD42-40 has been investigated. The performance of centroiding algorithms and the charge cloud width have been measured using a CCD42-10, a device with the same pixel structure as the CCD42-40. The results showed that the spatial resolution of single photon detection can be improved using centroiding algorithms. The centroiding algorithms have been applied to sample images containing a spectrum from SAXES, where a resolution improvement has been demonstrated. However, the centroiding algorithms require the spectrometer to be operated in a single photon counting mode but the throughput of the spectrometer is significantly reduced when the detectors is read out at its current rate whilst the integration time is shortened. The 1 MHz readout rate of the detector results in a background noise level that is too high for centroiding algorithms to be used. Therefore, for SAXES to take advantage of centroiding algorithms whilst maintaining a reasonable throughput, a detector that allows a higher readout rate with a similar or lower background noise level is required.

One detector that can read out faster than a standard CCD, whilst maintaining a low effective readout noise, is the EM-CCD. Its avalanche multiplication register would allow pixel readout rates to be increased up to a few MHz, whilst the effective readout noise is reduced to sub-electron levels. A small area EM-CCD is the CCD97, which was taken to PolLux for experimental campaign 3 to determine the suitability of an EM-CCD as a new detector at SAXES.

6.11 Conclusions

The setup in the PolLux experimental chamber has been successfully adapted for a CCD to be operated when its pixels are at the focal point of the X-rays focussed by the FZP arrangement. During experimental campaign 2, single X-rays have been observed with a CCD42-10 (a device with the same pixel architecture as the CCD42-40 currently installed at SAXES). The typical X-ray events have pixels with signal above the noise floor in a pixel area smaller than a 3×3 pixel area, so centre of gravity centroiding algorithms have been applied using pixel signals in areas equal or smaller than 3×3.

X-rays have been focussed onto sub-pixel areas, and the resulting uncorrected centroid locations have been distributed in the expected regions of the pixel, demonstrating experimentally that centroid algorithms can be applied to determine the sub-pixel interaction position. To develop the η correction functions, the X-rays in the 0^{th} order diffraction pattern were assumed to be in a flat distribution across the pixel and isolated events, where over 90% of the pixel signal is collected in a single pixel, were excluded. For the nine centroid algorithms under investigation, the η correction successfully removed bias from the centroid position.

1D horizontal scans across the pixel structure have been recorded for 530 eV, 680 eV, 850 eV and 1000 eV photons. The higher energy X-rays can be centroided more accurately, which was expected from the signal to noise ratios and simulation results from Chapter 5. The resolutions vary across the pixel according to the centroiding algorithm, where an improved accuracy is achieved if more of the pixels containing better signal to noise ratios are included. The '2 variable' and '3 variable' algorithms performed best across the sub-pixel regions and energy range; the resolutions improved at the higher photon energies but were all less than 5.5 µm (FWHM) (Figure 6.28), a measurement that includes an unknown contribution from the X-ray spot size.

The charge cloud width has been measured using two methods adapted from the literature to suit the charge cloud widths observed here. A charge cloud with a Gaussian profile extending over a 3×3 pixel area was found to be a suitable approximation for measuring the charge cloud widths in the CCD42-10. The general trend of a wider charge cloud for lower photon energies, agreeing with the principle of electrons being generated at the back surface having longer time to diffuse laterally before collection, has been observed with measured widths in the range of 9 µm to 15 µm (FWHM). The results also indicate that changing the diffusion time by varying the depletion depth (changing the number of electrode phases on during integration) can change the charge cloud width. The charge cloud width measurements are not directly comparable to the charge cloud dominated resolution of the CCD42-40 at SAXES (24 µm FWHM [7]) because including pixilation of the detector degrades the resolution further. The 24 µm measurement was also carried out with the photons incident at 20° to the detector surface, increasing the average effective distance of interaction from the depletion region.

The resolution has been measured at better than 5 µm (FWHM) with the optimum centroid algorithms across the energy range, achieving the goal set for the SAXES upgrade plan. Therefore, images have been recorded at SAXES with the CCD42-40 operating in a photon counting mode. Due to its good performance and small pixel area, the 2×2 corrected centroid algorithm has been applied to the spectra, improving the spectral line width and demonstrating the spatial resolution of the detector is improved when centroiding algorithms are applied. However, the integration time of greater than 10 seconds is too long for photon counting because a significant proportion of pile-up events are discarded, preferentially from the central region of the spectral lines where the flux is highest. The preferential rejection leads to an effective broadening of the spectral feature and a systematic error in the relative counts in spectral features of different intensities.

Operation of the SAXES camera in a photon counting mode whilst reading out at a 100 kHz pixel readout rate significantly reduces the throughput of the spectrometer. Increasing the pixel readout rate to 1 MHz available with the current camera electronics is also not suitable for

centroiding as the readout noise increases to a level where single photons are not easily identified in the image and the accuracy of centroiding algorithms will be significantly degraded. Therefore, the current camera system is not suited for operation in a low noise single photon counting mode without a reduction in throughput. To maintain the throughput, a detector capable of a faster readout rate whilst maintaining a low effective readout noise is required.

Chapter 7: Resolution Improvements with EM-CCDs

7.1 Introduction

The current CCD used in SAXES can be operated in a photon counting mode that allows centroiding algorithms to be applied to improve the resolution of the spectrometer, as described in Chapter 6. However to accomplish this, the CCD42-40 must be operated with short integration times and at a pixel readout rate of 100 kHz (42 seconds readout time) to maintain sufficiently low background noise, which significantly reduces the throughput of the spectrometer. Reading out the CCD42-40 at a faster pixel readout rate (e.g. 1 MHz) increases the readout noise such that photon counting is no longer possible, therefore an alternative detector must be used if centroiding algorithms are to be applied whilst maintaining the throughput of the spectrometer.

The ideal detector would be able to operate at a fast readout rate with low noise, allowing the proportion of time spent during integration to be maximised whilst still enabling photon counting. Even when operating at a fast readout rate, the effective readout noise must be very low to allow X-rays to be identified above the noise floor and centroided most accurately. The Electron-Multiplying CCD (EM-CCD) is an ideal candidate: its avalanche gain register allows signal electrons to be multiplied before they are passed through the readout chain and converted into the voltage domain (Section 3.4). Multiplying the electron signal before read out effectively reduces the readout noise so an EM-CCD can be operated at pixel readout rates of a few MHz in a high-gain mode that reduces the effective readout noise to a sub-electron level. In this chapter, the spatial resolution of centroiding algorithms are investigated for X-ray events detected in EM-CCDs. Images were recorded during experimental campaign 3 at the PolLux spectromicroscope that contained single photon interactions, upon which the centroiding algorithms could be applied. The results obtained allowed the proof of concept of centroiding events detected with an EM-CCD to be demonstrated.

7.2 Probing the sub-pixel of an EM-CCD (CCD97)

The CCD97 was chosen as the most suitable EM-CCD to test at PolLux: its small size simplified its incorporation into the setup at PolLux and increased the allowable frame rate with the test electronics. An effective combined background noise level of less than 0.8 electrons rms was achieved throughout the experimental campaign, which was partially due to a re-design of the mechanical and cooling setup that incorporated the CCD97 into the vacuum chamber at PolLux, compared to those used in campaign 2 (Chapter 6).

7.2.1 Improvements to the PolLux experimental setup

Building on experience gained with the setup during experimental campaigns 1 and 2, several improvements were made to the setup used to adapt PolLux to probe the sub-pixel of an EM-CCD for campaign 3. To reduce the operating temperature of the device, a Polycold® Compressor and Cryotiger head with a Standard PT-30 gas blend was used due to its improved cooling power over the Standard PT-14 gas blend [98]. The heat transfer between the detector and Cryotiger head was improved by redesigning the cold-finger to increase the surface area touching the device package and to improve the flexibility and range of movement of the translational stages, the thermal connection was changed from bent copper sheets to four copper braids (Figure 7.1). New cooling mechanics were designed for attaching the braids to the Cryotiger head, and a new cold-finger was milled from a single block of copper to interface between the braids and the back of the CCD's package, allowing the detector to be cooled to approximately -90°C during operation.

To improve the efficiency of the pixel scanning, the translational stage and camera were both controlled through MATLAB, providing an environment where both the Dynamic Link Libraries of the XCAM camera control system and EPICS channels of the translational stages could be interfaced (see Section 6.2.2 for further description). Translational stage movement and image capture was scripted and run automatically across a large number of sub-pixel locations without any user input. This allowed the 2D raster scans analysed in this chapter to be a practical and efficient form of experimental data to be collected.

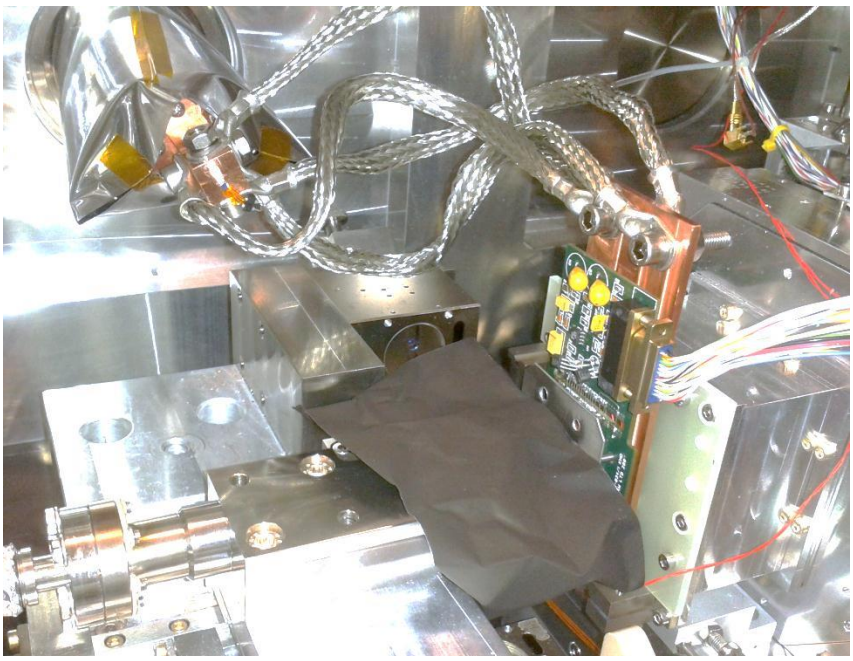

Figure 7.1. The adapted setup used in the PolLux experimental chamber for campaign 3. The X-rays are incident from the pipe (bottom-left) onto the CCD97 that is hidden by the black anodised foil. The detector's pins are connected to the green PCB, and clamped to the cold-finger using the steel sheet. The cryotiger head (top-left) is wrapped in aluminised Mylar to reduce radiative coupling, whilst a cold path is provided down tinned copper braids to the detector. This cooling setup was redesigned from campaign 2 to improve the cooling and allow the copper braids to be used effectively.

7.2.1.1 Operation of the CCD97

The CCD97 used in this work is a thinned back-illuminated device from e2v, operated in a windowed mode. An image is integrated for 0.01 seconds before a region of interest of 13×15 pixels surrounding the focussed X-ray spot is read out. This area is sufficiently large to observe the majority of the X-rays in the 0^{th} order diffraction ring whilst allowing capacity for movement when translating the focussed 1^{st} order diffraction spot. The windowing mode greatly speeds up the frame rate, allowing 26.7 windowed regions to be recorded per second with the test electronics.

The background noise in the images is dominated by the stray light in the chamber. For the 850 eV and 1000 eV data sets the total background noise is between 0.35 and 0.6 electrons rms, and for the 530 eV and 680 eV data sets it is between 0.55 and 0.8 electrons rms. The stray light was minimised by using anodised black aluminium foil to baffle around the detector.

7.2.1.2 *Locating the focal point of the 1st order diffraction X-rays*

Any measurements of the centroiding algorithms at PolLux contain a contribution from the spot size of the 1st order diffraction pattern from the FZP, therefore a significant effort was made to position the photosensitive region of the CCD pixel as close to the focal point as possible in order to minimise the spot size. Once 1000 eV X-rays were being observed in the windowed region of the detector, the CCD was translated in the *z* direction close to the focal point by maximising the ratio of signal in the central pixel compared to those surrounding it (Figure 7.2).

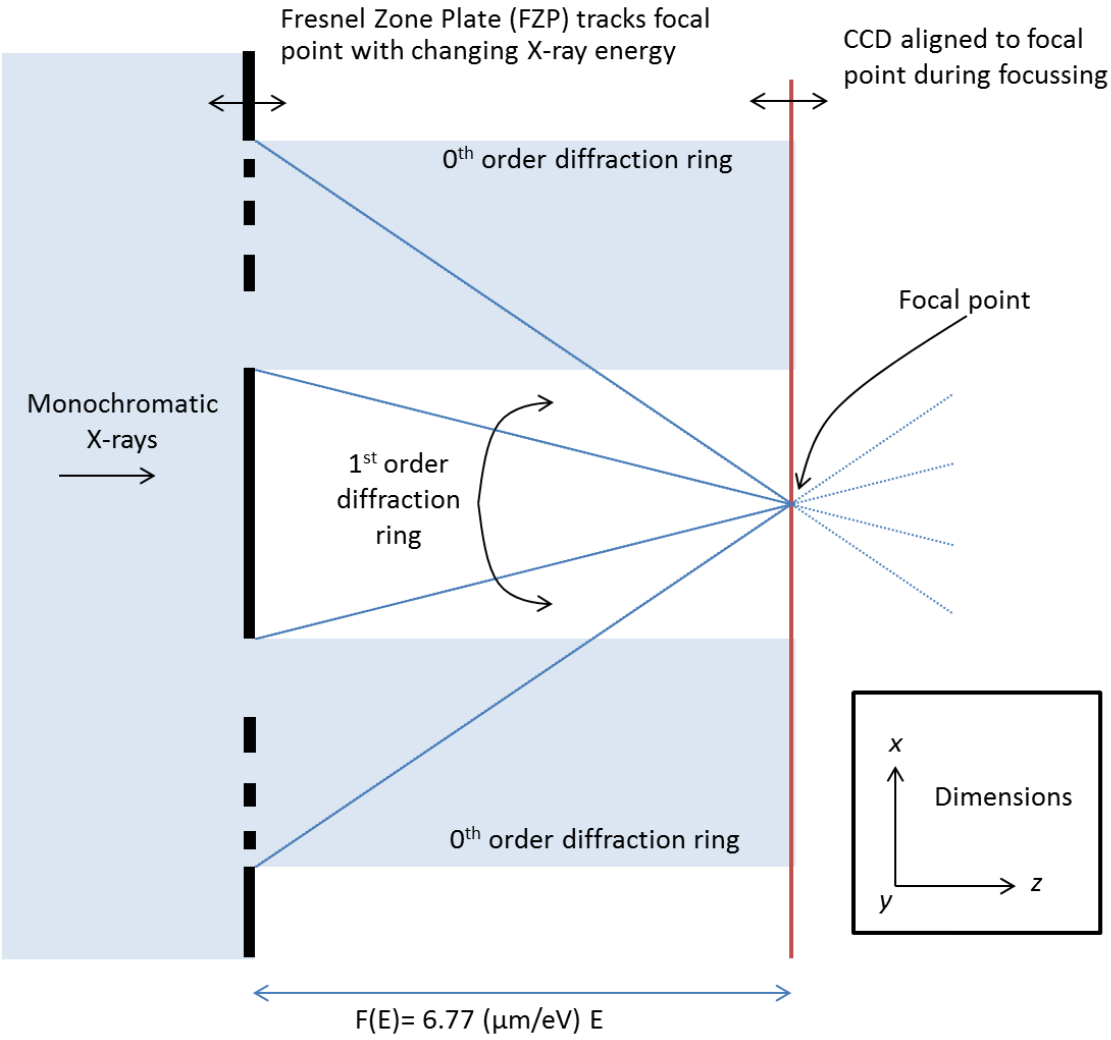

Figure 7.2. A schematic of the PolLux light path beyond the FZP with a CCD placed at the focal point of the 1st order diffraction focus. X-rays pass straight through the FZP in the 0th order diffraction ring and higher than 1st diffractions orders are not shown. The CCD is translated in the z direction to be aligned at the focal point for the current X-ray energy. When the photon energy is changed, the FZP is translated in the z direction to preserve the location of the focal point.

To confirm the focal distance objectively, the average X-ray event width as sampled by the pixels was measured over a range of focal distances (*z* locations) for the CCD translational stage. This was achieved by scanning the 1st order diffraction spot along the row, measuring the pixel signals surrounding the pile-up of photons in the 1st order spot at each location. The sampled signals were used to construct histograms which contained a peak with contributions from the spot size, and the pixel sampled charge spreading. The width of the Gaussian-like distribution reached a minimum at the *z* location of 22 mm (measured from an arbitrary zero point) as seen in Figure 7.3. The minimum indicates the focal point therefore the focussing translational stages were left at this location to capture the 2D raster scan at 1000 eV. The 850 eV data set was collected after automatically tracking the focal point with the FZP stage, where the FZP stage has been pre-programmed with the equation describing the energy dependant focal distance, $F(E) = 6.77$ (µm/eV) E (*Equation 3.4*). After the 2D scans at 850 eV and 1000 eV, the energy was changed to 530 eV and two further focus scans show the spot size was still a minimum at 22 mm (Figure 7.3).

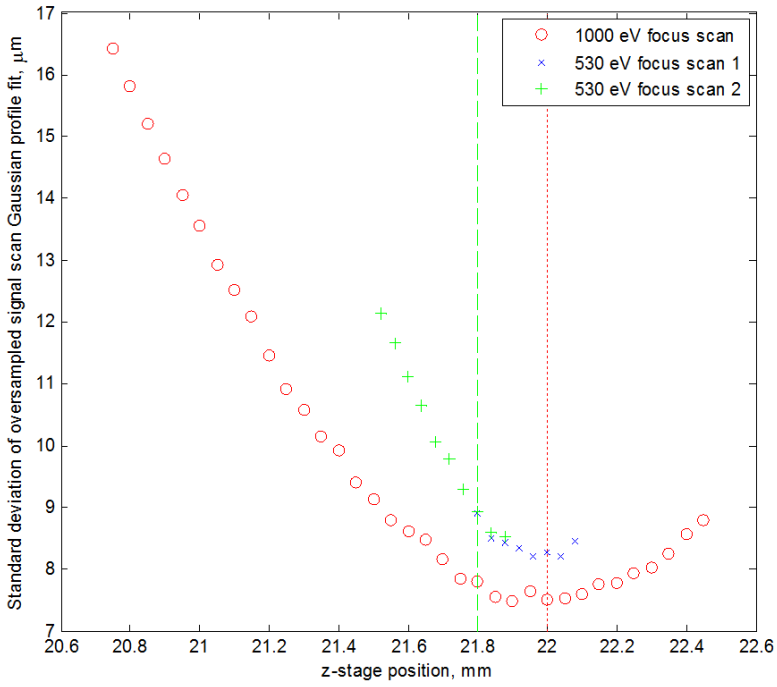

Figure 7.3. The width of the oversampled pixel signals from a row scan at each z-stage position is shown, for a single scan with 1000 eV photons and two scans with 530 eV photons. After the 1000 eV scan, the z-stage was left at 22 mm (close to the focal point), and after the 530 eV scans it was left at 21.8 mm (approximately 0.2 mm from the focal point).

However, initial analysis during the experimental campaign indicated the focal point had shifted to a stage position of 21.8 mm, due to the spot shifting by a row between energies, therefore the 530 eV scan was obtained at 21.8 mm (0.2 mm from the real focal point), with the FZP stage automatically translating for the 680 eV scan. The two lower energy scans were therefore obtained with the CCD approximately 0.2 mm from the focal point. The defocussing of the 1st order diffraction spot does not allow a pixel map of centroid resolution to be obtained, but has enabled a method of analysis that deconvolves the spot size from the resolution measurement, giving a more accurate measure of the centroid algorithm performance when the beam width is deconvolved.

7.2.1.3 Data collection and reduction

As described above, two 2D scans were obtained using 850 eV and 1000 eV photons with the CCD approximately at the focal point of the 1st order diffraction spot. A further two data sets were obtained using 530 eV and 680 eV photons at approximately 0.2 mm away from the focal position. Each data set is a raster scan consisting of 324 positions in an 18×18 grid (1 µm steps). For each raster scan, the flux is manually tuned by adjusting the entrance slits to the beamline to try and maximise the proportion of images that contain a single photon in the 1st order diffraction spot. At each position, 2100, 3500, 2000 and 2000 images were recorded for the 530 eV, 680 eV, 850 eV and 1000 eV photons respectively (Table 7.1).

Table 7.1. Summary of the four data sets collected with the CCD97.

Photon energy, eV	Approximate distance from focal point, mm	Number of images recorded at each raster scan position	Average number of single photon images per raster scan position after data reduction
530	0.2	2100	405
680	0.2	3500	660
850	0	2000	255
1000	0	2000	345

Each data set is reduced using the same method as described in Chapter 6 for the 1D scan CCD42-10 data, where images that contain the signal from a single photon in the area of the focussed 1st order X-ray spot are kept. The average number of images per scan position that

remain after the data reduction process is shown in Table 7.1. The remaining images each contain a single photon interaction event to which centroid algorithms can be applied.

7.2.2 Centroiding proof of principle

The centre of gravity centroid algorithms described in Section 6.4 have been applied to the single photon interaction events observed with the CCD97. It has been concluded in the previous chapters that the η correction algorithm should be applied to correct for the systematic error when using centroiding algorithms, therefore results using uncorrected algorithms are omitted from this chapter.

The η correction functions have been determined and applied using the same methods as in the CCD42-10 data sets (Chapter 6): single photon interaction events in the 0^{th} order outer ring of the images are extracted; the isolated events (defined as those with a proportion of signal in the central pixel that is greater than 0.9) are discarded; and the centroid locations of the remaining events are histogrammed to generate the η correction function. Isolated events are extremely rare for 530 eV and 680 eV photons, but form a significant peak in the distributions for 850 eV and 1000 eV photons (Figure 7.4) due to more interactions occurring in the depletion region as a result of the increased attenuation length at higher photon energies.

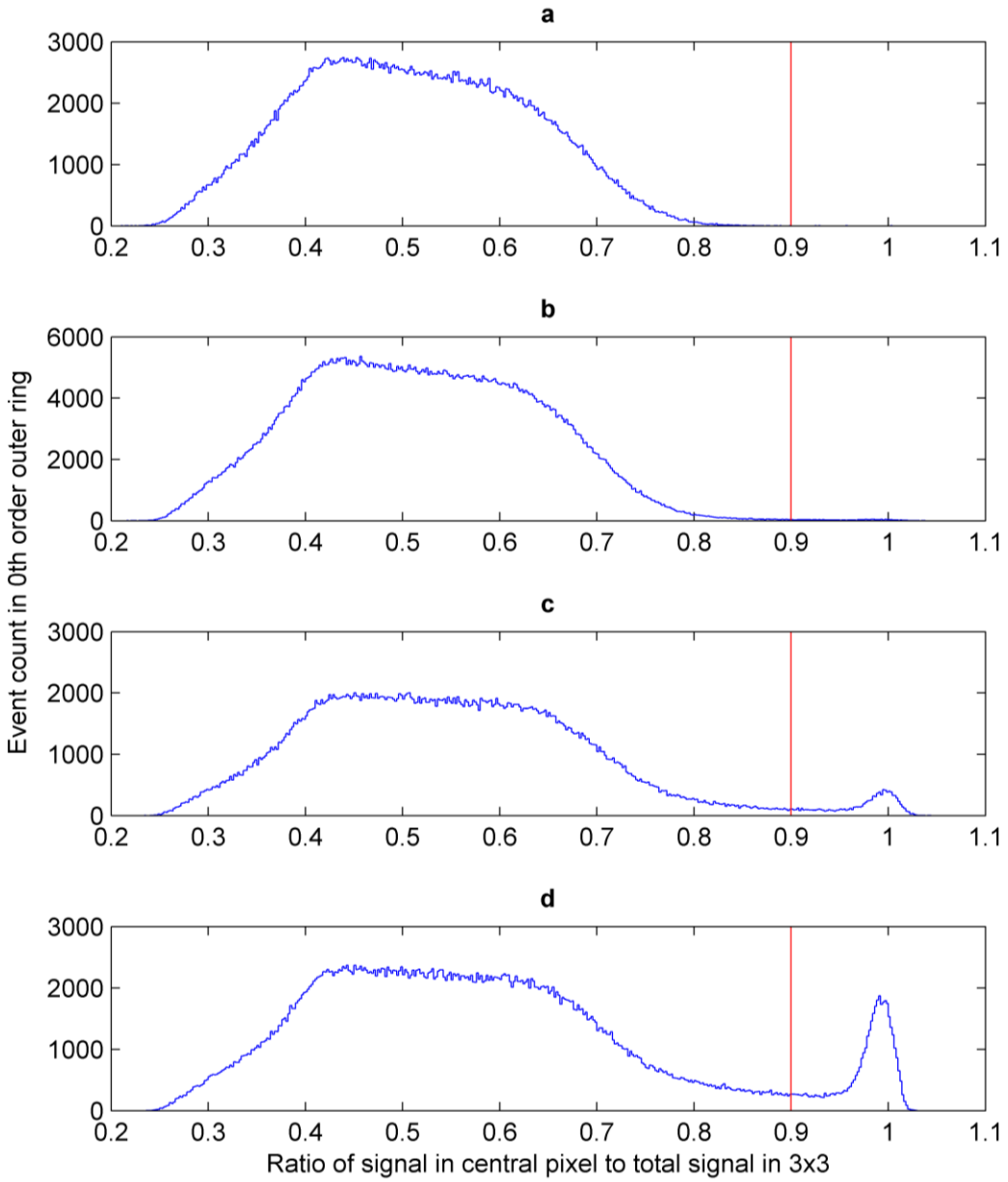

Figure 7.4. The proportion of signal in the central pixel is shown for the events extracted from the 0^{th} order diffraction ring. ***(a)***, ***(b)***, ***(c)*** *and* ***(d)*** *are for 530 eV, 680 eV, 850 eV and 1000 eV photons respectively. The isolated event threshold at 0.9, above which events are not included in the η correction function distributions, is shown as a vertical red line.*

The centroid locations of 1000 eV photons at a single scan position that were calculated using the corrected 3×3 centre of gravity algorithm are shown in Figure 7.5. As observed with the CCD42-10, the centroid locations from a single scan position are collected in a sub-pixel area, in an approximate Gaussian distribution. When binned in the *y* direction, a secondary peak is observed at the centre of the pixel (0 µm) which is formed by isolated events. When the scan

location is shifted across the pixel, the distribution of centroid locations undergoes a corresponding shift.

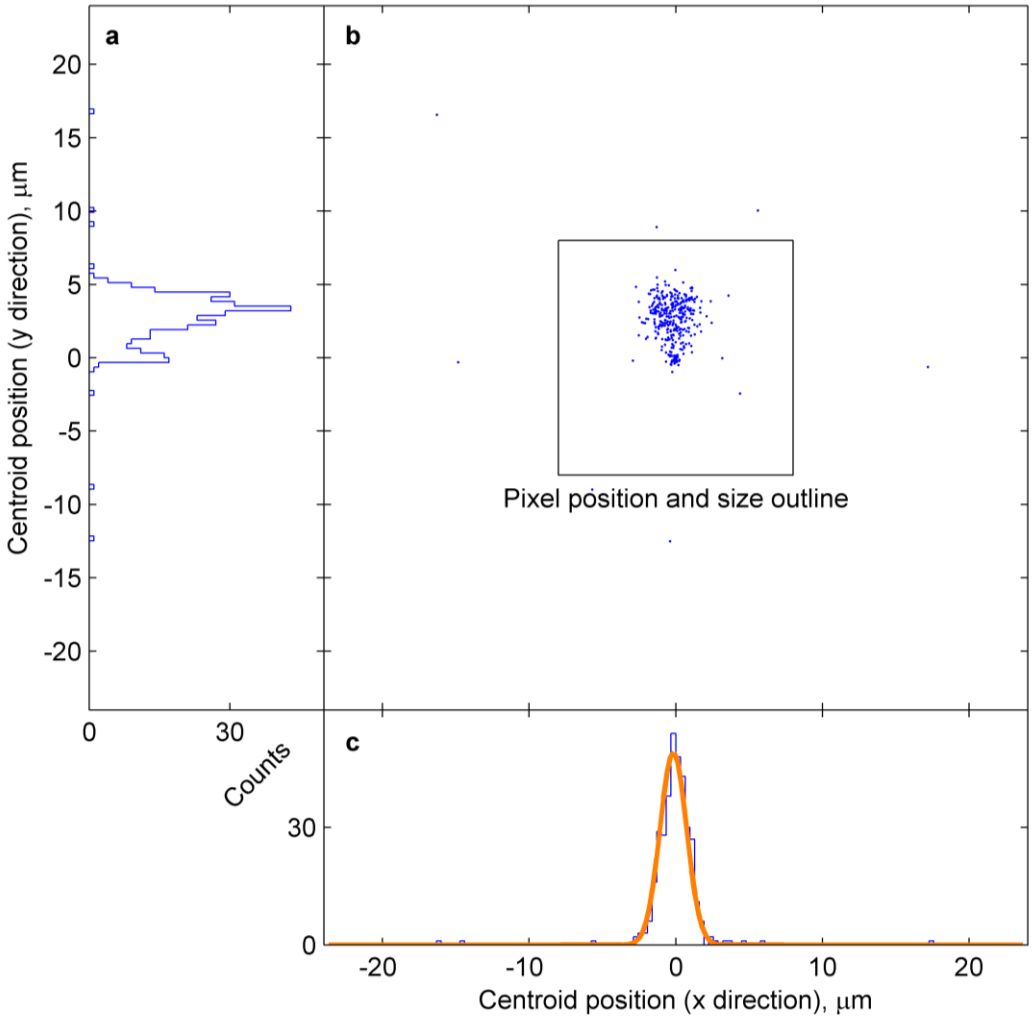

Figure 7.5. Centroid locations, determined by a corrected 3×3 centre of gravity algorithm for an example 1000 eV X-ray spot location. ***(a)*** *and* ***(c)*** *The centroids are binned into a single dimension (blue), and a Gaussian profile is fitted whose width measures the resolution achieved (orange).* ***(b)*** *The centroids are plotted in 2D relative to the pixel position, shape and size.*

7.2.3 Typical X-ray event analysis

When the event grades observed with the CCD42-10 were analysed, an observed X-ray event was classed as a certain grade if its shape matched the pixels that were over a threshold level. The threshold levels of 4 and 5 times the background noise standard deviations from the background offset were used for the CCD42-10, which was between 24 and 30 electrons above the background level (Section 6.3.6). The effective background noise level is much lower in the CCD97

data, therefore a threshold of 4 or 5 standard deviations results in a pixel with a lower level of signal to be included in the event grading, and event grades containing more than 4 pixels are significantly more common (Figure 7.6).

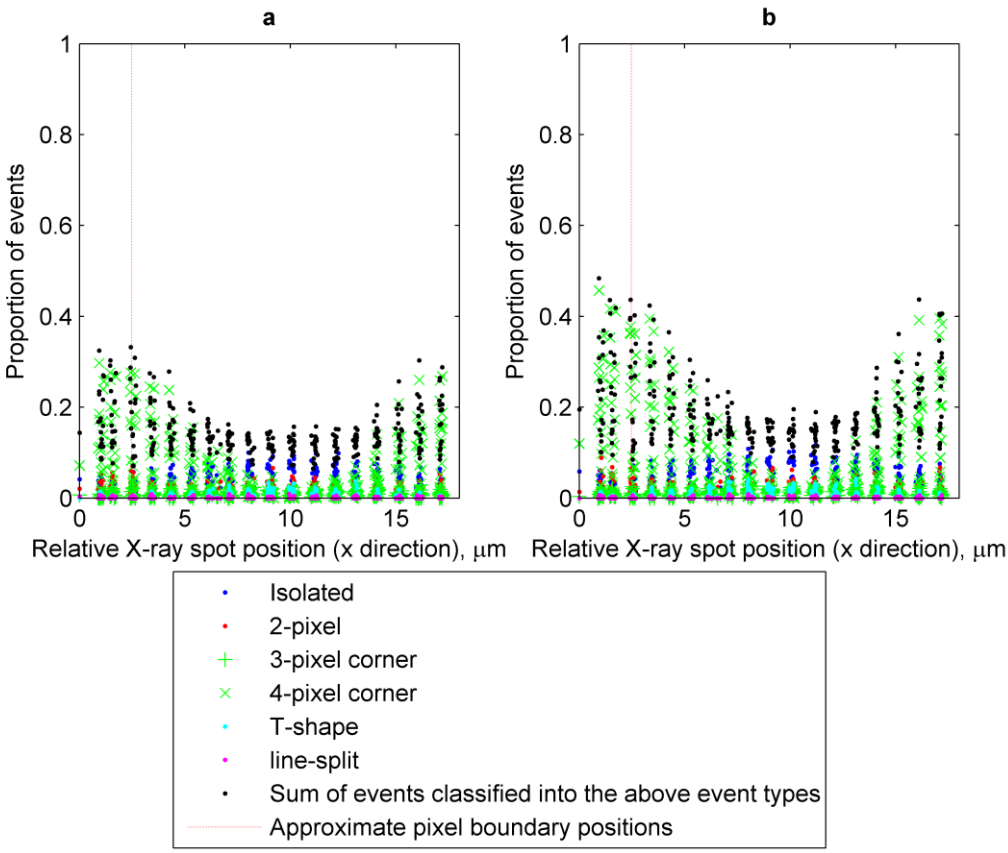

*Figure 7.6. The proportion of events observed with 1000 eV photons in the CCD97 forming the event grades described in Section 6.4 is significantly lower than observed in the CCD42-10, at both thresholds of **(a)** 4 and **(b)** 5 standard deviations from the background noise level. The background noise level in the CCD97 is much lower, therefore pixel signals containing fewer electrons are included in the event grading and event grades containing more than 4 pixels are more common.*

A threshold level of 27 electrons in the CCD42-10 data (average of 24 and 30 electrons c.f. Section 6.3.6) is equivalent to a threshold of 42.4 standard deviations from the mean background level in the CCD97 data. When this threshold level is applied, the trends of event grades observed across the pixel are very similar to those observed with the CCD42-10. The proportion of each event grade is shown as a function of the distance between the X-ray spot location (determined by the average corrected 3×3 centroid location) and the centre of the pixel in Figure 7.7.

Similar trends observed in the CCD42-10 grading are seen in the CCD97 event grades, but more trends can be observed due to the 2D information in the data:

- isolated events are common close to the centre of the pixel;
- 2-pixel events become more common close to the edge of the pixel;
- corner split events containing 3-pixel events are observed more often when the interaction occurs close to the border of the pixel;
- corner split events containing 4-pixel events are significantly more common towards the corner of the pixel; and
- T-shaped and line-split events are rare with the CCD97 at these threshold levels.

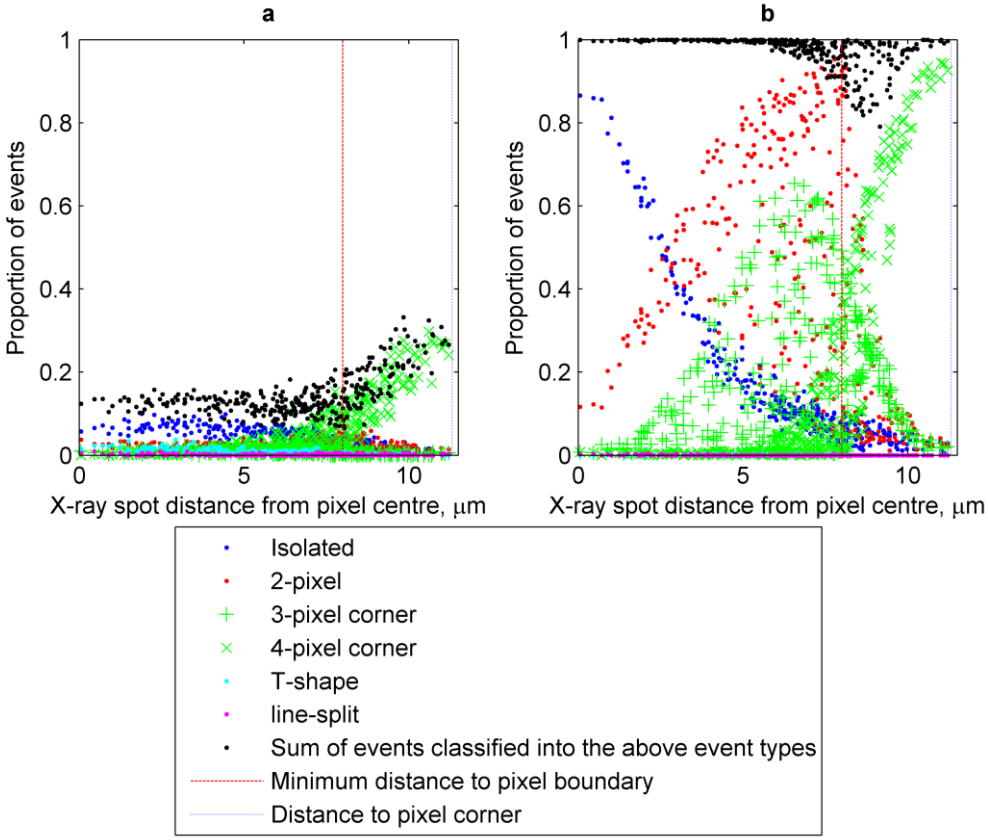

*Figure 7.7. The proportion events that form as a selection of event grades are shown as a function of the spot location for a threshold level of **(a)** 4 and **(b)** 42.4 standard deviations from the mean background level. The spot location is determined using the average 3×3 corrected centre of gravity centroid at each grid location. The pixel is assumed to be 16 μm square, so the shortest distance to the edge of the pixel is 8 μm (red dashed line), and the distance to the pixel corner is at approximately 11.3 μm (blue dotted line).*

The threshold level of 42.4 standard deviations above the noise level ignores a significant amount of signal, so more information about the actual event grades can be obtained using lower threshold levels. The number of pixels above threshold levels of 4 and 5 standard deviations from the mean is shown in Figure 7.8 for 1000 eV and 530 eV photons. For both energies, the events containing between 4 and 8 pixels above the threshold level dominate across the entire pixel area, but the average event becomes more split when the interaction occurs closer to the edge of the pixel. The events are commonly split across more than 4 but less than 9 pixels; therefore centre of gravity centroid algorithms that are applied to the pixels in a 3×3 pixel area rather than just a 2×2 pixel area should be investigated for the CCD97.

7.2.4 Sub-pixel performance of centroiding algorithms at 850 eV and 1000 eV

The '2 variable', '3 variable' and 'outer' centroiding algorithms described in Section 6.4 have been applied to the single photon interaction events observed in the focussed X-ray spot formed by the 1st order diffraction from the FZP. The resolutions obtained by each algorithm in the *x* direction (along rows, across columns) are shown as a function of the relative X-ray spot position in the *x* direction in Figure 7.9 and Figure 7.10 for 1000 eV and 850 eV photons respectively. Similarly, the resolutions in the *y* direction as a function of the spot *y* location are shown in Figure 7.11 and Figure 7.12 for 1000 eV and 850 eV photons respectively. The errors shown are derived from the 95% confidence levels of the Gaussian profile fit to the centroid locations.

Once again, the resolutions achieved with the 'outer' algorithms are worse than achieved with the '2 variable' and '3 variable' algorithms at both energies and in both dimensions. The '2 variable' and '3 variable' algorithms perform best at the edges of the pixels, and achieve a relatively constant spatial resolution in the centre half of the pixel. Isolated events are forming a second peak of centroid locations at the centre of the pixel, as seen in the *y* dimension of Figure 7.5, widening the Gaussian profile fit when the peaks are in close proximity. The effect is most noticeable in the 1000 eV data where more isolated events are present, and the hypothesis is supported by the fact there is a slight improvement in the resolution at the centre of the pixel where both the split and isolated events are centroided to the same location.

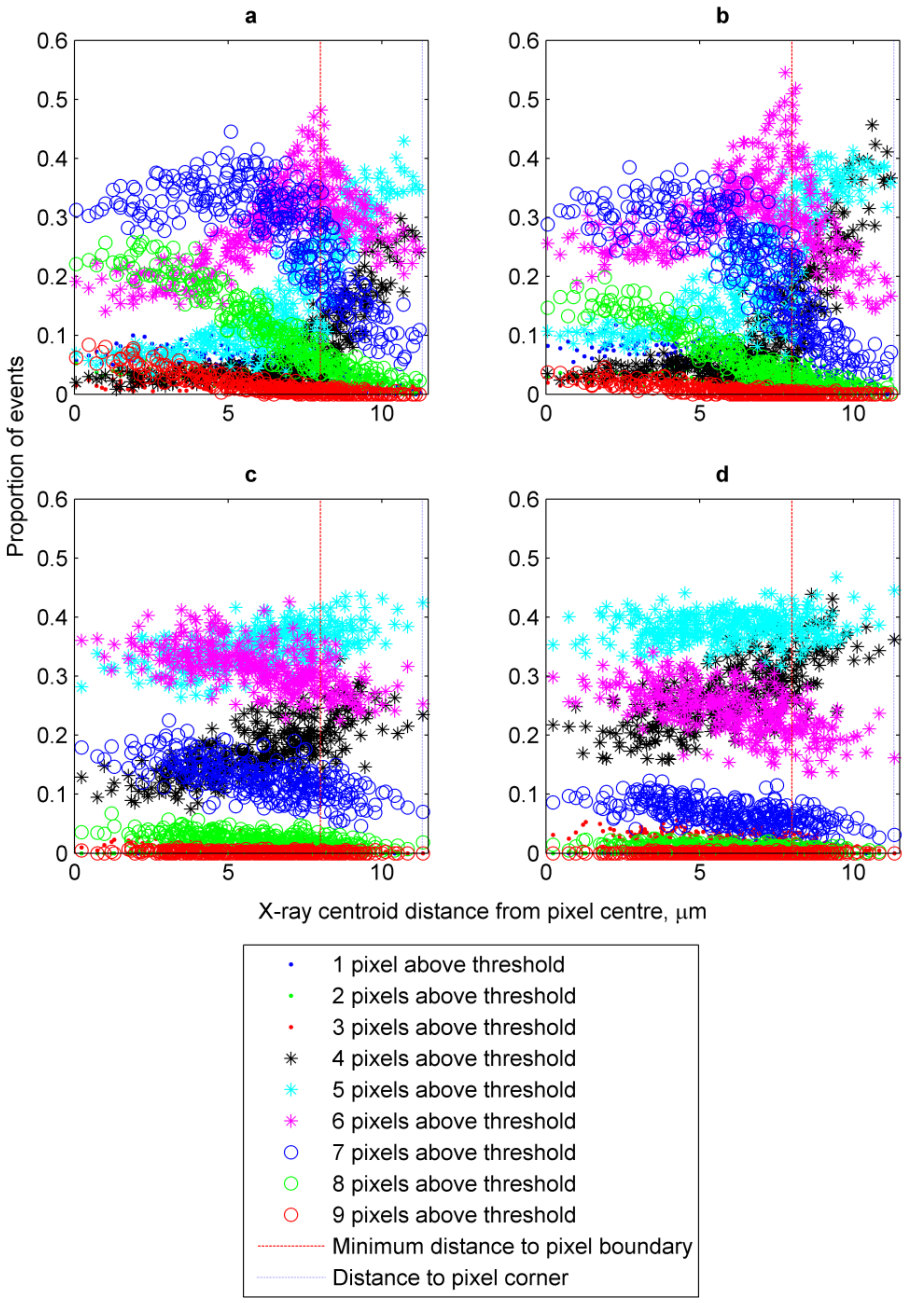

Figure 7.8. ***(a)*** *The proportion of events observed that have a given number of pixels with signal over 4 standard deviations from the background level, for 1000 eV photons. The same is shown in* ***(b)*** *for a threshold of 5 standard deviations, for 1000 eV photons.* ***(c)*** *and* ***(d)*** *show the distributions for 530 eV photons, with thresholds of 4 and 5 standard deviations from the background level respectively.*

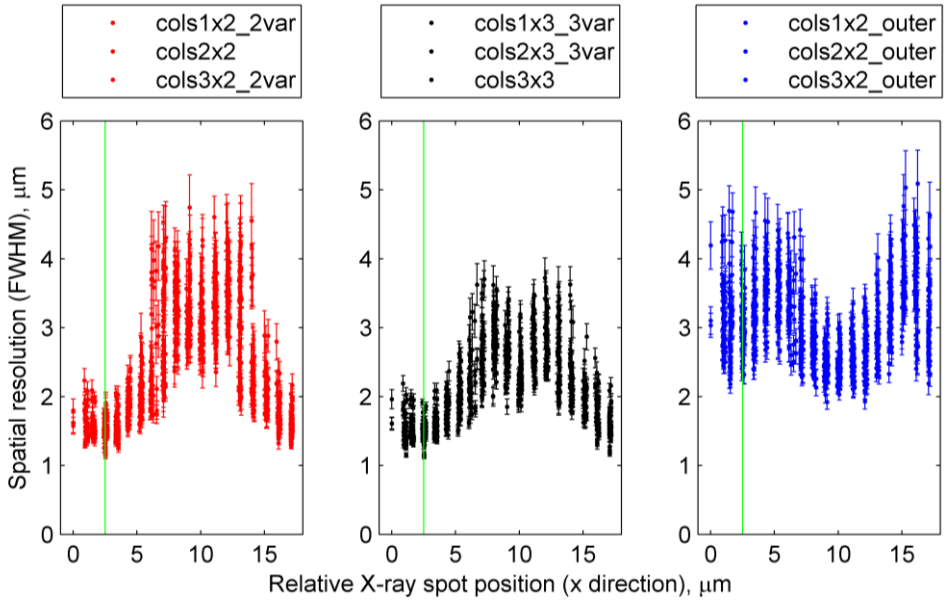

Figure 7.9. The spatial resolution of centroid algorithms plotted as a function of stage position across the pixel. These plots show the resolutions measured across the columns (x dimension) for 1000 eV photons. Approximate pixel boundaries are shown by the green vertical lines.

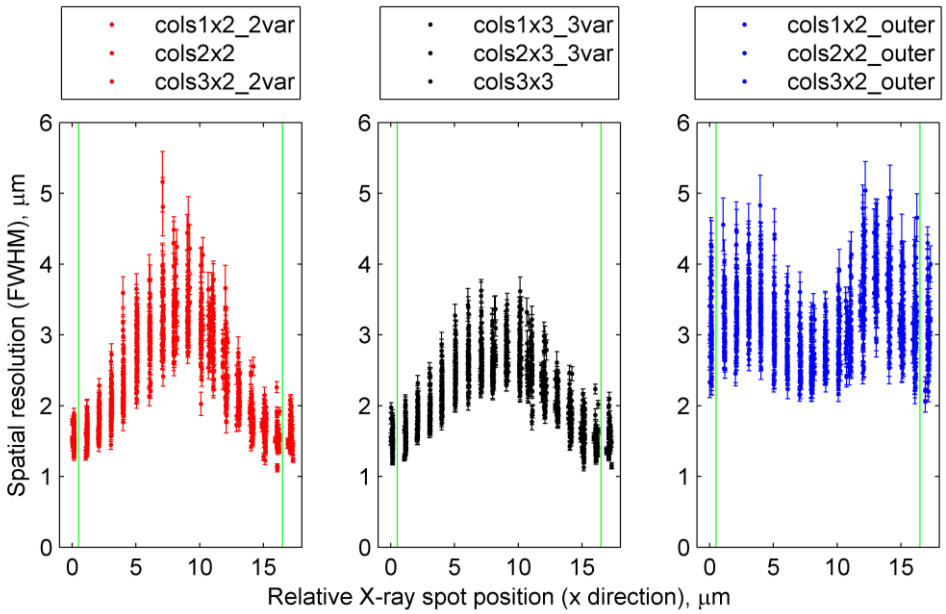

Figure 7.10. Same as Figure 7.9, for 850 eV photons, with the resolution measured across the columns (x dimension).

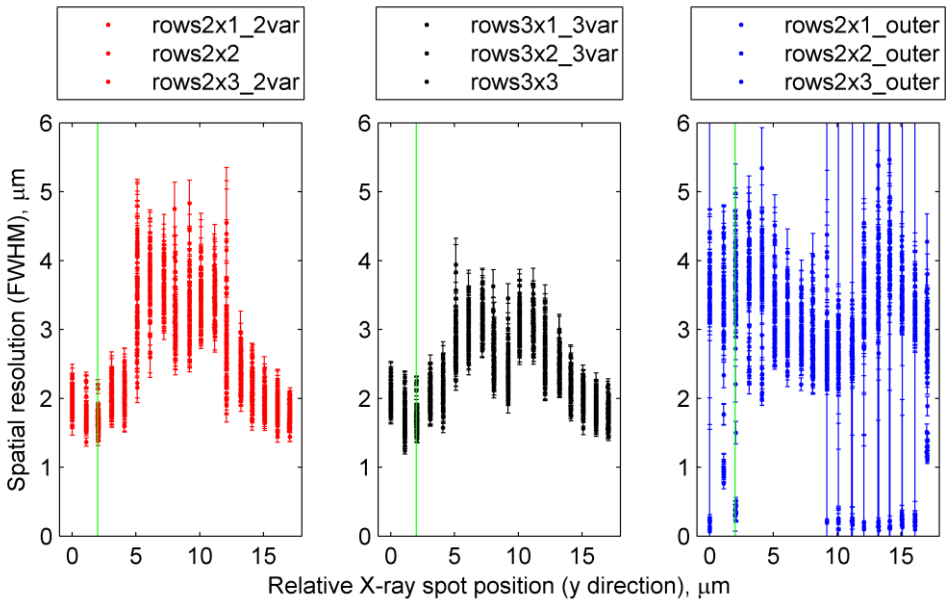

Figure 7.11. Same as Figure 7.9, for 1000 eV photons, with the resolution measured across the rows (y dimension).

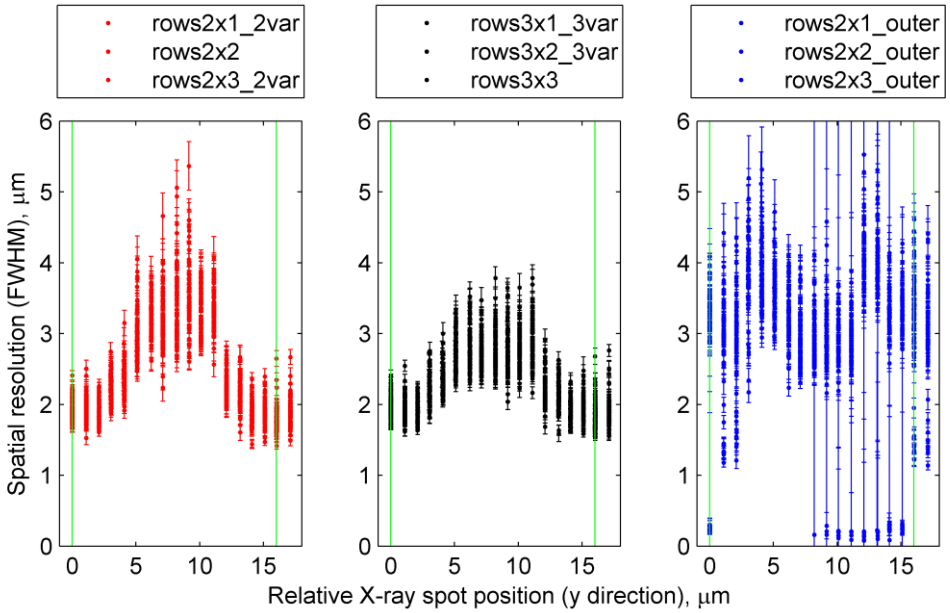

Figure 7.12. Same as Figure 7.9, for 850 eV photons, with the resolution measured across the rows (y dimension).

To compare the resolutions achieved with the '2 variable' and '3 variable' algorithms as a function of 2D sub-pixel interaction position relative to the pixel boundaries, Figure 7.13 and Figure 7.14 are presented containing the 1000 eV and 850 eV data respectively. The data points are calculated by averaging the resolution achieved at that spot location using the type of algorithm (either '2 variable' or '3 variable') and the errors are determined from the average error for each algorithm type. A larger square data point at a spot location represents a smaller average error, where the minimum and maximum average errors are 0.03 µm and 0.65 µm.

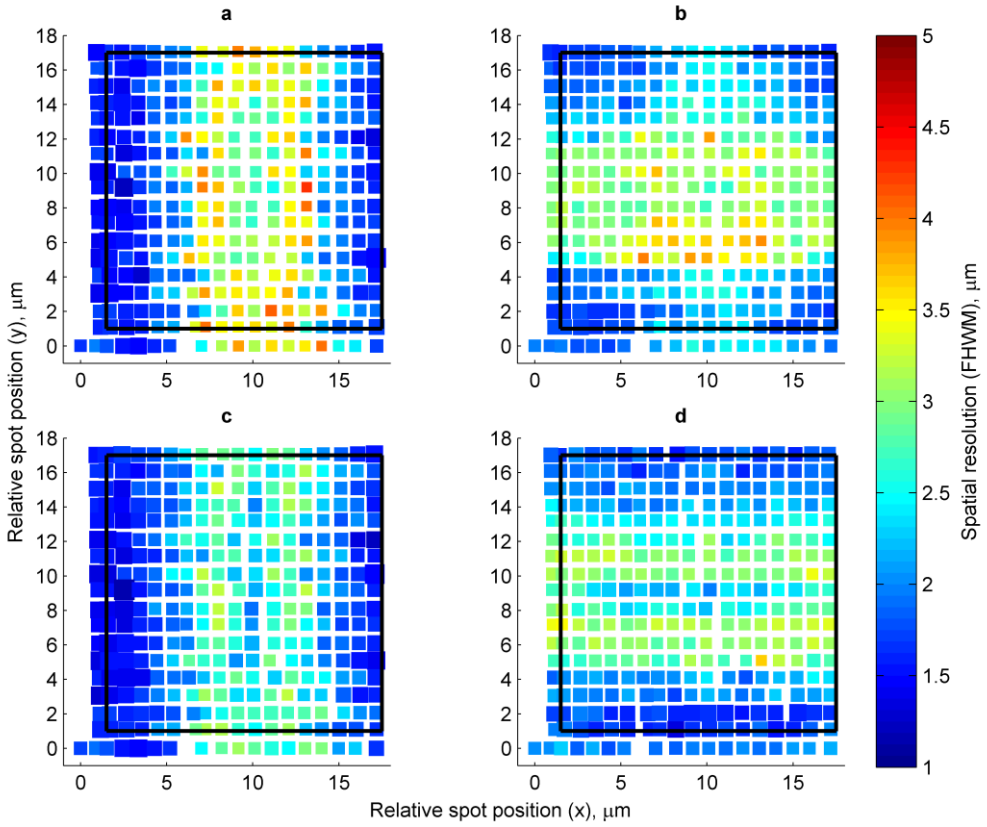

*Figure 7.13. The spatial resolution achieved with the '2 variable' (**a**, **b**) and '3 variable' (**c**, **d**) algorithms at each sampled sub-pixel location is shown for the 1000 eV photons. The resolution in the x (y) direction is shown in **a** and **c** (**b** and **d**), and a black rectangle is overlaid to show the approximate location of the pixel boundaries.*

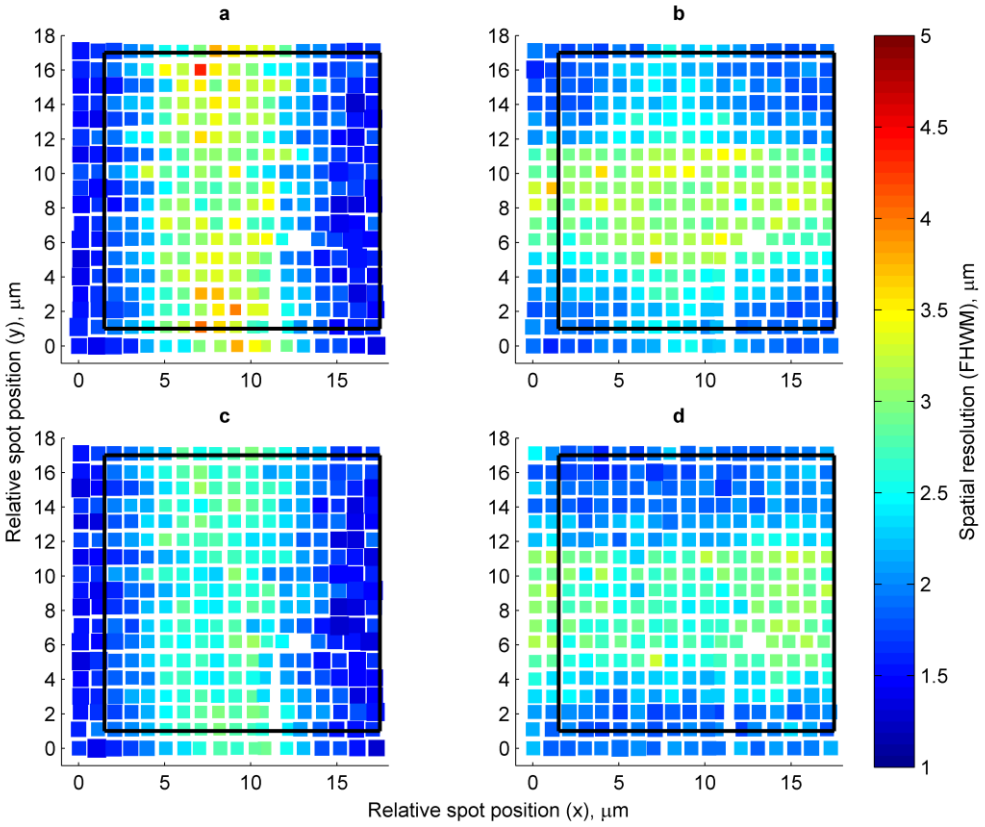

*Figure 7.14. Same as Figure 7.13 for 850 eV photons. The spatial resolution achieved with the '2 variable' (**a**, **b**) and '3 variable' (**c**, **d**) algorithms is shown at each spot position. The resolution in the x (y) direction is shown in **a** and **c** (**b** and **d**), and a black rectangle is overlaid to show the approximate location of the pixel boundaries.*

To measure the overall resolution averaged across the pixel for each algorithm, direction (*x* or *y*) and photon energy, the centroid locations from every spot location are selected. Each centroid location is offset by the average centroid location for its beam spot position constructing a point spread function (PSF), Figure 7.15 for example. The PSFs are fitted with a 2D Gaussian profile with independent standard deviations for the horizontal and vertical spreads resulting in the fitted widths shown in Figure 7.16.

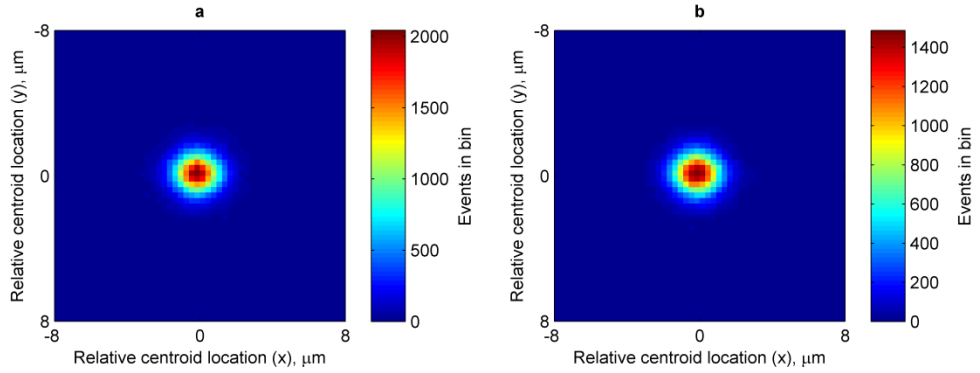

*Figure 7.15. The point spread functions constructed from all the centroid locations calculated using the corrected 3×3 centre of gravity algorithm, for **(a)** 1000 eV and **(b)** 850 eV photons.*

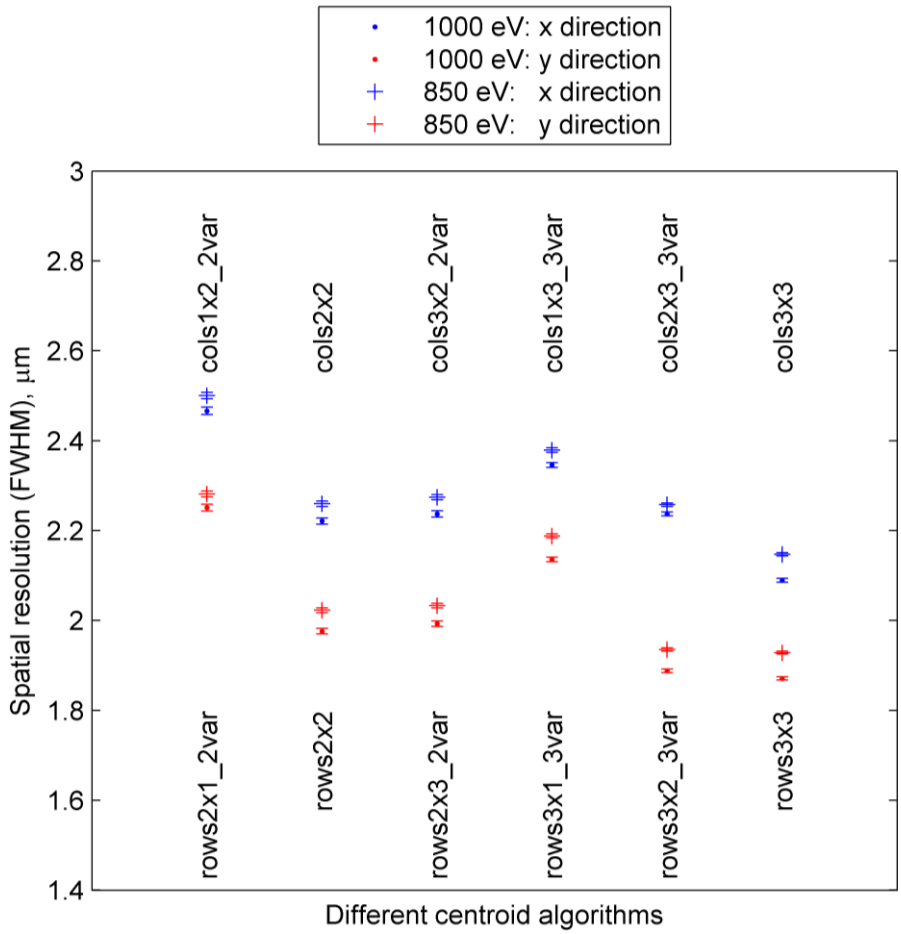

Figure 7.16. The spatial resolution for each photon energy, algorithm and dimension are measured by fitting the PSFs (like Figure 7.15) with a 2D Gaussian profile. The 95% confidence levels in the fitted parameter are shown in the figure, but are all less than 0.008 µm so are barely visible.

Across all the algorithms, the resolutions achieved in the *y* direction are better than in the *x* direction by approximately 0.2 µm. The difference may be due to the charge cloud in the *y* direction being wider, which would result in the signal being more split in the *y* direction. This will be discussed further in Section 7.3. The resolutions with 1000 eV photons are also approximately 0.04 µm better than when the algorithms are applied to the 850 eV events, which could be due to the improved signal to noise ratio, or a systematic error such as the beam size being larger for the 850 eV events.

The algorithm that performs best in both directions and for both energies is the corrected centre of gravity algorithm applied across a 3×3 pixel area, with the measured resolutions shown in Table 7.2. The best-case resolutions, with values around 2 µm (FWHM), agree well with the resolution expected from simulating events in an EM-CCD (Figure 5.21).

Table 7.2. Spatial resolution (FWHM) achieved with the corrected centre of gravity algorithm applied across a 3×3 pixel area, as measured by a Gaussian profile fit to the PSF for each energy data set and in each direction. Errors are less than 0.004 µm.

Photon energy	**850 eV**	**1000 eV**
x direction, µm	2.15	2.09
y direction, µm	1.93	1.87

The resolution measurements include a contribution from the size of the focussed X-ray spot whose size is known to be between 20 nm (the minimum size at the focal point [71]) and 1.87 µm (the best resolution achieved with the centroiding algorithms). Therefore, these measurements for the achieved resolution at 850 eV and 1000 eV are worst-case, and the deconvolved spatial resolution measurement may be smaller than those presented if the beam size is taken into account.

The 850 eV and 1000 eV data sets were recorded with the CCD close to the focal point, as confirmed by the Gaussian-like PSFs (Figure 7.15). However the lower energy data sets, observing 530 eV and 680 eV photons, were collected with the CCD approximately 0.2 mm from the focal point. The defocussing of the 1st order diffraction spot allows the spot contribution to the resolution measurement to be deconvolved, as described in the following sections.

7.2.5 Deconvolving the X-ray spot size from the 530 eV and 680 eV spot

Unlike the 850 eV and 1000 eV data sets, the 530 eV and 680 eV scans were recorded with the CCD located at 0.2 mm from the focal point. This opens up the possibility of deconvolving the shape of the 1st order diffraction pattern from the centroiding accuracy PSFs. In this section, limits on the size of the 1st order diffraction pattern are geometrically derived to be compared to the distributions of centroid locations. The worst-case resolution is measured from these distributions, before a model is used to deconvolve the 1st order diffraction pattern to obtain a measurement of the resolution.

7.2.5.1 Calculating geometric limits on the expected defocussed spot size

When the CCD is shifted away from the energy dependant focal distance, $F(E)$, the distribution of X-rays diffracted from the FZP in the 1st order forms a ring with an outer diameter d_{image}. From the geometry in Figure 7.17, the relationship in *Equation 7.1* can be derived given that f is the distance from the FZP to the CCD.

$$d_{image} = \frac{f - F(E)}{F(E)} d_{FZP} \qquad \textit{Equation 7.1}$$

The 850 eV and 1000 eV data sets analysed in the previous section were recorded when the CCD was located approximately at the focal point. d_{FZP} = 240 µm for the FZP and the spot size (d_{image}) was measured to be less than 1.87 µm at 1000 eV and less than 1.93 µm at 850 eV (Table 7.2), therefore the following limits can be set for the maximum offset between the CCD and the focal point using *Equation 7.1*.

1000 eV: $$|f - F(E)| < 52.7\ \mu m \qquad \textit{Equation 7.2}$$

850 eV: $$|f - F(E)| < 46.3\ \mu m \qquad \textit{Equation 7.3}$$

The more restricting limit is set by the result at 850 eV in *Equation 7.3*, and so shall be carried forward. The 530 eV and 680 eV data sets were recorded with the CCD shifted at a distance of approximately 0.2 mm from the focal point (location B in Figure 7.17), in the direction away from the FZP, therefore limits can be set on $f - F(E)$ for the two lower energy data sets.

530 eV and 680 eV: $$153\ \mu m < f - F(E) < 247\ \mu m \qquad \textit{Equation 7.4}$$

Equation 7.4 can be used to set the expected limits on the outer diameter of the defocussed 1st order diffraction ring, d_{image}, that is observed in the 530 eV and 680 eV data sets.

530 eV: $$10.3\ \mu m < d_{image} < 16.5\ \mu m \qquad \textit{Equation 7.5}$$

680 eV: $$8.0\ \mu m < d_{image} < 12.8\ \mu m \qquad \textit{Equation 7.6}$$

The limits shown in *Equation 7.5* and *Equation 7.6* suggest that the expected ring-like defocussed 1st order X-rays will result in X-rays interacting across an area of roughly half to a full pixel which implies that the individual locations in the raster scan cannot be used to investigate the resolution at each sub-pixel location. However, the PSF from all centroid locations can be combined and as shown in the next section, the centroiding resolution is sufficiently small to resolve the ring-like distribution of X-ray interaction locations.

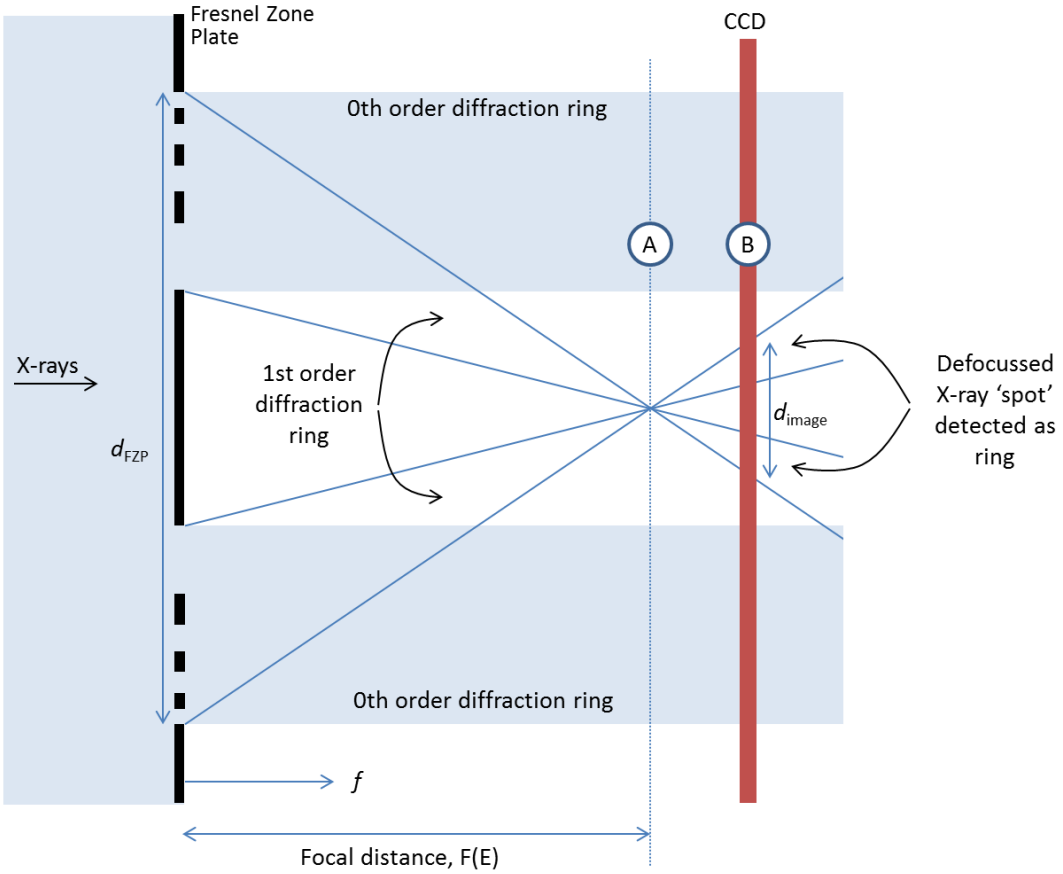

Figure 7.17. A schematic of the experimental setup whilst the 530 eV and 680 eV data sets were recorded: the CCD was placed at location B, approximately 0.2 mm from the focal point (location A).

7.2.5.2 Observing the defocussed 1st order X-ray diffraction ring

The distribution of X-rays incident on the FZP is not a flat field, as observed in the 0th order diffraction ring in the average image recorded at each energy (Figure 7.18 a and b). The distribution of X-rays in the 1st order diffraction ring is seen in the PSF formed from the centroid locations of the X-rays in the defocussed spot (Figure 7.18 c and d). The distributions are mirrored about their centres due to the CCD being placed beyond the focal point. The dimensions of the

PSF relative to the pixel size can be observed, and are within the ranges expected by the analysis in the previous section (*Equation 7.5* and *Equation 7.6*).

The PSF is rotationally averaged (Figure 7.18 e and f), and a cross-section taken to reduce the following analysis in this section to a 1D problem (Figure 7.18 g and h). The outer ring widths of the cross-sections are within the expected ranges for d_{image}, as shown by the red horizontal scales. A worst-case resolution limit can be measured from the cross-sections by fitting a portion of the ring using a Gaussian profile (shown). The worst-case resolution limits for the '2 variable' and '3 variable' algorithms are shown in Figure 7.19.

In order to improve on this worst-case measurement, the X-ray distribution within the ring must be deconvolved from the cross-section. Whereas this was not possible for the Gaussian-like PSF obtained at 850 eV and 1000 eV, it is now possible with the ring shape distributions obtained using the lower energy photons.

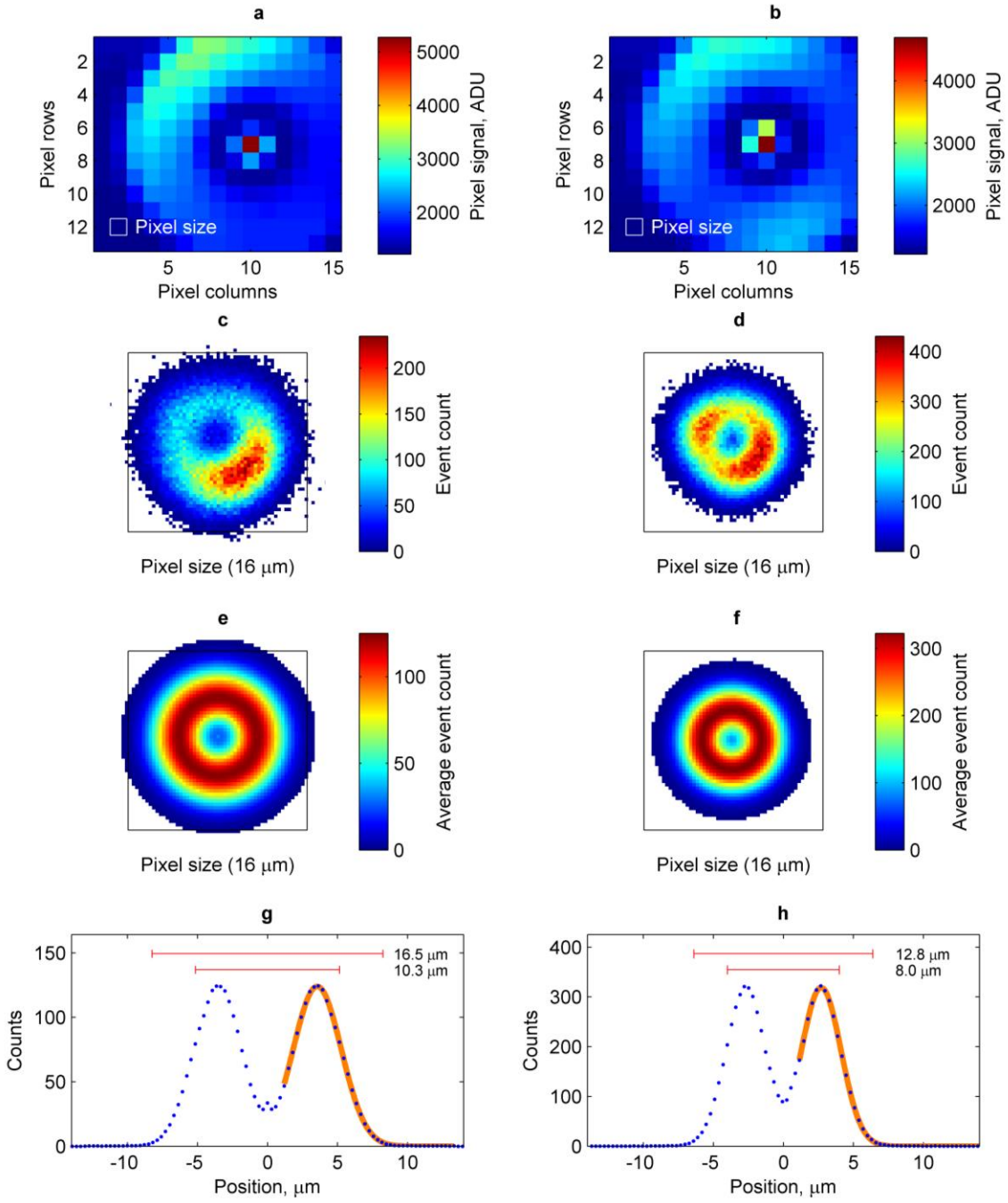

Figure 7.18. The plots for 530 eV (680 eV) are shown on the left (right). ***(a)*** *and* ***(b)*** *The average image recorded.* ***(c)*** *and* ***(d)*** *The distribution of centroid locations from the photon interaction events in the 1st order diffraction spot.* ***(e)*** *and* ***(f)*** *The distribution of centroid locations when rotationally averaged.* ***(g)*** *and* ***(h)*** *A Gaussian profile can be fitted to a portion of the cross-section to determine a worst-case resolution measurement.*

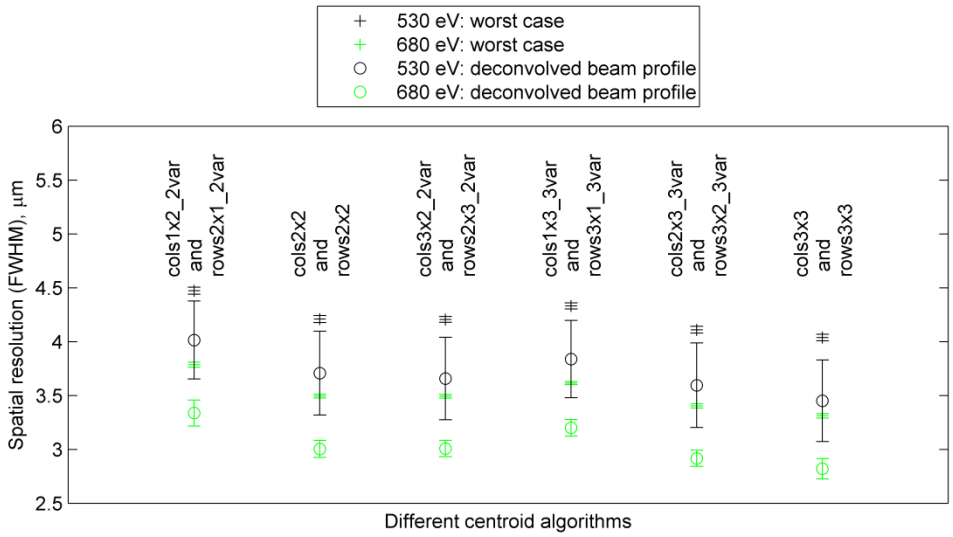

Figure 7.19. The worst-case resolutions, obtained by fitting the ring feature of the rotationally averaged centroid location cross-section, and the resolutions with the beam profile deconvolved (Section 7.2.5.3) are shown for each of the '2 variable' and '3 variable' centroiding algorithms. The errors shown are from the 95% confidence levels of the fitting parameters.

7.2.5.3 Deconvolving the defocussed X-ray spot from the cross-section centroid distribution

Assuming the rotationally averaged distribution of X-rays in the defocussed 1st order ring is radially constant, its cross-section can be modelled using two top-hat functions (Figure 7.20). The inner and outer (d_{image}) diameters of the top-hat ring are scaled to represent the changing distribution as the CCD is shifted towards and away from the focal point. The top-hat functions are then convolved with a Gaussian profile whose width models the centroid accuracy contribution to the PSF.

The experimental cross-section (Figure 6.18 g and h) is fitted using the convolved Gaussian profile and top-hat distribution, where the projected X-ray distribution width d_{image} and the width of the Gaussian profile are varied. The resulting fits to the X-ray distribution cross-section obtained using the corrected 3×3 centre of gravity algorithm are shown for 530 eV and 680 eV in Figure 7.20.

The centroid resolution is measured by the FWHM of the Gaussian profile in the best fitting model obtained using a least square regression fit. The resolutions obtained by deconvolving the top-hat beam profile with the '2 variable' and '3 variable' algorithms are shown in Figure 7.19, where they can be compared with the worst-case measurements.

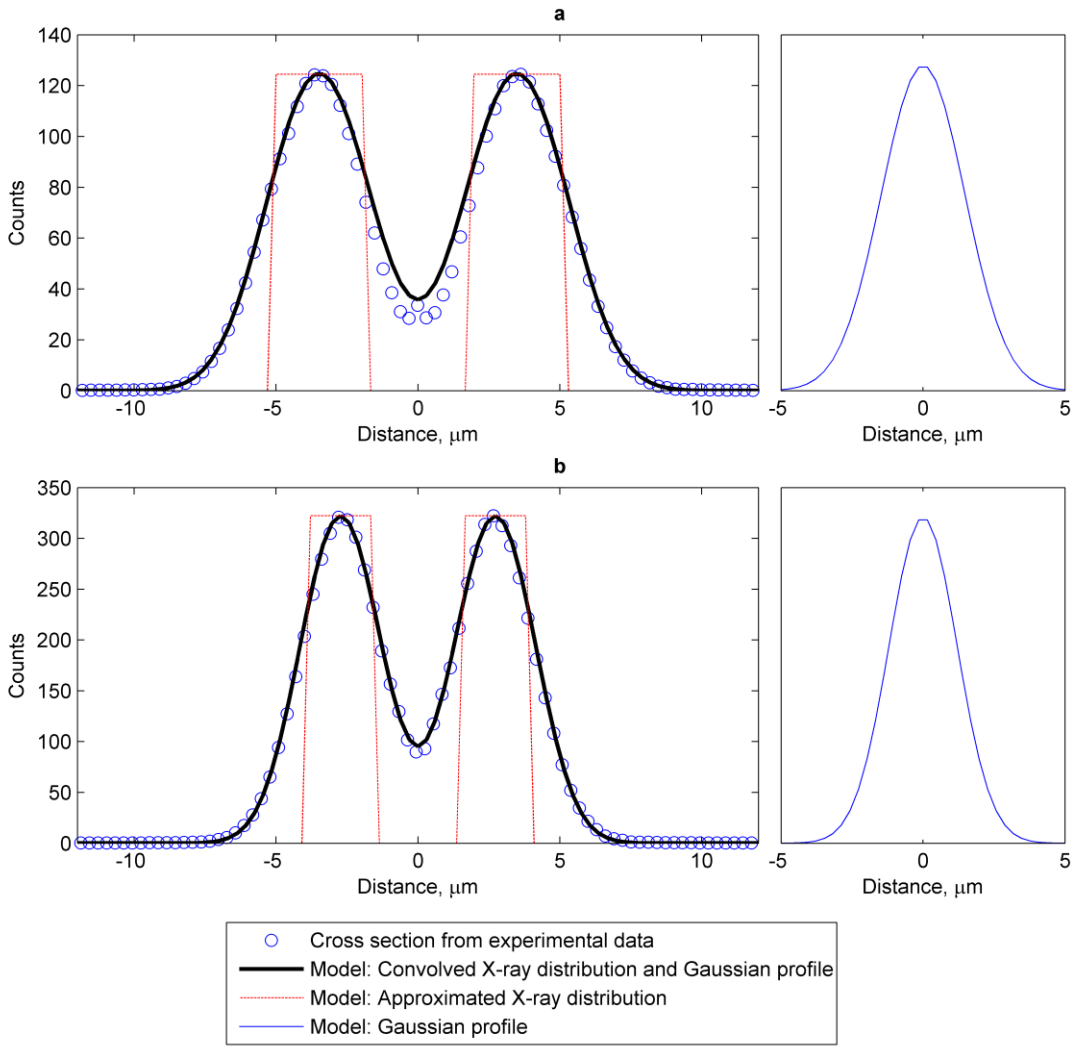

*Figure 7.20. The cross-section of the rotationally averaged **(a)** 530 eV and **(b)** 680 eV centroid location histogram (blue circles) is taken from Figure 7.18 g and h. The cross-sections are modelled using top-hat functions to represent the averaged incident X-ray distribution (red dashed line) convoluted with a Gaussian (blue solid line). The least square regression fit is shown (black solid line).*

The fitted X-ray distribution width, d_{image}, for each algorithm is shown in Figure 7.21. The fitted widths are expected to be energy-dependent but algorithm-independent and in general the fitted d_{image} values agree with this expectation, although there is a relatively large variation between the 680 eV values. The limits calculated geometrically in Section 7.2.5.1 are shown for comparison, and the fitted values appear at the lower range of or smaller than the expected limits. It is likely that the X-ray distribution in the ring is not well modelled by the two top-hat functions, but is a smoother function. To compensate for this in the model used here, the fitted

d_{image} is too small and the fitted Gaussian is too wide. This reasoning suggests that the deconvolved resolutions measurements in Figure 7.19 are also worst-case.

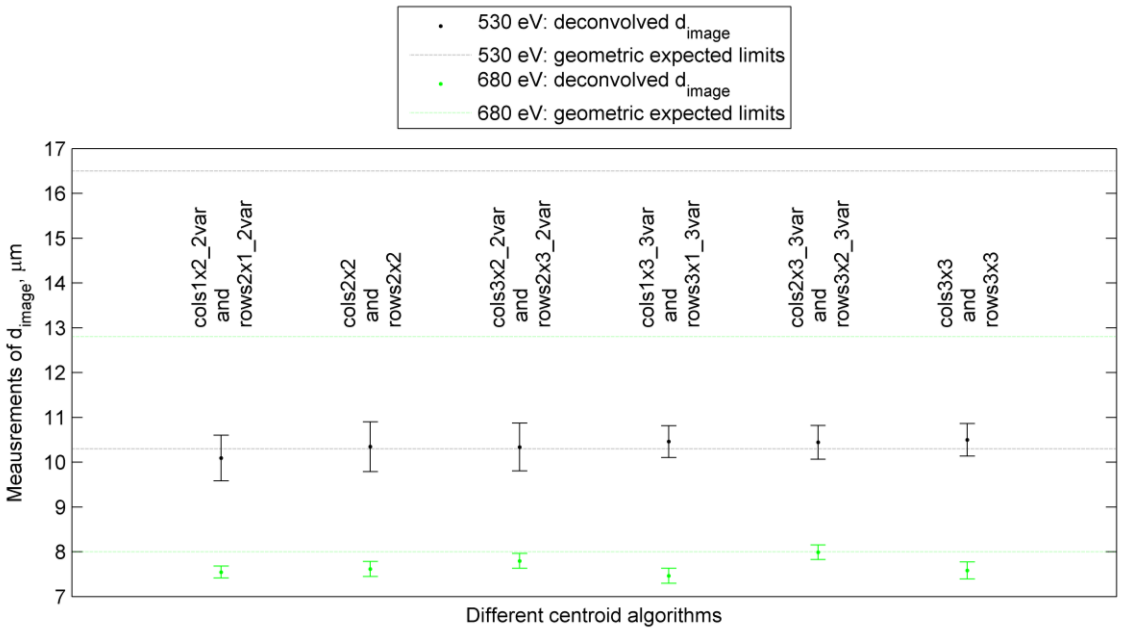

Figure 7.21. The fitted widths of the X-ray interaction distribution, d_{image}, from deconvolving the rotationally averaged centroid distribution cross-section Figure 7.20.

Of the 6 centroiding algorithms investigated, the centre of gravity algorithm that is applied across a 3×3 pixel area (cols3x3 in the *x* direction and rows3x3 in the *y* direction) performs with the best resolution, summarised in Table 7.3. The worst-case resolution determined by fitting the ring feature of the PSF is 4.04±0.03 µm and 3.31±0.02 µm for 530 eV and 680 eV photons respectively. A top-hat model has been used to deconvolve the X-ray spot shape distribution, resulting in a fitted spatial resolution of 3.45±0.38 µm and 2.82±0.09 µm for 530 eV and 680 eV photons respectively. The deconvolved spatial resolution results are also worst-case, as the real X-ray distribution in the 1st order diffraction ring is not flat with sharp sides like the top-hat function.

Table 7.3. Spatial resolution measurements obtained at 530 eV and 680 eV using the η-corrected centre of gravity centroid algorithm applied across a 3×3 pixel area.

Worst-case resolution measurements	**530 eV photons**	**680 eV photons**
Resolution without deconvolving	4.04±0.03 µm	3.31±0.02 µm
Resolution with the X-ray source size deconvolved	3.45±0.38 µm	2.82±0.09 µm

7.2.6 Discussion of the spatial resolution measurements with the CCD97

Spatial resolution measurements obtained using centroid algorithms applied to soft X-ray events detected using a CCD97 have been presented in this chapter. Following the successful experimental campaign and results obtained during campaign 2 at PolLux, the setup was modified to improve the device cooling and streamline the process of recording images whilst the X-ray spot was rastered across a 2D grid of sub-pixel locations. The process was efficient enough to allow a 2D raster scan at four different soft X-ray energies and the improved cooling, combined with operating the EM-CCD at a high gain setting, allowed the detector to be operated with a background noise of below 0.8 electrons rms throughout the experiment.

A more objective method was employed for ensuring the detector was at the focal point of the 1st order diffraction pattern from the FZP, than during campaign 2 with the CCD42-10. The 1000 eV and 850 eV data sets were recorded with the CCD less than 52.7 µm from the focal point (*Equation 7.2*) however, an error during the experimental campaign resulted in the low energy data sets (680 eV and 530 eV) being recorded with the CCD shifted by 0.2 mm away from the focal point.

The well-focussed X-ray spot in the higher energy data sets allowed the spatial resolution to be investigated as a function of sub-pixel interaction position, and the overall PSF of the centroid algorithms were measured showing a consistently better resolution in the *y* direction than the *x* direction (Figure 7.16). The X-ray spot is defocussed into a clearly resolvable ring-like structure in the lower energy data sets, therefore it was possible to model the X-ray distribution diffracted by the FZP and deconvolve the contribution of the source from the resolution measurements (Section 7.2.5).

Across the energy range from 530 eV to 1000 eV, the η-corrected centre of gravity algorithm that was applied to a 3×3 pixel area resulted in the best resolution. The resolutions achieved by this

algorithm, shown in Table 7.2 and Table 7.3, have been summarised in Table 7.4 and compared to the resolution performance predicted by simulation (Section 5.4) in Figure 7.22.

Table 7.4. The worst-case spatial resolution measurements achieved with the CCD97, from the data recorded during campaign 3 at PolLux.

Energy, eV	Spatial resolution (FWHM), µm	Method of measurement
530	3.45±0.38	The 1st order diffraction distribution has been deconvolved from the PSF measurement
680	2.82±0.09	
850 (errors < 0.004 µm)	*x* direction: 2.15 *y* direction: 1.93	The PSF is fitted by a 2D Gaussian profile
1000 (errors < 0.004 µm)	*x* direction: 2.09 *y* direction: 1.87	

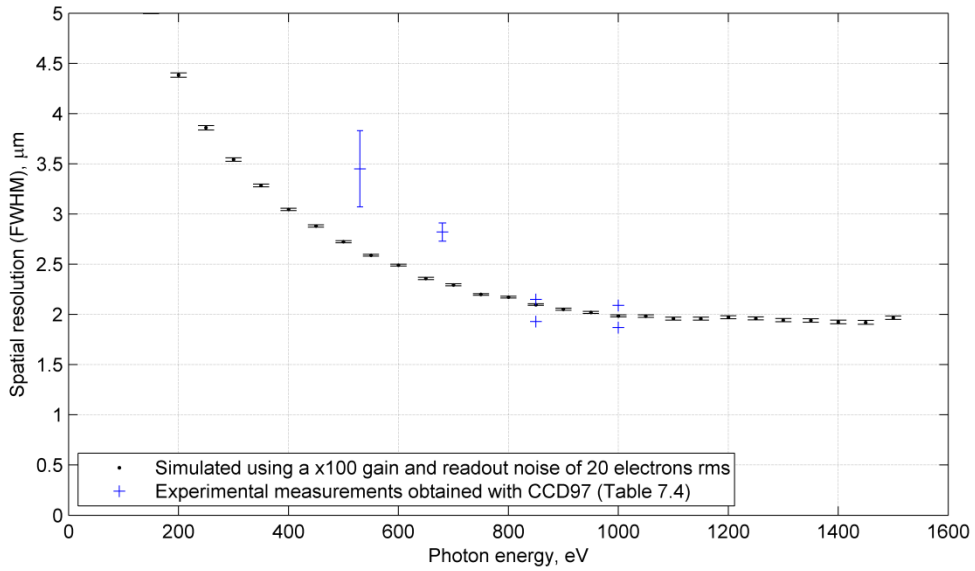

Figure 7.22 The spatial resolution achievable with the corrected centre of gravity algorithm applied across a 3×3 pixel area is worse at lower energies in both the simulated (Figure 5.20) and experimental measurements.

The measurements at 530 eV and 680 eV are worse than predicted by the simulation, but are worst-case estimates as the deconvolving process assumes the X-ray distribution is flat. Using a more rounded distribution of X rays would result in the centroid resolution being measured to be better. It would also result in a better agreement between the data and the model used here.

The measurements at 1000 eV and 850 eV are in good agreement with the spatial resolution predicted by simulation. However, the spatial resolution achieved with the CCD97 is approximately 0.2 µm more accurate in the *y* direction than in the *x* direction. This result is consistent for all the '2 variable' and '3 variable' algorithms investigated. It is proposed that this result must be due to the average charge cloud shape sampled by the CCD97 pixels being asymmetric. An asymmetric diffusion or collection process that leads to preferential charge sharing in a particular dimension is of particular interest for SAXES, as orientating the energy dispersive direction along the rows or columns could vary the resolution by approximately 10%.

7.3 The charge cloud shape in the CCD97

In Section 6.5, two techniques were introduced that can be used to extract the average charge cloud shape sampled by the pixels from a large set of images containing single photon interactions at known locations within the pixel. The first technique to be described is referred to as the 'differential method', where the average charge cloud as sampled by the pixels is differentiated with respect to the interaction location. The second technique uses the systematic errors of the uncorrected 3×3 centre of gravity centroid algorithm to infer back the charge cloud width.

7.3.1 Differential method

To apply the differential method, the average signals in the pixels surrounding X-rays interacting at the 1st order diffraction spot are recorded for each raster scan location and the mean pixel signals are plotted as a function of the X-ray interaction location across the pixels, as in Figure 7.23. When these plots are differentiated in the *x* and *y* dimensions, the resulting distributions (Figure 7.24) contain two positive and two negative occurrences of a peak function. The peak function is the average charge cloud shape at the point that is collected by the potential wells, after the charge cloud has diffused from the original X-ray interaction point.

The four occurrences of the peak function are averaged (Figure 7.25) and fitted with a 2D Gaussian profile to measure the width of the distribution for each energy. The average interaction depth of the photon increases as the photon energy increases therefore the charge cloud shape becomes narrower. The shorter the distance between the interaction point and the depletion

depth, the less time the electron cloud has to diffuse laterally in the CCD before being captured by the pixel potential wells.

To compare the observed charge clouds with the Gaussian profile fits, the difference is shown in Figure 7.26. At 850 eV, and more prominently at 1000 eV, the charge cloud shape has a significantly higher signal at the centre of the peak than the Gaussian profile fit. The increased proportion of isolated events at the higher energies is likely to cause this.

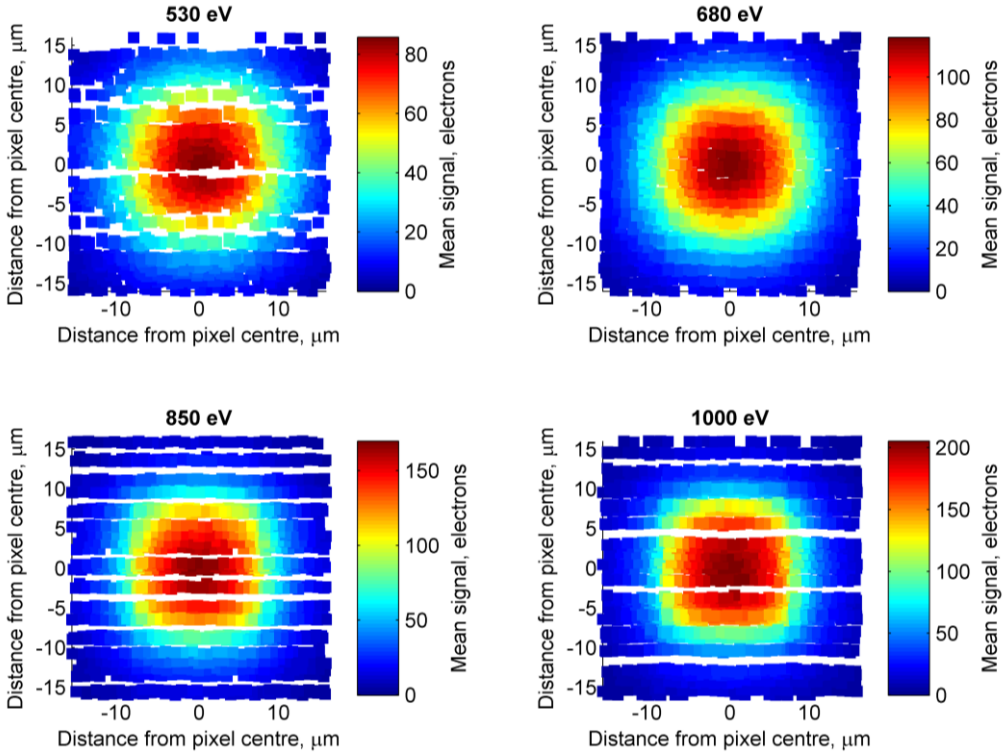

Figure 7.23. The average pixel signals recorded for single photon interactions, as a function of the X-ray interaction location. These are not plots of the charge cloud shapes: the colour scale of each point shows the signal in the charge cloud integrated across a pixel area centred at that point's x and y location.

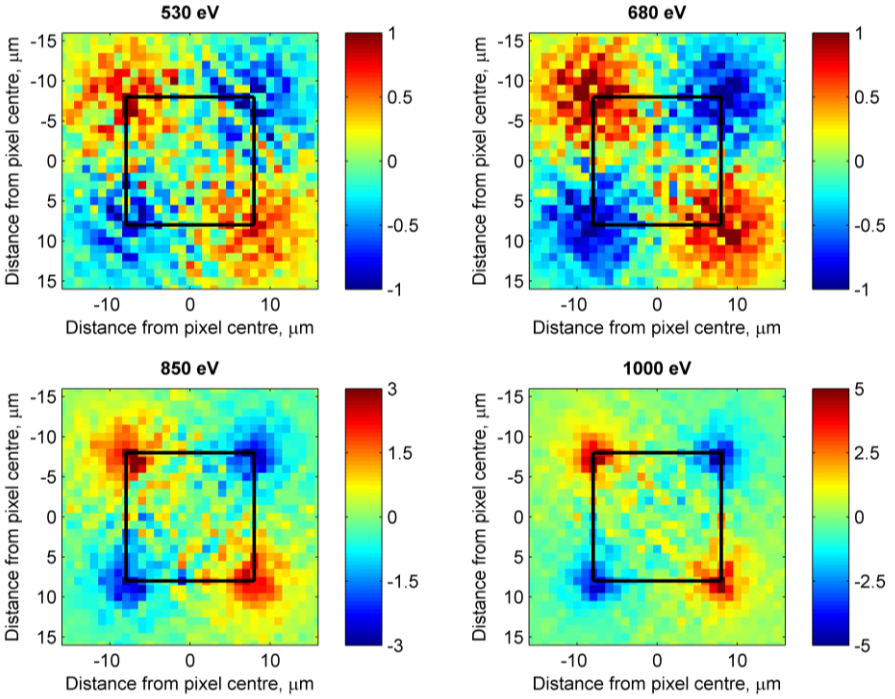

Figure 7.24. The plots from Figure 7.23 are differentiated in the x *and* y *dimensions resulting in distributions with two positive and two negative occurrences of the charge cloud shape in the corners of the pixel. The colour scales are in arbitrary units.*

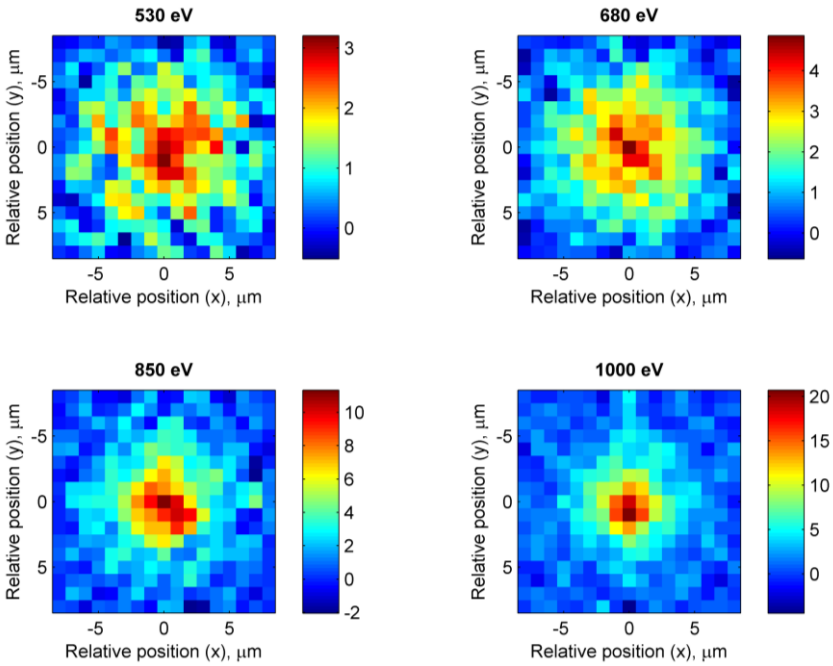

Figure 7.25. The average charge cloud shapes observed using the CCD97. This is determined by summing the charge cloud shape occurrences shown in Figure 7.24. The colour scales are in arbitrary units.

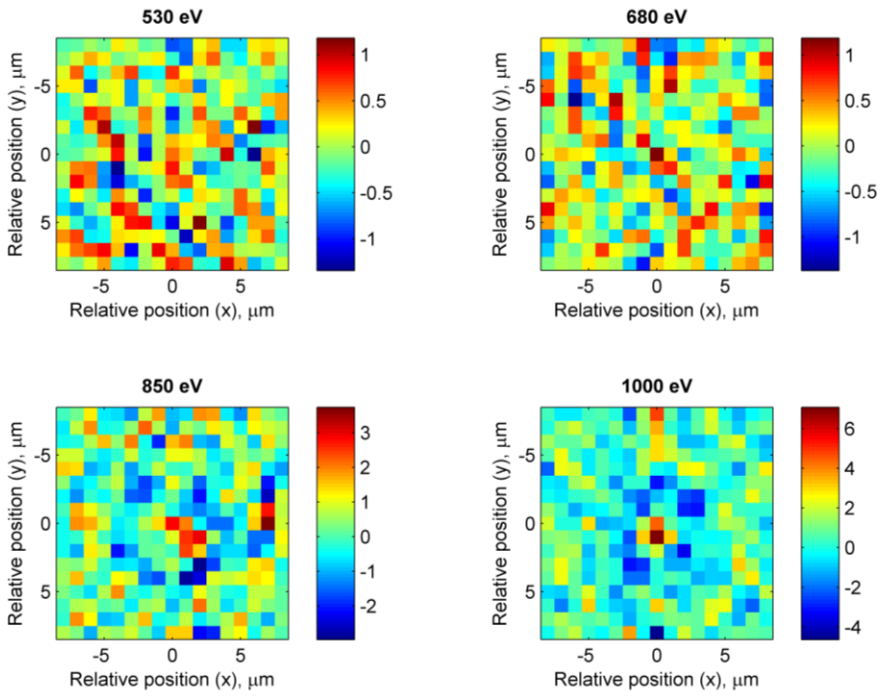

Figure 7.26. The 2D Gaussian profile fit subtracted from the observed values of the charge cloud shapes shown in Figure 7.25 (observed – fitted). The colour scales are in arbitrary units.

7.3.2 Systematic error of centroiding algorithm

The second method used to measure the charge cloud width utilises the systematic error of the centre of gravity algorithms. The expected systematic difference between the real interaction position and the location resulting from a centre of gravity centroid algorithm can be calculated as a function of interaction across the pixel, for a known charge cloud shape. The charge cloud shape when summed into one dimension is assumed to be a Gaussian profile, and the locations obtained by the uncorrected 3×3 centre of gravity algorithm is compared with the relative translational stage positions across the pixel. The systematic error is plotted and fitted for both the *x* and the *y* dimensions in Figure 7.27 and Figure 7.28 respectively.

In general, the distributions are fitted well by the expected relationship that assumed a Gaussian profile showing that the average charge cloud width is approximately Gaussian. However at 1000 eV, a significant number of isolated events are observed with centroid locations towards the centre of the pixel which do not correlate well with the remaining data. The fitted line is biased to the shape formed by the X-ray events that share charge between pixels, therefore the charge cloud widths produced by this method tend to ignore the contribution of the isolated events. The implication of this is that the charge cloud widths measured with the differential method are narrower than the measurements with the systematic error method, a relationship observed in the next section.

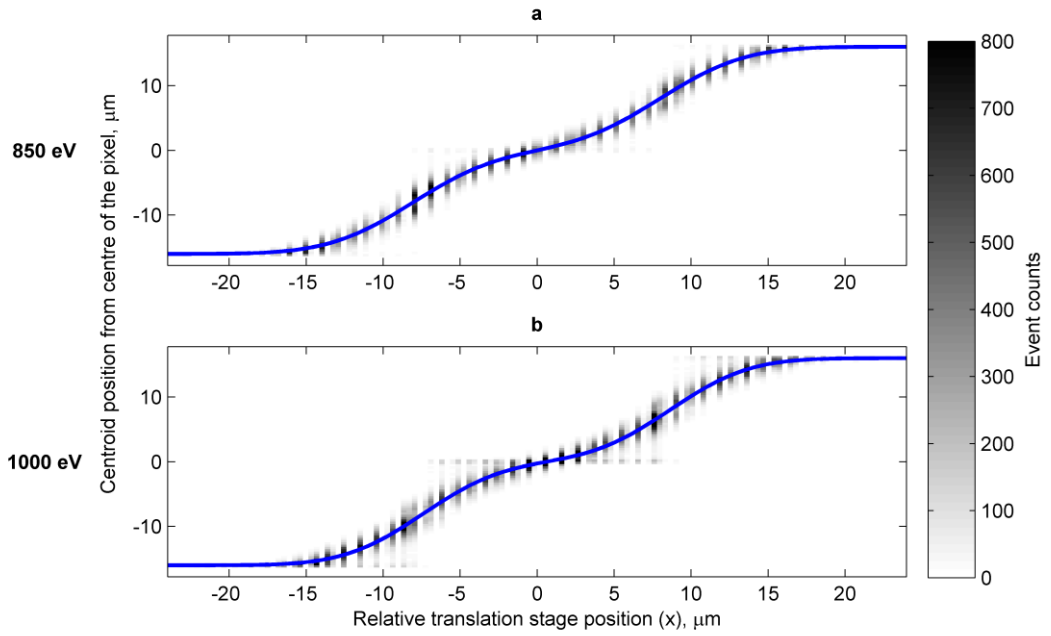

*Figure 7.27. A systematic error is observed between the interaction location (given by the relative translational stage position) and the centroid position calculated using the uncorrected 3×3 centre of gravity algorithm. The distribution is fitted by the expected systematic error calculated assuming a Gaussian charge cloud shape (blue line). The distributions for the 850 eV **(a)** and 1000 eV **(b)** events are shown for the* x *dimension.*

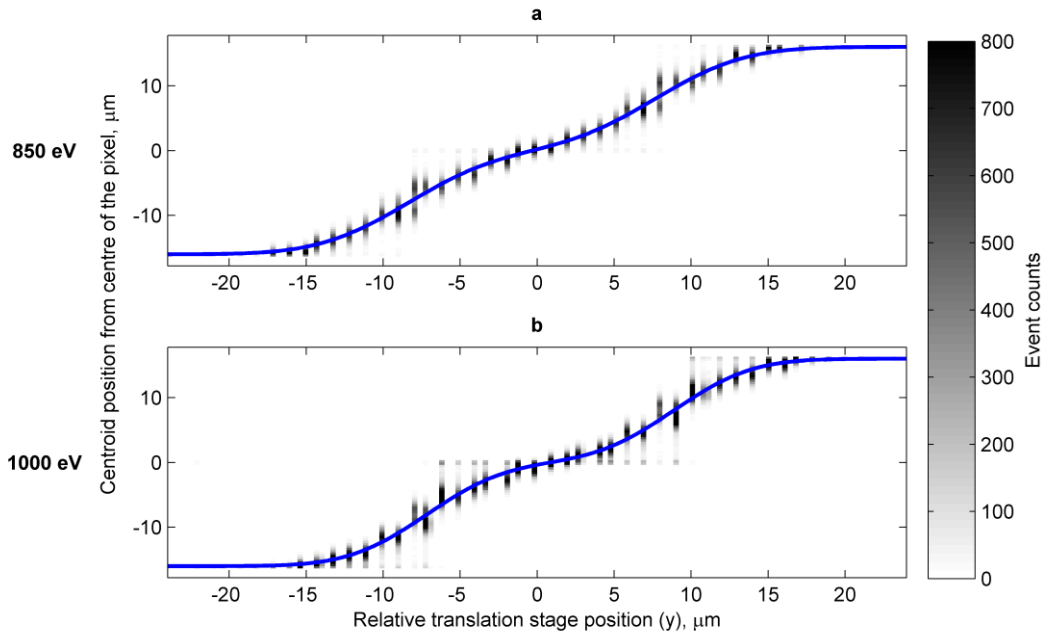

*Figure 7.28. As in Figure 7.27, but here the distributions for the 850 eV **(a)** and 1000 eV **(b)** events are shown for the* y *dimension.*

7.3.3 The charge cloud widths measured in the CCD97

The charge cloud width has been measured using the differential method [67] and a method that uses the systematic error of centre of gravity centroiding algorithms [104]. The resulting widths are shown in Figure 7.29, where the general expected trend of a narrower charge cloud for higher energy photons is observed.

Although obscured by the errors within the data points, the differential method measures a wider charge cloud in the *y* direction than in the *x* direction for all the 850 eV and 1000 eV data sets. This result is in agreement with the better spatial resolution achieved in the *y* direction observed in Figure 7.16: a wider charge cloud results in a larger proportion of signal being collected beyond the central pixel, therefore the average signal to noise ratio in the outer pixels increases and the centroiding algorithm is more accurate.

However, the same relationship between *x* and *y* charge cloud widths is not measured with the systematic error method: the systematic error method measures a wider charge cloud than the differential method because isolated events are more ignored by the fitting in the systematic error method. Unfortunately the systematic error method cannot be reliably applied to the 530 eV and 680 eV data sets as the stage location does not accurately describe the interaction positions since the 1st order diffraction X-ray spot was defocussed.

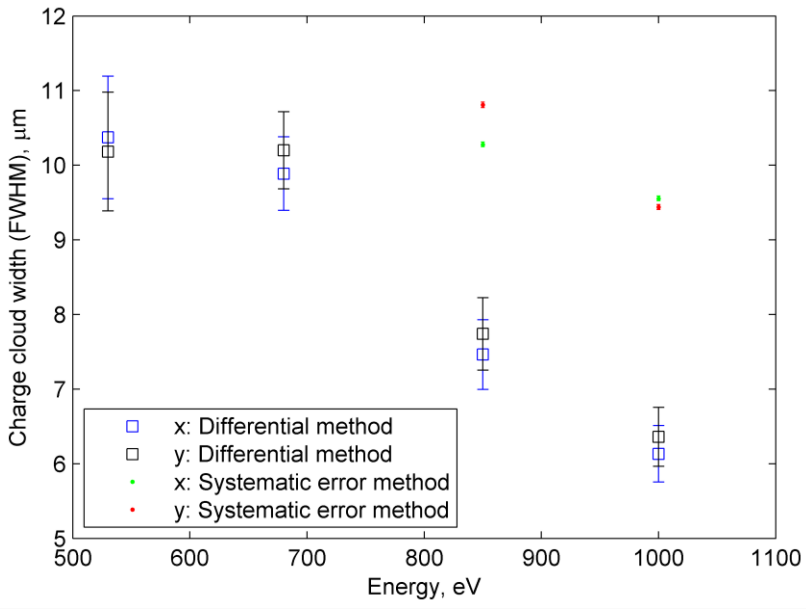

Figure 7.29. The charge cloud widths measured by the two methods described in the previous sections. Errors are shown for all points, obtained from the 95% confidence levels of the fit parameters, but are hardly visible on the systematic error method.

7.3.4 The point spread function of the CCD97

Two methods for analysing the data obtained with the CCD97 have been presented to determine the width of the charge cloud that is sampled by the pixels at the depletion depth. The differential method determines the shape without assuming the shape is, for example, Gaussian and includes the isolated events but the resulting charge cloud density distributions can be noisy when the cloud is spread across a wide area (Figure 7.25). A narrow peak from isolated events appears in the overall charge shape in the 850 eV and 1000 eV data sets, whilst these events are generally ignored by the method utilising the systematic error of a linear centroiding algorithm. The influence that isolated events have on the charge cloud width measurements explains the different charge cloud widths measured by the two methods (Figure 7.29).

The differential method measures the average charge cloud collected by the CCD97 pixels to be between approximately 6 µm and 11 µm wide (FWHM). These widths are narrower than those measured in the *x* dimension in the CCD42-10 (8 µm to 13 µm with the differential method), suggesting the CCD97 has a deeper field-free region.

A better resolution has been achieved in the *y* direction than the *x* direction in the CCD97 (Section 7.2.6) at 850 eV and 1000 eV, coinciding with a wider charge cloud width measured in the *y* direction at these energies (Figure 7.29). The errors in the charge cloud widths do not allow firm conclusions to be drawn, but it is a possibility that the wider charge cloud in the *y* direction is responsible for the resolution result. Charge cloud asymmetry could be due to the depletion region not being at a constant depth throughout the pixel, caused by the asymmetric structure of the gates and implants that define the potential well. It is conceivable that when operated with one of its two phases on during integration, the gate potential is applied across half of the pixel (8 µm vertical × 16 µm horizontal). However, the buried-channel extends approximately 12 µm wide across the electrode structure, filling an area of approximately 16 µm by 12 µm in the vertically and horizontal directions respectively. When the electrode potential and buried-channel dimensions are taken into consideration together, the buried-channel potential well is approximately 8 µm high in the *y* direction and 12 µm wide in the *x* direction. Therefore the asymmetry in the charge cloud dimensions could therefore originate from the potential well asymmetry. To confirm the potential well shape, a detailed simulation using appropriate software package such as SILVACO TCAD [105] could be obtained that incorporates the CCD97 implants that allow the CCD97 to be readout out using a 2-phase clocking scheme.

All the measurements presented for the charge cloud widths are narrower than the 24 µm (FWHM) reported as the charge cloud width of the CCD42-40 in SAXES during the camera's commissioning [7]. The 24 µm width is the effective PSF of the detector, when the charge cloud has been integrated over the pixel structure making the resolution worse than either the diffusion

in the field-free region or pixilation considered individually. Since the widths of the PSF and charge cloud differ so significantly, it is important to clarify which value is being reported.

7.4 Summary

In the previous chapter, centroiding was shown to be able to improve the spatial resolution obtained by the current detector at SAXES, when it is operated in a photon counting mode. Changing the operating mode of the current CCD42-40 from integrating to photon counting would require a significant drop in the throughput of the spectrometer and therefore an alternative detector is required that can read out faster whilst maintaining a low effective readout noise.

The Electron-Multiplying CCD is a candidate technology and an experimental campaign was undertaken at the PolLux spectromicroscope to investigate the resolution of algorithms applied to single photon events detected with the CCD97. The 3×3 corrected centre of gravity algorithm performed best for the events in the CCD97 and the measured resolutions as described in this chapter are summarised in Table 7.5. The results obtained with the CCD97 were better than the resolutions obtained with the CCD42-10 detector investigated Chapter 6, and are sufficiently good to consider the EM-CCD for a future photon counting and centroiding camera at SAXES.

Table 7.5. A summary of the CCD97 resolution measurements presented in this chapter.

Detector	**Photon energy, eV**	**Resolution (FWHM) measured with X-rays incident normal to the detector, µm**
Upgrade requirement	-	Effective goal < 5
CCD97	530	3.45±0.38
	680	2.82±0.09
	850	2.15±0.004 (*x* direction) 1.93±0.004 (*y* direction)
	1000	2.09±0.004 (*x* direction) 1.87±0.004 (*y* direction)

The average charge cloud integrated over by the pixels in the CCD97 is measured for the four photon energies to be approximately 2 µm to 3 µm narrower than measured in the CCD42-10 (comparing Figure 7.29 to Figure 6.40), when using the differential method. The systematic error

method measures a wider average charge cloud width, which may be due it being less sensitive to isolated events, and therefore the method fits to the wider events from interactions in the field-free region. Using the differential method, the charge cloud width in the *y* direction has been measured wider than in the *x* direction at 680 eV, 850 eV and 1000 eV. This may be the reason why the centroiding resolution is more accurate in the *y* direction: the wider charge cloud results in more spread and greater signal to noise in the adjacent pixels.

7.5 Conclusions

2D raster scans of an 850 eV and 1000 eV X-ray spot across a CCD97 pixel have allowed the centroid resolution as a function of sub-pixel interaction position to be measured. The resolution of the centroid algorithms investigated improves close to the edges of the pixels, and is degraded at the centres of the pixels, partially due to an increased proportion of isolated events. The measured PSFs of centroid locations averaged across the raster scan locations are narrower in the *y* than the *x* direction by approximately 0.2 µm, a difference that is probably due to the variation in depletion depth across the pixel. During 530 eV and 680 eV raster scans, the X-ray spot was defocussed which has allowed the contribution of the X-ray spot size to be deconvolved from the overall resolution measurement. The worst-case resolution measurements (Table 7.4) are all better than the 5 µm (FWHM) goal set for the SAXES resolution improvement upgrade.

Table 7.4. The worst-case spatial resolution measurements achieved with the CCD97, from the data recorded during campaign 3 at PolLux.

Energy, eV	Spatial resolution (FWHM), µm	Method of measurement
530	3.45±0.38	The 1st order diffraction distribution has been deconvolved from the PSF measurement
680	2.82±0.09	
850 (errors < 0.004 µm)	*x* direction: 2.15 *y* direction: 1.93	The PSF is fitted by a 2D Gaussian profile
1000 (errors < 0.004 µm)	*x* direction: 2.09 *y* direction: 1.87	

The CCD97 data sets recorded during campaign 3 have also been analysed to measure the charge cloud widths. The differential method of measuring the charge cloud widths fully incorporates isolated events, like the spatial resolution measurements. Where the resolution was better in the

y than the *x* direction at 850 eV and 1000 eV, the charge cloud width is measured by the differential method to be wider in the *y* than the *x* direction. This result is consistent with the proposition that a wider charge cloud results in more signal in the outer pixels, improving the signal to noise ratios and therefore improving the resolution of centroiding algorithms. The charge clouds are measured to be between 6 µm and 11 µm (FWHM), smaller than the widths measured in the CCD42-10 pixel (between 9 µm and 15 µm FWHM). However, the improved signal to effective readout noise ratio of the EM-CCD results in centroid algorithms being more accurate when applied to X-ray events observed in the CCD97.

The resolution results obtained with the EM-CCD in this chapter are better than the goal of 5 µm (FWHM) set for a camera upgrade at SAXES, where the detector is oriented at 20° relative to the incident photons. The measurements have been obtained with the detector normal to the incident photons, therefore the projection of the interaction depth distribution across the plane of the detector when the incident angle is more acute will have to be investigated to determine its effect on the resolution. Ignoring this effect for now, the CCD97 meets the resolution requirements but it is not the most suitable detector for SAXES due to its relatively small area compared to the current detector, the CCD42-40. A larger area EM-CCD is the CCD207-40. Whilst the CCD97 and CCD207-40 have the same pixel architecture expected from manufacture, a further experimental campaign was undertaken to verify its performance and suitability for a future camera upgrade at SAXES.

Chapter 8: SAXES System Upgrade

8.1 Introduction

SAXES, a high resolution dispersive spectrometer designed for RIXS, has a resolution limited by the spatial resolution of its current detector, a CCD42-40. The detector is operated in an integrated mode, where the spatial resolution is dominated by the error introduced by charge from the majority of X-ray interactions being sharing between neighbouring pixels, limiting the resolution to 24 μm [7]. Investigations described in this thesis have shown through simulation and experimental measurements that single photon events observed in the current CCD can be centroided to a resolution that depends primarily on the background noise in the image and the energy of the photon.

Application of centroiding algorithms to images recorded at SAXES have demonstrated that significantly shorter integration times than currently used are required to operate in a suitable photon counting mode. Reducing the integration time by a factor of up to 100 and using the same readout time leads to a significant reduction in the throughput of the spectrometer and whilst improvements to the resolution of SAXES are desirable, significant reductions in the throughput are not because RIXS is a photon-starved technique and experimental time is already oversubscribed. To help mitigate the reduction in throughput, the readout time has been reduced by using the 1 MHz pixel readout rate available with the current camera system, however the increased readout rate leads to an increased readout noise in the images which hinders event detection and significantly degrades the resolution achievable using centroid algorithms.

The EM-CCD has been introduced as a solution to achieving low effective readout noise whilst operating at a faster readout rate that maintains a reasonable throughput at the spectrometer. Centroiding of events simulated and experimentally observed in a CCD97 have also shown that better spatial resolutions can be achieved with EM-CCDs operating at high gain than with the current SAXES camera so it has been proposed that an upgraded camera at SAXES using EM-CCDs is developed to benefit from the spatial resolution improvements expected from centroiding.

8.2 A camera for SAXES based on a large area EM-CCD

An EM-CCD suitable for a SAXES camera upgrade would ideally be a similar size to (or larger than) the current CCD42-40. The CCD97 investigated in Chapter 7 is much smaller than the CCD42-40 (Table 8.1) therefore the observable energy range of excitations would be smaller and the number of photons observed in a single image would be reduced if it was used in a RIXS camera. A

sufficiently wide energy range must be observable to record a RIXS spectrum, and a wider detector can image a wider scattering angle increasing the number of photons.

The pixel and gain register architecture of the CCD207-40 is similar to those of the CCD97 so the X-ray detection and charge diffusion dynamics are expected to be the same. Therefore the results achieved with the CCD97 are expected to be directly transferable and the CCD207-40 has been proposed as a suitable large area EM-CCD.

The CCD207-40 is approximately the same size as the CCD42-40. However it has larger pixels and it can be read out in a 2-phase rather than 3-phase clocking scheme, decreasing the parallel transfer time. To further increase the frame rate, the avalanche gain feature can be used to multiply the signal level before the readout noise is applied to maintain an effective sub-electron readout noise whilst the pixel readout rate is increased.

Table 8.1. The properties of the detectors described in this section.

Device	Pixel size	Imaging Pixels	Imaging Area	Readout
CCD42-40	13.5 µm	2048 × 2048	27.6 mm × 27.6 mm	Full
CCD97	16 µm	512 × 512	8.2 mm × 8.2 mm	Frame transfer
CCD207-40	16 µm	1632 × 1608	26.1 mm × 25.7 mm	Full

8.3 Spatial resolution tests with the CCD207-40

To confirm that the CCD97 results described in Chapter 7 are transferable to the CCD207-40, a setup was designed to allow a CCD207-40 to be operated in the PolLux spectromicroscope to repeat a selection of the measurements. New mechanical components were designed to fit the detector onto the translational stage platform downstream of the FZP in the experimental chamber at the PolLux. A CCD207-40 headboard was not already available; therefore one was designed and populated to connect clocks directly to the pins on the CCD's package whilst bias lines were filtered before connection (Figure 8.1). The CCD output is amplified before being passed off the board, to be connected out of the chamber.

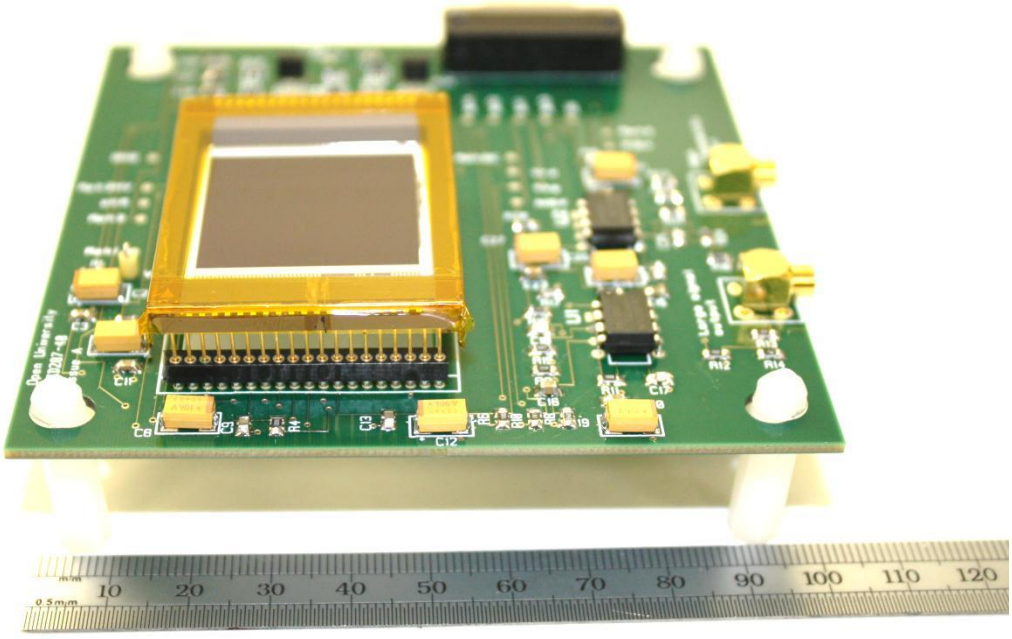

Figure 8.1. A CCD207-40 is shown placed in the headboard produced for campaign 4. The ruler's scale is in millimetres. Bias and clock lines are supplied onto the board with the micro D-type connector at the far side of this photograph, and the outputs are amplified and passed off the headboard through the MCX-jack connectors on the right-hand side.

8.3.1 Experimental setup

The mechanical support for the CCD207-40 and headboard produced for campaign 4 is shown *in situ* in Figure 8.2. Although the Cryotiger cooling setup operated well during campaign 3, it had to be transported to the Swiss Light Source for the experiment. To simplify the logistics of campaign 4, the cooling setup was modified to utilise liquid nitrogen. A mixture of liquid and gaseous nitrogen was flowed through a copper tube that passed into the vacuum chamber and a cold sink on the copper tube was connected to the cold-finger in contact with the back surface of the detector package detector using two tin-coated copper braids. The detector was again controlled using an XCAM camera drive system, where the clock sequence was programmed to allow windowed operation of the detector for the purpose of this experiment. 525 frames were captured reading out a windowed region surrounding the X-ray distribution, the average of which is shown in Figure 8.3, where the X-rays from the 0^{th} and 1^{st} diffraction orders are clearly visible.

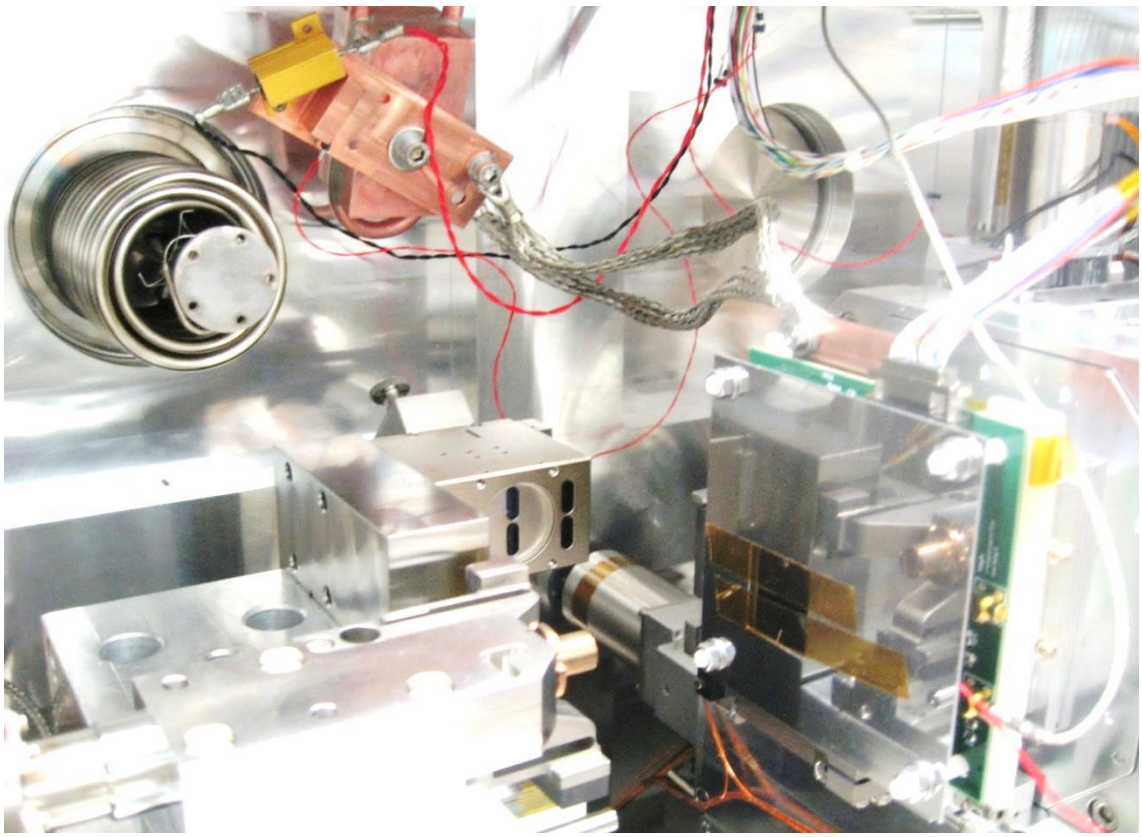

Figure 8.2. The setup is adapted in the PolLux experimental chamber to allow the 1st order diffraction X-rays from the FZP to be focussed on the pixels of the CCD207-40. The two strips of Kapton tape placed across the hole in the clamp protect the detector during setup and are removed before experimentation.

The 1st order diffraction spot was focussed in a sub-pixel using the same method as described in Section 7.2.1.2, by summing the signal across each column of 3 pixels in the region of the focussed spot shown in Figure 8.4 a. This measures the signal in the charge cloud which is integrated over each 3 pixels area. The shape of the pixel sampled charge cloud is oversampled by scanning the spot in the *x* dimension, resulting in Figure 8.4 b, where the distribution is fitted by a Gaussian profile. The width of the Gaussian profile is measured across a range of distances between the CCD and the FZP, to determine a minimum (Figure 8.5). The CCD was placed at the minimum, i.e. the focal point, before the flux was tuned to maximise the number of frames in which a single photon is observed in the 1st order focussed spot.

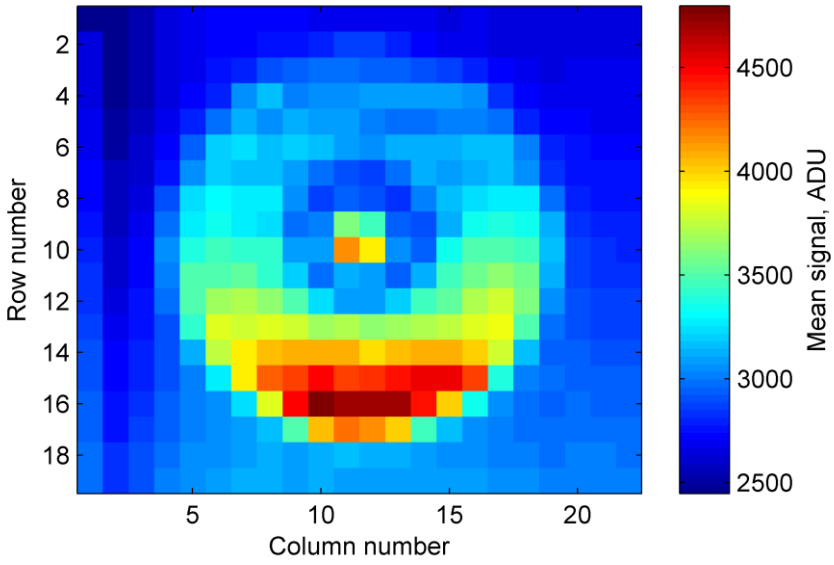

Figure 8.3. Average frame from a set of 525 test images recorded once the windowed region had been identified.

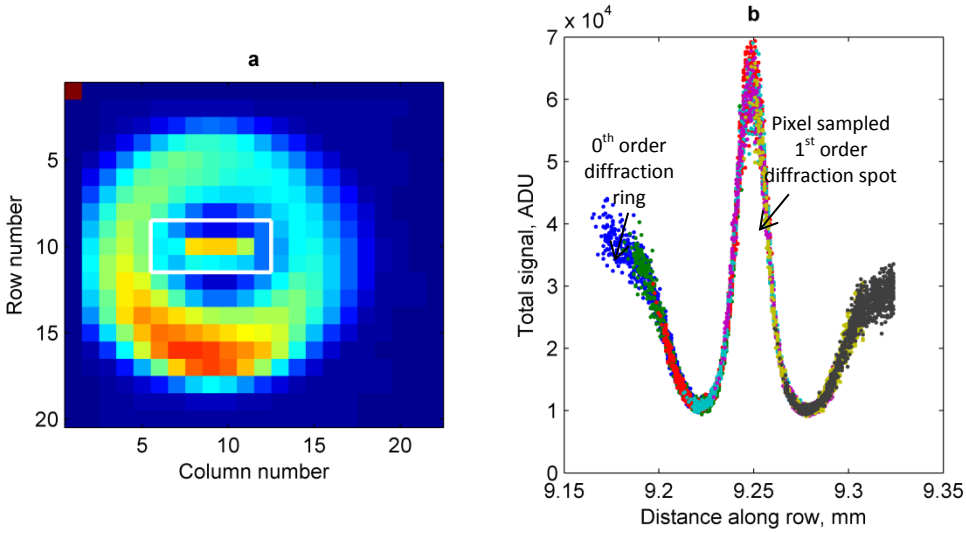

*Figure 8.4. The X-ray spot was scanned in 1D across the detector resulting in **(a)** the average image. At each step of the scan, the signals in the 3 rows of pixels surrounding the 1st order diffraction spot (white rectangle) were used to measure the average charge cloud shape as measured by the pixels **(b)**.*

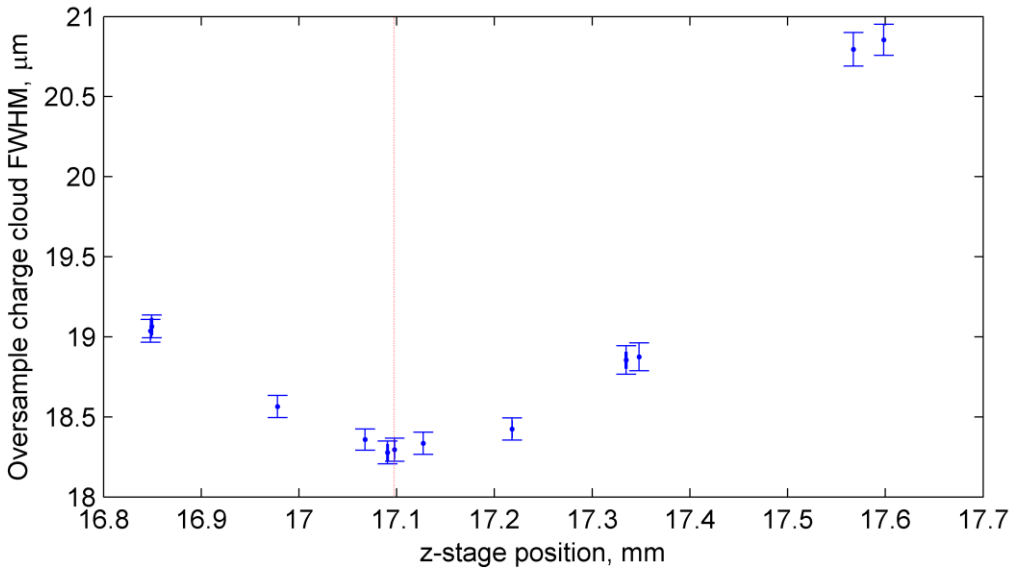

*Figure 8.5. The width of the pixel sampled charge cloud is measured at a range of distances between the CCD and FZP (*z-stage position*). The width is a minimum at the focal point, shown by the vertical red dashed line.*

8.3.2 2D raster scan

The CCD207-40 contains approximately 8 times more pixels than the CCD97 therefore a significantly larger area required dumping whilst reading out in a windowed mode. To improve the frame rate with the CCD207-40, the windowed region was reduced to 13×15 and further reduced to a 9×12 pixel area, allowing frame rates of 5.0 Hz and 6.7 Hz respectively to be achieved with the test electronics (c.f. 26.7 Hz achieved with the CCD97 during campaign 3 operating at the same pixel readout rate). To further mitigate the effect of the frame rate on the data collection, the number of frames collected per sub-pixel location in the raster scan was reduced to 1000 frames.

When the raster scan was initiated the temperature of the detector, measured by a PT1000 platinum resistance thermometer glued to the detector package, was -78°C. Due to the operation of the detector, the temperature rose in the first hour and a half before reaching equilibrium at -74°C for the rest of the scan. The average frame collected during the raster scan for the first 100, 1000, 10 000 and 100 000 frames is shown in Figure 8.6. Throughout the averaged images, the average signal observed in rows 7 to 12, for columns 2 and 6 is significantly lower than the surrounding pixels. The effect is observed in the first set of frames recorded during focussing, and therefore damage must have occurred during the flux adjustment. Average images from the first sets of frames recorded during the raster scan clearly show the pixels read out beyond row 7 in columns 2 and 6 no longer containing the expected levels of charge.

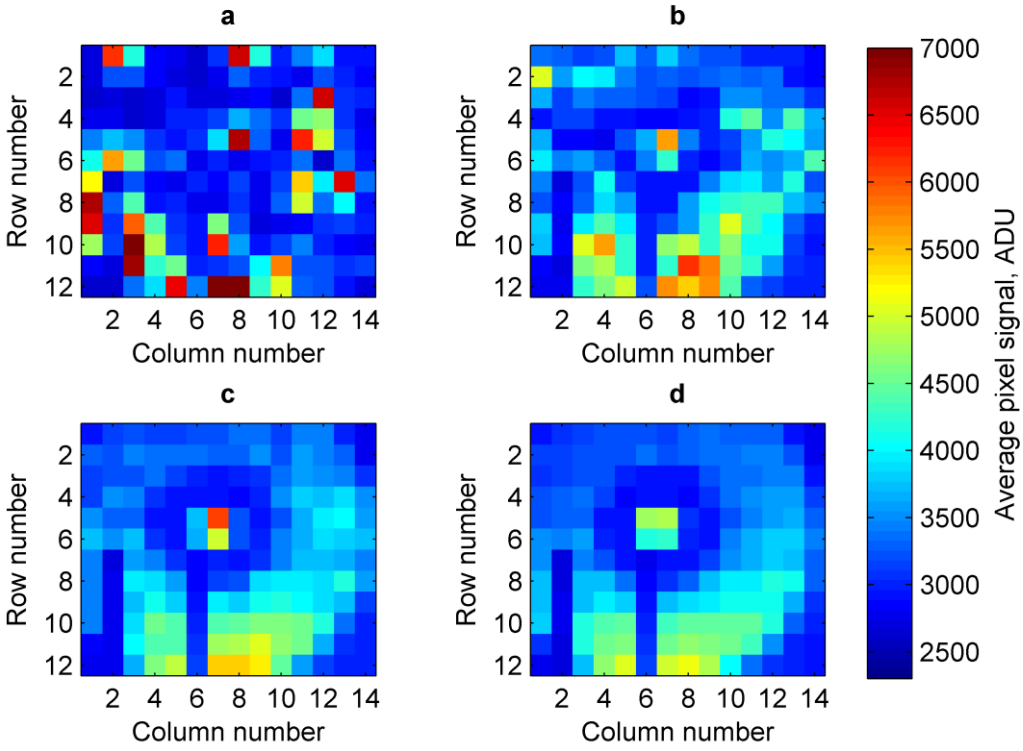

*Figure 8.6. The average image from the first **(a)** 100, **(b)** 1000, **(c)** 10 000 and **(d)** 100 000 frames recorded in the raster scan with the CCD207-40 show damage has occurred in columns 2 and 6 (c.f. Figure 8.3).*

8.3.3 Radiation damage in the CCD207-40

The damage observed in Figure 8.6 is assumed to be due to an effect caused by exposure to the soft X-rays as no other likely explanation for the damage observed has been conceived. Exposure to tens of kRads of ionising radiation leads to two observable effects in buried-channel CCDs [106,107]:

- **Flat-band voltage shift:** Positive charge builds up in the oxide layer due to holes being left behind by the ionised electrons that are mobile enough to diffuse out resulting in the effective potential applied to the MOS capacitor becoming more positive. Therefore a more positive potential is produced in the silicon in the area of the damage.
- **Increased dark current:** the ionisation close to the oxide-semiconductor boundary generates interface states that increase the generation of surface dark current. In surface-channel detectors, the traps may also decrease charge transfer efficiency.

The detector was maintained at approximately -74°C during this testing, therefore dark signal generation was at a low level, and it is reasonable that no increase can be observed in the images.

However, a hypothesis to explain how a localised flat-band voltage shift can result in the loss of charge transfer ability in isolated pixels will be presented below.

The level of flat-band voltage shift depends on the radiation dose in the oxide layer between the gate electrode and photo-sensitive silicon, at the front surface of the detector. The dose absorbed in the oxide layer is calculated in units of Rads, where 1 Rad = 0.01 J/kg, which requires the number of 1000 eV photons that interacted in the volume of silicon dioxide to be determined.

97 minutes passed between recording the last frame in the focussing procedure and the first frame of the raster scan analysis. In PolLux's typical operation, the maximum flux on the detector in the 1st order diffraction spot is 1.25×10^{8} photons per second [71] so a theoretical maximum of 7.28×10^{11} photons could have been incident in the central spot if the beamline shutter and slits were opened fully for the whole duration (which was not the case). The pixel spot was focussed to a maximum area approximately 2 µm in diameter, as will be confirmed by the spatial resolution measurements presented in Section 8.3.4, meaning the photons would have interacted within an area of 3.14×10^{-8} cm^{2}, extending in a cylinder through the detector from the back face to front surface of the device.

Using an oxide thickness of 85 nm [108] and assuming the oxide layer is between 13 µm and 16 µm from the back surface of the detector, between 0.01% and 0.03% of the 1000 eV photons incident on the back surface would interact in the oxide layer. At the upper limit of the flux and exposure time estimates, the dose in the oxide layer is between 1.5 GRads and 4.4 GRads. However, during the flux adjustment the beamline shutter was not open for the entire 97 minutes, and the maximum flux is likely to have been several orders of magnitude less than 1.25×10^{8} photons per second as the slits were not opened fully. Therefore, the flux estimate is reduced to 5000 photons per second (equivalent to 1000 photons in the central spot per frame recorded) and the exposure time to 10 minutes, resulting in an estimated dose in the oxide layer between 6.1 kRads and 18.1 kRads.

Here, two pixels in two separated columns in the centre of the image area have stopped transferring charge. The columns adjacent to the damaged pixels do not appear to be affected, which implies that the hole build-up occurs in the region of the buried-channel rather than the channel-stop. A single transfer in the 2-phase clocking scheme of an undamaged CCD207-40 is shown in Figure 8.7 (Section 3.3.2.2). Charge is transferred by generating a more positive potential under an adjacent electrode, causing electrons to drift underneath it. However, if a significant level of positive charge was built-up in the oxide layer, the effective voltage shift of the MOS capacitor could reach a level where the potential well under the electrode is more positive than its neighbours at all times during the charge transfer clocking sequence. Examples of this

situation are illustrated in Figure 8.8 and Figure 8.9, where the potential barrier generated by the more positive potential well inhibits the transfer of charge along the array.

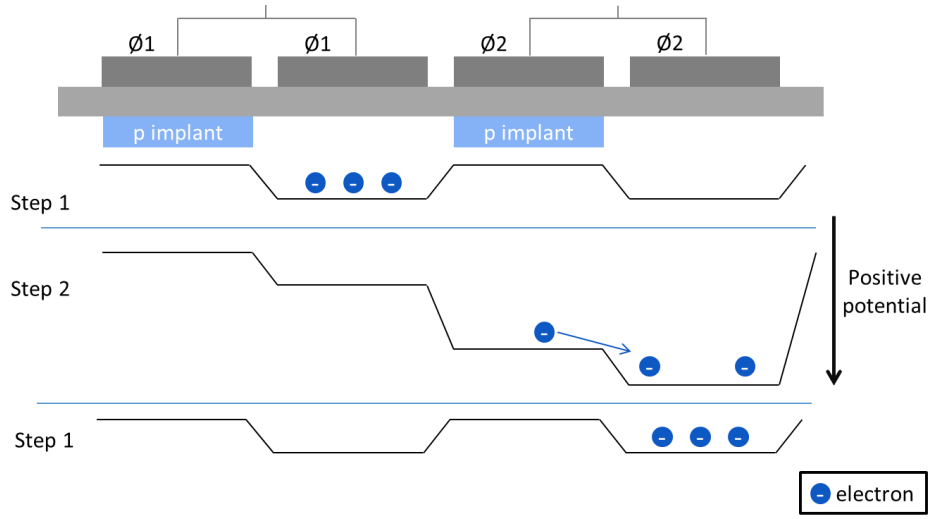

Figure 8.7. A transfer in the 2-phase clocking scheme where electrons stored under Ø1 are transferred to under Ø2, as observed in an undamaged CCD207-40.

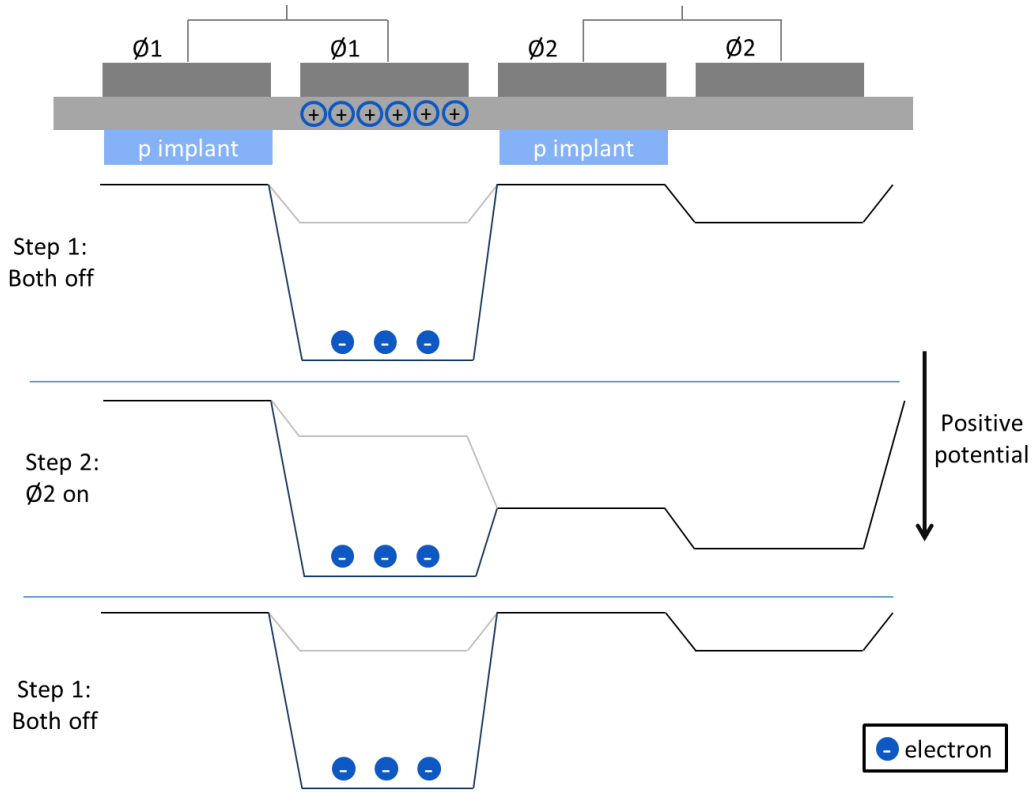

Figure 8.8. When an excess of holes is present under the electrode without the p implant, the potential under the electrode is shifted more positive than neighbouring electrodes, inhibiting charge transfer.

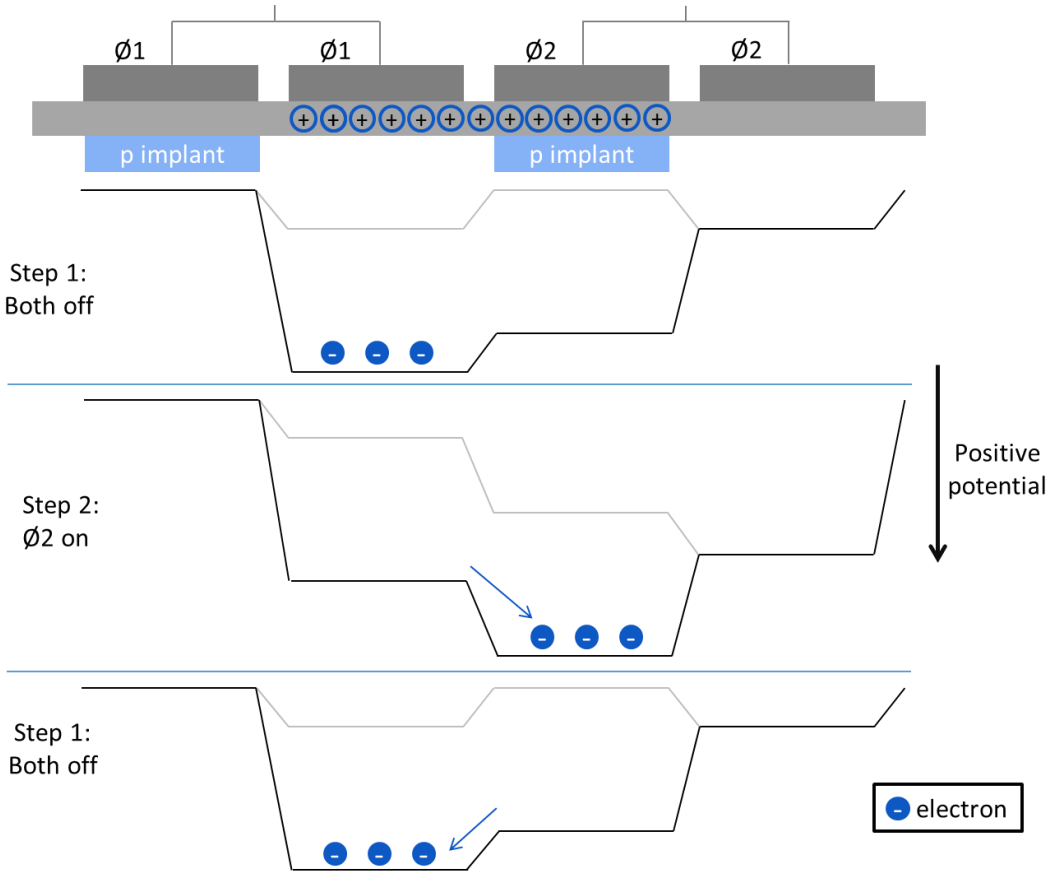

Figure 8.9. If excess holes are present in the dielectric layer underneath neighbouring electrodes, transfer, the more positive potential wells resist transfer of the charge out from underneath the damaged electrodes.

Whilst this damage might be considered concerning for the use of back-illuminated CCDs to directly detect soft X-rays, the experiment demonstrated an extreme case. Firstly, the flux was at a high level as the photons were focussed directly from the beamline onto a small region of the device, and the detector was normal to the incident beam. In most other applications, the flux is significantly lower and so the dose is decreased reducing the number of holes generated in the oxide. In cases such as at SAXES, the detector is at an angle to the incident X-rays and so the proportion of photons that penetrate to the oxide is reduced as the effective thickness of the detector is greater. Secondly, illuminations are generally flatter across the detector, so any voltage shifts that occur are relatively uniform across the detector, rather than the step changes under adjacent electrodes predicted here. Lastly, the damage here was inflicted over a short time frame and with the detector at approximately -74°C. If this dose was applied to the detector across a longer period of time or at warmer temperatures, the holes in the oxide could migrate

out and recombine, annealing the voltage shift. These reasons lead to conclusion that the damage in the CCD207-40 observed during this testing should not be observed in a future the SAXES camera.

8.3.4 Spatial resolution measurements

The detector was operated with no image clocks on during integration, whilst a raster scan was performed collecting charge in the potential wells defined by the implants that allow the CCD207-40 to be read out with a 2-phase clocking scheme. In the raster scan, there are 40 sub-pixel locations where the 3×3 pixel area of the central spot does not extend down to the damaged pixel in row 7 of the image frame (referenced to Figure 8.6). An average of 63±16 single photon interaction events are extracted from the focussed X-ray spot, a lower yield than in previous experimental campaigns because the CCD207-40 is a large area device which requires significantly longer time to read out and to acquire measurements across a sufficient number of sub-pixel locations in the limited test time, only 1000 frames captured at each. The observed events have been centroided, resulting in the resolutions and average sub-pixel locations shown in Figure 8.10.

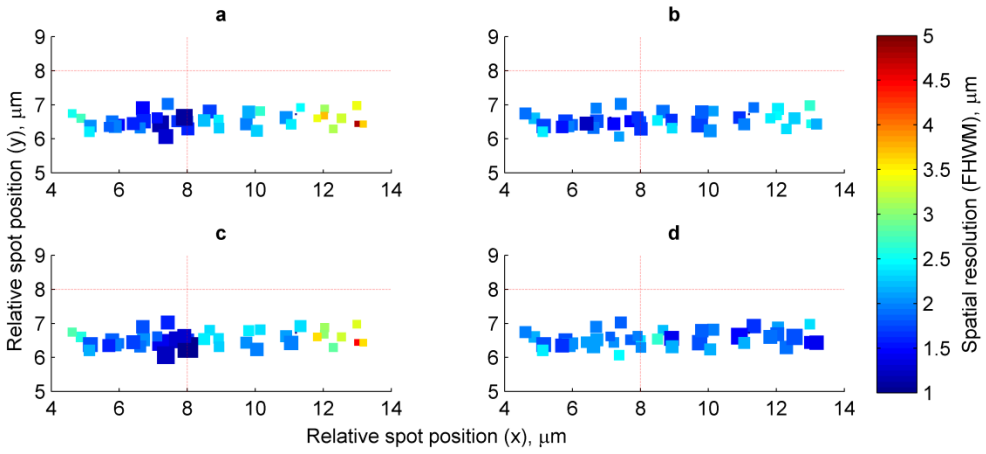

*Figure 8.10. The mean centroid locations are shown for the valid sub-pixel raster scan positions, where dashed red lines mark the pixel boundaries. The colour scale maps the spatial resolution at each location whilst the data point increases in size as the resolution measurement is determined with greater accuracy. The spatial resolutions results are the averages obtained using the '2 variable' (**a** and **b**) and '3 variable' (**c** and **d**) algorithms, where **a** and **c** are in the* x *direction and **b** and **d** are in the* y *direction.*

Whilst the number of events observed at each sub-pixel location is low, and the sub-pixel locations are biased towards the top of the pixel, the 2463 centroids can be used to calculate a PSF using the same method as in the CCD97 data analysis. For example, the PSF calculated using the corrected centre of gravity algorithm applied across a 3×3 pixel area is shown in Figure 8.11. The widths of the PSFs obtained with each algorithm for events in the CCD207-40 are shown in Figure 8.12. The PSFs are a geometric average from the sub-pixel locations at which the X-rays were focussed and so a systematic bias may be present as the locations are all located at the top of the pixel and are not distributed across the full width of a pixel in the *x* direction.

When compared to the CCD97 results (Figure 7.16), the resolutions achieved with the CCD207-40 are consistent at approximately 2 µm. However, the measurements taken with the CCD207-40 show the resolution in the *x* direction is better than in the *y* direction. This may be due to the systematic bias of the CCD207-40 data set, where the sub-pixel regions sampled are only in a strip across the top of the pixel (Figure 8.10). Alternatively, the difference could be due to the CCD207-40 being operated with no phases on during integration time whereas the CCD97 was operated with one of its two phases on. A raster scan with the CCD207-40 operating with one of its two phases on was obtained but the X-rays were focussed in one of the defected columns.

Despite the limitations of this data set, the measurements presented strongly indicate that the CCD207-40 will be able to achieve similar resolutions as those presented for the CCD97 in Chapter 7. Therefore, the CCD207-40 is a suitable candidate detector for the SAXES camera upgrade.

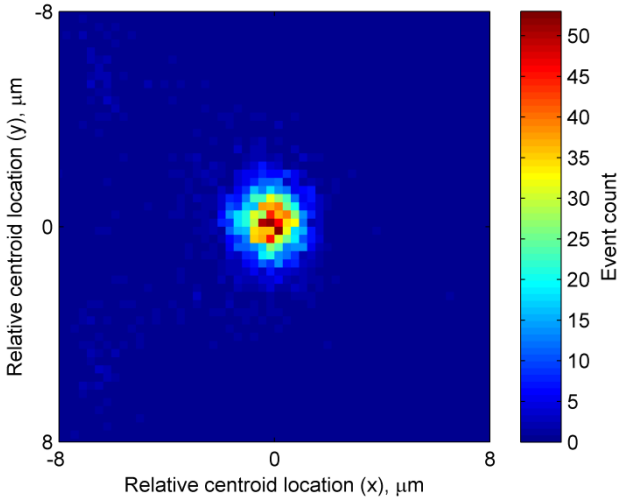

Figure 8.11. Over all sub-pixel locations, the centroids obtained using the corrected centre of gravity algorithm applied across a 3×3 pixel area surrounding 1000 eV events are distributed about their mean as shown. A 2D Gaussian profile is fitted to this distribution to measure the average resolution obtained with the algorithm across the sub-pixel locations.

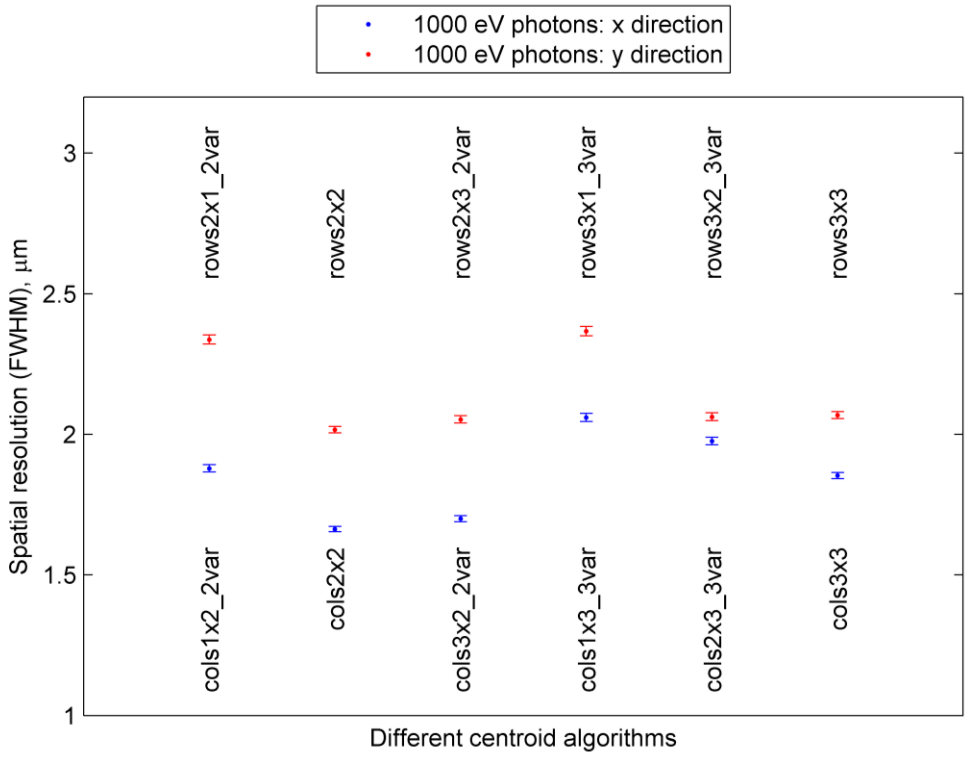

Figure 8.12. The widths of the PSFs obtained for each '2 variable' and '3 variable' centroid algorithm are determined using a 2D Gaussian profile fit. Errors obtained from the 95% confidence limits in the fitted parameters are shown but are small.

8.4 Varying the incident angle in a CCD207-40 based SAXES camera

To get the most from the detector in SAXES, it is important to ensure it is operated and positioned in the camera optimally. Two important parameters are the readout rate and the angle at which the detector is oriented relative to the incident X-ray beam.

When the angle between the incident X-ray beam and the CCD is varied, the effective area, quantum efficiency, flux in the detector plane and effective energy resolution is changed. The CCD42-40 camera system is currently installed at SAXES with X-rays incident at approximately 20° to increase the effective pixel density in the energy plane, improving the energy resolution (Figure 8.13). However, the distribution of interaction depths is projected onto the CCD detector plane for isoenergetic photons incident at the same point of the back surface of the detector which degrades the spatial resolution. The effects of varying the angle are summarised in Table 8.2.

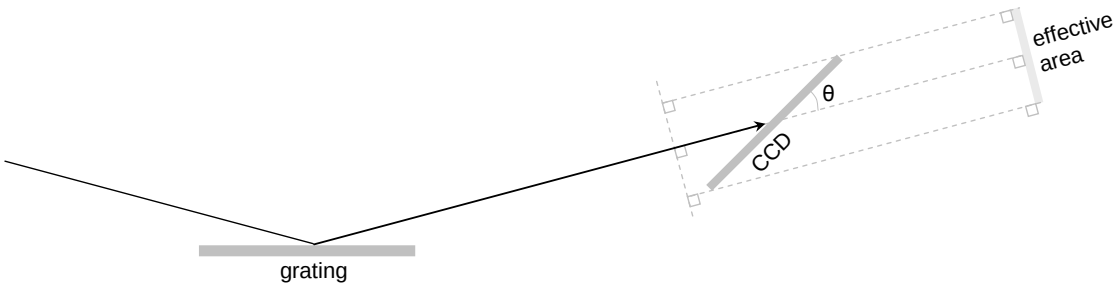

Figure 8.13. The angle of the X-rays incident on the detector, θ, is defined here. The effective area of the detector (shown) is dependent on the angle, as is the quantum efficiency, flux in the detector plane and effective energy resolution.

Table 8.2. The effects of varying the X-ray incident angle on the detector.

Feature	Angle dependence	Effect of changing the incident angle from 20° to 90° (normal) for a photon counting camera
Effective area	CCD image area $* \sin(\theta)$	Improvement: either a wider energy range can be observed or a region of interest around the spectrum will cover fewer rows
Flux in the detector plane	flux in energy plane/ $\sin(\theta)$	Degrade: The spectrum will be split across fewer pixels increasing the chance of pile-up and requiring shorter integration times.
Quantum efficiency (Section 8.4.1)	Quantum efficiency is primarily reduced by photons either being absorbed in the insensitive back surface or passing through the photosensitive silicon undetected.	Photons with a short attenuation length are more likely to interact in the dead area at the back surface at 20°. Photons with a long attenuation length are more likely to pass through the photo-sensitive silicon undetected at 90°.
Effective energy resolution (Section 8.4.2)	If photons are not incident normal to the detector, the interaction depth distribution is mapped into the plane of the detector. However, the effective pixel size in the energy plane also varies, changing the effective resolution.	Normal incident photons are not distributed in the plane of the detector due to their interaction depth, but at normal incidence the pixel size (and therefore the spatial resolution) is not effectively reduced in the energy plane.

8.4.1 Quantum efficiency

The effect of varying the incident angle is a straightforward geometric relationship for the effective detector area and flux in the detector plane, but is more complicated in the case of the detector Quantum Efficiency (QE) due to the energy-dependent attenuation length. The attenuation lengths in silicon and silicon dioxide for the relevant energy range are shown in Figure 8.14. A simulation has been written to demonstrate the change in the quantum efficiency of a typical detector across the energy and angle range. The simulation assumes a 0.05 µm SiO_2 layer with a QE of 0, and a 0.05 µm p+ doped region at the back surface, in which the QE is assumed to be linearly dependent on the distance through the p+ layer. The QE is assumed to be 100% in the 13 µm silicon and any reflections are ignored.

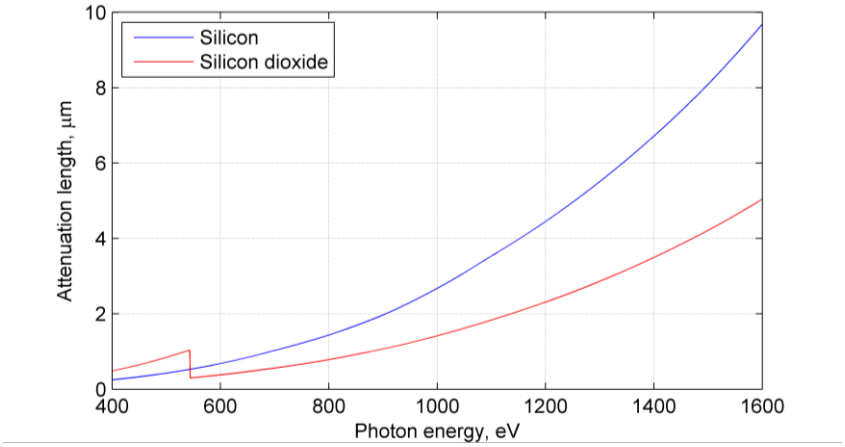

Figure 8.14. The attenuation length of X-rays in silicon and silicon dioxide for a range of soft X-ray energies (c.f. Figure 3.2)

The simulation result is shown in Figure 8.15. Where the average interaction depth is close to the back surface at lower energies and smaller angles, the quantum efficiency is limited by the proportion of photons absorbed in the silicon dioxide and p+ back surface passivation region. At higher energies the QE is reduced at angles closer to normal incidence due to photons passing through the detector without interacting. The back surfaces of e2v detectors are treated similarly, therefore the quantum efficiency for the lower energy photons will not vary significantly between the current detector, the CCD42-40, and the CCD207-40.

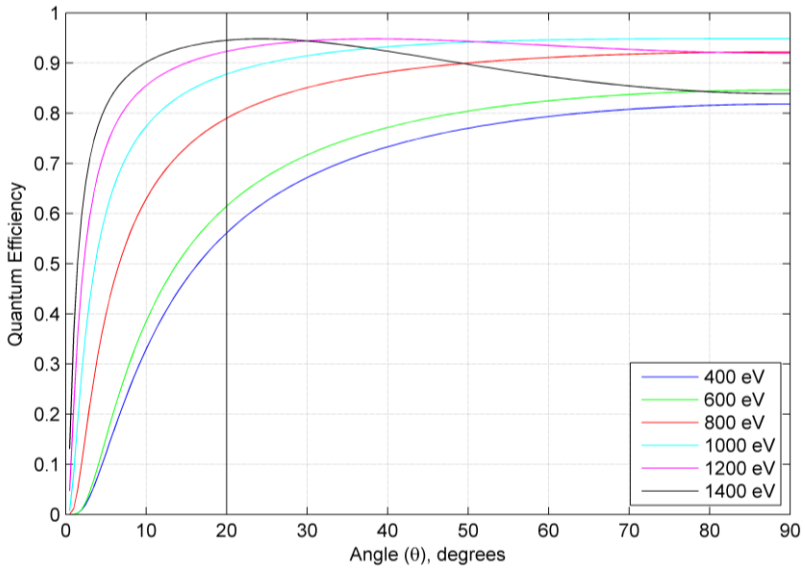

Figure 8.15. The simulated energy and angle dependent quantum efficiency is shown for a 13 µm thick sensor.

8.4.2 Detector resolution

The detector resolution also varies with both photon incident angle and energy. Consider a number of photons of the same energy incident normally at the same location on the back surface of a detector (at 0 µm in Figure 8.16). The PSF of the detector is given by the charge cloud width as sampled by the pixel structure, or by the accuracy of the centroid algorithm used. However, if the incident angle is not normal, the interaction depth distribution is projected into the plane of the detector and the PSF is widened, Figure 8.16 c. Smaller angles and photons with longer attenuation lengths result in a bigger change in the width of the PSF, as shown in Figure 8.17.

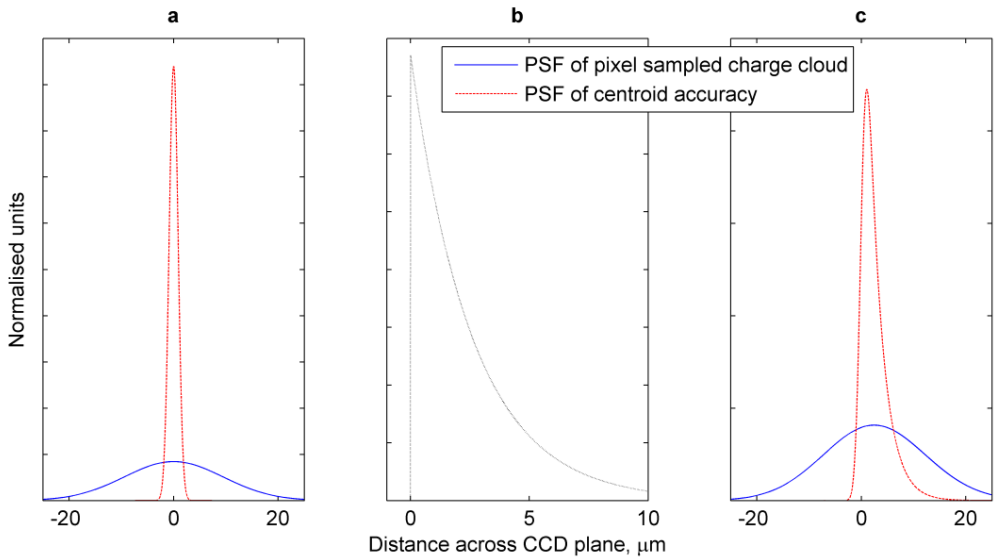

Figure 8.16. ***(a)*** *Point spread functions for the integration mode and centroid limited cases for photons incident normal to the detector.* ***(b)*** *When photons are not incident normal to the detector, their interaction depth distribution is projected onto the CCD plane.* ***(c)*** *When photons are not incident normal to the detector plane, the projection of the interaction depth distribution is convolved with the point spread functions.*

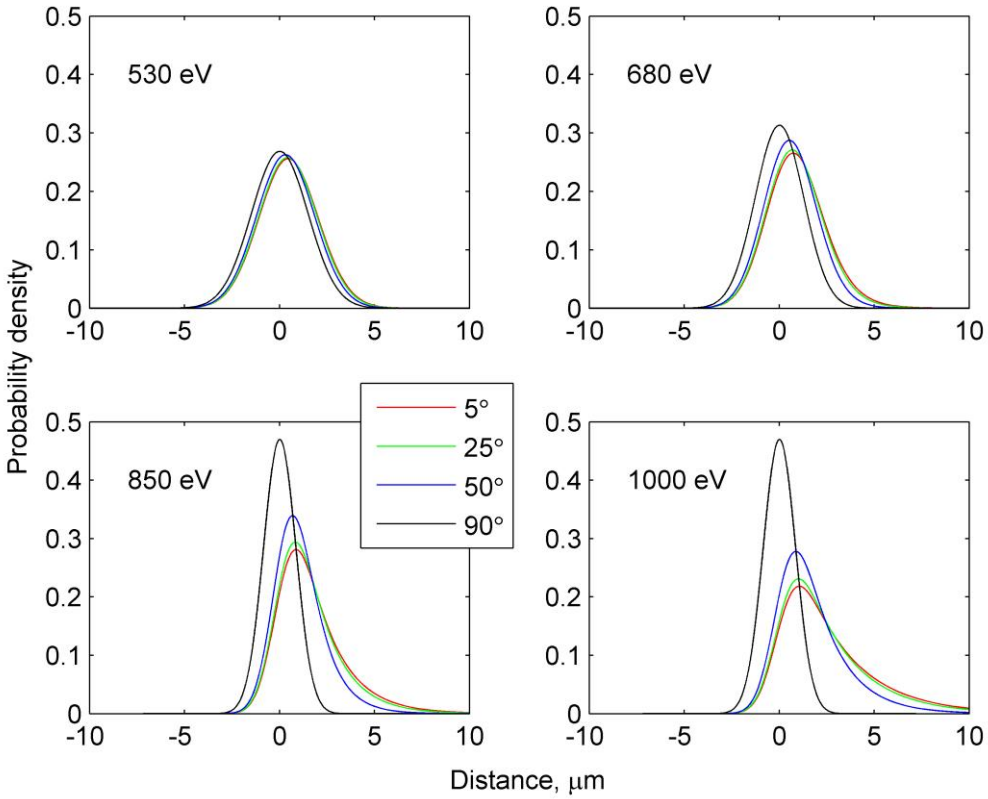

Figure 8.17. The PSF increases in width more significantly at higher energies (where the attenuation length is longer), and at more acute incident angles.

The centroid resolutions are modelled with Gaussian profiles with FWHMs of 3.5 µm, 3.0 µm, 2.0 µm and 2.0 µm at 530 eV, 680 eV, 850 eV and 1000 eV respectively, matching the results achieved with the CCD97 (Table 7.4), and convolved with the energy-dependent interaction depth projected onto the CCD-plane according to the incident angle (e.g. Figure 8.17). The resolution of the detector in the plane of the CCD is measured from the FWHM of the convolved overall resolutions, and shown as a function of energy and angle in Figure 8.18. For comparison, an estimate of the detector PSF is also shown for when the detector is operated in an integrating mode, reaching a width of approximately 24 µm at an incident angle of 20° [7]. The goal of a 5 µm resolution in the plane of the detector whilst oriented at 20° is also shown.

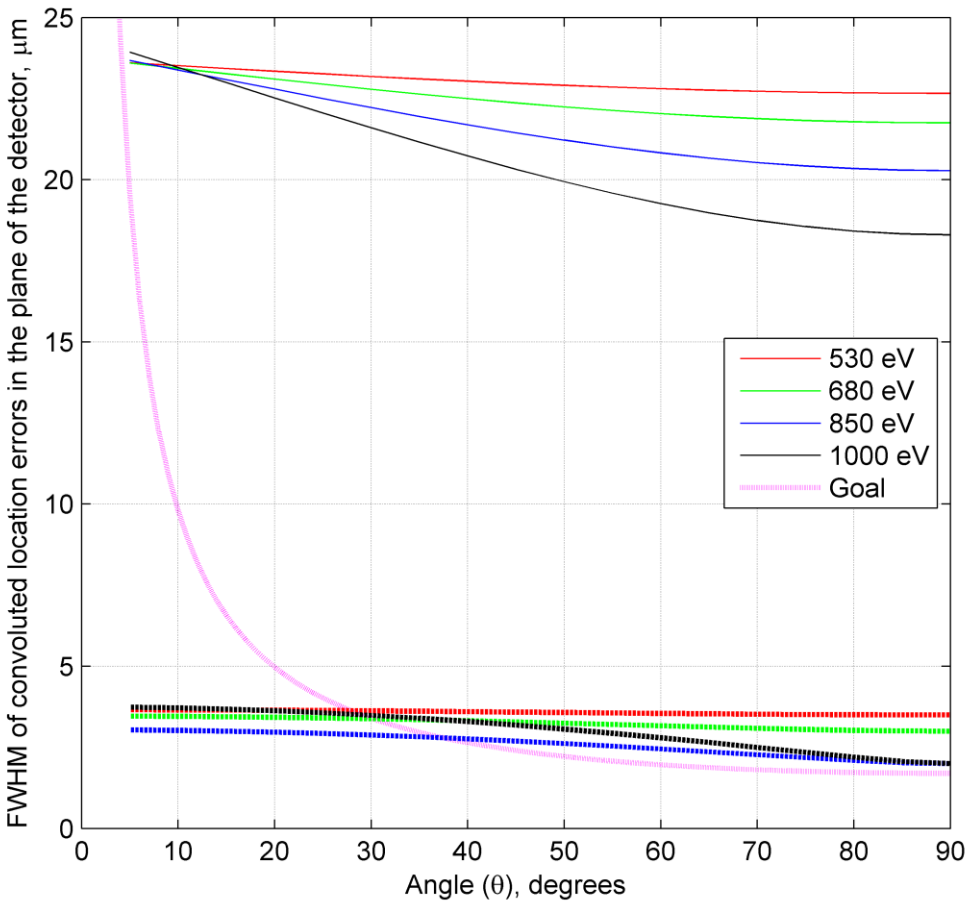

Figure 8.18. The FWHM of the centroid PSF convolved with the exponential interaction depth distribution that is projected onto the CCD plane (thick dashed lines) can be compared to PSF of the detector whilst operating in integrating mode (solid lines). The resulting resolutions are measured in the plane of the CCD.

To determine the effective detector resolution in the plane perpendicular to the incident X-rays (the energy-dispersed dimension), the resolutions from Figure 8.18 are multiplied by $\sin(\theta)$ (Figure 8.19). For the 1000 eV photons, the effective detector resolution is initially degraded as the incident photon angle is varied away from normal due to the projection of the interaction depth distribution. However as the angle is reduced towards 40°, the angle between the energy plane and CCD plane outweighs the interaction depth effect, and the resolution improves. At lower energies, where the attenuation length is short, the projection of the interaction depth distribution does not outweigh the effect of projecting from the CCD plane into the energy-plane.

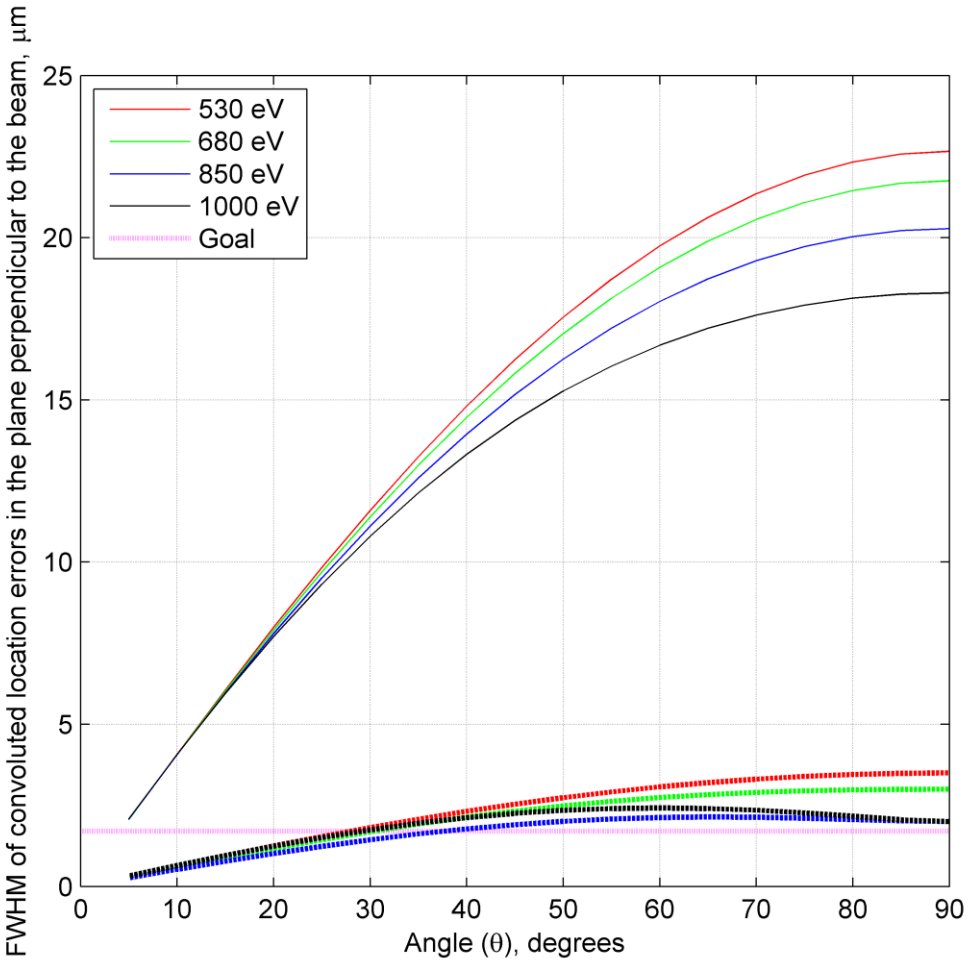

Figure 8.19. The effective resolution of the detector is measured in the plane perpendicular to the incident photons, whilst operating in centroiding mode (thick dashed lines) and integrating mode (solid lines).

The energy resolution goal is to achieve a resolution in the plane of the detector of better than 5 µm (FWHM), measured when the X-rays are incident at an angle of 20°. Centroiding events observed with an EM-CCD can achieve this goal when the incident angle is maintained more acute than 30°, for photons with energies greater than 530 eV. The increase in effective pixel density dominates the gain in resolution when the CCD is tilted, such that at angles closer to normal incidence, the resolution is effectively degraded.

8.4.3 The optimum detector angle

To decide on the optimum detector angle, the user must weigh up the effects described in Table 8.2. The default choice for the user would be an angle of 20°, matching the current detector therefore as the current camera has a suitable effective area, and a CCD207-40 would not provide

much less, the effective area is not an important parameter in the decision. The quantum efficiency could be improved for the lower energies by changing the incident angle to normal to the detector, but the effective resolution of the detector would become worse and at angles greater than 30°, the resolution goal would not be achieved.

The final parameter that varies is the effective flux incident on the detector: changing the photon's angle of incidence into the detector from 20° to normal would increase the flux per pixel by a factor of approximately 2.9. The increase in effective flux would be undesirable and may result in degrading the resolution and spectrometer throughput, as described in Section 8.5.

8.5 Varying the detector readout rate

The SAXES camera must operate in a mode that maximises the number of photons detected by the CCD that can be used to construct a spectrum. In integration mode this is achieved by using long integration times, minimising the proportion of total time that is spent reading the detector out. In a centroiding mode the number of photons that centroid algorithms can be applied to must be maximised. As centroiding algorithms are most accurately applied to isolated single photon events, shorter integration times are used to prevent pile-up of the photons in the image. In centroiding mode a compromise must be made between short integration times to maximise the proportion of photons in an image that are detected as isolated single photon events and minimise the proportion of time spent during read out.

The SAXES observations of a Carbon-tape elastic line, introduced in Section 6.8, are used to determine the typical highest flux that a SAXES camera would observe. A Monte Carlo simulation calibrated against the SAXES observations determines the yield of photons that centroid algorithms can be applied to when observing spectral features across the appropriate range of flux levels. The integration time, readout rate and photon flux variable spaces are studied.

8.5.1 Number of centroidable photons per detector duty cycle

The detector is integrated for τ_I seconds for each image before reading out the detector for τ_R seconds (number of pixels to be read out divided by the pixel readout rate), whilst a photon flux $\mathcal{F}$ (photons cm^{-2} second^{-1}) is incident on the detector. Therefore, assuming that photons detected during readout cannot be used, the effective number of photons observed by the detector during one image capture is $\mathcal{P} = \mathcal{F}\tau_I$ (photons cm^{-2} image^{-1}).

Single photon events detected by the device must be sufficiently isolated within the image such that their electron charge clouds do not overlap each other in the pixels that centroiding

algorithms are applied to. Higher flux lines observed under longer integration times may experience pile-up, where the signal from one photon appears in the same pixels as another photon. Ignoring pile-up events would lead to the flux in higher flux lines being systematically underestimated closest to the peak, but including them lowers the resolution as they cannot be centroided as accurately.

The density of interaction events that centroid algorithms can be applied to in one image will be some function of $\mathcal{P}$, i.e. $\mathbb{G}(\mathcal{P})$ (centroidable photons cm^{-2} image^{-1}). Therefore the density of interaction events that centroid algorithms can be applied to, observed per second, is $\mathbb{G}(\mathcal{P})/(\tau_I + \tau_R)$ (centroidable photons cm^{-2} s^{-1}), when averaged across the complete integration and readout cycle. The efficiency of the camera as a detector of photons in centroidable events is then given by the proportion of all the photons incident on the detector that centroid algorithms can be applied to, $\mathcal{C}_{eff} = [\mathbb{G}(\mathcal{P})/(\tau_I + \tau_R)]/\mathcal{F}$.

The integration time that maximises $\mathcal{C}_{eff}$ for typical fluxes observed by the SAXES camera can be determined to maximise the throughput of the spectrometer. The maximum $\mathcal{C}_{eff}$ can be compared with the current camera system's typical throughput of 93.5% (using an integration time of 600 seconds, a readout time of 42 seconds and detecting in an integrating mode).

8.5.2 Typical readout times and fluxes observed by a CCD207-40 camera

The CCD207-40 has an image area of 1608 rows by 1632 columns (approximately 2.6 megapixels) and a single output node (Figure 8.20). Each pixel is 16 µm square, resulting in a light sensitive region that is 2.57 cm by 2.61 cm (area of 6.72 cm^2). The full-frame readout time for a selection of pixel readout rates are given in Table 8.3. In some cases, the spectra may be contained in a region of interest on the device that is significantly smaller than the full device. The readout time can be reduced by binning the rows that do not contain any spectral information, and reading out only the rows in the region of interest. As an example, the approximate readout times for a region of interest 400 rows by 1632 columns (Figure 8.20) is also shown in Table 8.3.

The typical fluxes that would be observed by the camera if installed at SAXES can be measured from the 'C-tape' images introduced in Section 6.8. The highest flux of photons is observed in the 'slope region' of the image, which was defined to be a region of 20×2048 pixels surrounding the elastic spectral line observed. The 'slope region' (each 13.5 µm square in the CCD42-40) has an area of 0.075 cm^2 and therefore, from the analysis in Section 6.8, the average flux on the area is between 111±7 and 126±11 photons cm^{-2} second^{-1}. However, the photons are distributed in a Gaussian-like profile across the rows of the region with a standard deviation of approximately 2.4 pixels. Therefore the average flux across the areas within 1, 2 or 3 standard deviations (σ)

from the centre of the Gaussian distribution can also be calculated. The results are summarised in Table 8.4. It is clear that the flux in the centre of the spectral feature is significantly greater than the flux averaged across the entire region. One should note that the flux values are measured in the plane of the current detector i.e. 20° to the incident photons.

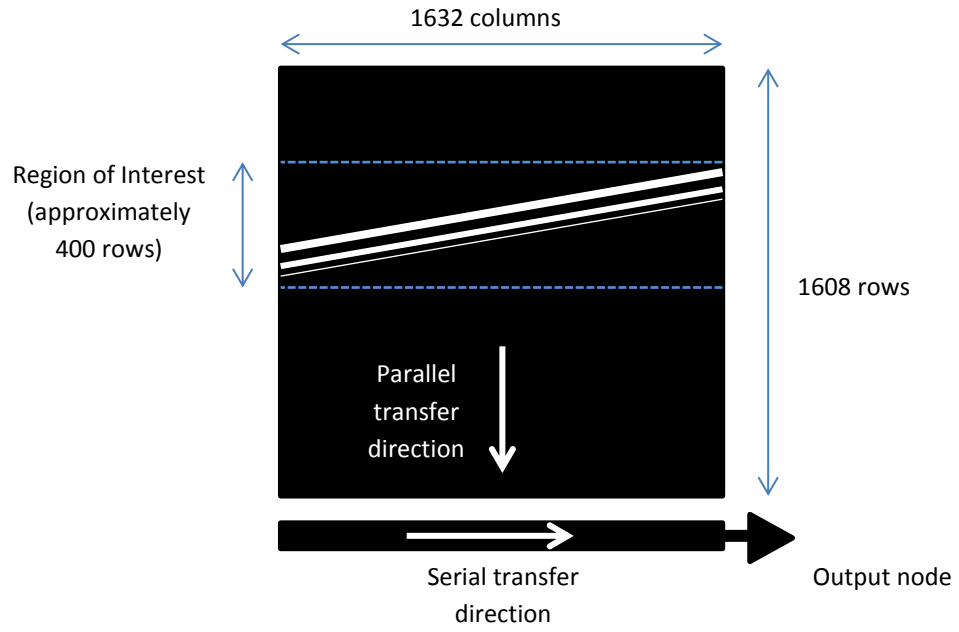

Figure 8.20. Schematic diagram of a CCD207-40 detector. A sketched spectrum is shown with photons of the same energy being detected in diagonal lines across the device, contained within a region of interest that is 400 rows by 1632 columns.

Table 8.3. The time taken to read out the CCD207-40 for a range of readout rates.

Readout rate (MHz)	τ_R **Full-frame readout time (seconds)**	**Approximate readout time for a region of interest of 400 rows by 1632 columns (seconds)**
0.1	26.27	6.56
1	2.66	0.68
2	1.34	0.36
3	0.91	0.25

Table 8.4. The average flux observed in the C-tape spectral feature, in the plane of the CCD.

				Flux (photons cm^{-2} $second^{-1}$)	
	Region width (pixels)	**Area of region (cm^2)**	**Proportion of photons in area**	**Minimum**	**Maximum**
Slope region	20	0.075	1	111±7	126±11
3 σ	14.28	0.053	0.9973	156±9	176±15
2 σ	9.52	0.036	0.9545	234±14	265±23
1 σ	4.76	0.018	0.6827	467±28	529±45

8.5.3 Producing simulated images with given flux levels

A Monte Carlo simulation is constructed to determine how the proportion of events that can be centroided varies with the flux incident upon a detector. Typical events are formed at random locations in the detector using the event simulation package described in Chapter 4. The simulated image is analysed to determine the proportion of centroidable events at set flux levels, i.e. $\mathbb{G}(\mathcal{P})$.

To produce the simulated image, an array with 1608 rows and 1632 columns is defined to match the size of the CCD207-40 sensor. The pixel signals of a single photon interaction event is determined across a 5×5 pixel area, with the charge splitting between pixels modelled using a solution to the diffusion equation [66] in a 16 µm square pixel. The electron signals due to single photon interactions are added to the array at random locations within randomly chosen pixels, avoiding an area of 2 pixels width around the outside to prevent any complications from the finite array size. The interaction depth distribution of the photons is determined using the attenuation length of 1000 eV photons (2.68 µm) incident normal to the device. The results presented here are not sensitive to the photon energy or the incident angle, as the events are well contained within the 2×2 or 3×3 pixel areas.

To determine the proportion of centroidable events, the events are extracted following the procedure described in Section 6.8, using both the 3×3 and 2×2 pixel area algorithms. The 2×2 event extraction allows for a higher proportion of photons to be centroided as fewer are discarded due to interacting in close proximity to other photons, as seen in the plot of $\mathbb{G}(\mathcal{P})$ in Figure 8.21.

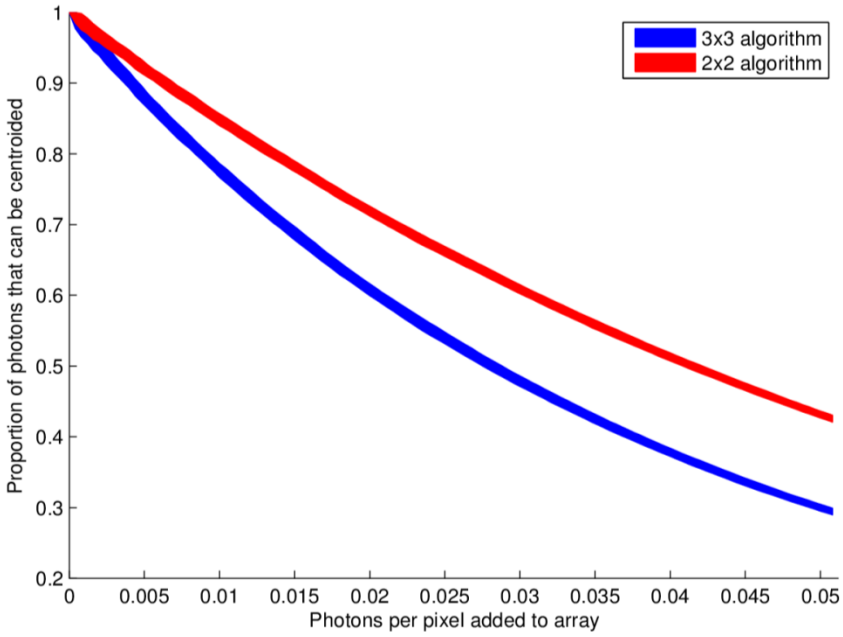

Figure 8.21. The proportion of photons in an image that the centroid algorithms can be applied to, $\mathbb{G}(\mathcal{P})$, is greater for the 2×2 centroid algorithm than the 3×3 centroid algorithm. The mean and standard deviation of 100 simulation runs is calculated. The thickness of the lines drawn in blue and red show the proportion of photons within 1 standard deviation from the mean of the simulation runs.

8.5.4 Yield of centroidable events

The spectrometer user wishes to maximise the number of photons detected, to build up a spectrum with significant statistics in as short a time as possible. However, the user also hopes to apply centroiding algorithms to isolated events in order to improve the spatial resolution of the detector, improving the energy resolution of the spectrometer.

When using a camera system with a set readout rate to observe a spectral feature with a given photon flux, the user wishes to maximise the proportion of centroidable photons observed across the integration and readout cycle ($\mathcal{C}_{eff}$) by tuning the integration time. $\mathcal{C}_{eff}$ for the 2×2 centroid algorithm is calculated across the flux and integration time variable space for a range of readout times. Figure 8.22 and Figure 8.23 show $\mathcal{C}_{eff}$ for when the device is operated in full-frame and region of interest (400 rows) readout modes respectively. For comparison, the current SAXES camera operating at a readout rate of 100 kHz and integration time of 600 seconds uses 93.5% of the photons incident on the detector to construct a spectrum, with the remaining 6.5% lost during readout time.

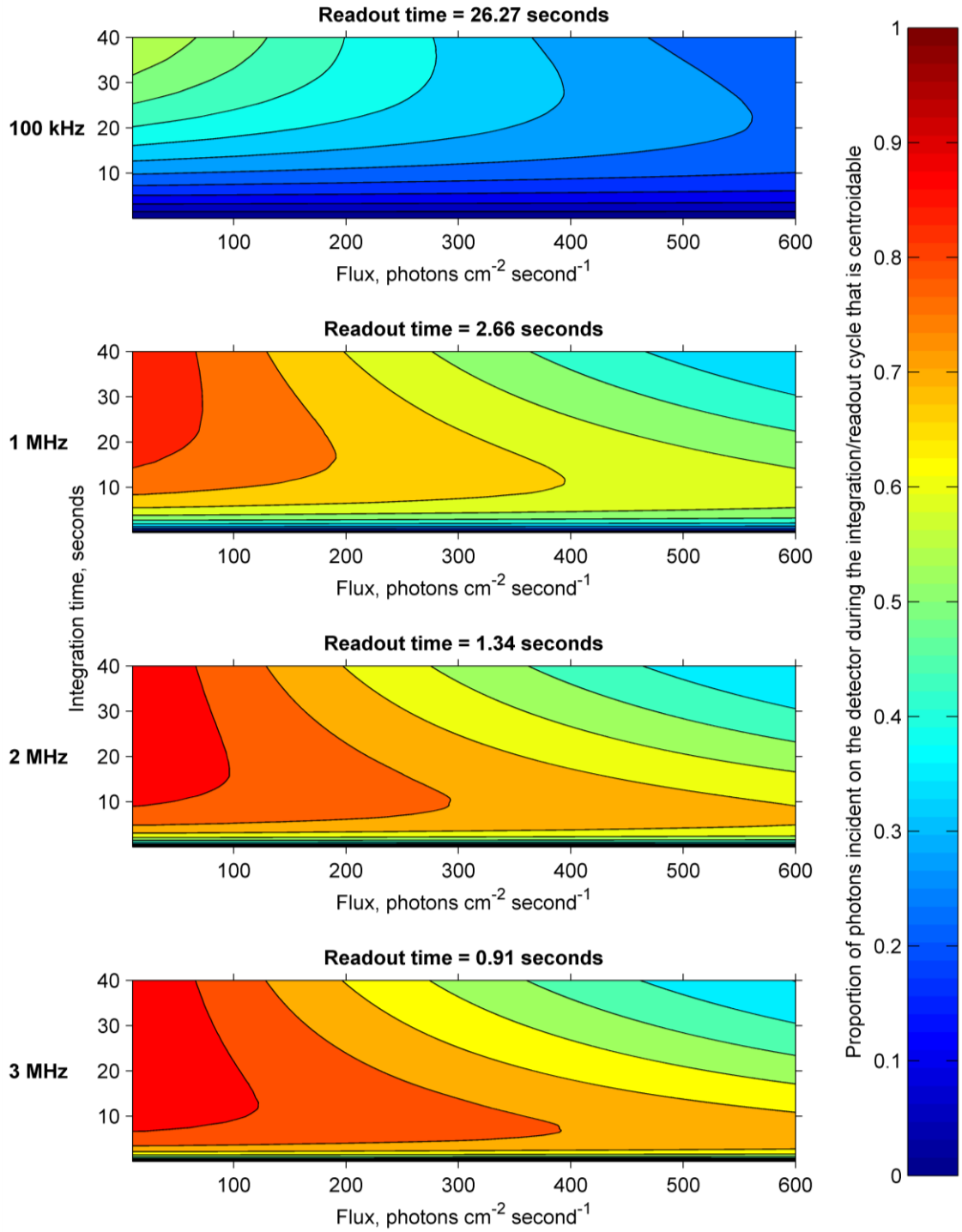

Figure 8.22. The proportion of photons incident on the detector during an integration and readout cycle that can be centroided ($\mathcal{C}_{eff}$) is shown for four different readout times. The readout times of 26.27 seconds, 2.66 seconds, 1.34 seconds and 0.91 seconds correspond to reading out the full-frame with pixel readout rates of 100 kHz, 1 MHz, 2 MHz and 3 MHz respectively.

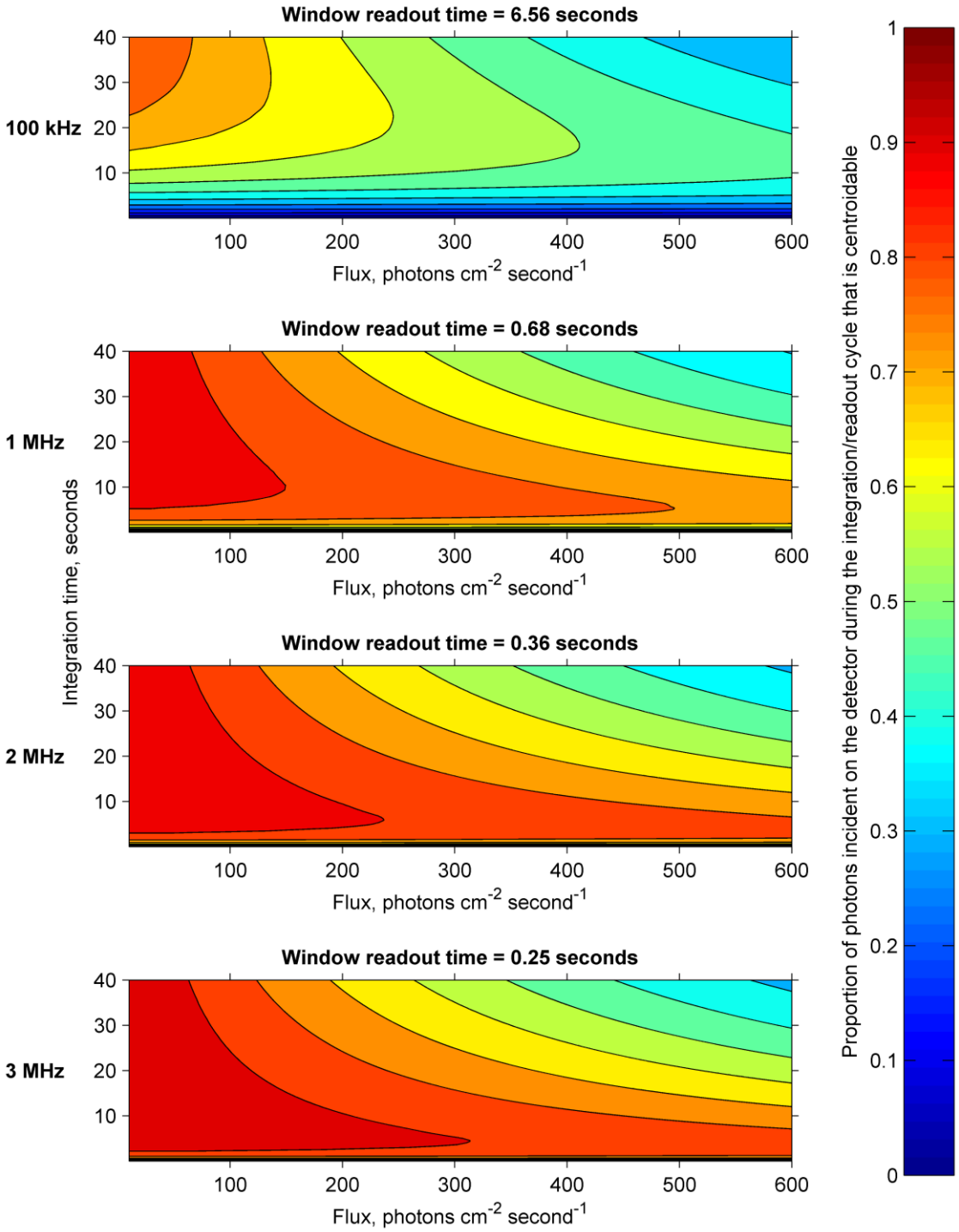

Figure 8.23. The proportion of photons incident on the detector during an integration and readout cycle that can be centroided (C_{eff}) is shown for four different readout times, assuming an area of interest 400 rows wide is read out. The readout times of 6.56 seconds, 0.68 seconds, 0.36 seconds and 0.25 seconds correspond with pixel readout rates of 100 kHz, 1 MHz, 2 MHz and 3 MHz.

The maximum proportion of centroidable photons observable at each flux level is increased by only reading out a region of interested 400 rows wide and by speeding up the readout rate. The proportion of photons that contribute to the spectrum with the current camera in integrating mode is 93.5%, assuming an integration time of 600 seconds and full-frame readout at a 100 kHz pixel readout rate, and irrespective of photon flux. The CCD207-40 based photon counting camera system approaches the same detection efficiency at lower flux rates, and when operating at the higher readout rates. However, at the expected flux rates at the centre of spectral lines, the proportion of photons incident on a single CCD207-40 that can be used to construct a spectrum will be lower than the current CCD42-40 integration mode camera system. To maintain or improve on the photon flux detected that can contribute to the spectrum constructed of centroidable events, the future camera upgrade could consist of multiple CCD207-40s, spread across the isoenergetic line.

The number of pile-up photons that must be discarded is greatest in the central proportion of spectral features where the flux is highest, leading to the spectral feature being effectively widened, as described in Section 6.8.3. To operate the centroiding camera in a higher spatial resolution mode, an integration time shorter than the best-case values given by Figure 8.22 and Figure 8.23 are recommended, to reduce the pile-up of photon interactions. If maximising the photon count rather than the resolution is preferred, a longer integration time may be used, but the relative photon counts in spectral features may be biased unless the preferential pile-up rejection is accounted for.

The yield of centroidable photons at the optimum integration times are shown in Table 8.5, for both the full-frame and windowed readout modes. The yield of photons if the camera was operating in integration mode at these optimum integration times are shown in brackets for comparison. The fastest readout rate (3 MHz in this investigation) results in the highest yield of photons that centroid algorithms can be applied to, across all the flux levels and using both modes. When considering a future SAXES camera system, the difference in yield between the different readout rates must be balanced with the relative costs and complexities. The yields can be compared with the typical yield of the current system, which is 93.5% when integrating for 600 seconds, and reading out over 42 seconds.

Table 8.5. The percentage of photons incident on the detector during an integration and readout cycle that can be centroided using a 2×2 algorithm ($\mathcal{C}_{eff}$) is shown here for a range of pixel readout frequencies. For each flux and readout time, it is assumed that the integration time that maximises the percentage of centroidable photons is used. The percentage of time that the camera spends during integration is shown in brackets.

Readout frequency (MHz)	**0.1**	**1**	**2**	**3**	**0.1**	**1**	**2**	**3**
Readout time (seconds)	**26.27**	**2.66**	**1.34**	**0.91**	**6.56**	**0.68**	**0.36**	**0.25**
Flux (photons cm^{-2} s^{-1})	**Full-frame**				**400 row region of interest**			
50	64.2 (79.2)	86.4 (92.2)	90.1 (94.9)	91.7 (96.0)	79.6 (89.0)	92.7 (96.5)	94.6 (97.2)	95.6 (97.4)
100	54.2 (70.9)	81.4 (90.4)	86.3 (92.1)	88.6 (93.9)	72.7 (85.1)	90.0 (94.8)	92.5 (96.3)	93.8 (96.9)
150	47.8 (66.5)	77.8 (88.7)	83.5 (91.6)	86.2 (92.0)	68.0 (81.1)	88.0 (93.9)	91.0 (95.3)	92.4 (96.2)
200	43.2 (62.5)	75.0 (86.1)	81.3 (90.3)	84.2 (91.2)	64.2 (79.2)	86.2 (92.0)	89.8 (95.1)	91.3 (95.6)
250	39.6 (59.6)	72.6 (84.9)	79.4 (88.8)	82.6 (90.6)	61.2 (77.4)	84.7 (91.7)	88.7 (94.0)	90.4 (95.2)
300	36.7 (57.1)	70.5 (83.6)	77.8 (88.6)	81.2 (90.2)	58.6 (75.1)	83.4 (91.5)	87.7 (93.5)	89.6 (94.9)
350	34.2 (53.6)	68.7 (81.9)	76.3 (87.0)	79.8 (88.7)	56.3 (72.6)	82.2 (90.8)	86.7 (92.5)	88.8 (94.1)
400	32.1 (51.4)	67.0 (81.0)	74.9 (86.0)	78.6 (88.0)	54.2 (70.9)	81.2 (90.2)	85.8 (91.6)	88.1 (93.4)
450	30.3 (49.1)	65.5 (79.7)	73.7 (85.1)	77.6 (88.4)	52.4 (70.0)	80.2 (89.1)	85.0 (92.1)	87.4 (93.3)
500	28.7 (47.8)	64.0 (79.0)	72.5 (84.8)	76.6 (87.3)	50.7 (69.1)	79.3 (88.6)	84.3 (91.3)	86.8 (92.6)
550	27.3 (46.4)	62.8 (78.9)	71.4 (84.7)	75.6 (86.2)	49.2 (67.5)	78.4 (88.8)	83.6 (91.7)	86.1 (91.9)
600	26.0 (44.5)	61.6 (77.9)	70.4 (83.5)	74.7 (85.7)	47.8 (66.5)	77.6 (88.5)	83.0 (91.0)	85.6 (92.6)

The integration times required to achieve the levels of performance specified in Table 8.5 are at a minimum when the photon flux is at a maximum (at 600 photons cm^{-2} $second^{-1}$). The shortest integration times are shown in Table 8.6, alongside the proportion of the camera cycle that is spent reading out. When the proportion of time spent during readout is large, a shutter will be required to prevent stray photons being detected. At higher readout rates, the optimum proportion of time spent during readout is similar to the current system (6.5% when integrating for 10 minutes and reading out for 42 seconds), which does not use a shutter. The minimum optimum integration times are relatively short, with a significant percentage of the time spent during readout. To prevent stray photons being detected in the wrong area of the device during readout, a shutter system may be required.

Table 8.6. The minimum integration times and associated proportions of time spent during readout, for the performances in Table 8.5 at a flux of 600 photons cm^{-2} s^{-1}.

Readout rate (MHz)		**0.1**	**1**	**2**	**3**
Minimum integration time (seconds)	**Full-frame**	21.1	9.28	6.78	5.47
	Region of interest	12.98	4.92	3.61	2.70
Percentage of time spent during readout (%)	**Full-frame**	55	22	17	14
	Region of interest	34	12	9	8

8.5.5 The yield of centroidable photons

At the optimum integration times for the expected typical flux levels and readout rates, the proportion of centroidable photons that contribute to the spectrum is lower than the current proportion of photons incident on the detector in integration mode that contribute to the spectrum. The throughput of the spectrometer can be maintained by including more detectors and therefore increasing the length of the spectral line that is observed.

The flux levels investigated here assume that the detector is at 20° to the incident photons. Rotating the detector to normal to the beam would increase the effective flux on the detector by a factor of approximately 2.9, leading to the yield of centroidable photons to be further reduced if the same area of the detector is read out. However the region of interest that is required to be read out to observe the same energy range of the spectrum would also be reduced by a factor of 2.9, increasing the frame rate.

8.6 Recommendations for SAXES system upgrade

The research described in this chapter and earlier in this thesis has demonstrated that a photon counting camera based on a CCD207-40 would be capable of operating with a resolution better than an effective detector resolution of 1.71 µm (FWHM), measured in the energy dispersive plane normal to incident photons. The results have led to the following recommendations for a future SAXES camera.

- **Detector choice**: The CCD207-40 is a suitable detector for a future centroiding camera.

The electron multiplying gain register allows operation at fast readout rates with sub-electron readout noise therefore the spectrometer throughput can be maintained whilst the centroiding accuracy is better than could be achieved with a standard CCD with a readout noise of 4 electrons rms (such as the current camera system). The image area of the CCD207-40 is similar to that of the CCD42-40, and therefore a comparable energy range can be dispersed across and recorded in each spectrum.

- **Readout rate**: A pixel readout rate faster than 1 MHz is recommended.

Increasing the readout rate of the CCD207-40 will improve the throughput of the spectrometer by increasing the proportion of time spent during integration. This will be especially important whilst operating in centroiding mode to observe high flux lines. A faster readout rate will also allow a shorter integration time to be used, reducing pile-up in the image, which will limit the broadening of spectral lines caused by the rejection of pile-up events.

- **Readout noise:** The CCD207-40 should be operated at high gain to reduce the readout noise to a sub-electron level.

The centroiding spatial resolution degrades with increase readout noise, but the multiplication noise plateaus at high levels of gain. Therefore, the gain should be used to its full effect by increasing the gain to minimise the effective readout noise.

- **Angle of incidence**: The angle between the incident photons and the plane of the detector should be maintained at 20°.

The advantages of maintaining the angle at approximately 20°, including a better effective detector resolution and reduced effective photon flux, outweigh the quantum efficiency and effective energy range benefits of setting it closer to 90°.

- **Detector orientation**: Spectra should be dispersed up the columns of the detector.

The resolution has been measured to be approximately 10% better in the *y* than the *x* direction in the CCD97, which is a more conclusive result than achieved with the CCD207, therefore it is

recommended that the detector is oriented such that the *y* direction (column) is oriented close to parallel to the energy dispersive direction. This orientation may have a small effect on the detector resolution, but more importantly it will increase the frame rate when operating in a windowed mode and allow closer mounting if the standard CCD207-40 packages are used.

- **Windowed readout:** The camera should be able to read out the detector in a windowed mode.

When the spectral features of interest do not extend across the entire device, the throughput of the spectrometer can be greatly increased by only reading out the pixels within a region of interest from the detector.

- **Shutter requirements**: A shutter will be required to control the exposure of the detector.

The optimum integration times required for acquiring the maximum number of centroidable photons per second depend on the readout time but are less than 10 seconds for pixel readout rates faster than 1 MHz. To prevent smearing of spectral lines from X-rays being observed during readout time, a shutter will be required.

- **Computational support:** Sufficient computational power and support will be required.

The data rate output from a detector operating in a photon counting mode will be greatly increased from the current camera operating in integration mode. The appropriate computational support must be available to both save and process the images (event identification and centroiding).

- **η algorithm calibration:** Pre-calibration of the non-linear centroiding algorithm will be required during commissioning.

A population of X-ray events must be recorded and used to construct the η correction function. Populations of events must be obtained from a flat illumination at a range of X-ray energies during commissioning to allow the η correction to be applied during experimentation.

Whilst the CCD207-40 has been investigated in this work, if the resources were available a more ideal detector could be designed and manufactured. This bespoke detector could use a frame transfer architecture to minimise loss of exposure time due to readout. A photosensitive region in the energy-dispersive dimension of approximately 2.6 cm would still be desirable, but the detector could be significantly wider than the CCD207-40 (2.6 cm wide) to increase the throughput. Multiple outputs could reduce the readout time, compensating for the increased imaging area. Unfortunately, the costs of developing bespoke CCD for RIXS are not currently

feasible and therefore this work has focussed on developing a system around an available EM-CCD.

8.7 Summary

Results presented in Chapter 7 showed that the CCD97, a small area EM-CCD, was capable of achieving a detector resolution better than the goal of 5 µm (FWHM). Therefore, the EM-CCD could be considered as a suitable detector for a future SAXES camera system upgrade which allows for X-ray event centroiding. However, the CCD97 is a small area detector which would reduce the throughput and energy range of SAXES and so a detector of similar imaging area to the current CCD42-40 was required. This led to the CCD207-40 being identified as the most suitable EM-CCD for SAXES and another experimental campaign was undertaken at PolLux to take measurements that confirmed that this large area EM-CCD was capable of achieving a similar centroiding resolutions as the CCD97 (Table 7.5).

Table 8.7. A summary of the resolution measurements presented in Chapters 7 and 8 for EM-CCDs (c.f. Table 7.5).

Detector	**Photon energy, eV**	**Resolution (FWHM) measured with X-rays incident normal to the detector, µm**	**Effective detector resolution (FWHM): Measured in the energy plane with photons incident at 20°, µm**
Upgrade requirement	-	Effective goal < 5	Effective goal < 1.71
CCD97	530	3.45±0.38	1.23±0.13
	680	2.82±0.09	1.11±0.03
	850	2.15±0.004 (*x* direction) 1.93±0.004 (*y* direction)	1.06±0.001 (*x* direction) 0.99±0.001 (*y* direction)
	1000	2.09±0.004 (*x* direction) 1.87±0.004 (*y* direction)	1.27±0.001 (*x* direction) 1.20±0.001 (*y* direction)
CCD207-40	1000	1.66±0.01 (*x* direction) 2.02±0.01 (*y* direction)	1.14±0.003 (*x* direction) 1.25±0.003 (*y* direction)

To ensure that a CCD207-40 camera system is capable of operating in a photon counting mode with a suitable throughput at SAXES, optimum integration times were determined for a range of flux rates and camera pixel readout frequencies. If the detector is read out at 1 MHz pixel rate, and observes a feature with the same flux rate as in the centre of the example ‘C-tape’ elastic line,

the effective throughput of the detector will drop from 93.5% (current detector in integrating mode) to 63.1% (centroiding mode). If a future camera consisted of multiple CCD207-40s, operated at fast pixel readout rate and/or observed lower flux spectral features, the effective throughput could surpass the current camera setup.

The goal of a 5 µm (FWHM) detector spatial resolution is for a detector oriented at an angle of 20° to the incident photons, i.e. the goal is equivalent to a 1.71 µm (FWHM) detector resolution in the plane normal to the X-ray path. Measurements at the PolLux specromicroscope have been made with photons incident normal to the detector, so the resolution results must be convoluted with the error introduced by the random interaction depth when converted to a detector at an angle of 20° (Table 8.7). To prevent the random interaction depth distribution introducing additional error to the resolution, a camera upgrade could orientate the detector normal to the incident photons. The proposition that changing the incident angle of the photons towards a normal incidence would improve the overall effective resolution of the detector was investigated, as it would also improve the quantum efficiency at lower energies as well as increase the imaging area and flux. However, the effective detector resolution is not necessarily improved once the resolution has been mapped into the energy plane for angles larger than 30° (Figure 8.19) and the increase in effective flux on the detector would have a detrimental effect on its throughput when operated in a photon counting mode.

8.8 Conclusions

Following the successful proof of principle of centroiding events observed with the small area CCD97, campaign 4 was undertaken using a large area EM-CCD, the CCD207-40. During the test campaign, the transfer of charge from particular pixels stopped performing as expected. In Section 8.3.3 it has been hypothesised that a large number of 1000 eV X-rays were incident on the device, resulting in a build-up of immobile holes in the oxide layers under a small area of the pixel. The increase in positive charge resulted in a localised increase in the potential well depth so the charge transfer clocking scheme no longer transferred charge to the neighbouring pixel. The radiation damage that occurred and the large area of the detector led to a limited data set being collected to determine the resolution of centroiding algorithms in the CCD207-40. However, as the pixel structure of the CCD207-40 is identical to the CCD97's, and the results presented show that the two devices achieved similar performances expected from the simulations in Section 5.4.2, the resolution achievable with the CCD207-40 in a possible future camera for SAXES is better than the 5 µm (FWHM) goal.

The centroid resolution results achieved with the CCD207-40 have been measured with the photons incident normal to the detector surface. The 5 µm (FWHM) spatial resolution goal is for a detector at 20° to the incident photons at SAXES. The effects of varying the incident angle on the CCD resolution, effective area and flux, and quantum efficiency have been investigated. The improved effective spectrometer energy resolution obtained by rotating the detector to approximately 20° to the incident photons outweighs the error of the interaction depth distribution. The effective area and QE are currently sufficient or tolerable at SAXES so a 20° angle is sufficient, but the effect on the spectrometer throughput by the varying flux has required a more detailed investigation. Simulating the flux levels observed in the example images from SAXES examined in Section 6.8 suggests that if the CCD207-40 was normal to the incident photons, the increased effective flux level would degrade the throughput significantly. To operate with a maximum centroidable photon throughput, a CCD207-40 based camera system at SAXES must be operated with a fast readout rate, but with a multiplication gain sufficiently large to maintain a signal to effective readout noise ratio that allows an accurate centroiding resolution. Centroiding events in images simulated with the expected flux levels on a CCD207-40 suggest that a readout rate faster than 1 MHz should be used whilst operating in a windowed mode, with integration times shorter than 10 seconds.

Chapter 9: Conclusions and Future Work

RIXS is quickly becoming one of the most important spectroscopic techniques that enable the bonding, structure and properties in materials to be investigated. RIXS can be used to study charge-neutral excitations in solid, liquid or gaseous samples across a range of photon energies, polarizations and scattering angles but has only emerged in the past few decades due to the improved resolution of instrumentation and brilliance of tuneable X-ray sources.

SAXES is a world-leading RIXS spectrometer at the SLS, with a resolution of greater than 12 000 ($E/\Delta E$) at 930 eV. Currently, the dominant sources of error in the energy resolution are the grating's slope error and the detector's spatial resolution, which is limited by the sharing of charge between pixels. The main research goal of this thesis has been to understand and characterise charge spreading, leading to the application of an appropriate centroiding algorithm to single photon events recorded by the SAXES camera. A spatial resolution goal of better than 5 µm (FWHM), assuming the detector plane is at 20° to incident photons, has been set which is a vast improvement from the current charge sharing limited case of 24 µm (FWHM) [7].

9.1 Summary of chapter conclusions

Models and experimental data have been compared to study the splitting of signal across multiple pixels from soft X-ray interactions in the field-free region of back-illuminated CCDs. Following a review of solutions and empirical fits found in the literature, the solution to the diffusion equation from Pavlov and Nousek [66] has been shown to agree best with experimental results. Applying this solution in a simulation package has allowed large populations of X-ray events detected in a CCD to be simulated, allowing centroiding algorithms that estimate the position of interaction to be tested. A systematic bias was observed when using the linear centre of gravity algorithm, but the η correction algorithm was shown to account for this bias, improving the overall spatial resolution when applied. The simulations described in this thesis showed that the spatial resolution of centroiding algorithms applied to soft X-ray events was dependent on the signal to background noise ratio of the image, but at high signal to background noise ratios the spatial resolution was limited by the stochastic nature of the diffusion process, reaching a minimum spatial resolution better than 2 µm (FWHM).

To experimentally verify the charge spreading models and the simulation results, an experimental setup where the photon interaction position can be determined and compared to the centroid location was required. The PolLux spectromicroscope at the SLS was adapted to allow a CCD to be operated at the focal point of the 1st order diffraction from a FZP. During a series of experimental

campaigns, the experimental setup was improved to optimise the data collection and detector cooling methods. The sub-micron X-ray spot was scanned across the pixel of a CCD42-10, a device with the same architecture as the CCD42-40 currently installed at SAXES, at four soft X-ray energies. Analysis of the single photon events recorded verified that the centre of gravity centroid algorithm incorporating the η correction could measure a spatial resolution of better than 5.5 µm (FWHM) at 530 eV, improving to better than 3.5 µm at 1000 eV. These measurements include an unknown contribution from the X-ray spot size, but indicate that the resolution goal of better than 5 µm could be achieved with centroiding algorithms applied to events in the SAXES camera. Centroiding algorithms have been applied to test images recorded at SAXES as a proof of principle that the resolution can be significantly improved however, to operate the SAXES camera in a photon counting mode rather than its current integrating mode, the integration time would have to be reduced significantly. Operating with a reduced integration time with the same readout time leads to a lower spectrometer throughput which is not an ideal situation for RIXS, a photon-starved technique.

Therefore, as the readout noise of the current SAXES camera when operating in its faster readout rate mode is too high for accurate photon counting or centroiding, the EM-CCD was proposed as an alternative detector technology capable of operating at a few MHz pixel readout rates whilst maintaining a sub-electron effective readout noise. A test campaign at PolLux was undertaken to verify the application of centroid algorithms to events observed in a CCD97. Spatial resolutions better than 2.15 µm (FWHM) at 850 eV and 1000 eV were achieved, with a contribution from the X-ray spot size. The resolutions at these energies were approximately 0.2 µm better in the *y* than the *x* direction, corresponding to a wider charge cloud width in the *y* than the *x* direction. Measurements at 530 eV and 680 eV taken with the spot defocussed allowed the spot size's contribution to be deconvolved from the spatial resolution, leading to worst-case measurements of 3.45±0.38 µm and 2.82±0.09 µm (FWHM) respectively. All resolutions achieved with the CCD97 have been significantly better than the 5 µm (FWHM) goal for the SAXES upgrade therefore the CCD207-40, a large area EM-CCD has been proposed for a future camera.

A further test campaign at PolLux confirmed that the CCD207-40 was capable of achieving the same spatial resolution as the CCD97, as expected by the same pixel architecture of these two devices. However, during testing the CCD207-40 was damaged such that charge stopped transferring through two pixels. It has been proposed that this is due to a localised build-up of holes under the gate, forming a region of deep potential that trapped charge and inhibited the charge transfer process. This is not expected to be a problem with the flux rates and angle of incidence at SAXES. An investigation into the required readout rates for a CCD207-40 based SAXES camera has been carried out, determining that the camera should be capable of readout rates

faster than 1 MHz, with integration times shorter than 10 seconds whilst reading out a windowed region of interest. The integration time should be tuned according to the flux rate of the spectral line being observed to allow the highest count rate of centroidable photons possible.

9.2 SAXES system upgrade

Following the successful investigations described in this thesis, discussions have been initiated between PSI and a camera design and manufacturing company to produce a new camera for SAXES. The final design is yet to be finalised, but the recommendations described in Section 8.6 are being contributed to the design process. At the time of writing a baseline design using three CCD207-40s, oriented with the detector plane at approximately 20° to the incident photons, has been drafted. Post-processing of the images recorded will apply the event detection, non-linear centroiding using the η correction, and spectra extraction algorithms developed and verified in this thesis. It is hoped that a new camera system will be commissioned at SAXES by mid-2015.

Alongside the negotiations with PSI, discussions are on-going with representatives at the Diamond Light Source to install a centroiding camera system at the RIXS spectrometer currently under construction at the I21 beamline [10]. Similar discussions are being initiated with other RIXS beamlines in the community, such as the Advanced X-ray Emission Spectrometer on beamline 26 at ESRF [13].

9.3 Future work

The application of centroiding algorithms at SAXES is severely limited by pile-up. Only single photon events have been investigated here, but it may be possible to determine the interaction position of, for example, double events to sub-pixel accuracy. The resolution achievable is not expected to be as good as with isolated events, but the process may be useful in high flux, low resolution applications.

Centroiding algorithms discussed in this thesis have all been applied across pixels in fixed areas, therefore no thresholding or pixel selection has been required. However, algorithms could be considered where only pixels with signal above a set level from the noise floor are used to calculate the centroid position. This may lead to improved centroid accuracy.

The effect of varying the depletion depth on the charge cloud width was briefly investigated using data obtained with the CCD42-10. A further experimental campaign, where the effect of varying the substrate potential and gate potentials during integration is investigated in the CCD97 or CCD207-40 would help to support the preliminary observations made in the CCD42-10 and could

advise on the best operational mode for a future SAXES camera. It is predicted that operation with no phases high during integration and a high substrate potential would decrease the depletion depth, increasing the charge splitting and therefore improve the centroiding accuracy. However, further beamtime would have to be awarded on the PolLux beamline for such an investigation to be completed.

The charge cloud in the CCD97 has been measured to be asymmetric, leading to improved centroiding accuracy in the *y* direction. However the opposite has been observed in the incomplete CC207-40 data. Future simulation of the potential well structures in, for example, TCAD SILVACO [105] would confirm the expected variation in depletion depth and help identify the differences between the dimensions and operational modes.

Localised loss of charge transfer capability has been observed in the back-illuminated CCD207-40 campaign. It has been proposed that the effect has been caused by a build-up of holes in a well-defined region. However no accurate measure of the dosage is known, and the damage only became apparent during the full analysis of the results, taking several weeks of data analysis, so no investigations have been carried out to investigate this hypothesis. The hypothesised damage process is not a concern for a possible future SAXES camera, but the localised and high flux conditions may occur in other applications such as X-ray Free Electron Lasers [109,110] and the damage mechanism is more of a concern for front-illuminated CCDs.

References

[1] Schlappa J, Wohlfeld K, Zhou K J, Mourigal M, Haverkort M W, Strocov V N, Hozoi L, Monney C, Nishimoto S, Singh S, Revcolevschi A, Caux J-S, Patthey L, Rønnow H M, van den Brink J and Schmitt T 2012 Spin-orbital separation in the quasi-one-dimensional Mott insulator Sr_{2}CuO_{3}. *Nature* **485** 82–5

[2] Schlappa J, Schmitt T, Vernay F, Strocov V N, Ilakovac V, Thielemann B, Rønnow H M, Vanishri S, Piazzalunga A, Wang X, Braicovich L, Ghiringhelli G, Marin C, Mesot J, Delley B and Patthey L 2009 Collective Magnetic Excitations in the Spin Ladder Sr_{14}Cu_{24}O_{41} Measured Using High-Resolution Resonant Inelastic X-Ray Scattering *Phys. Rev. Lett.* **103** 47401

[3] Braicovich L, van den Brink J, Bisogni V, Moretti Sala M, Ament L J P, Brookes N B, De Luca G M, Salluzzo M, Schmitt T, Strocov V N and Ghiringhelli G 2010 Magnetic Excitations and Phase Separation in the Underdoped La_{2-x}Sr_{x}CuO_{4} Superconductor Measured by Resonant Inelastic X-Ray Scattering *Phys. Rev. Lett.* **104** 77002

[4] Nordgren J, Bray G, Cramm S, Nyholm R, Rubensson J-E and Wassdahl N 1989 Soft x-ray emission spectroscopy using monochromatized synchrotron radiation *Rev. Sci. Instrum.* **60** 1690–6

[5] Hague C F, Underwood J H, Avila A, Delaunay R, Ringuenet H, Marsi M and Sacchi M 2005 Plane-grating flat-field soft x-ray spectrometer *Rev. Sci. Instrum.* **76** 023110

[6] Tokushima T, Harada Y, Ohashi H, Senba Y and Shin S 2006 High performance slit-less spectrometer for soft x-ray emission spectroscopy *Rev. Sci. Instrum.* **77** 063107

[7] Ghiringhelli G, Piazzalunga A, Dallera C, Trezzi G, Braicovich L, Schmitt T, Strocov V N, Betemps R, Patthey L, Wang X and Grioni M 2006 SAXES, a high resolution spectrometer for resonant x-ray emission in the 400-1600 eV energy range *Rev. Sci. Instrum.* **77** 113108

[8] Tsunemi H, Mori K, Miyata E, Baluta C, Burrows D N, Garmire G P and Chartas G 2001 Improvement of the spatial resolution of the ACIS using split-pixel events *Astrophys. J.* **554** 496–504

[9] Li J, Kastner J H, Prigozhin G Y and Schulz N S 2003 Refining Chandra/ACIS subpixel event repositioning using a backside-illuminated CCD model *Astrophys. J.* **590** 586–92

[10] IXS beamline User Working Group 2011 IXS: A Two-Branch Beamline for Inelastic X-ray Scattering **SCI-BLP-05**

[11] Grande M, Maddison B J, Howe C J, Kellett B J, Sreekumar P, Huovelin J, Crawford I A, Duston C L, Smith D, Anand M, Bhandari N, Cook A, Fernandes V, Foing B, Gasnaut O, Goswami J N, Holland A, Joy K H, Kochney D, Lawrence D, Maurice S, Okada T, Narendranath S, Pieters C, Rothery D, Russell S S, Shrivastava A, Swinyard B, Wilding M and Wieczorek M 2009 The C1XS X-ray Spectrometer on Chandrayaan-1 *Planet. Space Sci.* **57** 717–24

[12] Den Herder J W, Brinkman A C, Kahn S M, Branduardi-Raymont G, Thomsen K, Aarts H, Audard M, Bixler J V, den Boggende A J, Cottam J, Decker T, Dubbeldam L, Erd C, Goulooze

H, Gudel M, Guttridge P, Hailey C J, Al Janabi K, Kaastra J S, de Korte P A J, van Leeuwen B J, Mauche C, McCalden A J, Mewe R, Naber A, Paerels F B, Peterson J R, Rasmussen A P, Rees K, Sakelliou I, Sako M, Spodek J, Stern M, Tamura T, Tandy J, de Vries C P, Welch S and Zehnder A 2001 The reflection grating spectrometer on board XMM-Newton *Astron. Astrophys.* **365** L7–17

[13] Dallera C, Puppin E, Trezzi G, Incorvaia N, Fasana A, Braicovich L, Brookes N B and Goedkoop J B 1996 Soft X-ray emission spectroscopy at ESRF beamline 26 based on a helical undulator *J. Synchrotron Radiat.* **3** 231–8

[14] Kotani A and Shin S 2001 Resonant inelastic x-ray scattering spectra for electrons in solids *Rev. Mod. Phys.* **73** 203–46

[15] Hämäläinen K and Manninen S 2001 Resonant and non-resonant inelastic x-ray scattering *J. Phys. Condens. Matter* **13** 7539–55

[16] Ament L J P, van Veenendaal M, Devereaux T P, Hill J P and van den Brink J 2011 Resonant inelastic x-ray scattering studies of elementary excitations *Rev. Mod. Phys.* **83** 705

[17] Schnürer M, Streli C, Wobrauschek P, Hentschel M, Kienberger R, Spielmann C and Krausz F 2000 Femtosecond X-ray fluorescence *Phys. Rev. Lett.* **85** 3392

[18] Penner-Hahn J E 1999 X-ray absorption spectroscopy in coordination chemistry *Coord. Chem. Rev.* **190-192** 1101–23

[19] Auger P 1975 The Auger effect *Surf. Sci.* **48** 1–8

[20] Damascelli A 2004 Probing the electronic structure of complex systems by ARPES *Phys. Scr.* **T109** 61–74

[21] Monney C, Bisogni V, Zhou K J, Kraus R, Strocov V N, Behr G, Malek J, Kuzian R, Drechsler S-L, Johnston S, Revcolevschi A, Geck J and Schmitt T 2013 Determining the Short-Range Spin Correlations in the Spin-Chain Li_ {2} CuO_ {2} and CuGeO_ {3} Compounds Using Resonant Inelastic X-Ray Scattering *Phys. Rev. Lett.* **110** 087403

[22] Krause M O 1979 Atomic radiative and radiationless yields for K and L shells *J. Phys. Chem. Ref. Data* **8** 307–27

[23] Winick H 1994 *Synchrotron radiation sources: a primer* (Singapore: World Scientific)

[24] Schulz L, Bieri T, Gaiffi N and Steinacher M 2003 Status report of the SLS storage ring vacuum system: experience after two years of operation *PSI - Sci. Tech. Rep. 2003* **VI** 28–9

[25] Joho W, Muñoz M and Streun A 2006 The SLS booster synchrotron *Nucl. Instruments Methods Phys. Res. Sect. A Accel. Spectrometers, Detect. Assoc. Equip.* **562** 1–11

[26] Wiedemann H 2003 *Synchrotron radiation* (Verlag Berlin Heidelberg New York: Springer)

[27] Attwood D T, Naulleau P, Goldberg K A, Tejnil E, Chang C, Beguiristain R, Batson P, Bokor J, Gullikson E M, Koike M, Medecki H and Underwood J H 1999 Tunable coherent radiation in the soft X-ray and extreme ultraviolet spectral regions *IEEE J. Quantum Electron.* **35** 709–20

[28] Margaritondo G 1995 A primer in synchrotron radiation: Everything you wanted to know about SEX (Synchrotron Emission of X-rays) but were afraid to ask *J. Synchrotron Radiat.* **2** 148–54

[29] Sasaki S, Kakuno K, Takada T, Shimada T, Yanagida K and Miyahara Y 1993 Design of a new type of planar undulator for generating variably polarized radiation *Nucl. Instruments Methods Phys. Res. Sect. A Accel. Spectrometers, Detect. Assoc. Equip.* **331** 763–7

[30] Schmidt T, Imhof A, Ingold G, Jakob B and Vollenweider C 2007 A fixed gap APPLE II undulator for SLS *Ninth International Conference on Synchrotron Radiation Instrumentation* vol 879 (Daegu: American Institute of Physics) pp 400–3

[31] Strocov V N, Schmitt T, Flechsig U, Schmidt T, Imhof A, Chen Q, Raabe J, Betemps R, Zimoch D, Krempasky J, Wang X, Grioni M, Piazzalunga A and Patthey L 2010 High-resolution soft X-ray beamline ADRESS at the Swiss Light Source for resonant inelastic X-ray scattering and angle-resolved photoelectron spectroscopies *J. Synchrotron Radiat.* **17** 631–43

[32] Dinardo M E, Piazzalunga A, Braicovich L, Bisogni V, Dallera C, Giarda K, Marcon M, Tagliaferri A and Ghiringhelli G 2007 Gaining efficiency and resolution in soft X-ray emission spectrometers thanks to directly illuminated CCD detectors *Nucl. Instruments Methods Phys. Res. Sect. A Accel. Spectrometers, Detect. Assoc. Equip.* **570** 176–81

[33] Sasaki T A, Chugan N and Muramatsu Y 2001 Performance of soft X-ray emission spectrometer employing charge-coupled device detector *Nucl. Instruments Methods Phys. Res. Sect. A Accel. Spectrometers, Detect. Assoc. Equip.* **467-468** 1489–92

[34] Strocov V N 2011 Private communication

[35] Henke B L, Gullikson E M and Davis J C 1993 X-Ray interactions: photoabsorption, scattering, transmission, and reflection at E = 50-30000 eV, Z=1-92 *At. Data Nucl. Data Tables* **54** 181–342

[36] Einstein A 1905 Über einen die Erzeugung und Verwandlung des Lichtes betreffenden heuristischen Gesichtspunkt *Ann. Phys.* **322** 132–48

[37] Einstein A 1965 Concerning an heuristic point of view toward the emission and transformation of light *Am. J. Phys.* **33** 367

[38] Berger M J, Hubbell J H, Seltzer S M, Chang J, Coursey J S, Sukumar R, Zucker D S and Olsen K 2010 XCOM: Photon Cross Section Database (version 1.5)

[39] Janesick J R 2001 *Scientific charge-coupled devices* (Bellingham, WA: SPIE Press)

[40] Geist J and Wang C S 1983 New calculations of the quantum yield of silicon in the near ultraviolet *Phys. Rev. B* **27** 4841–7

[41] Geist J and Zalewski E F 1979 The quantum yield of silicon in the visible *Appl. Phys. Lett.* **35** 503–5

[42] Lumb D H 1990 Applications of charge coupled devices to X-ray astrophysics missions *Nucl. Instruments Methods Phys. Res. Sect. A* **288** 219–26

[43] Everhart T E and Hoff P H 1971 Determination of kilovolt electron energy dissipation vs penetration distance in solid materials *J. Appl. Phys.* **42** 5837

[44] Hopkinson G R 1987 Analytic modeling of charge diffusion in charge-coupled-device imagers *Opt. Eng.* **26** 766–72

[45] Boyle W S and Smith G E 1970 Charge coupled semiconductor devices *Bell Syst. Tech. J.* **49** 587–93

[46] Walden R H, Krambeck R H, Strain R J, McKenna J, Schryer N L and Smith G E 1972 The buried channel Charge Coupled Device *Bell Syst. Tech. J.* **51** 1635–40

[47] Kraft R P, Burrows D N, Garmire G P, Nousek J A, Janesick J R and Vu P N 1995 Soft x-ray spectroscopy with sub-electron readnoise charge-coupled devices *Nucl. Instruments Methods Phys. Res. Sect. A* **361** 372–83

[48] Holland A D, Turner M J L, Abbey A F and Pool P J 1996 MOS CCDs for the EPIC on XMM *EUV, X-Ray, and Gamma-Ray Instrumentation for Astronomy* vol 2808 (Denver, CO: SPIE) p 414

[49] Bailey P, Cross M, Pool P J, Castelli C M, Holland A D, Lumb D H, van Essen P, Verhoeve P, Jansen F A and de Korte P A J 1990 Soft X-ray performance of back-illuminated EEV CCDs *EUV, X-Ray, and Gamma-Ray Instrumentation for Astronomy* vol 1344 (San Diego, CA: SPIE) pp 356–71

[50] Huang C M, Burke B E, Kosicki B B, Mountain R W, Daniels P J, Harrison D C, Lincoln G A, Usiak N, Kaplan M A and Forte A R 1989 A new process for thinned, back-illuminated CCD imager devices *International Symposium on VLSI Technology, Systems and Applications* (Taipei: Proceedings of Technical Papers) pp 98–101

[51] Howes M J and Morgan D V 1979 *Charge-coupled devices and systems* (Chichester, England and New York: Wiley-Interscience)

[52] Seabroke G M, Holland A D, Burt D and Robbins M S 2009 Modelling electron distributions within ESA's Gaia satellite CCD pixels to mitigate radiation damage *Astronomical and Space Optical Systems* vol 7439 (San Diego, CA: SPIE) p 743905

[53] Johnson J B 1928 Thermal agitation of electricity in conductors *Phys. Rev.* **32** 97–109

[54] White M H, Lampe D R, Blaha F C and Mack I A 1974 Characterization of surface channel CCD image arrays at low light levels *IEEE J. Solid-State Circuits* **sc-9** 1–13

[55] Hynecek J 2001 Impactron — A new solid state image intensifier *IEEE Trans. Electron Devices* **48** 2238–41

[56] Robbins M S and Hadwen B J 2003 The noise performance of Electron Multiplying Charge-Coupled Devices *IEEE Trans. Electron Devices* **50** 1227–32

[57] Tutt J H, Holland A D, Hall D J, Harriss R D and Murray N J 2012 The noise performance of Electron-Multiplying Charge-Coupled Devices at X-ray energies *IEEE Trans. Electron Devices* **59** 167–75

[58] e2v technologies plc. 2006 CCD42-10 Inverted Mode Sensor Datasheet, Sensor A1A-100023 Issue 8

[59] e2v technologies plc. 2003 A1A-CCD42-40 Front Illuminated AIMO Ceramic Compact Pack Issue 4

[60] Endicott J 2011 Private communication

[61] e2v technologies plc. 2004 CCD97-00 Back Illuminated 2-Phase IMO Series Electron Multiplying CCD Sensor Datasheet, A1A-CCD97BI_2P_IMO Issue 3

[62] Princeton Instruments (Roper Scientific) 2013 X-ray cameras

[63] Kirkpatrick S 1979 Modeling diffusion and collection of charge from ionizing radiation in silicon devices *IEEE Trans. Electron Devices* **ED-29** 1742–53

[64] Janesick J R, Elliott T, Collins S, Daud T and Campbell D 1987 Charge-coupled device advances for x-ray scientific applications in 1986 *Opt. Eng.* **26** 262156

[65] McCarthy K J, Owens A, Holland A D and Wells A A 1995 Modelling the X-ray response of charge coupled devices *Nucl. Instruments Methods Phys. Res. Sect. A Accel. Spectrometers, Detect. Assoc. Equip.* **362** 538–46

[66] Pavlov G P and Nousek J A 1999 Charge diffusion in CCD X-ray detectors *Nucl. Instruments Methods Phys. Res. Sect. A Accel. Spectrometers, Detect. Assoc. Equip.* **428** 348–66

[67] Hiraga J, Tsunemi H, Yoshita K, Miyata E and Ohtani M 1998 How big are charge clouds inside the Charge-Coupled Device produced by X-ray photons? *Jpn. J. Appl. Phys.* **37** 4627–31

[68] Tsunemi H, Hiraga J and Yoshita K 2000 Comparison of methods of measuring the primary charge-cloud shape produced by an X-ray photon inside the CCD *Phys. Res. Sect. A Accel. Spectrometers, Detect. Assoc. Equip.* **439** 592–600

[69] Prigozhin G, Butler N R, Kissel S E and Ricker G 2003 An experimental study of charge diffusion in the undepleted silicon of X-ray CCDs *IEEE Trans. Electron Devices* **50** 246–53

[70] Tsunemi H, Yoshita K and Kitamoto S 1997 New technique of the X-Ray efficiency measurement of a Charge-Coupled Device with a subpixel resolution *Jpn. J. Appl. Phys.* **36** 2906–11

[71] Raabe J, Tzvetkov G, Flechsig U, Boge M, Jaggi A, Sarafimov B, Vernooij M G C, Huthwelker T, Ade H, Kilcoyne D, Tyliszczak T, Fink R H and Quitmann C 2008 PolLux: A new facility for soft x-ray spectromicroscopy at the Swiss Light Source *Rev. Sci. Instrum.* **79** 113704

[72] Wintz S, Strache T, Körner M, Fritzsche M, Markó D, Mönch I, Mattheis R, Raabe J, Quitmann C, McCord J, Erbe A and Fassbender J 2011 Direct observation of antiferromagnetically oriented spin vortex states in magnetic multilayer elements *Appl. Phys. Lett.* **98** 232511

[73] Tzvetkov G, Graf B, Fernandes P, Fery A, Cavalieri F, Paradossi G and Fink R H 2008 In situ characterization of gas-filled microballoons using soft X-ray microspectroscopy *Soft Matter* **4** 510–4

[74] Raabe J and Watts B 2013 PolLux at the Paul Scherrer Institut

[75] Fano U 1947 Ionization yield of radiations. II. The fluctuations of the number of ions *Phys. Rev.* **72** 26–9

[76] Bertolini G and Coche A 1968 *Semiconductor Detectors* (Amsterdam: North-Holland)

[77] Kurniawan O and Ong V K S 2007 Investigation of range-energy relationships for low-energy electron beams in silicon and gallium nitride. *Scanning* **29** 280–6

[78] Bootsma T M V, van Zwet E J, Brinkman A C, den Herder J W, de Jong L, de Korte P and Olsthoorn S M 2000 Synchrotron calibration and response modelling of back-illuminated XMM-RGS CCDs *Nucl. Instruments Methods Phys. Res. Sect. A Accel. Spectrometers, Detect. Assoc. Equip.* **439** 575–81

[79] Hopkinson G R 1983 Charge diffusion effects in CCD x-ray detectors: I. Theory *Nucl. Instruments Methods Phys. Res.* **216** 423–9

[80] Widenhorn R, Weber-Bargioni A, Blouke M M, Bae A J and Bodegom E 2010 Charge diffusion in the field-free region of charge-coupled devices *Opt. Eng.* **49** 044401

[81] Groom D E, Eberhard P H, Holland S E, Levi M E, Palaio N P, Perlmutter S, Stover R J and Wei M 1999 *Point-spread function in depleted and partially depleted CCDs*

[82] Eskin J D and Blouke M M 2009 Improvements in modeling of diffusion-limited point spread function in solid-state detectors *IEEE Trans. Electron Devices* **56** 2468–72

[83] Robbins M S 2011 Private communication

[84] Tutt J H, Holland A D, Murray N J, Hall D J, Harriss R D, Clarke A and Evagora A M 2012 The noise performance of Electron-Multiplying Charge-Coupled Devices at soft X-Ray energy values *IEEE Trans. Electron Devices* **59** 2192–8

[85] Alexander B F and Ng K C 1991 Elimination of systematic error in subpixel accuracy centroid estimation *Opt. Eng.* **30** 1320–31

[86] Jia H, Yang J and Li X 2010 Minimum variance unbiased subpixel centroid estimation of point image limited by photon shot noise *J. Opt. Soc. Am. A* **27** 2038–45

[87] Straulino S, Adriani O, Bonechi L, Bongi M, Bottai S, Castellini G, Fedele D, Grandi M, Papini P, Ricciarini S B, Spillantini P, Taccetti F, Taddei E and Vannuccini E 2006 Spatial resolution of double-sided silicon microstrip detectors for the PAMELA apparatus *Nucl. Instruments Methods Phys. Res. Sect. A Accel. Spectrometers, Detect. Assoc. Equip.* **556** 100–14

[88] Schubert A, Bergamaschi A, David C, Dinapoli R, Elbracht-Leong S, Gorelick S, Graafsma H, Henrich B, Johnson I, Lohmann M, Mozzanica A, Radicci V, Rassool R, Schädler L, Schmitt B, Shi X and Sobott B 2012 Micrometre resolution of a charge integrating microstrip detector with single photon sensitivity *J. Synchrotron Radiat.* **19** 359–65

[89] Turchetta R 1993 Spatial resolution of silicon microstrip detectors *Nucl. Instruments Methods Phys. Res. Sect. A Accel. Spectrometers, Detect. Assoc. Equip.* **335** 44–58

[90] Rao C R 1968 *Linear Statistical Inference and its Applications* (New York: John Wiley & Sons)

[91] Van Trees H L 1968 *Detection, Estimation and Modulation Theory, Part I* (New York: Wiley)

[92] Winick K A 1986 Cramer-Rao lower bounds on the performance of charge-coupled-device optical position estimators *J. Opt. Soc. Am. A* **3** 1809–15

[93] Chao J, Ward E S and Ober R J 2012 Fisher information matrix for branching processes with application to electron-multiplying charge-coupled devices. *Multidimens. Syst. Signal Process.* **23** 349–79

[94] Thomas S 2004 Optimized centroid computing in a Shack-Hartmann sensor *Advancements in Adaptive Optics* vol 5490 (Glasgow, Scotland: SPIE) p 1238

[95] Ober R J, Ram S and Ward E S 2004 Localization accuracy in single-molecule microscopy *Biophys. J.* **86** 1185–200

[96] Hall D J, Soman M, Tutt J, Murray N, Holland A, Schmitt T, Raabe J, Strocov V N and Schmitt B 2012 Improving the resolution in soft X-ray emission spectrometers through photon-counting using an Electron Multiplying CCD *The 9th international conference on Position Sensitive Detectors* vol 7 (Aberystwyth, U.K.: Journal of Instrumentation) p C01063

[97] Lide D R 2003 *CRC Handbook of Chemistry and Physics* (Boca Raton, FL: CRC Press)

[98] Brooks Automation Incorporated 2008 Polycold ® PCC Compact Coolers Efficient Heat Removal for Demanding Applications

[99] Xcam Ltd. 2008 CCD Controller System USB2REM: Operating Manual and Test Results for Controller System 239 1–45

[100] Dalesio L R, Hill J O, Kraimer M, Lewis S, Murray D, Hunt S, Watson W, Clausen M and Dalesio J 1994 The experimental physics and industrial control system architecture: past, present, and future *Nucl. Instruments Methods Phys. Res. Sect. A Accel. Spectrometers, Detect. Assoc. Equip.* **352** 179–84

[101] MathWorks 2013 MATLAB

[102] Terebilo A 2001 Channel Access Client Toolbox for MATLAB *Accelerator and Large Experimental Physics Control Systems* vol eConf C011 (San Jose, USA) p 543

[103] Soman M R, Hall D J, Tutt J H, Murray N J, Holland A D, Schmitt T, Raabe J and Schmitt B 2011 Improving the spatial resolution of a soft X-ray Charge Coupled Device used for Resonant Inelastic X-ray Scattering *13th International Workshop on Radiation Imaging Detectors* vol 6 (Zurich, Switzerland: Journal of Instrumentation) p C11021

[104] Yoshita K, Tsunemi H, Miyata E, Gendreau K C and Bautz M W 1999 Improvement of the position resolution of the CCD for X-ray use *IEEE Trans. Nucl. Sci.* **46** 100–6

[105] Silvaco 2013 Technology Computer Aided Design (TCAD) software

[106] Allinson N M, Allsopp D W E, Quayle J A and Magorrian B G 1991 Effects of soft X-ray irradiation on solid-state imagers *Nucl. Instruments Methods Phys. Res. Sect. A Accel. Spectrometers, Detect. Assoc. Equip.* **310** 267–72

[107] Janesick J, Elliott T and Pool F 1989 Radiation damage in scientific Charge-Coupled Devices *IEEE Trans. Nucl. Sci.* **36** 572–8

[108] Evagora A M 2012 *Factors affecting EMCCD technology for use in space* (Open University)

[109] Altarelli M, Brinkmann R, Chergui M, Decking W, Dobson B, Düsterer S, Grübel G, Graeff W, Graafsma H, Hajdu J, Marangos J, Pflüger J, Redlin H, Riley D, Robinson I, Rossbach J, Schwarz A, Tiedtke K, Tschentscher T, Vartaniants I, Wabnitz H, Weise H, Wichmann R, Witte K, Wolf A, Wulff M and Yurkov M 2006 *The European X-ray free-electron laser* (Hamburg, Germany: DESY XFEL Project Group)

[110] Patterson B D, Abela R, Braun H-H, Flechsig U, Ganter R, Kim Y, Kirk E, Oppelt A, Pedrozzi M, Reiche S, Rivkin L, Schmidt T, Schmitt B, Strocov V N, Tsujino S and Wrulich A F 2010 Coherent science at the SwissFEL x-ray laser *New J. Phys.* **12** 035012